To the Graduate Council:

I am submitting herewith a dissertation written by Hwa-Perng Henry Kao entitled "Dislocation Structure, Deformation Structure, Strengthening Mechanisms and Embrittlement Causes of Ordered Ni_4Mo Alloy." I have examined the final copy of this dissertation for form and content and recommend that it be accepted in partial fulfillment of the requirements for the degree of Doctor of Philosophy, with a major in Metallurgical Engineering.

C R Brooks

C. R. Brooks, Major Professor

We have read this dissertation
and recommend its acceptance:

E. E. Stansbury

Medvedeff

Stanley E Becker

Accepted for the Council:

Lewinkel

Vice Provost
and Dean of The Graduate School

DISLOCATION STRUCTURE, DEFORMATION STRUCTURE, STRENGTHENING MECHANISMS AND EMBRITTLEMENT CAUSES OF ORDERED NI_4MO ALLOY

A Dissertation

Presented for the

Doctor of Philosophy

Degree

The University of Tennessee, Knoxville

Hwa-Perng Henry Kao

March 1986

ACKNOWLEDGEMENTS

I express my sincere gratitude to Prof. Charlie R. Brooks for his continued encouragement, advice, patience and understanding during the course of my doctoral work.

A special word of thanks to Dr. C. T. Liu of Oak Ridge National Laboratory (ORNL) for helpful discussions and the supply of some of the material and permission to use some equipment. The support of the doctoral committee members in providing valuable suggestions is truly appreciated.

I am especially thankful to Dr. B. F. Oliver for his generous help in alloy preparation; to Mr. J. Lehman, Dr. J. A. Horton and Dr. J. Bently (ORNL) for their helpful discussions in TEM work; to Dr. B. Borie for his helpful discussions in X-Ray work; and to Dr. C. L. White (ORNL) for his helpful discussions in Auger electron analysis work.

I also wish to thank Mr. E. H. Lee, Mrs. M. Winsbro (in ORNL) and Mr. H. B. Thompson, Mr. M. Rogers and B. McGill for their contributions to the success of this work.

Some valuable help came from my classmates Vijay Vasudevan, Y. C. Lin and J. P. Zhou and I want to thank them. I especially thank Ashok Choudhury for performing the Auger analysis.

The financial support from the Chung-Shan Institute of Science and Technology in Taiwan (R.O.C.) is gratefully acknowledged.

Finally, I would like to thank my wife, Hu-Shan, for without her consistent encouragement and moral support, I would not have lasted the rigors of student life.

ABSTRACT

The primary purpose of the present research was to investigate the strengthening mechanisms, deformation mechanisms and embrittlement causes of ordered Ni_4Mo from the microstructural and especially the dislocation structure viewpoint.

The following experiments were performed for samples aged at 725°C and 775°C for up to 100,000 minutes. (1) The long-range order parameter and the domain size as a function of aging time were measured. (2) The microstructure for various aging treatments was characterized using optical microscopy, SEM and TEM. (3) The tensile yield strength, elongation and microhardness were measured at 25°C as a function of aging time. (4) The fracture surface of the tensile samples were characterized by SEM. (5) The fracture surfaces for one aging treatment were analyzed by Auger spectroscopy.

Yield strength and elongation were measured at temperature from 300 to 1000°C. The fracture surfaces were characterized by SEM. TEM was used to characterize the dislocation structure of undeformed aged samples, of aged samples after deformation, of aged samples deformed in situ in the TEM and of samples tensile tested at high temperatures.

Upon aging, the strength approximately doubled, but the alloy became very brittle (e.g., less than 4% elongation), fracturing intergranularly along the high angle, prior α boundaries. It was found that the degree of long-range order is much more important in strengthening than is the domain size.

The dislocation structure of deformed Ni_4Mo consisted mainly of overlapping {111} intrinsic stacking faults, which were bounded by widely separated 1/6<112>, single Burgers vector, type dislocations. Upon sufficient deformation, these bands thickened into twins. The dislocations easily passed through the ordered domains, but piled up at the high angle grain boundaries, with which they were incompatable. Continued deformation caused these boundaries to separate, causing brittle intergranular fracture.

The main strengthening factors are the development of long-range order, which limits the slip systems, and the development of a dislocation structure consisting of widely separated partial dislocations, which cannot cross slip. This is probably due to a great reduction in the stacking fault energy upon ordering. The Auger analysis did not indicate any impurity segregation which might have caused grain boundary weakness.

CONTENTS

CHAPTER		PAGE
1.	INTRODUCTION	1
2.	LITERATURE REVIEW	6
2.1	Mechanisms of Strenghening in Ordered Alloys	6
2.1.1	General Comments	6
2.1.2	Ordering Hardening	6
2.1.3	Domain Hardening	10
2.1.4	Defect Hardening	12
2.1.5	Phase Transformation Hardening	12
2.1.6	Impurity Hardening	13
2.2	Introduction to Ni_4Mo Alloys	15
2.2.1	Phase Diagram	15
2.2.2	Crystal Structure of Ni_4Mo	18
2.2.3	Domain Interfaces of Ni_4Mo	24
2.2.4	Long Range-order in β-phase	27
2.2.5	Short-range Order in α-phase	29
2.2.6	Transition of SRO to LRO	34
2.2.7	Kinetics of Transformation (α-β)	36
2.2.8	Dislocation Structure	38
2.2.9	Strengthening Mechanisms	45
2.2.10	Embrittlement's Causes and Fractography	50
3.	EXPERIMENTAL PROCEDURES	53
3.1	Alloy Preparation	53
3.2	Heat Treatment	53
3.3	Metallography	56
3.4	LRO Parameter Measurement by X-ray Diffraction	57
3.5	Tensile Testing	59
3.6	Scanning Electron Microscopy	61
3.7	Transmission Electron Microscopy	61
3.8	Microhardness Measurement	64
3.9	Auger Electron Microanalysis	66

CHAPTER PAGE

4. RESULTS AND DISCUSSIONS..... 68

4.1 Mechanical Properties..... 68

4.1.1 General Comments..... 68
4.1.2 Part 1: Aging Effect..... 68
4.1.3 Part 2: Quenching Temperature Effect. 87
4.1.4 Part 3: High Temperature Softening Resistance..... 92
4.1.5 Part 4: LRO Effect..... 97
4.1.6 Part 5: Grain Size Effect..... 103
4.1.7 Closure..... 109

4.2 Microstructural Observations..... 110

4.2.1 Microstructure Changes with Aging Time..... 110
4.2.2 Fracture Morphology of Ordered Ni Mo Tensile Tested at 25°C..... 122
4.2.3 Fracture Morphology of Ni_4Mo Tensile Tested at Elevated Temperatures..... 130

4.3 Transmission Electron Microscopy..... 133

4.3.1 Superlattice Diffraction Pattern of Ni_4Mo..... 133
4.3.2 Domain Structure and Domain Size Measurement..... 138
4.3.3 Grain Boundary Recrystallization..... 138
4.3.4 General Deformation Structure in SRO Condition..... 142
4.3.5 Deformation Structure in High LRO Condition..... 145
4.3.6 Trace Analysis of Plastic Deformation Bands..... 148
4.3.7 Burgers Vector Analysis of Matrix Dislocations..... 154
4.3.8 Burgers Vector Analysis of Glide Dislocations..... 158
4.3.9 Evidence of 5 Unit Superdislocations.. 158
4.3.10 Stacking Fault Analysis..... 168
4.3.11 Interaction of Gliding Dislocations with Grain Boundary..... 169

CHAPTER PAGE

4.3.12 Glide System Analysis..... 178
4.3.13 Observations of Dislocations Generated in Situ Using a TEM Deformation Stage. 193

4.4 Auger Electron Analysis of Fracture Surface.. 208

4.5 Strengthening Mechanism During Aging..... 221

4.6 Dislocation Structure and Strengthening..... 226

4.7 The Cause of Embrittlement in Ordered Ni_4Mo.. 229

5. CONCLUSIONS AND RECOMMENDATIONS..... 231

REFERENCES..... 236

VITA..... 244

LIST OF TABLES

TABLE		PAGE
1.	Axial Relation of Six Variant Domains of β to the Original α	23
2.	Chemical Composition of the Ni_4Mo Alloy Used in This Research	54
3.	The Effect of Aging Time at 725°C and 775°C on the Mechanical Properties Measured at 25°C	69
4.	The Effect of Aging Time at 725°C and 775°C on the Domain Size	74
5.	The Effect of Aging Time at 725°C and 775°C on the LRO Parameter S	75
6.	The Effect of Quenching Temperature on the LRO Parameter S	88
7.	The Effect of Quenching Temperature on the Mechanical Properties as Measured at 25°C	90
8.	The Elevated Temperature Mechanical Properties of Ni_4Mo for Small Domain Size Condition	93
9.	The Elevated Temperature Mechanical Properties of Ni_4Mo for Large Domain Size Condition	98
10.	The Room Temperature Mechanical Properties of Ni_4Mo for Different LRO Parameter Values	100
11.	The Effect of Quenching Temperature on the LRO Parameter for Large Domain Size Condition	101
12.	The Effect of Annealing Temperature and Time on the α Grain Size	105
13.	The Effect of Prior α Grain Size on the Mechanical Properties Measured at 25°C	106
14.	Burgers Vector Analysis of Matrix Dislocation	157
15.	Burgers Vector Analysis of the Partial Dislocations in the Bands	161

TABLE PAGE

16. Burgers Vector Analysis of the Superdislocation. 165

17. Burgers Vector Analysis of Gliding Partial Dislocations on the (111) Plastic Deformation Plane..... 186

18. Domain Type Determination..... 169

19. Gliding Simulation and Check of the Nearest Neighbor (N.N.) Bonding Change..... 192

20. The Auger Electron Microanalysis of Ni_4Mo Alloy. 219

LIST OF FIGURES

FIGURE		PAGE
1.	A Superdislocation	8
2.	Flow-Stress Variation (Schematic) with Quenched-in Order for Several Superlattice Alloys	9
3.	Creation of Additional Domain Boundary by Slip.	11
4.	Grain Boundary Hardening in NiGa	14
5.	Ni-Mo Phase Diagram	16
6.	Comparison of Composition and Temperature Range of Stability of α and β	17
7.	The Crystal Structure of β (Ni_4Mo)	19
8.	Schematic Diagram of the β Lattice Showing the Relation between the fcc α and the bct Ordered Lattice	21
9.	Atomic Arrangement in the (001) Plane of the Fully Ordered Ni_4Mo Structure	22
10.	Schematic Representation of the Axial Relation Inside Different Type Domains of Ni_4Mo	25
11.	Models for β-domain Boundaries	28
12.	Reciprocal Lattice for the β Phase	30
13.	X-ray Intensity Distribution of Diffuse Intensity	33
14.	Isothermal Time-Temperature-Transformation Diagram for the Ordering Reaction in a Ni-20Mo Alloy	37
15.	Dislocation Structure of Ni and Ni-Mo Alloys in the α Condition	39
16.	The Close-packed (111) Plane of Completely Ordered β	43

FIGURE PAGE

17. The Close-packed (111) Plane of β, Showing Glide Which Could Occur by Superdislocations Containing 5, 3 or 2 Dislocations..... 44

18. Effect on Properties of Aging Quenched α at 700°C..... 47

19. Tensile Yield Strength and Ductility at 25°C as a Function of Aging Time for β and $\alpha+\beta$ Alloys..... 51

20. Design of the Tensile Specimen..... 60

21. The Preparation of TEM Specimens from Tensile Sample's Broken Area..... 62

22. The Deformation Stage and the In Situ Tensile Thin Foil Specimen Used in It..... 64

23. The Dimension of Tensile Specimens Used in the Auger Electron Microanalysis..... 67

24. Effect of Aging Time at 725°C on the Mechanical Properties Measured at 25°C..... 71

25. Effect of Aging Time at 775°C on the Mechanical Properties as Measured at 25°C 72

26. Effect of Aging Time on the Domain Size (Semi-log plot)..... 76

27. Effect of Aging Time on the Long-Range Order Parameter (Semi-log plot)..... 77

28. Effect of Aging Time on the Domain Size (Log-log plot)..... 79

29. Effect of Aging Time on the Long-Range Order Parameter (Log-log plot)..... 80

30. The Relationship Between Yield Strength and Long-Range Order Parameter..... 83

31. The Relationship Between Hardness and Long-Range Order Parameter..... 84

FIGURE PAGE

32. The Relationship Between the Elongation and the Long-Range Order Parameter..... 85

33. Yield Strength as a Function of Domain Size..... 86

34. The Relationship Between the Long-Range Order Parameter and the Quenching Temperature..... 89

35. The Relationship Among the Mechanical Properties, Long-Range Order Parameter and Quenching Temperature..... 91

36. The Effect of Test Temperature on the Yield Strength and Elongation (The prior treatment consisted of aging at 725°C for 1000 minutes)... 94

37. Yield Strength as a Function of Test Temperature for the Ordered Ni_4Mo Alloy, the Commercial Alloys, 316 Stainless Steel, Hastelloy-X, Waspaloy and the Intermetallic Compound Alloy Ni_3Al..... 96

38. The Effect of Test Temperature on the Yield Strength and Elongation (The prior treatment consisted of aging at 850°C for 14,000 minutes). 99

39. The Relationship Between the Yield Strength and Hardness and the Long-Range Order Parameter, Compared Under the Same Large Domain Size..... 102

40. The Effect of Prior α Grain Size on the Yield Strength of Ordered Ni_4Mo Alloy (Yield strength vs. grain size d)..... 104

41. The Effect of Prior α Grain Size on the Yield Strength of Ordered Ni_4Mo Alloy (Yield strength vs. grain size $d^{1/2}$)..... 107

42. The Effect of Prior α Grain Size on the Yield Strength of Ordered Ni_4Mo Alloy (Yield strength vs. grain size $d^{3/4}$)..... 108

43. The Change of Optical Microstructure with Aging Time at 725°C..... 111

44. The Change of Optical Microstructure with Aging Time at 775°C..... 116

FIGURE PAGE

45. The Optical Microstructure after Aging 10 Days at 850 °C..... 118

46. The Change of Microstructure with Aging Time at 725 °C as Observed in the SEM..... 119

47. Fractography of Tensile Samples Tested at 25 °C.. 123

48. Cross-section Through Fracture Surface of Tensile Sample Aged 1000 Minutes at 725 °C..... 127

49. Cross-section Through Fracture Surface of Tensile Sample Aged 14,000 Minutes at 775 °C..... 128

50. Fractography of Tensile Samples Tested at Elevated Temperature..... 131

51. Fractography of Tensile Samples Tested at 1000 °C..... 132

52. Cross-section Through Fracture Surface of Tensile Sample Tested at 1000 °C..... 134

53. The Kikuchi Map and the Diffraction Pattern of Ni_4Mo..... 135

54. Dark Field TEM Micrographs Showing the Effect of Aging Temperature and Time on the Domain Size..... 139

55. TEM Micrographs Showing the Grain Boundary Coarsening by "Recrystallization"..... 140

56. Deformation Structure in the Short Aging Time Condition..... 143

57. Deformation Structure in the High LRO (S=0.9) Condition under Tensile Stress..... 146

58. Deformation Structure (Rolled 3%) in the High LRO (S=0.9) Condition..... 149

59. Deformation Structure (Rolled 8%) in the High LRO (S=0.9) Condition..... 150

FIGURE PAGE

60. Trace Analysis of the Plastic Deformation Bands..... 152

61. Burgers Vector Analysis of the Matrix Dislocations..... 155

62. Burgers Vector Analysis of the Partial Dislocations in the Plastic Deformation Bands... 159

63. 5 Unit Superdislocation..... 163

64. Another Example of 5 Unit Superdislocation..... 167

65. Schematic Illustration of Stacking Fault Contrast from Overlapping Intrinsic Stacking Faults..... 170

66. Overlapping Stacking Faults..... 171

67. Gliding Lattice Dislocations Reacting with High Angle Grain Boundaries..... 172

68. Gliding Lattice Dislocation Reacting with Low Angle Grain Boundary..... 175

69. Gliding Lattice Dislocation Reacting with Twin Boundary..... 176

70. Twisted Grain Boundary..... 177

71. Burgers Vector Analysis of Gliding Partial Dislocation in (111) Plastic Deformation Bands.. 180

72. Selected Area Diffraction Pattern of Grain Analyzed in Figure 71..... 188

73. Primitive Unit "Meshes" and the Stacking of Type D Domain of Ni_4Mo Viewed on (111) Plane..... 191

74. A Sequence of Change of Plastic Deformation Structure..... 195

75. Another Sequence of Change of Plastic Deformation Structure..... 197

76. The Deformation Structure Inside G1..... 199

77. The Deformation Structure Between G1 and G2..... 201

FIGURE PAGE

78. The Deformation Structure Between G2 and G3..... 202

79. A Typical Deformation Structure Formed by In Situ Straining..... 203

80. Another Typical Deformation Structure Formed by In Situ Straining..... 204

81. An Example of Piled-up Dislocations and Their Reaction with a High Angle Grain Boundary..... 205

82. Piled-up Dislocations Reacting with an Incoherent Twin Boundary..... 206

83. A Typical Stacking Fault Contrast Exhibiting a Periodic Sequence..... 207

84. SEM Micrograph Showing Area Analyzed in the Auger Microscope..... 210

85. Auger Electron Spectrum of the Area Shown in Figure 84..... 211

86. SEM Micrograph Showing Location of Spot Analysis D..... 213

87. Auger Electron Spectrum of the Selected Spot D (Figure 86)..... 214

88. SEM Micrograph Showing Location of Spot Analysis I..... 216

89. Auger Electron Spectrum of the Selected Spot I (Figure 88)..... 217

CHAPTER 1

INTRODUCTION

Nickel-molybdenum alloys are of industrial significance and commercial importance because of their good mechanical properties to moderately high temperatures and their excellent corrosion resistance in aqueous media, especially in nonoxidizing acid, even at high temperature (1-3). There are primarily two commercial Ni-Mo alloys, Hastelloy B and Hastelloy B2 (both based on the Ni-20 at.% Mo composition), which are used for their corrosion resistance.

In addition, the physical metallurgy of Ni-Mo alloys is of practical interest because of the ordered phases which appear in this system and which may have useful high temperature properties characteristic of some ordered intermetallic compounds. Also, such compounds form the strengthening precipitate in many superalloys, and the addition of Mo to the Ni-base superalloys may allow formation of Ni-Mo compounds.

A considerable amount of research has been conducted over the years in the Materials Science and Engineering Department at the University of Tennessee, Knoxville on Ni-Mo alloys. The research has centered around the physical metallurgy of this system, and has concentrated especially on the 20 at.% Mo composition, which forms a

long-range ordered, intermetallic compound below 868°C. The structure, mechanism and kinetics of the formation of this ordered phase have received considerable attention, with a great amount of effort given to correlating the ordered structure to properties.

The ordering process in the Ni-20 at.% Mo composition causes considerable changes in the mechanical properties, with strengthening being especially prominent. As in other ordering reactions, the strengthening is related to several factors, such as degree of order, antiphase boundary energy, elastic strain due to volume and shape change upon ordering, domain size, grain size, crystal structure, defect structure, etc. (4-8).

The influence of ordering in Ni_4Mo on the mechanical properties and deformation of Ni-Mo alloys has been investigated extensively (9-26). The properties are quite sensitive to the thermal history of the alloys, and significant strengthening can occur for some treatments. Very different conclusions have been drawn regarding the mechanisms of deformation and strengthening after different treatments, and no clearly substantiated models have been developed to correlate the structure and properties.

The key to understanding the mechanical behavior lies in understanding the interaction of dislocations with the strain field and the interfaces (domain boundaries and grain boundaries). Thus, it is clear that detailed, systematic studies of the effects of aging on the fine structure, deformation structure and the mechanical properties are necessary. This requires utilization of transmission electron microscopy to resolve the fine detail, and appropriate analysis of the structure from these observations.

One characteristic which greatly restricts the potential use of Ni_4Mo is the lack of ductility. As this alloy orders and strengthens, it becomes extremely brittle. The causes of this have never been established. Since such embrittlement occurs in other ordered alloys, the problem has received a lot of attention, and recently micro- and macro-alloying have proven effective in producing ductile, long-range ordered alloys (e.g., in Ni_3Al (8,27-33)). Thus, intimately associated with a study of strenthening mechanisms in Ni_4Mo is the search for the causes of the embrittlement.

The research described in this thesis was designed to determine the reasons that strengthening and accompanying embrittlement occur upon ordering in Ni_4Mo. To this end, several types of experiments were conducted, which are described briefly below.

1. The effect of aging times up to 100,000 minutes at 725 ℃ and 775 ℃ on the domain size, long-range order parameter, hardness, yield strength and elongation were determined. These data were used to ascertain what microstructural features were responsible for the strengthening that accompanied the ordering process.

2. Central to understanding the reasons that the factors established by the procedure in 1 affect the strength of Ni_4Mo is an understanding of the dislocation structure. Three kinds of deformation structures were produced for observation in the transmission electron microscope: (i) dislocation structure of the gage section of broken tensile samples; (ii) dislocations induced by cold rolling; (iii) in situ observations of dislocations in a straining stage of the microscope. The dislocations produced by these three methods were observed and characterized. The types of dislocations found were then compared to predictions based on various glide simulations of atomic models to establish a credible deformation mechanism.

3. The fracture surface topology of tensile samples for various heat treatments was characterized. This was correlated with the microstructure, and special attention was given to the grain boundary structure.

Attempts were made to detect segregants on the grain boundary surface using Auger spectroscopy.
Also attempts were made to observe the interaction of these grain boundaries with dislocations by in situ observations in the transmission electron microscope.

4. The tensile mechanical properties were measured as a function of test temperature, in order to evaluate the potential of ordered Ni_4Mo for use as a high temperature structural material. The dislocation structure of the samples was characterized using transmission electron microscopy and correlated with the mechanical properties.

CHAPTER 2

LITERATURE REVIEW

2.1 Mechanisms of Strengthening in Ordered Alloys

2.1.1 General Comments.

It is now apparent that ordered alloys may be hardened by virtually all the mechanisms applicable to metals and conventional alloys and, in addition, by several processes unique to this group: order hardening, defect hardening, and domain hardening. Some of these will now be discussed briefly. It is emphasized that any discussion of the mechanical behavior of ordered alloys must be made in terms of dislocation motion.

2.1.2 Ordering Hardening.

Sumino (34) proposed that ordering increases the number of unlike nearest neighbors and at the same time decreases the distance between them. This shortening of nearest neighbor distances may be viewed as a local strain field which would interact with the strain field of the dislocation. Consequently an additional energy of disorder would have to be supplied by the applied stress in order to move the dislocation. Sumino's theory also predicts that the yield point will have a maximum at the critical temperature T_C. Koehler and Seitz (35) pointed out that single dislocations generate a plane of disorder

(anti-phase boundary) when they move, and this should result in a high yield point. They further showed that when a second dislocation followed the plane of the first, reordering occurs. Consequently, if the two dislocations moved together as a superdislocation (Figure 1), there should be no net increase in disorder and therefore no increase in strength.

A summary of a proposed model of the dependence of the room temperature flow-stress of ordered alloys which have been quenched from a series of temperatures on the degree of order is shown in Figure 2 (36). A rise in room temperature flow-stress occurs with decreasing quenching temperature (or increasing degree of order) so long as unit dislocations control deformation behavior. At whatever degree of order that a sizeable proportion of superlattice dislocations is operative, the room temperature flow-stress drops suddenly for Cu_3Au, but gradually for other superlattices.

The only application of these models to order hardening in Ni-Mo alloys is that of Goodrum and Lefevre (22). They calculated the shear stress increment due to order for Ni-17 at.% Mo ordered alloy ($\alpha+\beta$ phases).

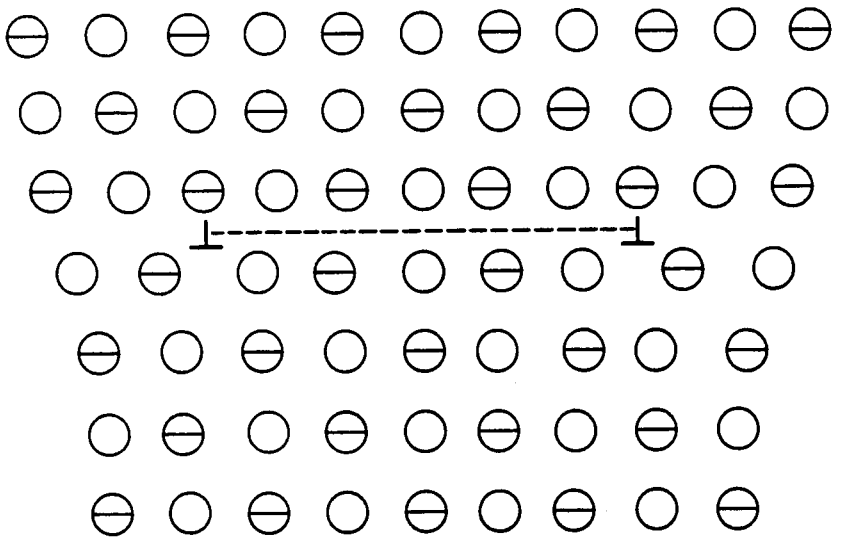


Figure 1. A superdislocation.

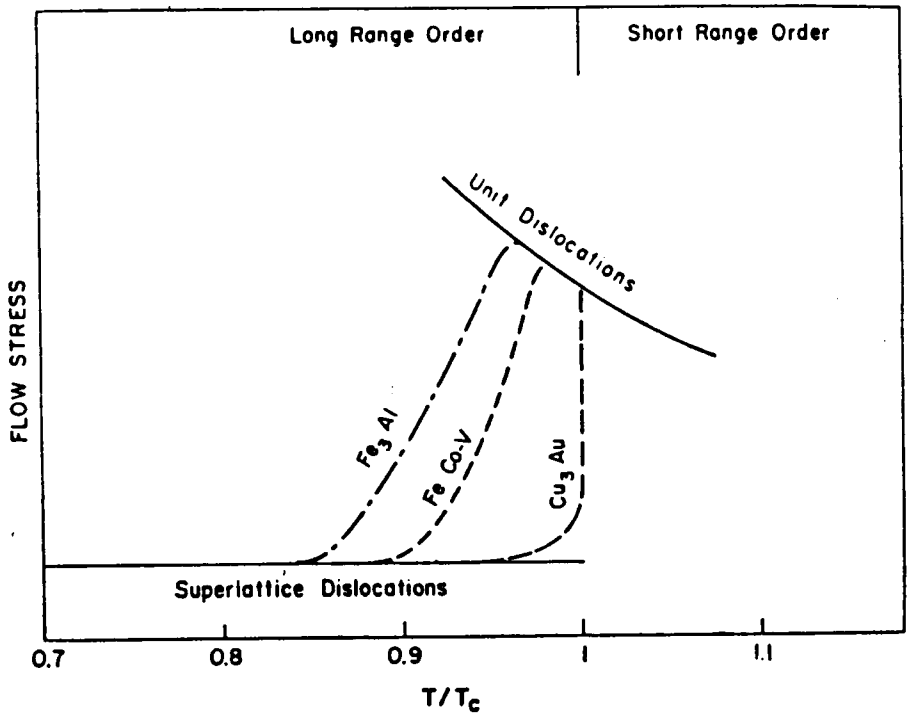


Figure 2. Flow-stress variation (schematic) with quenched-in order for several superlattice alloys (Ref.36).

2.1.3 Domain Hardening.

Ardley's results (37) show that the low temperature strength is dependent both on the degree of long-range order and on the size of anti-phase domains. That a domain boundary offers a resistance to slip can be seen qualitatively from Figure 3 which shows that slip creates additional anti-phase boundary and, therefore, additional energy must be expended. A maximum strength is formed at a critical domain size. Cottrell (38), who extended an earlier suggestion of Fisher (39), showed that the optimum size results from two opposing effects: the smaller the domain size the more anti-phase boundaries are created at an early stage of deformation and hence the harder it is to begin slip, yet the smaller the domain size, the more effectively disordered the material, the less the energetic difference between the slipped and unslipped conditions, and the weaker the material.

However, we can not completely control the order and domain size parameters independently by heat treatment. So we need to consider the ordering hardening and domain hardening effects simultaneously in studying strengthening mechanisms of ordered alloys.

Another significant factor is whether slip dislocations move singularly or in pairs (or other combinations) as superdislocations. It is expected that only when the spacing between paired dislocations is less

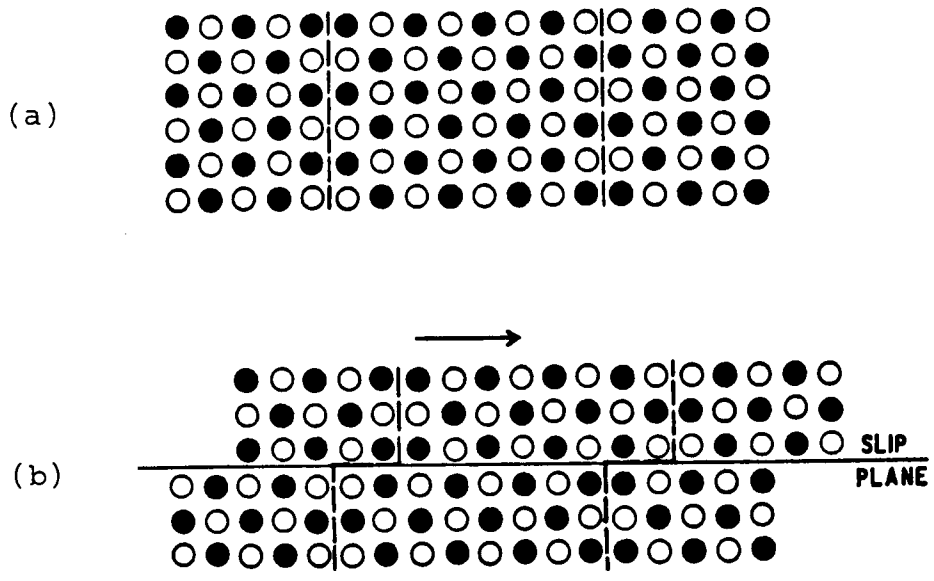


Figure 3. Creation of additional domain boundary by slip (Ref.3).
(a) Before slipping.
(b) After slipping.

than the diameter of the domains, is there a probability for the presence of superdislocations.

2.1.4 Defect Hardening.

It is the opinion of Guard and Westbrook (40) that in systems with a very high ordering energy, the hardening at non-stoichiometric compositions might arise from lattice defects which are required to maintain the number of electrons per unit cell at a constant value required for phase stability. These defects may consist of vacancies, substitutional and interstitial atoms. At low fractions of the melting point, where the deformation proceeds primarily by slip, any perturbation of the regular crystal lattice as afforded by point defects constitutes an impediment to slip, and the material is strengthened. At high homologous temperatures, deformation is diffusion controlled and defects should enhance plastic flow, and hence the material is softer.

2.1.5 Phase Transformation Hardening.

Compounds which order from a disordered solid solution undergo a crystallographic transformation (such as Ni_4Mo from f.c.c (α phase) structure transforming to b.c.t (β phase) structure), and the misfit produces stresses in the lattice; these internal stresses may be sufficient to make it more difficult to move dislocations. Stresses occasioned by the transformation itself can lead

to plastic deformation of the compound phase, e.g., by twinning. In addition, in order-disorder systems, the high coherency strain in the partially ordered state can give rise to very high strength or hardness surpassing the values for either the fully ordered or fully disordered states. Just as with precipitation hardening systems, prolonged heat treatment can result in "overaging" with consequent relaxation of these strains and lowering the strength. One coherency strain model has been proposed by Gerold and Haberkown (41).

2.1.6 Impurity Hardening.

Many intermetallic compounds suffer from intergranular brittleness at low temperatures. Apart from the question of restricted dislocation mobility, another important cause of this embrittlement may be impurity segregation to the grain boundaries during prior thermal or mechanical processing. Seybolt and Westbrook (42) have detected grain boundary hardening of up to 30% relative to the matrix of NiGa by means of microhardness measurements (see Figure 4). In this compound, grain boundary hardening is not a consequence of the precipitation of a second phase. Rather, it appears that oxygen, and perhaps other impurities, when occupying interstitial positions in the lattice, cause appreciable lattice distortion and hardening which frequently cause intergranular failure.

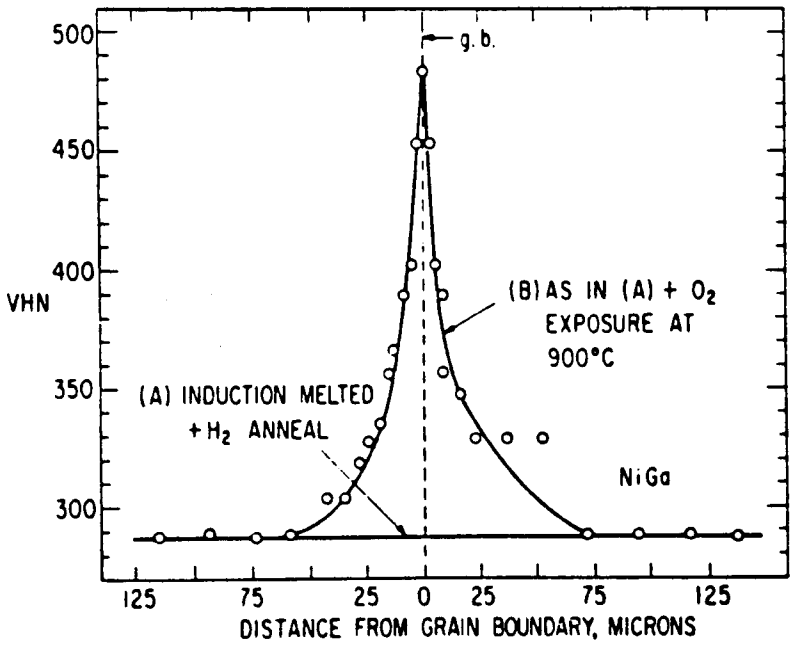


Figure 4. Grain boundary hardening in NiGa (Ref.42).

2.2 Introduction to Ni_4Mo Alloys

2.2.1 Phase Diagram.

Figure 5 (43) shows the phase relations in the Ni-Mo system. The solubility of Mo in Ni is considerable. There are three intermetallic (ordered) compounds which occur at or near stoichiometry: Ni_4Mo (β), Ni_3Mo (γ) and NiMo (δ). On heating β decomposes by a peritectoid reaction.

The literature associated with the Ni-Mo phase diagram is summarized in "Constitution of Binary Alloys"(44) and its supplements (43,45). Only more recent work and studies which elucidate details of the Ni-rich portion of the diagram (around β phase) are referred to here. This region as defined by Casselton and Hume-Rothery (46), Guthrie and Stansbury (47), and Heijwegen and Rieck (48) is shown in Figure 6. In addition, Kozlov and Kushnarenko (49) have proved that a 20.7 at.% Mo alloy is entirely β. Gust et al. (50) placed the existence region of β between 19.5 and 20.0 at.% Mo. There have been numerous investigations of the formation of β from α, but few give sufficient details about the exact composition of the alloys used to assist in defining the β-boundaries. However, considering the wealth of studies on β-alloys given as 20 at.% Mo, Brooks et al. (26) believe that β encompasses the stoichiometric Ni_4Mo.

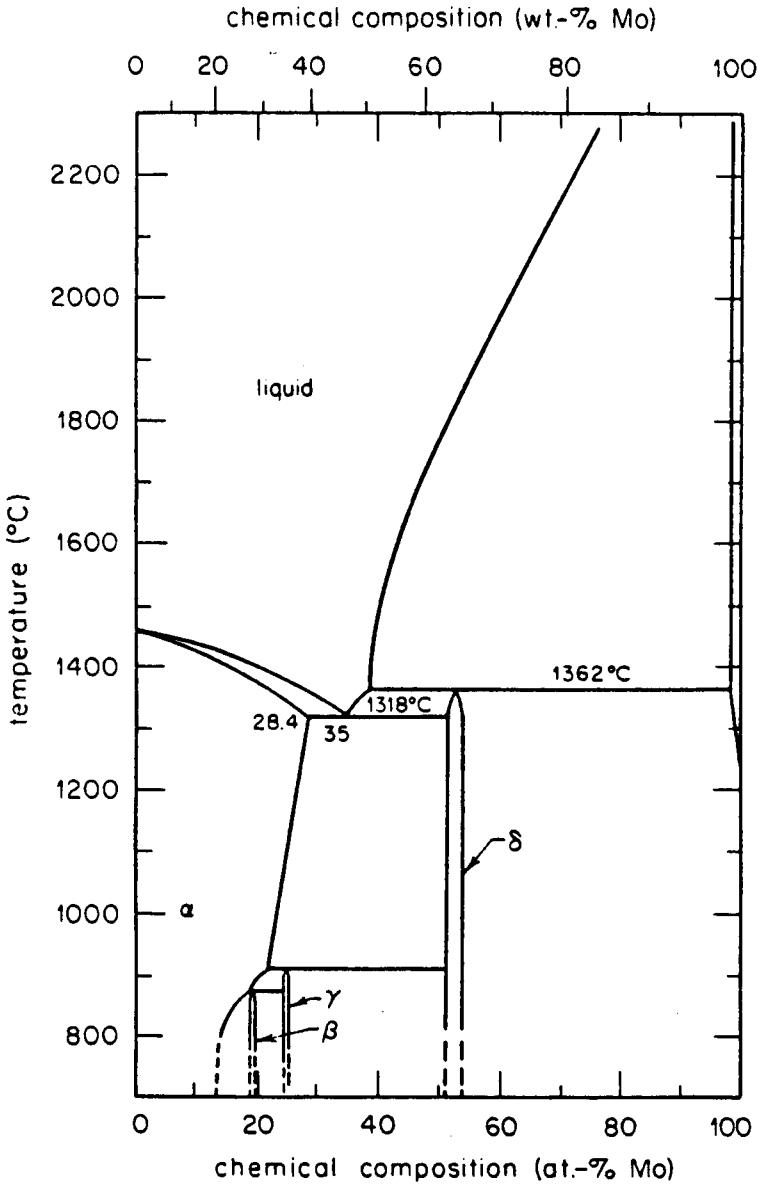


Figure 5. Ni-Mo phase diagram (Ref. 43).

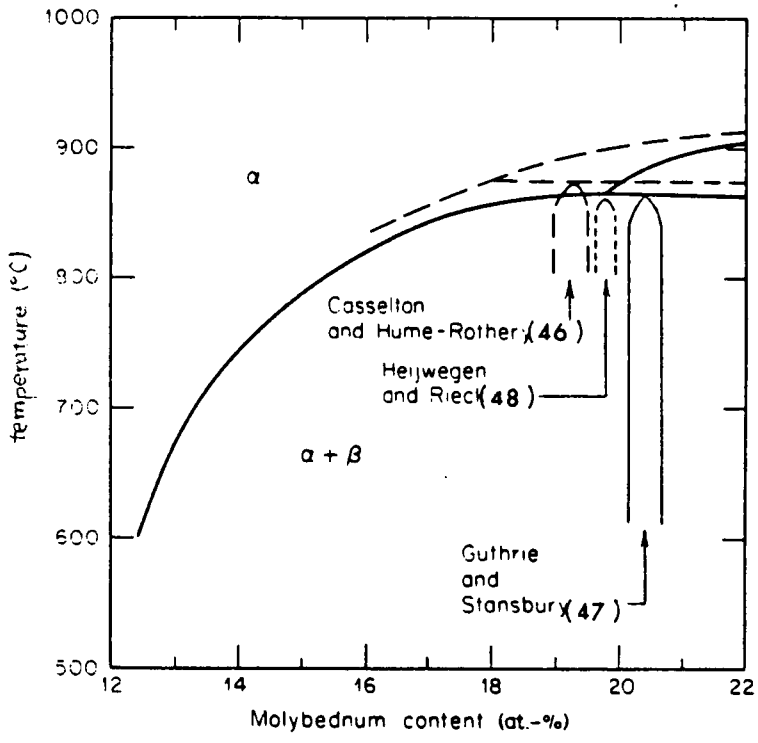


Figure 6. Comparison of composition and temperature range of stability of **α** and **β**.

Guthrie and Stansbury (47) placed the decomposition temperature of β at 868±5 °C. Recent electrical resistivity (51) and specific heat (26) measurements have confirmed the temperature to be 868±3 °C. Kozlov and Kushnarenko (49) placed the peritectoid temperature at 876±5 °C.

2.2.2 Crystal Structure of Ni_4Mo.

Grube and Schlect (52) were the first to report the existence of the β-phase (Ni_4Mo), and found it to be tetragonal with c/a ratio of 0.986. Harker (53) carried out a more detailed study based on powder-diffraction patterns. He found a Ni-18.7 at.% Mo alloy undergoes an ordering reaction below 840 °C which results in a slight tetragonal distortion of the cubic lattice. A new unit cell had to be used to describe the superlattice. This unit cell is body-centred tetragonal (bct) with space group I4/m and lattice parameters a=5.732 Å, c=3.571 Å, and c/a = 0.6231. The volume of this cell is 2.5 times the volume of the distorted fcc cell and contains ten atoms: Mo in the two positions with coordinates 0,0,0 and 1/2,1/2,1/2 and Ni in the eight positions with coordinates $x,y,0$; $\bar{x},\bar{y},0$; $\bar{y},x,0$; $y,\bar{x},0$; $x+1/2,y+1/2,1/2$; $\bar{x}+1/2,y+1/2,1/2$; $\bar{y}+1/2,x+1/2,1/2$; $y+1/2,\bar{x}+1/2,1/2$ where x=1/5 and y=2/5. This superlattice is classified as a D1a type. The crystal structure is shown in Figure 7.

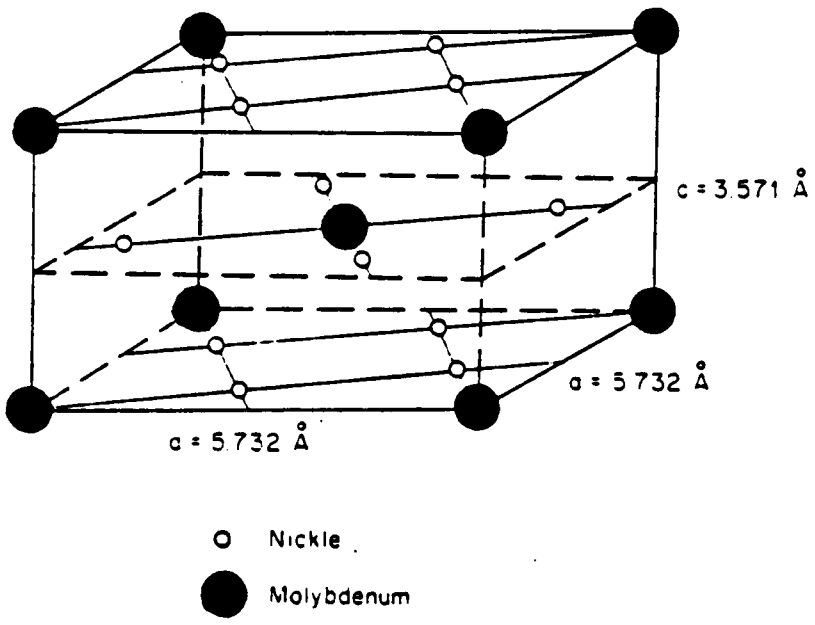


Figure 7. The crystal structure of $\beta(Ni_4Mo)$.

Later authors have confirmed the result of Harker. Guthrie and Stansbury (47) found the unit cell dimensions to be a = 5.727 Å, c = 3.566 Å, c/a = 0.623 while Casselton and Hume-Rothery (46) reported that a = 5.683 Å, c = 3.592 Å, and c/a = 0.632.

The orientation relationship between the β-phase and the parent fcc α solid solution may be understood by reference to Figure 8 (47) and Figure 9 (54).

Figure 8 shows the atomic arrangement on a (100) plane of the α-phase(47). The base of the fcc α is indicated by dashed lines; the solid lines show the base of the bct superlattice. Note that Mo atoms are placed so as to occupy every fifth position along a [110] direction in this plane. The c-axis of the bct cell is perpendicular to the plane of Figure 8 and parallel to one of the cube edges in the fcc α-phase.

Okamoto and Thomas (54) have shown (Figure 9) that two orientations, namely, type I and II structures, can be generated by a regular layering sequence of Ni and Mo atoms on the {420} planes. Similar layering on the remaining mutually orthogonal pairs of planes of the type {420} will generate type I or II structures with the c-axis along either the [010] or [100] cube axes. So this gives 3x2 = 6 different orientation variants for the β-phase. The axial relations of these six kinds of domains with respect to the α-lattice are given in Table 1

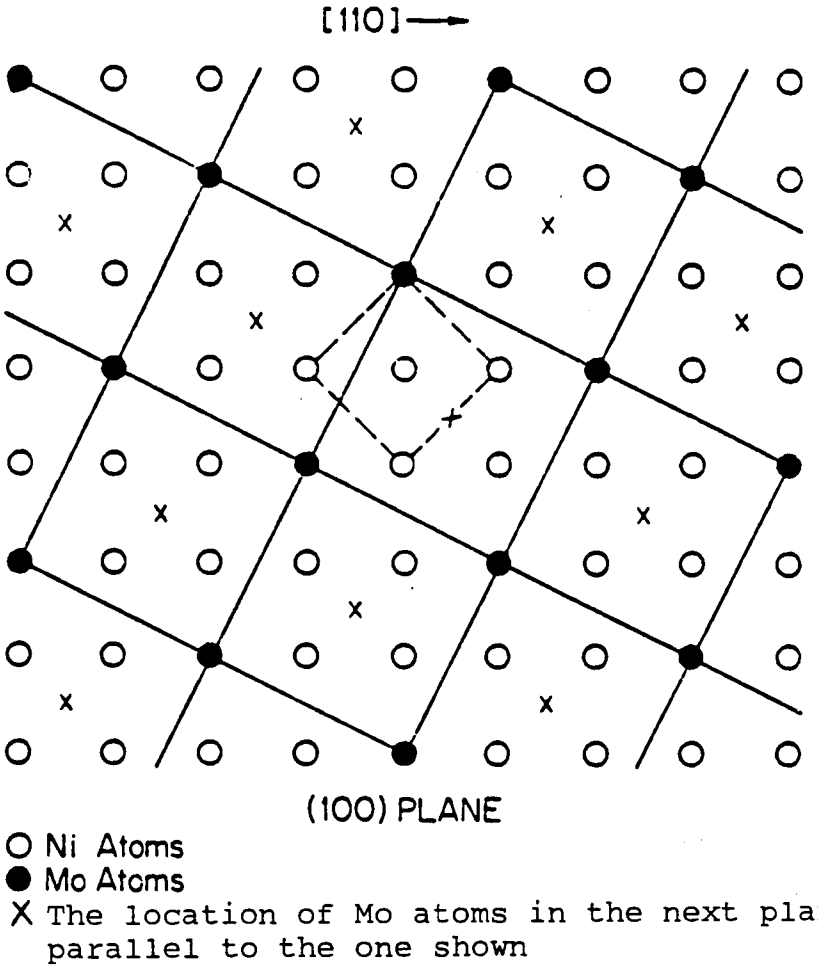


Figure 8. Schematic diagram of the β lattice showing the relation between the fcc α and the bct ordered lattice (Ref.47).

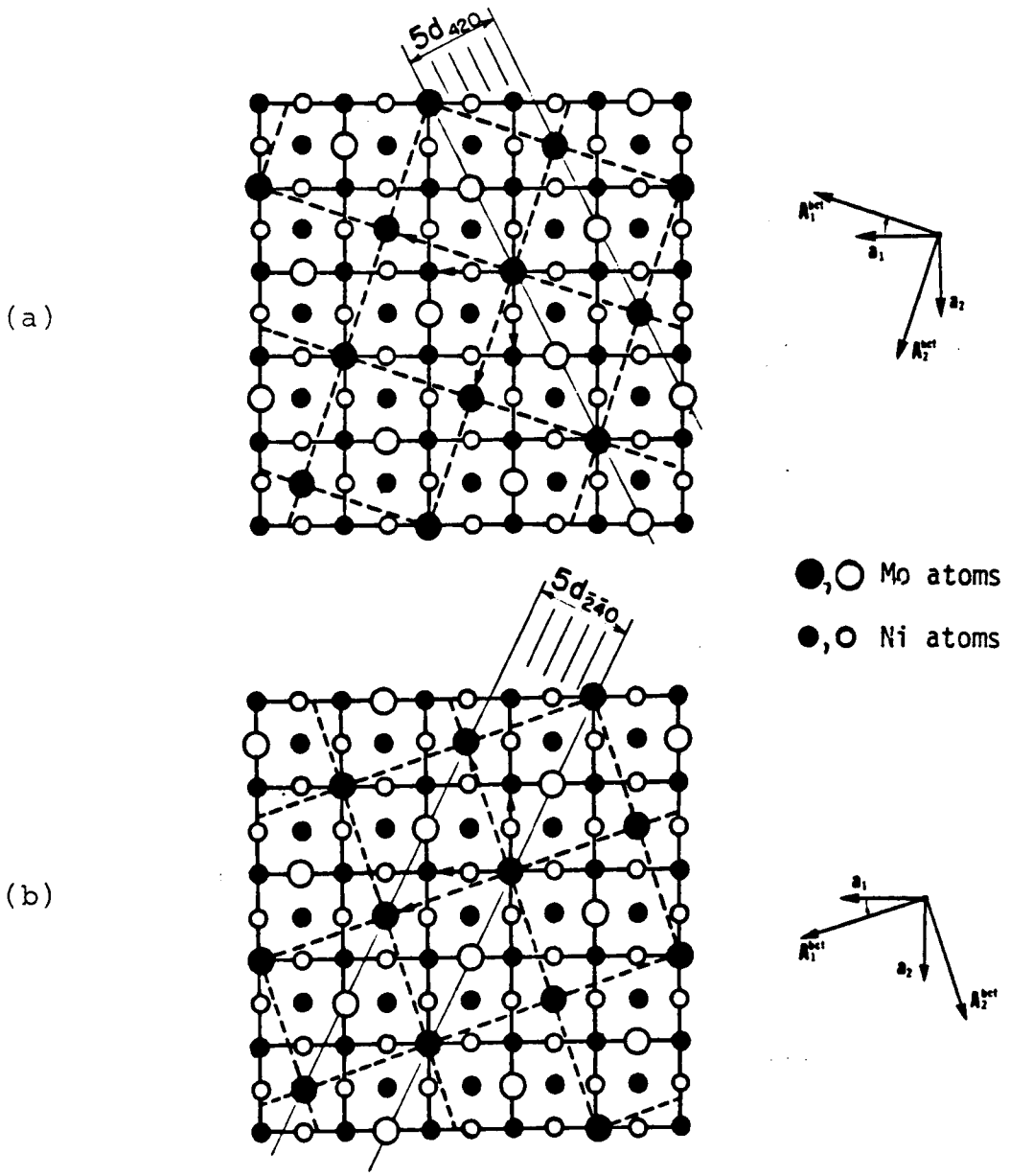


Figure 9. Atomic arrangement in the (001) plane of the fully ordered Ni_4Mo structure (Ref. 54).
(a) Type I.
(b) Type II.

Filled circles, zeroth layer; open circles, ½layer; dashed lines outline b.c.t. unit cell.

Table 1. Axial relation of six variant domains of β to the original α (Ref.15)

	a_1'	a'_2	a_3'
Domain A	$1/2(3a_1-a_2)$	$1/2(a_1+3a_2)$	a_3
Domain B	$1/2(3a_1+a_2)$	$1/2(-a_1+3a_2)$	a_3
Domain C	$1/2(3a_2-a_3)$	$1/2(a_2+3a_3)$	a_1
Domain D	$1/2(3a_2+a_3)$	$1/2(-a_2+3a_3)$	a_1
Domain E	$1/2(3a_3-a_1)$	$1/2(a_3+3a_1)$	a_2
Domain F	$1/2(3a_3+a_1)$	$1/2(-a_3+3a_1)$	a_2

(15) where a_1, a_2, a_3 and a_1', a_2', a_3' are the base vectors of α and β-lattices, respectively. The schematic representation of the two-dimensional primitive unit "mesh" for the six kinds of domains (defined in Table 1) as viewed on a (111) plane of the original α is shown in Figure 10a. The geometry of the A type domain also is illustrated in Figure 10b for a (100) plane. For any given orientation, the bct cell can have its origin at 5 different positions, so altogether there are 30 ways in which the bct cell can form from the fcc α-matrix.

2.2.3 Domain Interfaces of Ni_4Mo.

The numerous ways in which a β-domain may form from a single α-phase grain lead to three different types of domain interfaces. Ruedl et al. (55) have established the relationship between the types of domain interfaces which develop upon transformation from α to β. When there is a relative translation between two adjacent domains with the same orientation, e.g., type A, the interface is an antiphase boundary (APB), with the axial relations given in Table 1. Domains of type A and B are in antiparallel twin (APT) relation and each of these two types is in perpendicular twin (PT) relation with respect to the either four types C, D, E, and F. Similar relations hold for domains of type C and D, and for domain of type E and

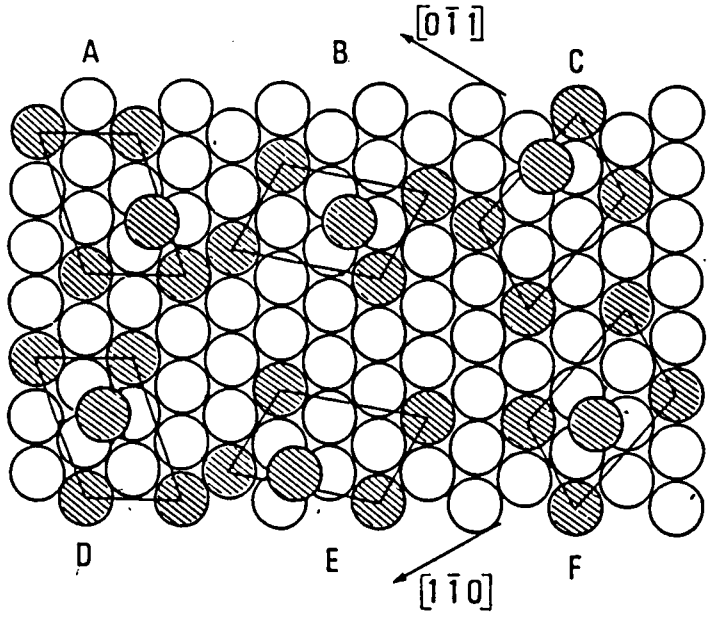
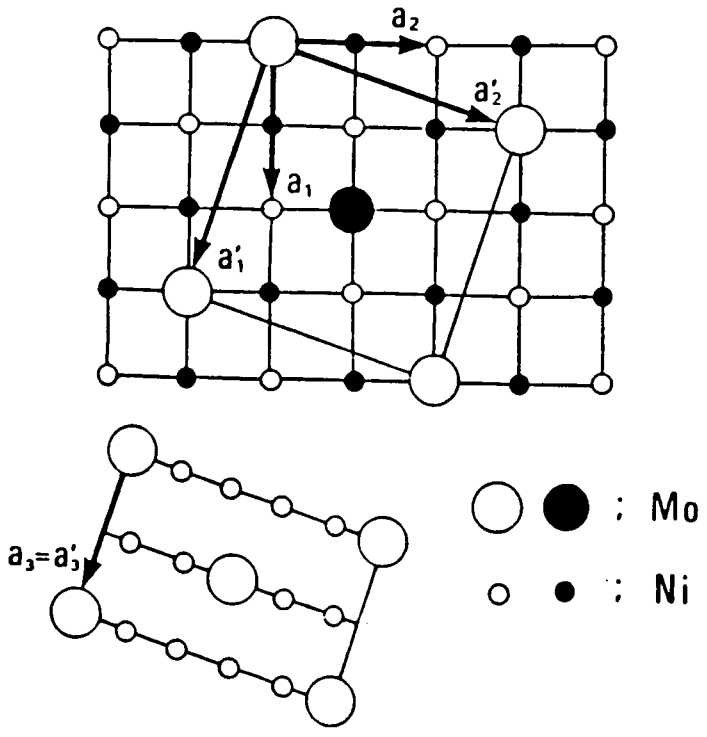


Figure 10. Schematic representationof the axial relation inside different type domains of Ni_4Mo (Ref.15).
(a) Primitive unit mesh for the six kinds of domains (defined in Table 1) viewed on (111) plane.



The positions of atoms in the first and third layers are represented by open circles and those in the second layer by closed circles.

Figure 10. (Continued).
(b) Type A domain shown on (100) plane.

F. For APB, the unit-cell axes of the superlattices in the adjacent domains are parallel to one another, but there is a lattice displacement across the boundary, as illustrated in Figure 11-(a) and 11-(b) for two possible displacement vectors. APT correspond to the interfaces between two orientations variants in which the c-axis of the superlattice are antiparallel (see Figure 11-(c)). It should be noted that the two domain lattices may be displaced relative to each other, generating a combination APB and APT. When the c-axis of adjacent superlattice domains are approximately perpendicular to each other, i.e., when they are along different cube directions in the disordered lattice, the interface is a PT interface (see Figure 11-(d) and 11-(e)).

2.2.4 Long-range Order in β-phase.

At 900-1250°C solution-treatment temperatures, Ni-Mo alloys which contain approximately 20 at.% Mo are SRO, single-phase, fcc solid solutions (46,47,56). At temperatures below 868°C these alloys can transform to the LRO β-phase. The transformation occurs most rapidly at about 775°C but is quite sluggish at temperatures below about 550°C (57,58-60). The results obtained by Lei (51) show that during this transformation the electrical resistivity decreases and hardness increases.

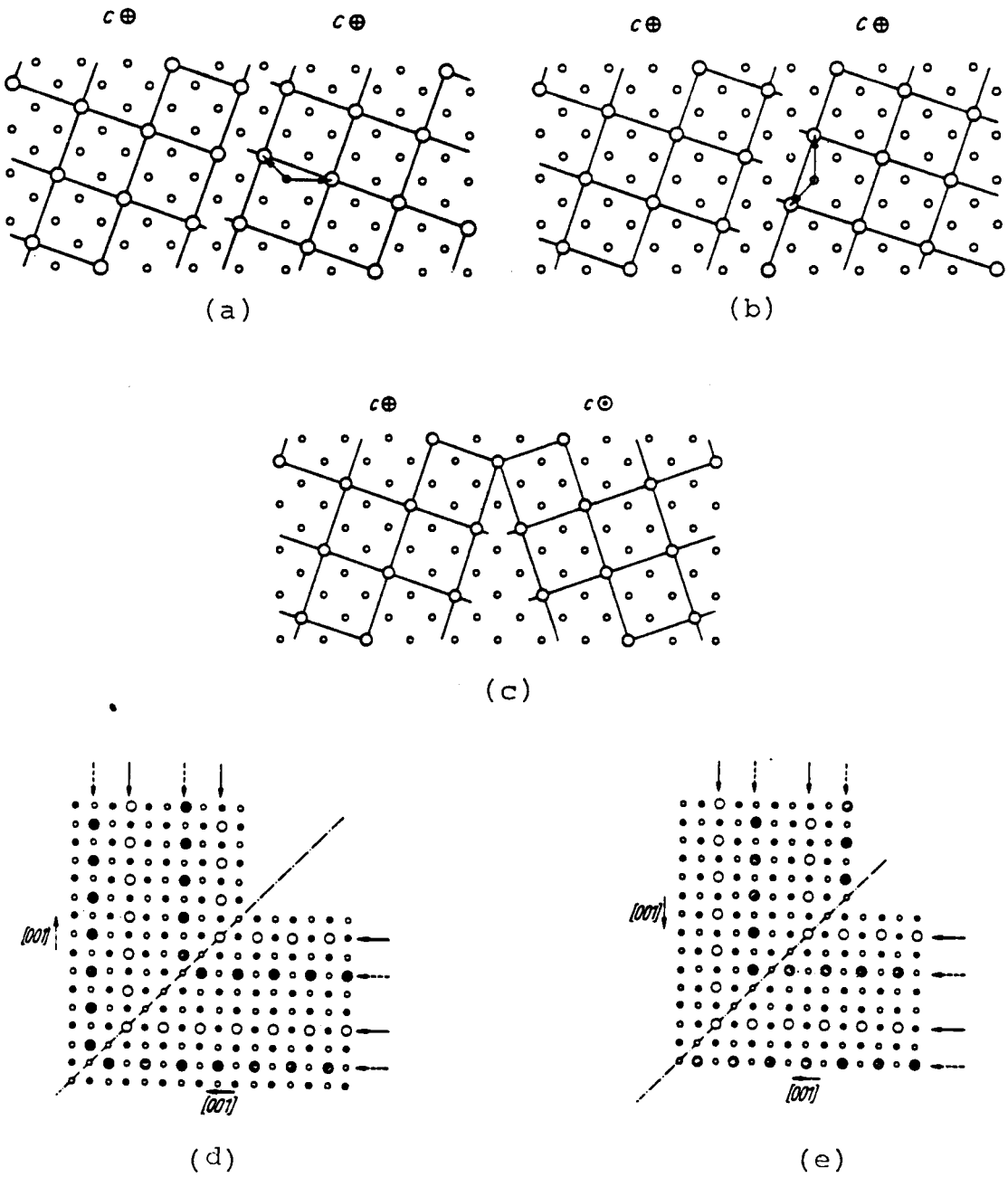
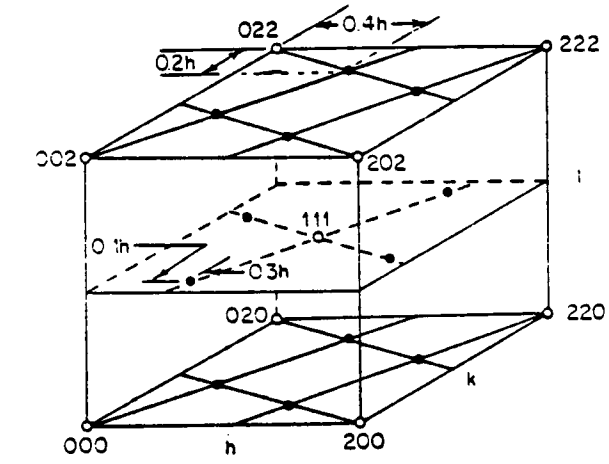


Figure 11. Model for β-domain boundaries (Ref.55).
(a),(b) Anti-phase Boundary.
(c) Anti-parallel Twin.
(d),(e) Perpendicular Twin.

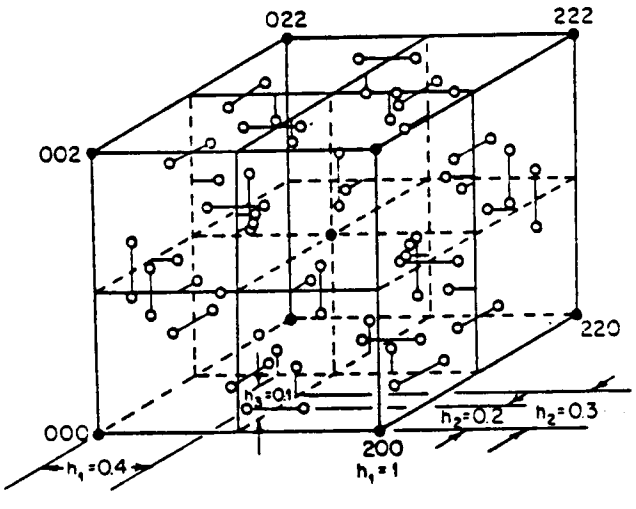
X-ray diffraction and selected-area electron diffraction are two powerful methods used to detect the LRO β-phase structure. Powder-diffraction patterns show superlattice reflections, and both single-crystal X-ray diffraction and selected-area electron diffraction provide sections through the reciprocal lattice. The six orientation variants of the β-phase in a single α-phase crystal produce a rather complex distribution of intensity in reciprocal space. The reciprocal lattice of fully ordered Ni_4Mo is shown in Figure 12-(a) in which only one variant is shown, and the indices are given with respect to the fcc α-phase matrix. Figure 12-(b) shows the reciprocal-lattice for all six variants. Figure 12-(c) shows the [001] zone axis section, and illustrates superlattice reflections from two variants related to each other by the APT relationship.

2.2.5 Short-range Order in α Phase.

Structure varieties within the α-phase region of the Ni-Mo system were first suspected by Thomas (60) by electrical resistivity measurements. He observed that the resistivity of quenched or cold-worked alloys was higher than for slowly cooled alloys. This anomalous behavior was called the "K-state".

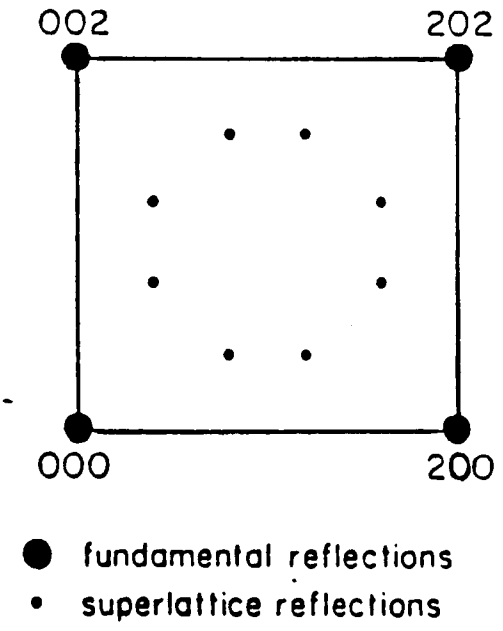


(a)



(b)

Figure 12. Reciprocal lattice for the β phase (Ref.52,58).
(a) Single variant.
(b) Six possible variants.



(c)

Figure 12. (Continued).
(c) (001) plane in reciprocal space.

The first structural studies of SRO in α-phase alloys, including quenched Ni-20Mo, were the X-ray diffuse-scattering measurements made by Spruiell and Stansbury (56). They found that the diffuse scattering produced by SRO contained maxima located at the {1,1/2,0} positions in reciprocal space, as shown in Figure 13-(a) for quenched Ni-20Mo alloy. Reheating the quenched Ni-20Mo alloy for 30 minutes at 650°C caused the diffuse maxima to spilt into peaks located near the positions of the superlattice reflections for LRO Ni_4Mo, as shown in Figure 13-(b). Clapp and Moss (61) were able to predict the positions of the {1,1/2,0} diffuse maxima by an approach based on statistical-thermodynamic arguments involving first-and second-neighbor interaction energies. Ruedl et al. (55) used TEM and selected-area electron diffraction to observe the {1,1/2,0} maxima in reciprocal space for quenched Ni_4Mo. They found very fine bright spots 10 A across in dark-field images obtained using the {1,1/2,0} SRO spots, and suggested that these were microdomains. A more detailed X-ray diffuse-scattering study of SRO in quenched Ni-20Mo alloy and the transition to the LRO state has been carried out by Chakravarti et al. (62). There have been several other extensive studies of SRO in the Ni-20Mo alloy and its transformation to the LRO state using electron microscopy techniques (54,63-71). Thomas and co-workers (54,65,71) suggested a microdomain

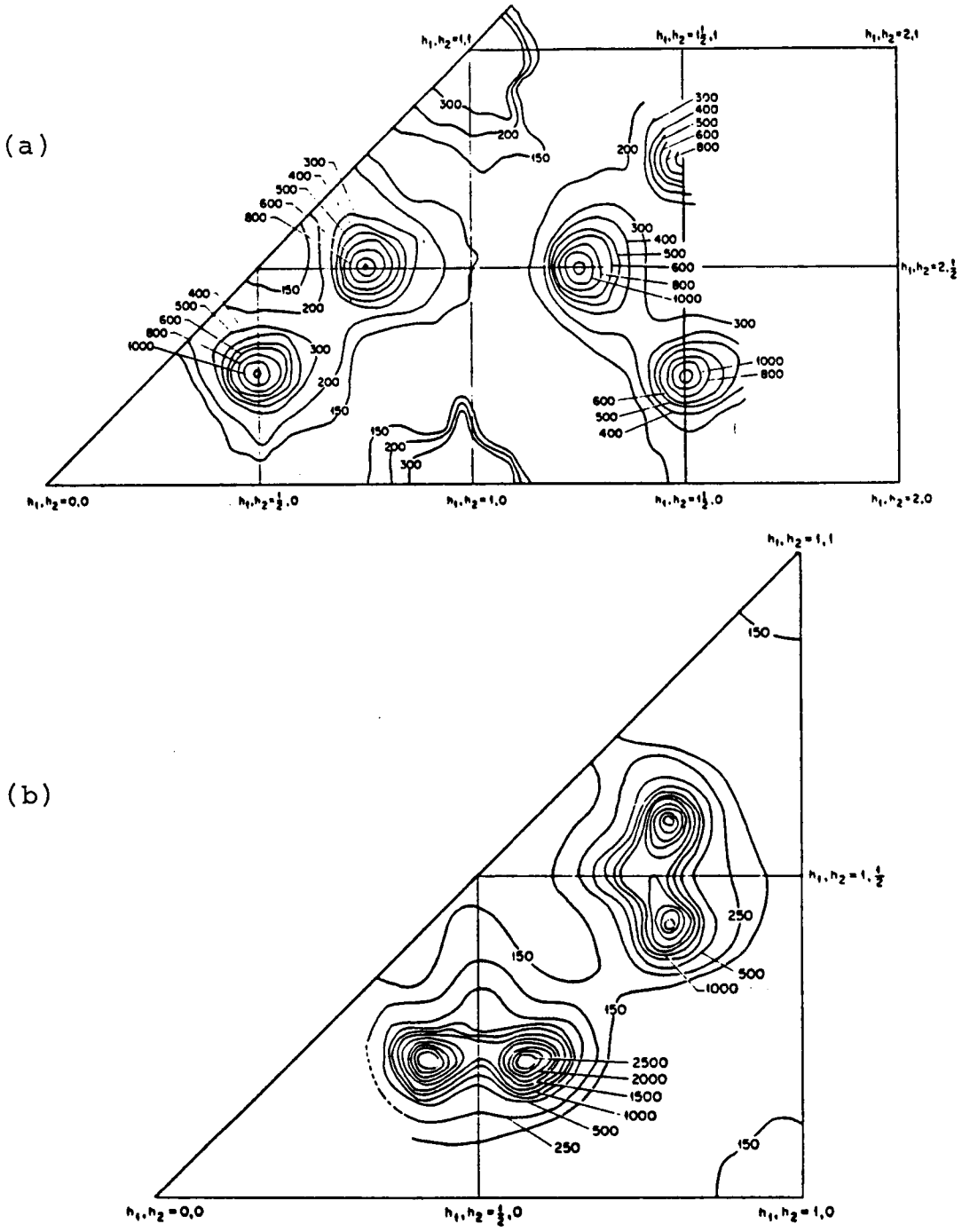


Figure 13. X-ray intensity distribution of diffuse intensity (at-167°C) in the $h_1,h_2,0$ plane of reciprocal space for Ni-20Mo (Ref.56). (a) Quenched from 1000°C into ice water. (b) Quenched and aged for 1 hr at 653°C.

model based on an imperfect D1a structure with DO_{22} like regions, and a multiple-microdomain model with poorly ordered microdomains having the DO_{22}, D1a, and Ni_2Mo structures. However, Van Tendeloo (63), Lefevre and Newman (72) and Chevalier and Stobbs (67,69) have concluded that no microdomains exist in the as-quenched state. They suggested a "static-concentration wave-packet" model of the SRO state to explain the "speckle" in $\{1,1/2,0\}$ dark-field images. The controversy between these two different models still has not been settled.

2.2.6 Transition of SRO to LRO.

Upon aging the SRO alloy, the $\{1,1/2,0\}$ SRO maxima first become more intense (56,67), after which there is an increase in diffuse streaking in the diffraction patterns, followed by the formation of three-dimensionally isolated scattering at the D1a superlattice position (56,67). At first the D1a superlattice reflections seem to coexist with the SRO maxima, but the latter soon disappear. Once the diffraction pattern shows the D1a superlattice reflections, the β-domains become clearly visible in dark-field images obtained from superlattice reflections (66). This suggests that the domains already possess a high degree of order.

With small domains, bright-field images have a "basket-weave" appearance. Tanner and Leamy (73) attributed this feature to elastic coherency strains. Further aging produces the soap-froth structure of antiphase domains.

Most investigators believe that the transition is first-order, proceeding via nucleation and growth (13,14,58,67), at least at temperature above 700°C. But Cook (75) suggested a continuous fashion when aging at lower temperature.

Some investigators have examined compositions to the nickel-rich side of Ni_4Mo (20,24,76,77). Nesbit and Laughlin (78) distinguished the behaviour of 16.7 at% Mo alloy at 750°C from that at 700°C. At 750°C they found that the β-superlattice peaks appeared suddenly and independently of the $\{1,1/2,0\}$ SRO peaks, which they interpret as support of a nucleation and growth mechanism. At 700°C the β-superlattice reflections formed by a continuous transfer of diffracted intensity from the SRO maxima, suggesting a homogeneous transformation occuring by a mechanism of spinodal ordering.

2.2.7 Kinetics of Transformation ($\alpha \rightarrow \beta$).

The kinetics of transformation in Ni-20Mo alloy have been examined by methods which include TEM, microhardness measurement (51,79), electrical resistivity measurement (26) and wide angle X-ray diffraction techniques (80).

The ordering reaction shows a classical C-shaped time-temperature-transformation diagram, as shown in Figure 14. This curve was determined from resistivity measurements made after cooling rapidly from 1000 °C to the transformation temperature.

Ling and Starke (14,81) proposed that the order-disorder transformation is diffusion controlled, and the kinetics of the transformation should be treated by diffusion theory. For aging at 650 and 700 °C, they found that the ordering kinetics followed $1-S = \exp.(-Kt)$ equation. They also proved that the rate of domain growth during isothermal aging is analogous to that of grain growth and follows the rate equation $D^n - D_o^n = K \cdot t$. The parameter n is mainly dependent on the impurity content. A typical value of n is 2.8. Vasudevan (82) observed that cold work prior to aging enhanced the kinetics of ordering of Ni_4Mo at 700 °C, but the reason is not known.

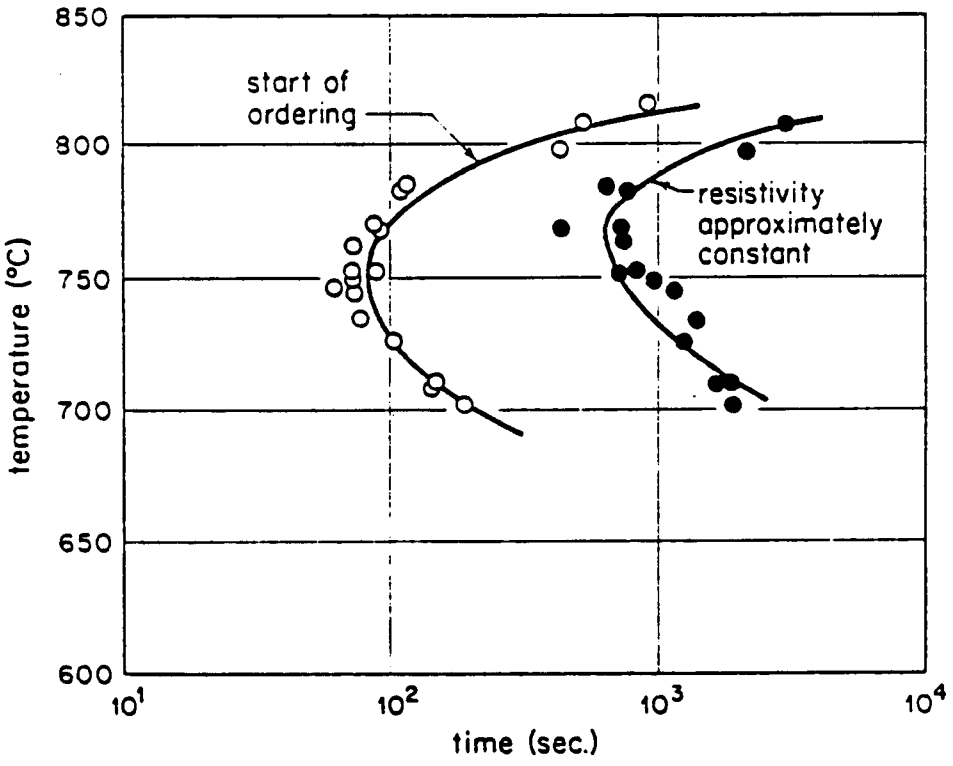


Figure 14. Isothermal time-temperature-transformation diagram for the ordering reaction in a Ni-20Mo alloy (Ref. 26).

The points show the start of ordering, and the time at which the resistivity remains constant for at least an hour, although this is not the equilibrium resistivity. The samples were held at 1000°C for about 10 minutes, then cooled rapidly to the transformation temperature.

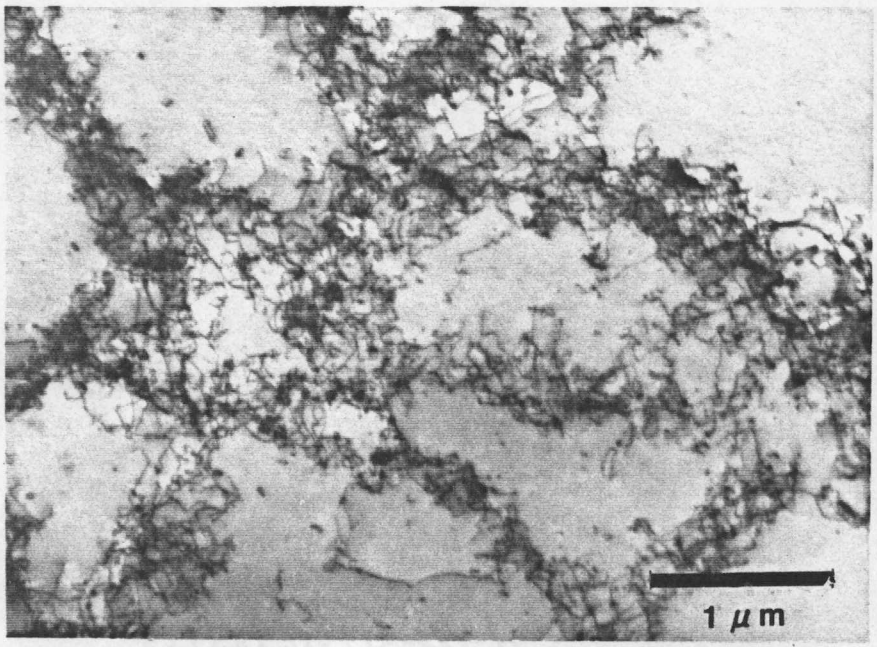
2.2.8 Dislocation Structure.

In pure nickel, slip occurs by movement of single dislocations on {111} planes (11,83,84). The dislocations are not restricted to bands, but easily form tangles as shown in Figure 15-(a) (11). For alloys containing from 0 to 10 at% Mo, single dislocations were found to be restricted to bands in which the dislocations were confined to a slip plane (Figure 15-(b)) (11,13,15,83,85).

The typical deformation microstructure of pure Ni and the two alloys which are in α phase (disordered condition) is compared in Figure 15 (11). The addition of Mo clearly causes the dislocations to be restricted to the slip plane, showing less cross-slip than pure Ni.

The effect of increasing the Mo content is to reduce the stacking fault energy, as found by Tiearney and Grant (84) and Nakada and Tisone (85). The lower stacking fault energy allows significant separation of a dislocation into partial dislocations, thus making cross-slip difficult to achieve. This is why the dislocations in the disordered condition (α-phase alloy) are always restricted in the slip plane. However, the separation of the partials is small, and stacking faults have not been observed.

(a)



(b)



Figure 15. Dislocation structure of Ni and Ni-Mo alloys in the α condition (Ref. 11).
(a) Dislocation structure of pure Ni strained in tension 3 %.
(b) Dislocation structure of Ni-10 at % Mo strained in tension 0.5 %.

(c)

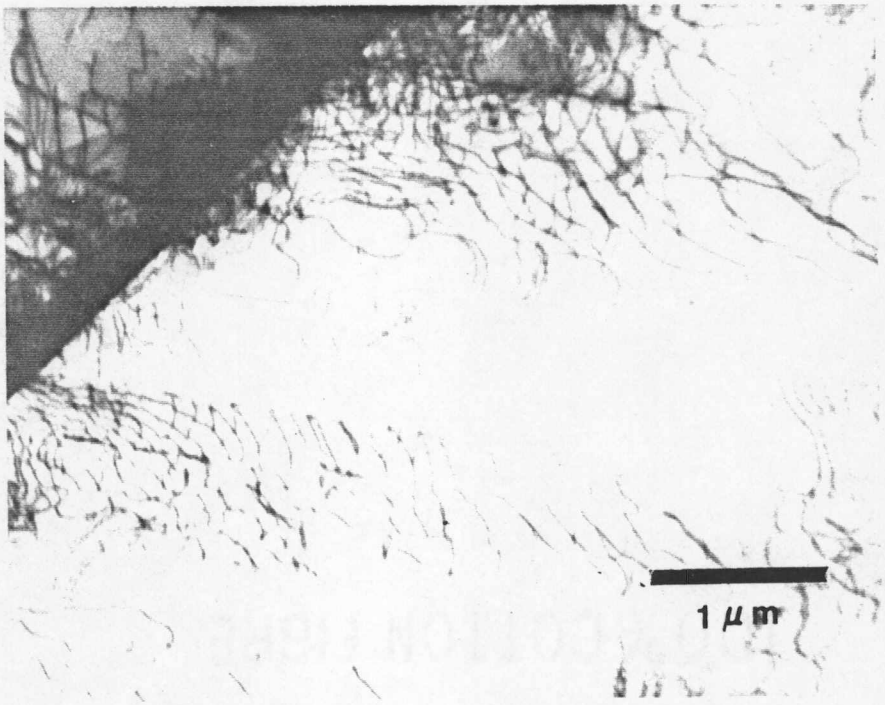


Figure 15. (Continued)
(c) Dislocation structure of Ni-20 at % Mo strained in tension 1.5 %.

Nosava and Polyakova (18,21) have observed the development of dislocations in Ni_4Mo deformed after aging at 700°C. For aging up to 30 hrs, the dislocation structure was identical to that in the as-quenched condition (see previous paragraphs). After aging for 100 hrs, slight deformation created single dislocation with some stacking faults. Heavy deformation generated numerous stacking faults and twins. After aging 400 hrs, even slight deformation created extensive stacking faults and twins. Nosava and Polyakova (18,21) showed that the stacking faults are bounded by Shockley a/6<112> partial dislocations. In summary, they observed deformation by single dislocations only, but many of these dissociated, forming many stacking faults. Also, twins were found when samples were deformed after longer aging time.

Saburi et al. (15) examined samples aged at 800 °C for times up to 165 hrs, then deformed by 5-10 % in compression. They observed bands and numerous twins, but no dislocations. Nesbit and Laughlin (24) examined a sample cooled slowly from α to 835°C, held for 500 hrs, cooled to 25 °C and then deformed 1 % by rolling. They found numerous stacking faults, widely separated partial dislocations, and twins; they identified the stacking faults as intrinsic, and the partial dislocations as of the 1/6<211> type. Some dislocations were seen to be unassociated with stacking faults. Nesbit and Laughlin

concluded that the deformation twins were composed of intrinsic stacking faults.

Some aspects of the dislocations structure can be explained in terms of the crystal structure of β. In Figure 16 is shown a close-packed (111) plane of completely ordered β(24). One would expect to observe superdislocations as they will minimize the area of APBs generately by slip. Slip in any of the three <110> direction will require the superdislocation to consist of five dislocations in order to bring the crystal back to coincidence on the movement of a dislocation. However, superdislocations containing five dislocations have been reported only by Nesbit and Laughlin (24) and Brooks et al. (26). The former found it in 15.6 at% Mo alloy; the latter found it in 20 at% Mo alloy.

Dislocation pairs have been observed in some deformed β-alloy (15). Ruedl et al. (55) pointed out that this may be another kind of superdislocation. Their reason is that the shortest repeat vector is not that involving five displacements, but the one marked O_1X in Figure 17. The second shortest path is O_2Y, and the third shortest O_3Z, is associated with slip along a <110> direction and the one involving five displacements.

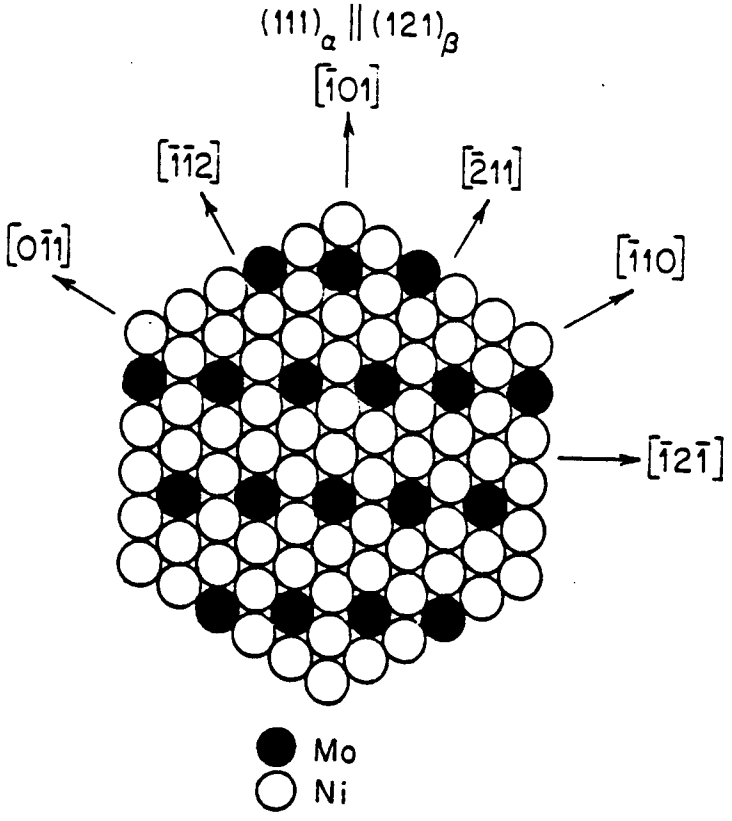
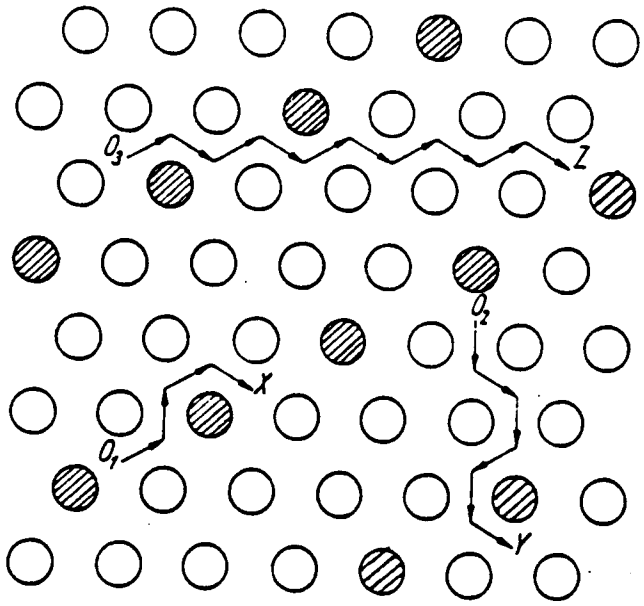


Figure 16. The close-packed (111) plane of completely ordered β (Ref. 24).



Geometry of close packed (111) layers of the ordered alloy Ni_4Mo. The open circles represent nickel and the cross-hatched circles molybdenum. The figure also shows the different glide paths for glide on the (111) plane; O_1X, O_2Y, and O_3Z correspond to four-, six-, and tenfold glide paths, respectively. It is assumed that splitting in partial dislocations has occurred.

Figure 17. The close-packed {111} plane of β, showing glide which could occur by superdislocations containing 5 (O_3Z), 3 (O_2Y) or 2 (O_1X) dislocations (Ref. 55).

The lack of observation of superdislocations in deformed β is puzzling. Two causes have been considered by Brooks et al. (26); [1] the large separation of partial dislocations makes the superdislocations difficult to recognize. [2] small domain size of the deformed β makes the superdislocations absent. The width of separation in superdislocations is determined by the difference between the repulsion energy of the five dislocations and the energy of the APB. The latter depends on the degree of order, and has been estimated by Chakravarti et al. (12) to be about 50 mJm^{-2} for the (111) plane, assuming perfect order. Using this value and following Flinn (86), Nosova and Polyakova (21) have estimated the separation of a pair of dislocations to be about 300 Å for screw dislocations and about 500 Å for edge dislocations. Thus a superdislocation consisting of five dislocations should be from 1500 to 2500 Å wide. It is possibly much larger than the common domain size of β phase. Anyway, this matter needs further investigation.

2.2.9 Strengthening Mechanisms.

Strengthening in ordered alloys is related to several factors, such as degree of order, APB energy, elastic strains arising from change in volume and shape upon ordering, domain size and crystal structure (5). In the Ni-20Mo alloy, the temperature and time of aging control

these factors. The mechanism of the formation of β-phase is complicated, as just discussed, and is temperature dependent. Thus, although strengthening occurs at all temperatures at which β is formed, the strengthening mechanism is not necessarily the same, nor is it necessarily the same as a function of time at a given aging temperature.

Detailed systematic studies of the effect of aging on the fine structure, deformation structure and mechanical properties are somewhat scare. However, there is considerable information (12,14,16-18,51) available for aging at 700°C. The results are summarized in Figure 18. The alloy increases in hardness considerably during aging, then passes through a maximum. The domain size increases monotonically, whereas the degree of long-range order attains a maximum value around 1000 minutes. The increase of lattice strain begins to level off also at about 1000 minutes.

These data are interpreted in the following way. For aging times up to about 50 minutes, the lattice strain is zero. Thus, hardening is due to an increase in domain size and in the degree of long-range order. Beyond 50 minutes, elastic strain is developed, but stabilizes in the same time range in which the hardness maximizes. Also beyond 50 minutes, the domain size continues to increase. Thus, hardening after 50 minutes is associated with the

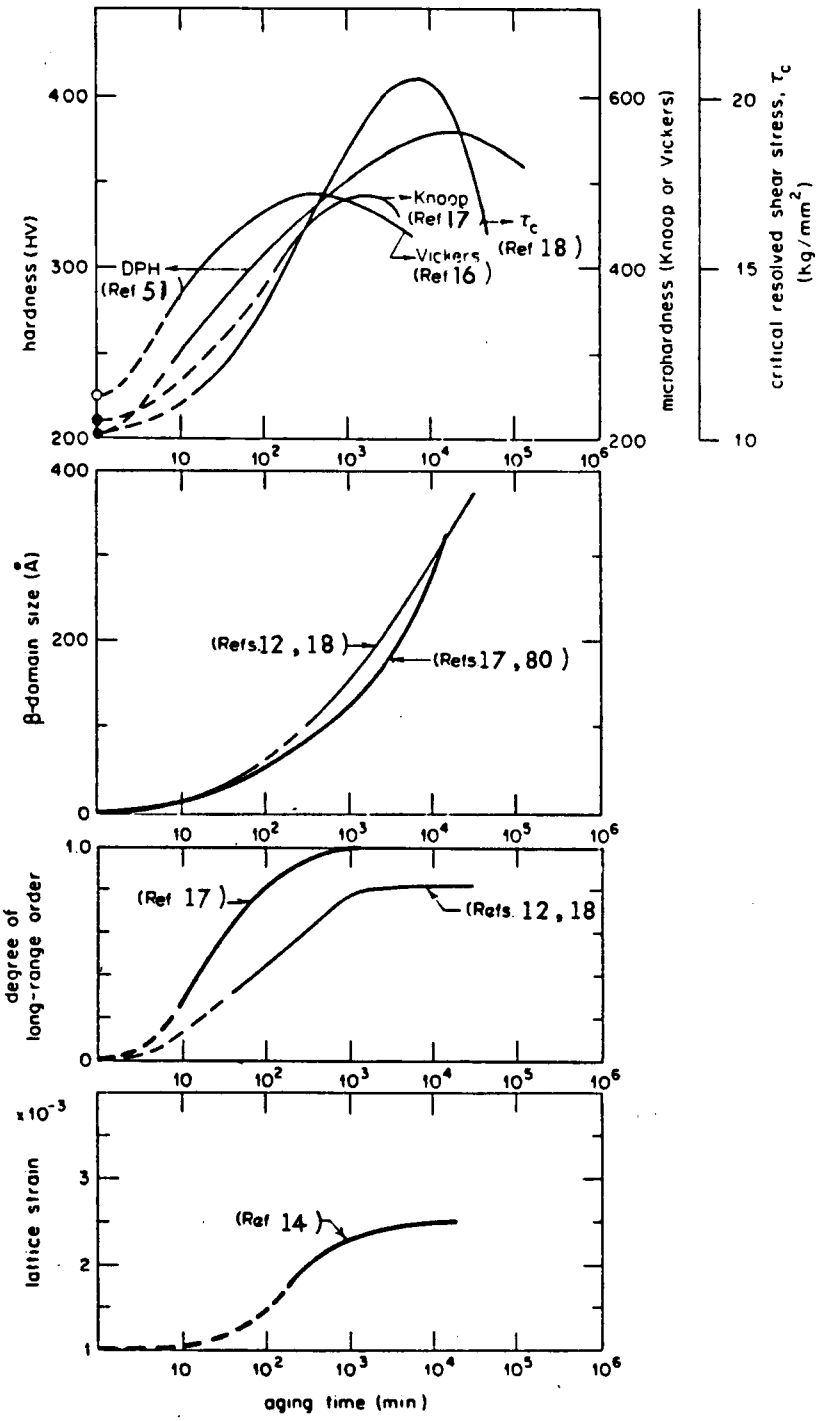


Figure 18. Effect on properties of aging quenched α at 700°C (Ref. 26).
(a) Hardness, critical resolved shear stress.
(b) β-domain size.
(c) LRO parameter.
(d) Average lattice strain.

degree of lattice strain. Ling and Starke (14) have interpreted these data to indicate that the strengthening (after 50 minutes aging time) is due to dislocation generation caused by the mismatch strains. If a significant number of dislocations are generated, then the interpretation of the strain measured by X-ray diffraction techniques is complicated because both the lattice mismatch strain and the dislocation strain contribute to this. However, because the strain measured on Ni filings is about the same as that obtained for the deformed β, Ling and Starke (14) concluded that the main contributor to the strain in β is dislocations. Thus, on aging at 700 °C the lattice-mismatch strains increase as the domains grow until, after about 50 minutes, the strain is sufficiently high for dislocations to be generated. It is this high dislocation density that is the main contributor to the lattice strain, and the cause of the strengthening on aging beyond 50 minutes.

Nosova and Polyakova (21,23) have interpreted these data at 700°C somewhat differently. They supposed that strengthening is due to the formation of APDs created from dislocation passage. The decrease in strength with long aging time is due to twinning. Snyder and Brooks (13) attributed the initial strengthening on aging at 775 °C to dislocations cutting domains. However, even when α is no longer discernable in the fine structure, the strength

continues to increase significantly. Thus, they have argued that the elastic strains are a major cause of strengthening. They attributed the eventual strength decrease to stress relief associated with the formation of twins.

Saburi et al. (15) attributed the initial strengthing on aging at 800°C to the domain cutting by dislocations. The eventual decrease in strength they also attributed to twinning.

Although it seems certain that strenghening during the early stages of the formation of β-domains is associated with dislocations cutting these domains, the causes of subsequent strengthening have not been separated clearly. Also the causes of overaging have yet to be established. Determining the complex dislocation structure and fine structure (domains and twins) is obviously of importance in understanding the whole problem. To fully establish the strengthening mechanism in β, on aging at different temperatures, we need to know the LRO parameter, the domain size and the elastic strains with aging time at different temperature, but these have been measured only for aging at 700°C.

2.2.10 Embrittlement's Causes and Fractography.

The formation of β in both stoichiometric and off-stoichiometric alloys leads to a reduction in ductility, as illustrated in Figure 19. Note that the embrittlement occurs before the maximum strength is attained. But Saburi et al. (15) found that in compression, the ductility remains high and essentially the same as that of α, independent of aging time. Nosova and Polyakova (18) also found that single crystals of β tested in tension showed significant ductility.

Fractography of tensile samples of quenched Ni-20Mo alloy (α-phase) revealed the fracture mechanism to be microvoid coalesence, but in the ordered alloy (β) the fracture is intergranular along the prior α-phase grain boundaries (13).

The reasons for the embrittlement and for the fracture mode are not very clear. Four major possible reasons have been proposed by investigators (12,15,26): [1] The β is a brittle ordered crystal structure because it has a limited number of slip systems. [2] Dislocations are difficult to cross slip in the ordered phase so that dislocations are restricted to their slip planes, which allow pile-ups to form at the former α grain boundary, leading to fracture initiation. [3] Recrystallized structure that forms along the prior α boundaries after sufficient aging at some temperatures could lead to a

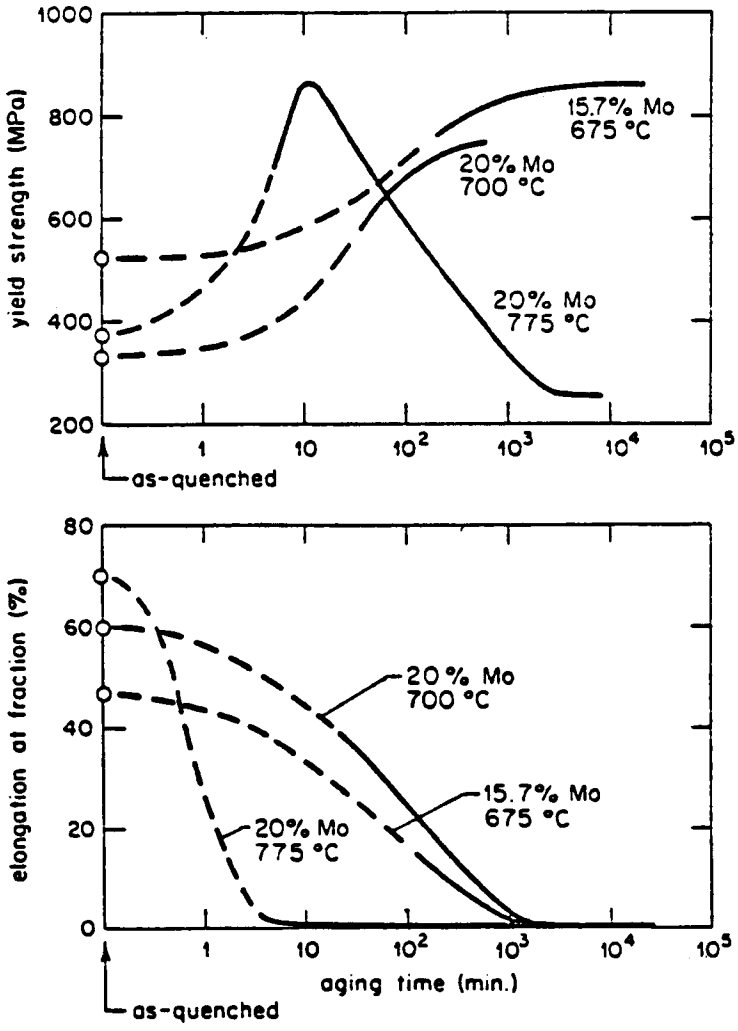


Figure 19. Tensile yield strength and ductility (elongation at fracture) at 25°C as a function of aging time for β and $\alpha+\beta$ alloys (Ref.12,13,20).

weakening of this region, and hence to fracture along the prior α boundaries (Chakravarti et al. (12)). [4] Segregation of impurities occurs on grain boundaries, which then act as strong barriers to slip. Obviously a more systematic study is needed to determine the cause of embrittlement.

Considerable effort is being devoted to improving the ductility of ordered alloys through such diverse techniques as refined grain size, microalloying with boron, and various rapid-solidification techniques. These same metallurgical processes should be applicable in Ni_4Mo alloys as methods of improving the toughness.

CHAPTER 3

EXPERIMENTAL PROCEDURES

3.1 Alloy Preparation.

The Ni_4Mo alloy was prepared by induction remelting of a Ni-Mo master alloy with nickel corrections, in a Balzers induction melting furnace under 10^{-5} torr vaccum condition, and casting into a water-cooled copper mold to produce ingots 0.75 inches in diameter and 2.5 inches long. The chemical analysis of this alloy is shown in Table 2. The impurities content has been controlled to a considerably low range. The ingots were homogenized at 1150°C for 100 hours in a high temperature, atmosphere controlled furnace using dry hydrogen and argon. They were then furnace cooled, reheated to 1000°C for 1 hour in argon and then water quenched to retain the soft f.c.c. (α) phase. The alloy ingots were subsequently rolled, with intermediate anneals in argon at 950-1000°C, to sheet 0.020 inch thick. The sheets were used to manufacture sheet-type tensile specimens.

3.2 Heat Treatment.

Sheet-type tensile specimens first were sealed in silica tubes under rough vacuum, held at 1000°C for 30 minutes and water quenched on breaking the silica capsules to retain the f.c.c. (α) phase. They were then

Table 2. Chemical composition of the Ni_4Mo alloy used in this research

Elements	Composition (wt.%)	Remarks
Ni	70.50 %	Wet method
Cu	5 PPM	
Co	5 PPM	
Fe	10 PPM	
Mn	1 PPM	
Cr	10 PPM	
S	< 3 PPM	
Si	0.5 PPM	SSMS
Al	0.3 PPM	method
Mg	3 PPM	
Na	0.5 PPM	
P	1 PPM	
Cl	0.1 PPM	
V	< 0.1 PPM	
B	< 0.1 PPM	
Ca	< 0.1 PPM	
F	< 0.1 PPM	
Li	< 0.1 PPM	
Mo	Remained	----

electropolished to remove the oxidation layer (electrolyte containing 130 ml H_2SO_4 and 870 ml methanol): Samples were then heat treated three different ways. (1) For investigating the aging effect, 725°C and 775°C were chosen as the aging temperature, because the aging effects of this alloy have not been investigated intensively before at these two temperatures. The aging times were 1, 3, 10, 30, 50, 100, 1,000, 10,000, 50,000 and 100,000 minutes. At the aging times less than 50 minutes, a neutral salt bath of 50 % KCl plus 50 % NaCl was used. For the times longer than 50 minutes, tensile specimens and samples from which to make TEM specimens were sealed in silica tubes under vacuum again, and aged in air. After aging at each temperature for the times indicated, the capsules were broken under water to arrest further transformation. (2) For investigating the influence of large domain size on the mechanical properties and dislocation structure (especially for checking the probability of appearance of five unit superdislocation), an aging temperature very close to Tc of 850°C was chosen. Tensile specimens were sealed in silica tubes, then first held at 850°C for 14,400 minutes (10 days), transferred to 725°C, kept 1,440 minutes (1 day), then broken under water. This treatment provides samples with a very large domain size and a high long-range order parameter at the same time. (3) For investigating the effect of quenching

temperature on the LRO parameter and the mechanical properties, it was felt that samples should be quenched directly into water, and not rely on breaking of silica tubes in water. Thus a vertical furnace utilizing a He atmosphere was used in which samples (not encapsulated) were quenched directly into water.

All the specimens were electro-polished again before tensile testing.

3.3 Metallography.

The samples in the ordered and disordered condition were metallographically prepared for optical microscopy. They were mounted in epoxy or Bakelite. For observing the side view of a broken surface, clamps are used often for mounting thin sheets of tensile specimens. After mounting, the specimens were ground and polished through 0.06 Al_2O_3 polishing powder. The etchants used to develop the microstructure were: (1) 1 part CrO_3 water solution (30 g CrO_3 powder in 100 ml water) plus 5 parts HCl acid. (2) 1 part HCl acid plus 1 part H_2O_2 plus 1 part methanol.

The specimens were examined and photographed under a Leitz optical microscope using Polaroid 55 film.

3.4 LRO Parameter Measurement by X-ray Diffraction.

The long-range order parameter was calculated from the integrated intensities of the superlattice and fundamental reflections using the relation (14):

$$S = \frac{E^s}{E^s} \cdot \frac{R^f}{R^f}$$

where S is the LRO parameter, E^s and E^f the measured integrated intensities of a superlattice and a fundamental reflection, respectively, and R^s and R^f are their calculated intensities. The intensities are calculated using the expressions:

$$R = v \cdot P \cdot F \cdot (LP) \cdot \exp(-2M)$$

$$R = P \cdot F \cdot (LP) \cdot \exp(-2M)$$

P is the multiplicity factor, F is the structure factor, LP the Lorentz-polarization factor and (-2M) is the temperature factor. The value of v in the calculation represents the probability of having a particular orientation of the ordered domain. Since there are six unique ways in which the ordered lattice can develop with respect to the disordered lattice, this factor is 1/6 if all orientations have equal probability of being present in the sample.

The $(110)_T$ superlattice and $(420)_C$ fundamental reflections were chosen to calculate S values because of their parallel crystallographic direction.

The theoretical R^f/R^s value was calculated as 13.6. However, the experimental result (using a sample aged 100,000 minutes at 775°C as a standard, assuming its S value is 1) for the value of R^f/R^s is 5.4, considerably smaller than the theoretical value. The source of error is inferred to be due to two things: (1) The temperature factor M for Ni_4Mo is unknown. In the calculation here, a weighted average of the values for Ni and Mo were used. (2) Some preferred orientation exists in the samples after annealing. Ling and Starke (14) considered that the domains which have their c-axis close to the sample surface normal will predominate in the late ordering stages since the contraction which occurs along the c-axis is more easily accommodated perpendicular than parallel to the surface. So the value of v will not be 1/6, but between 1/2 and 1/6, making R^f/R^s between 4.5-13.6. If it is true, the experimental result of 5.4 is acceptable.

Using experimental results, setting R^f/R^s equal to 5.4, a consistent S value close to unity was obtained for all the specimens after a long aging period.

The tensile specimens of different heat treatments were examined using a Rigaku X-ray diffractometer. The intensities of $(110)_T$ and $(420)_C$ were integrated by an accessory microprocessor. For each specimen, a diffractometer trace was obtained six times, and for each time E^s_{110}/E^f_{420} was determined, but only the average value is

reported. The reproducibility of the calculated S values is about ±0.02 for S>0.7, and about ±0.05 for S<0.7.

Values of S<0.3 are not reported as they showed extensive scatter.

3.5 Tensile Testing.

Tensile specimens were punched out directly by a hydraulic press using a tensile specimen forming die to produce a sample which conformed to ASTM E8-66 (Figure 20). Following the heat treatments described previously to obtain the disordered, partially ordered and fully ordered structures, the samples were electro-polished prior to testing.

Some tensile testing was performed at room temperature and some at elevated temperatures (from 300°C to 1000°C), using a screw driven Instron machine equipped with a collar for induction heating and with a high speed vacuum system containing a turbo vaccum pump. The machine was operated using a constant cross head speed, corresponding to a strain rate of 0.2/min.

The yield strength was taken from the load-extension curves at 0.2% strain, at 25°C, this stress was very close to the stress at which the curve deviated from the linear elastic part, but in the higher temperature tests the deviation was more. Thus in most cases the 0.2% yield

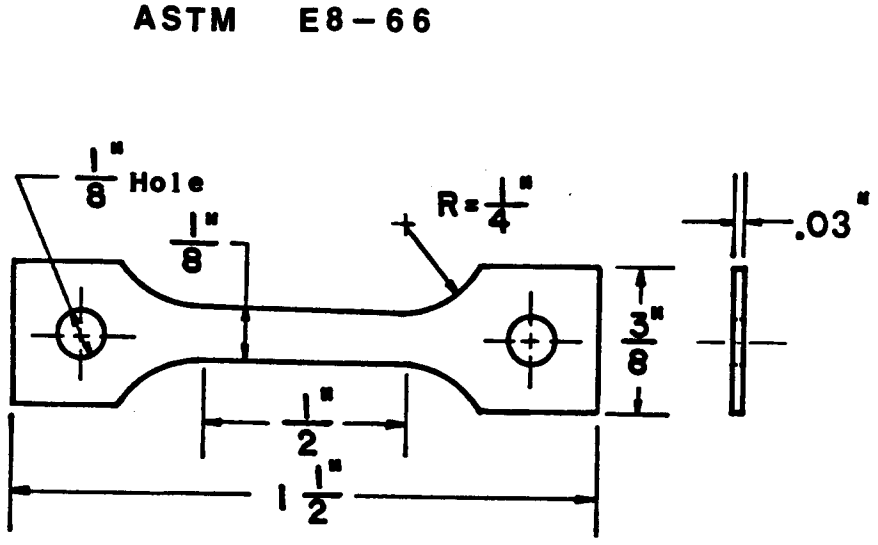


Figure 20. Design of the tensile specimen.

strength is a reasonable approximation of an apparent proportional limit.

Most tensile samples had an elongation greater than 0.2%. For samples which fractured with less than 0.2% strain, the yield strength and the fracture strain taken as the values at fracture.

3.6 Scanning Electron Microscopy.

An AMR 900 Scanning Electron Microscope was used to examine metallographic specimens and fracture surfaces. Gold coating was used on the metallographic specimens. The fracture surfaces were ultrasonically cleaned in acetone and then directly mounted onto the SEM stage.

3.7 Transmission Electron Microscopy.

Different thin foil specimens needed to be prepared, depending on the purposes of the observations.

For measuring the domain size and examining the general microstructures of the alloy treated for different aging periods, 3 mm diameter disks were punched from scrap material and heat treated with the tensile specimens.

For investigating the deformation structure of the alloy, specimens were prepared with some initial dislocations. Two ways were used: (1) To observe the dislocation structures at the region of fracture of the tensile samples, the process described in Figure 21 was used. (2) Disks which were punched from different heat

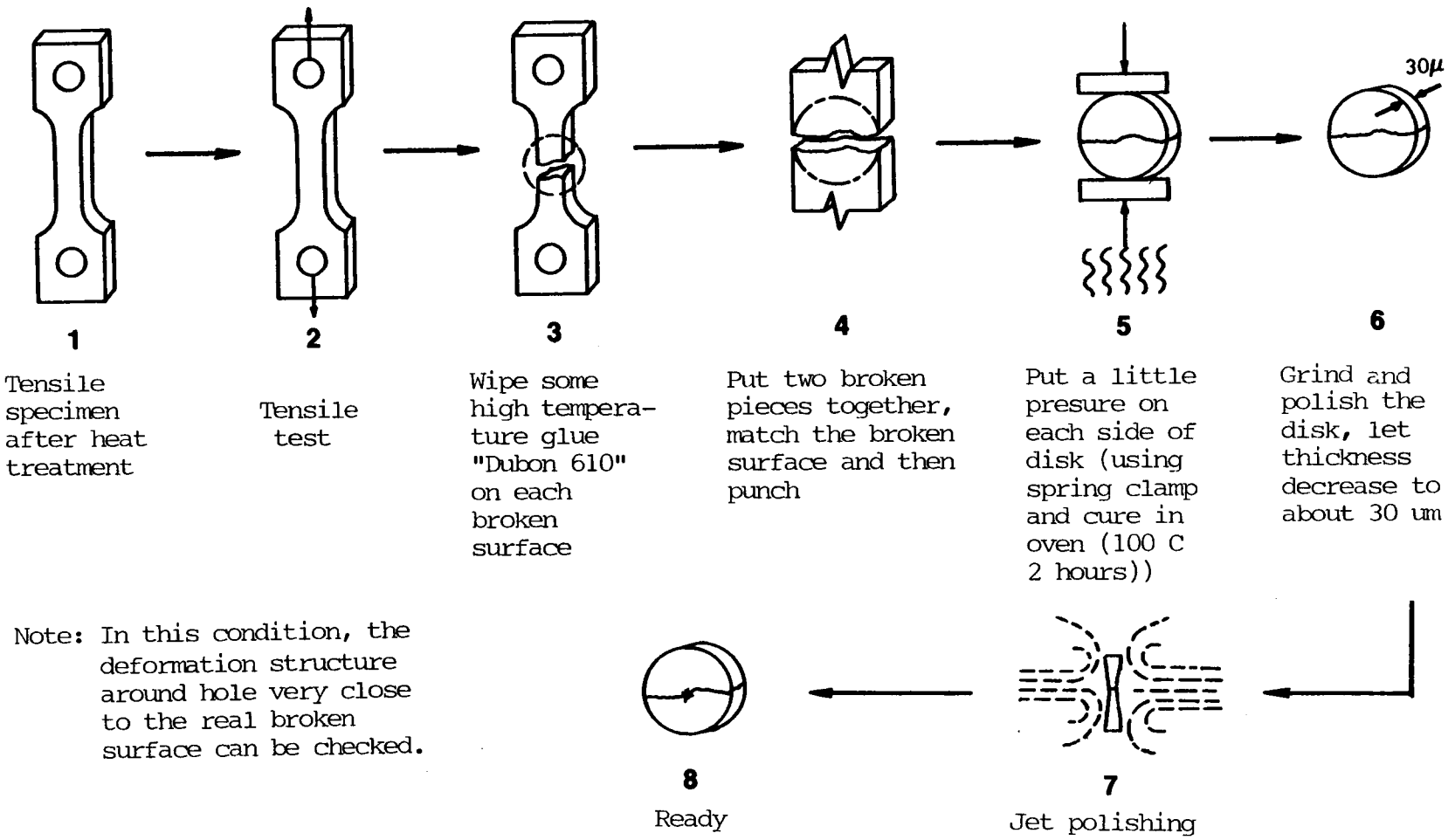


Figure 21. The preparation of TEM specimens from tensile sample's broken area.

treatment specimens were cold rolled, then thinned.

For observing the motion of dislocations and investigating the fracture mechanism of ordered Ni_4Mo alloy, samples were strained in a special stage (Figure 22a) in a Phillips EM 430 (350 KV) TEM at Oak Ridge National Laboratory. The special geometry shown in Figure 22b was required. Final thinning of these samples was carried out directly in a Struers "Tenupol", jet polishing device, which was equipped with a photo-cell to detect the light upon the initial penetration of the specimen, which cuts power of the cell off automatically. However, visual observation of the light penetration was found to be more effective. An electrolyte consisting of 640 ml H_3PO_4, 150 ml H_2SO_4, 210 ml H_2O and 35 ml HCl was used with a voltage of 19-20 volts, a current of 0.8-1.0 amperes, a flow rate of 6.5 (arbitrary units), and a temperature of 16-18 °C.

Observation of the thin foils was conducted in a Phillips EM 300 transmission electron microscope operated at 100 KV (UTK) and a JEOL 100CX operated at 120 KV (at Oak Ridge National Laboratory). For analysis of Burgers vector of dislocations, a double tilt specimen holder was often used.

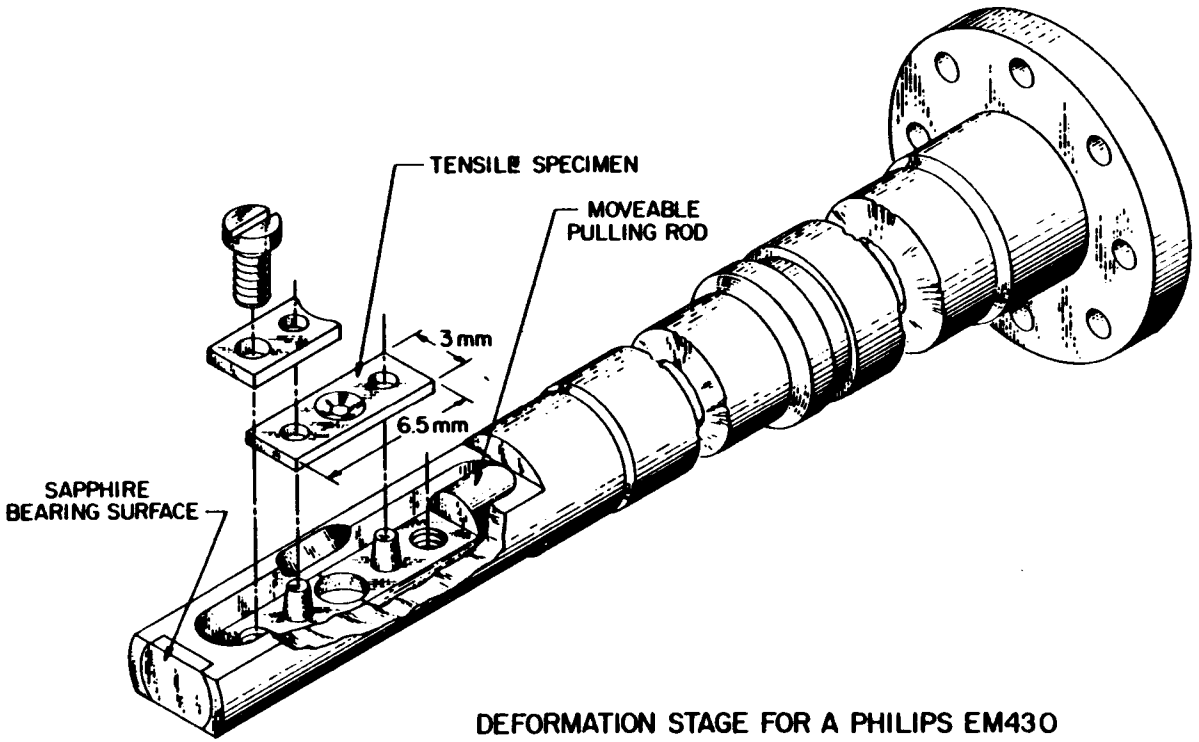


Figure 22. The deformation stage and the in situ tensile thin foil specimen used in it.
(a) Deformation stage for a Philips EM430.

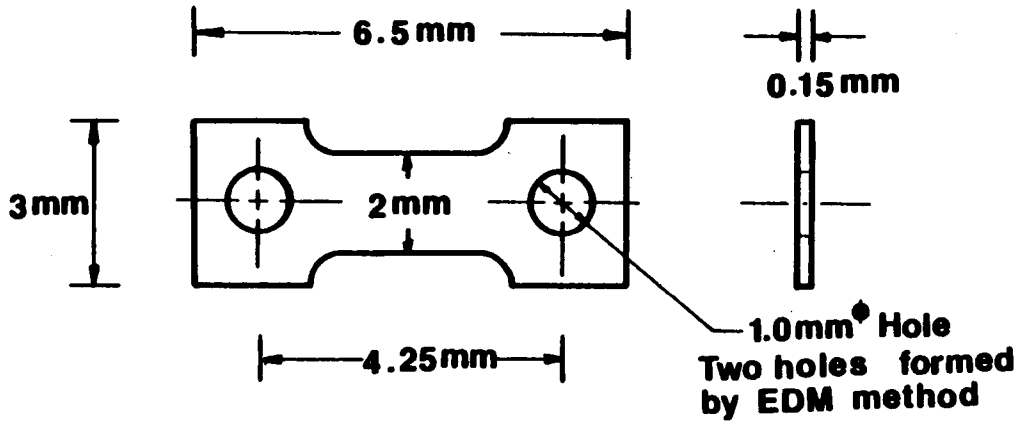


Figure 22. (Continued).
(b) The dimension of in situ tensile thin foil specimens used in the deformation stage of TEM.

3.8 Microhardness Measurement.

A Tukon microhardness tester (UTK) and a Shimadzu microhardness tester (at Oak Ridge National Laboratory) were used to measure the hardness. Usually a 10 Kg load was used and the testers were calibrated frequently using standard hardness blocks.

3.9 Auger Electron Microanalysis.

PHI 590 Scanning Auger Microprobe (Physical Electronics Inc.) was used to analyze the impurity element distribution on a fracture surface. The sample was fractured inside the high vacuum apparatus, and transferred under this vacuum to the Auger analysis chamber. After analyzing the fracture surface, it was sputtered with argon for 2 minutes, then areas were reanalyzed. This then was repeated after sputtering 8 more minutes.

These analyses allowed detection of segregants on the fracture surface, and also their concentration in the bulk below the surface.

The dimension of the specimens for this test is shown in Figure 23.

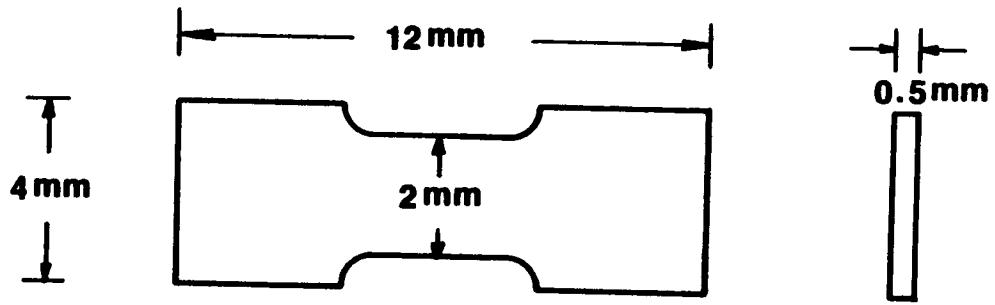


Figure 23. The dimension of tensile specimen used in the Auger Electron Microanalysis.

CHAPTER 4

RESULTS AND DISCUSIONS

4.1 Mechanical Properties

4.1.1 General comments.

There are six separate experiments involving tensile testing. The effects of aging, quenching temperature, LRO, and α grain size on the tensile properties measured at 25°C are described in Parts 1,2,4 and 5. In Part 3 are described the results of testing at high temperature for two different domain sizes. These experiments were used to evaluate the potential of ordered Ni_4Mo alloy as a high temperature structural material.

4.1.2 Part 1: Aging effect.

Two series of room temperature tensile tests were done to investigate the aging effect at 725°C and 775°C. The detailed heat treatments and the results of the tensile tests and microhardness measurements are shown in Table 3. These changes of mechanical properties with aging time at 725°C and 775°C are shown in Figure 24 and Figure 25. The results of domain size measurements are in Table 4, and the results of LRO parameter measurements are in Table 5. These results are also plotted in Figures 26 and 27.

Table 3. The effect of aging time at 725 °C and 775 °C on the mechanical properties measured at 25 °C

Sample Number	Aging Temp. (°C)	Aging Time (min.)	Hardness (DPH)	Y. S. (Ksi)	T. S. (Ksi)	Elongation
I-1	725	0	240	68.2	142.9	67.7%
I-2	725	0	248	74.7	154.4	63.4%
I-3	725	1	256	76.0	149.6	59.5%
I-4	725	3	261	84.1	155.0	47.2%
I-5	725	10	299	108.9	123.3	5.48%
I-6	725	30	323	118.4	137.5	4.2%
I-7	725	50	333	---	---	*
I-8	725	100	351	126.5	146.4	4.4%
I-9	725	1000	426	125.3	150.3	2.44%
I-10	725	1000	438	124.9	129.2	**
I-11	725	10000	426	96.9	96.9	**
I-12	725	36000	417	106.0	119.5	0.8%
I-13	725	50000	406	---	---	*
I-14	725	100000	403	93.2	107.8	0.9%
I-15	725	100000	405	94.4	104.6	0.7%
I-16	775	1	263	75.6	150.8	56.0%
I-17	775	3	346	128.5	148.5	4.4%
I-18	775	10	364	134.0	145.0	3.1%

Table 3 (Continued)

Sample Number	Aging Temp. (°C)	Aging Time (min.)	Hardness (DPH)	Y. S. (Ksi)	T. S. (Ksi)	Elongation
I-19	775	30	391	127.3	127.3	0.6%
I-20	775	50	393	---	---	*
I-21	775	100	407	126.4	126.4	Nil
I-22	775	1000	438	125.2	148.7	1.3%
I-23	775	10000	423	110.0	110.0	Nil
I-24	775	14000	417	105.6	113.3	0.7%
I-25	775	50000	403	85.3	91.7	0.1%
I-26	775	100000	383	---	---	*

*: Cracked during water quenching after aging heat treatment.

**: Broken at pin hole during tensile testing.

Heat Treatment Procedure: Step 1, Solution Heat Treatment: 1000°C, 30 min., then water quenched. Step 2, Aged 725°C and 775°C, 1 to 100,000 min. separately (less than 100 min. using salt bath, longer aging periods, samples were sealed in silica tubes under rough vacuum), then water quenched.

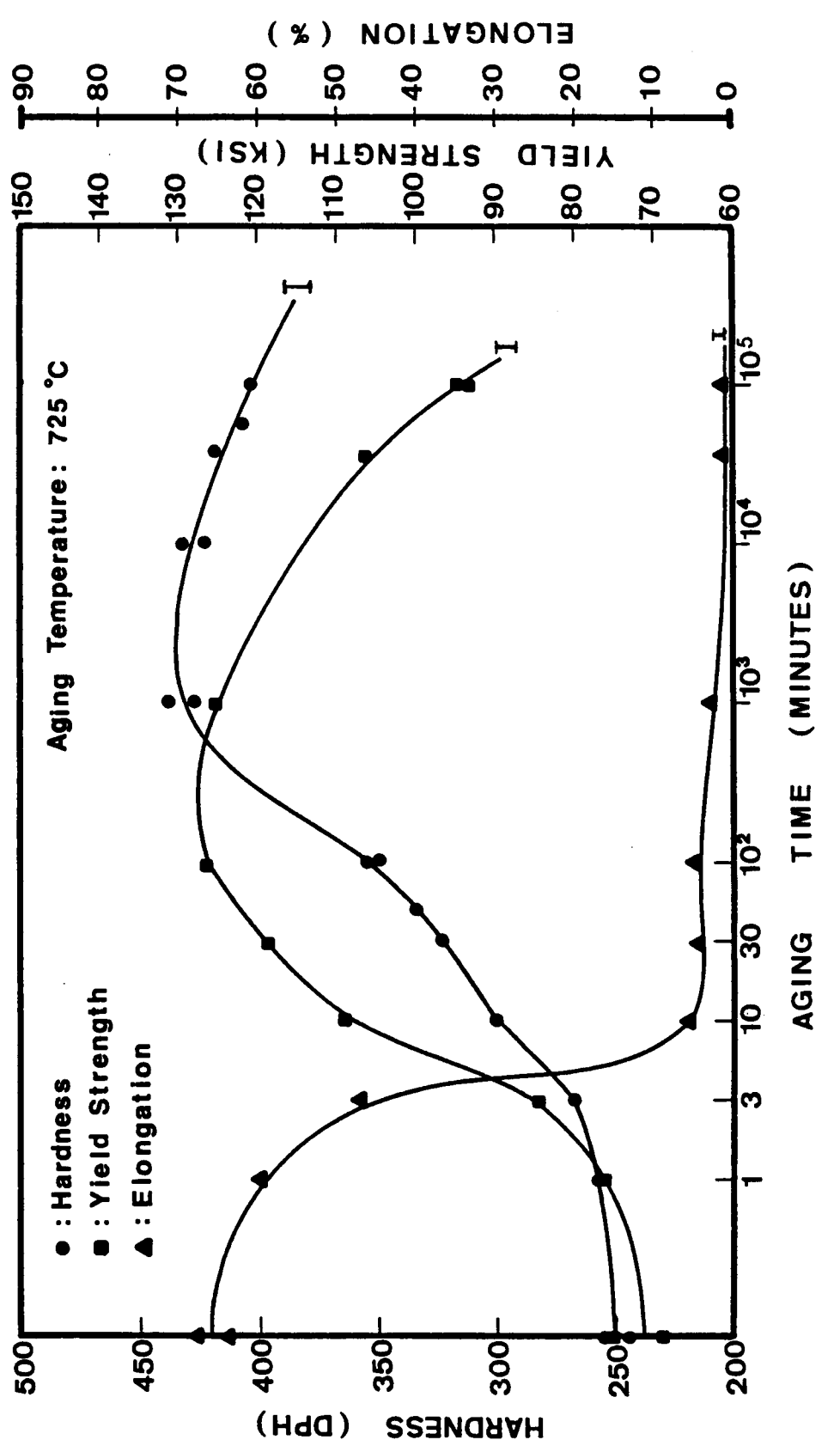


Figure 24. Effect of aging time at 725 °C on the mechanical properties as measured at 25 °C. (The bars at the end of the curves give an estimate of the measurement error.)

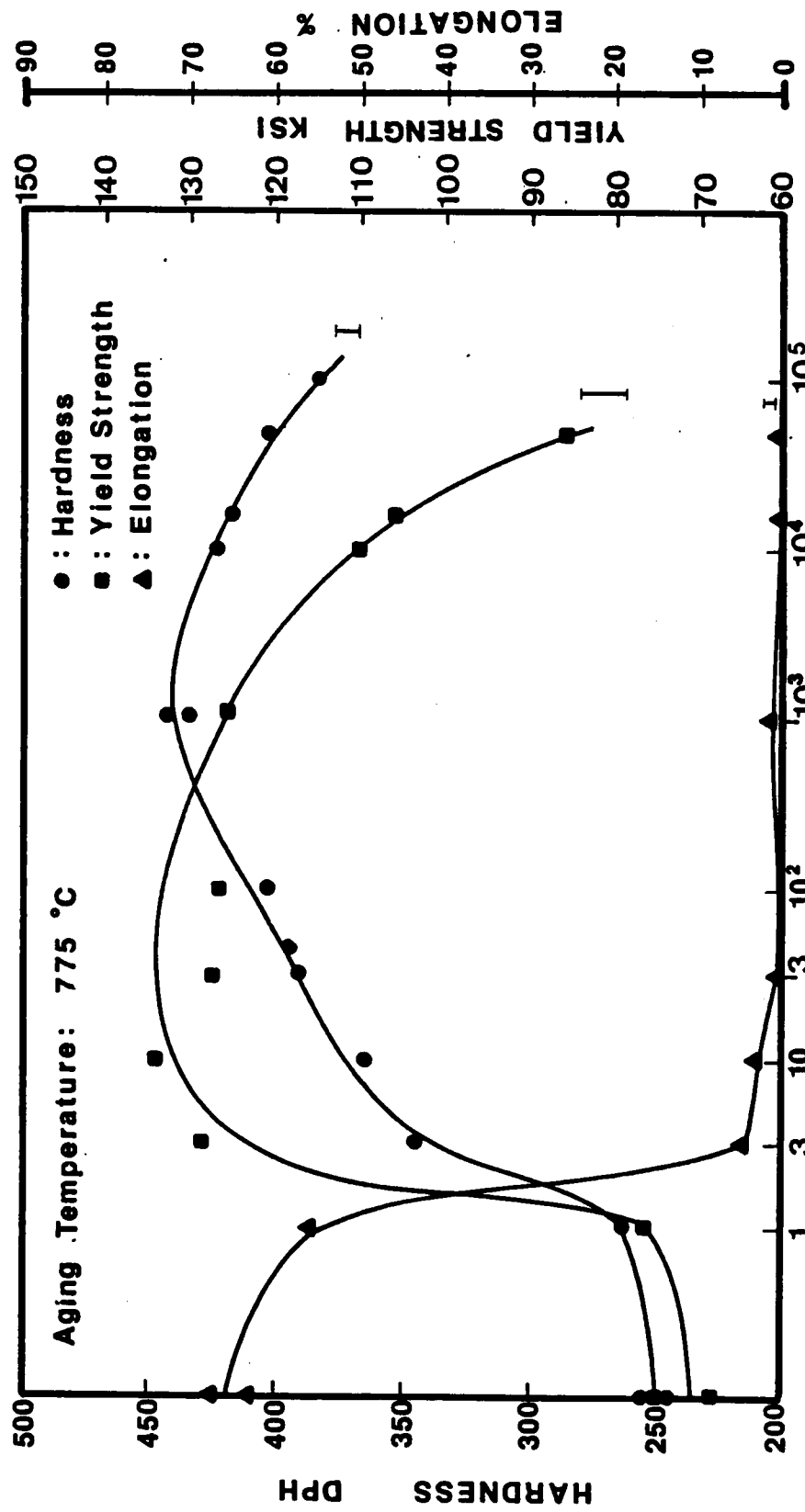


Figure 25. Effect of aging time at 775 °C on the mechanical properties as measured at 25 °C. (The bars at the end of the curves give an estimate of the measurement error.)

Table 4. The effect of aging time at 725 °C and 775 °C on the domain size (The domain size was measured from TEM observations, using CDF image of superlattice diffraction spots.)

Sample Number	Aging Temp. (°C)	Aging Time (min.)	Magnification	Measured Domain Size (mm)	True Domain Size (Å)	Average Domain Size (Å)
I-3	725	1	250,000	--	--	--
I-4	725	3	250,000	0.75	30	30
I-5	725	10	250,000	0.85	34	34
I-6	725	30	250,000	1.55	62	62
I-8	725	100	67,900	0.7	103	
			250,000	2.25	90	97
I-9	725	1000	67,900	1.65	243	243
I-11	725	10000	67,900	5.25	773	
			49,700	3.5	704	747
I-12	725	36000	36,040	4.5	1249	1249
I-14	725	100000	36,040	7.5	2081	2081
I-16	775	1	250,000	--	--	--
I-17	775	3	67,900	0.85	125	
			130,000	1.9	146	
			250,000	3.75	150	140
I-18	775	10	67,900	1.15	169	
			250,000	3.25	130	150
I-21	775	100	106,900	4.0	374	374

Table 4 (Continued)

Sample Number	Aging Temp. (°C)	Aging Time (min.)	Magnification	Measured Domain Size (mm)	True Domain Size (Å)	Average Domain Size (Å)
I-22	775	1000	49,700	6.75	1358	1358
I-23	775	10000	36,040	9.0	2497	
			36,040	10.0	2773	2640
I-25	775	50000	17,770	11	6190	
			14,370	7	4871	
			14,370	7	4871	5310
I-26	775	100000	14,370	10	6960	
			14,770	12.5	7034	7000
IV-1	850	14400	11,400	35	30700	
			11,400	45	39500	35000

--: No domain structure could be seen.

Table 5. The effect of aging time at 725 °C and 775 °C on the LRO parameter S

Sample Number	Aging Temp. (°C)	Aging Time (min.)	E_{110}	E_{420}	$\frac{E_{110}}{E_{420}}$	S
I-1	725	0	0	5085	0	0
I-4	725	3	130	5071	0.026	0.37
I-5	725	10	191	4124	0.046	0.50
I-6	725	30	448	6857	0.065	0.59
I-7	725	50	315	4480	0.070	0.62
I-8	725	100	455	5291	0.087	0.69
I-9	725	1000	2081	13434	0.155	0.91
I-11	725	10000	816	4557	0.18	0.99
I-13	725	50000	771	4238	0.182	0.99
I-14	725	100000	656	37312	0.176	0.97
I-17	775	3	221	3711	0.060	0.57
I-18	775	10	416	4900	0.085	0.68
I-19	775	30	684	6846	0.099	0.73
I-20	775	50	740	6912	0.107	0.76
I-21	775	100	717	6052	0.118	0.80
I-22	775	1000	691	4016	0.172	0.96
I-23	775	10000	1035	5568	0.186	1.0
I-25	775	50000	2358	13275	0.178	0.98
I-26	775	100000	721	3687	0.195	1.02

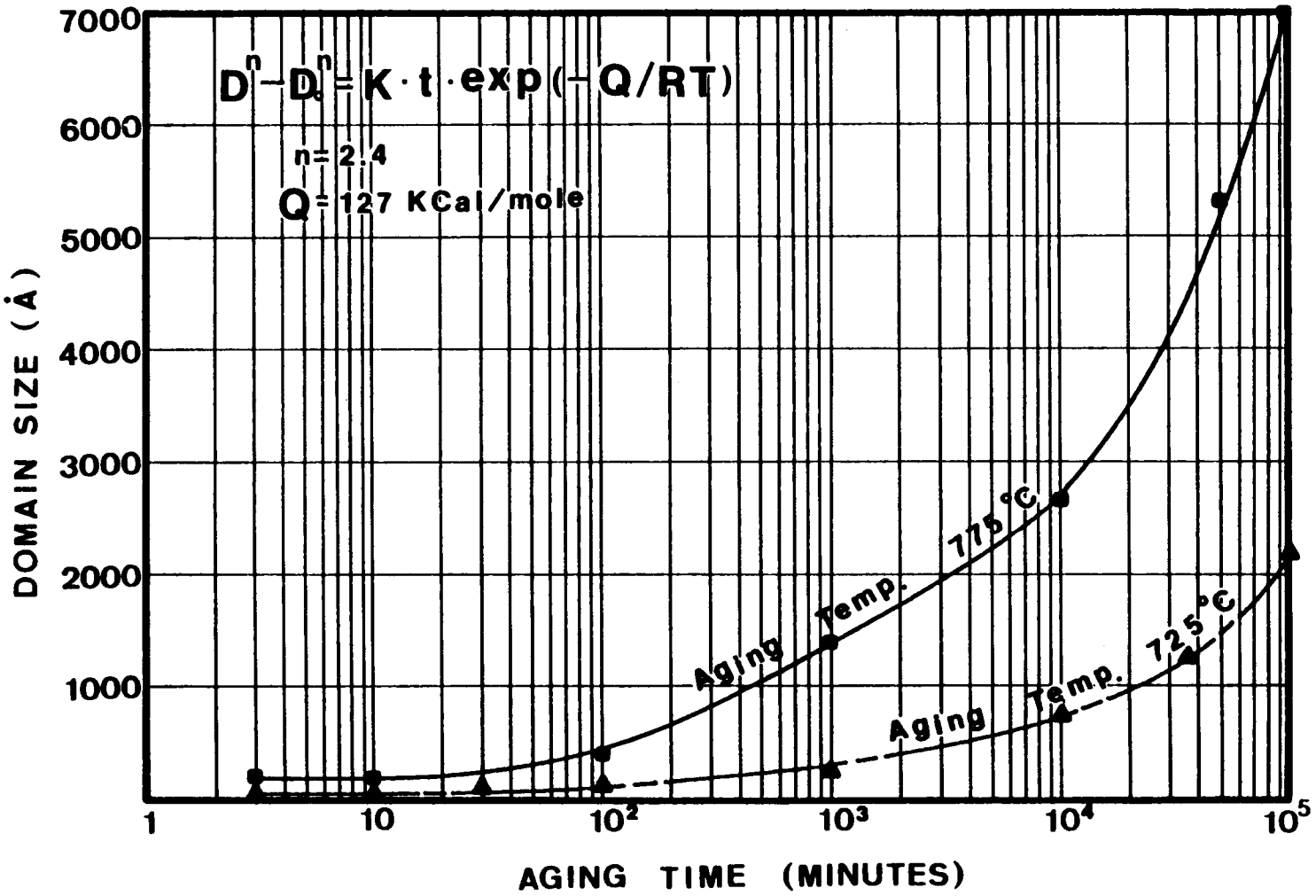


Figure 26. Effect of aging time on the domain size (semi-log plot). (The size of the symbols represents approximately the error in the measurement.)

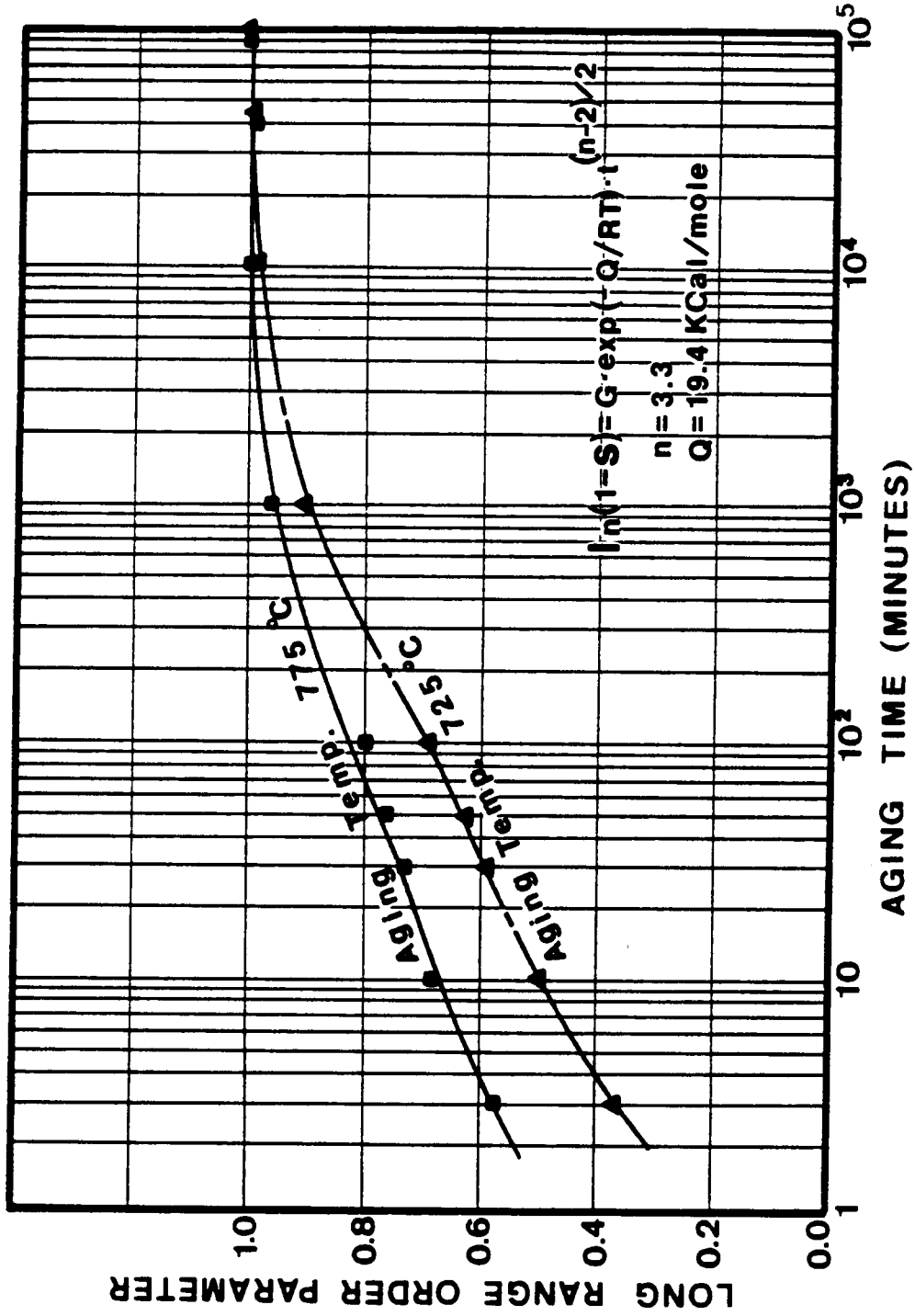


Figure 27. Effect of aging time on the long-range order parameter (semi-log plot). (The parameter accuracy is approximately ±0.02 for S>0.7 and ±0.05 for 0.7>S>0.3.)

It is seen in Figure 24 and Figure 25 that the yield strength and hardness increase with the aging time at the beginning, then reach maximum values, after which they decrease slowly. However, the ductility decreases to a very low value (<5%) before the yield strength and hardness ever approach their maximum values. The elongation continues to decrease with the aging time, and never increases even after a very long aging period (100,000 minutes).

The yield strength of Ni_4Mo almost doubles after ordering, so the ordering hardening effect is very obvious in this kind of alloy. However, the tensile strength of Ni_4Mo eventually continuously and slowly decreases with the aging time; a credible reason is that embrittlement can result in premature fracture.

The effect of aging time on the domain size and the LRO parameter is shown in Figures 26 and 27, respectively. The domain size is still increasing, at 100,000 minutes aging time, but the LRO parameter has attained a value of unity at about 10,000 minutes. If the data are ploted logarithimically they can be fitted by a straight line (Figure 28 and 29). The domain size growth rate follows the $D^n - D_o^n = K \cdot t$ rule, where n is 2.4. K is given by:

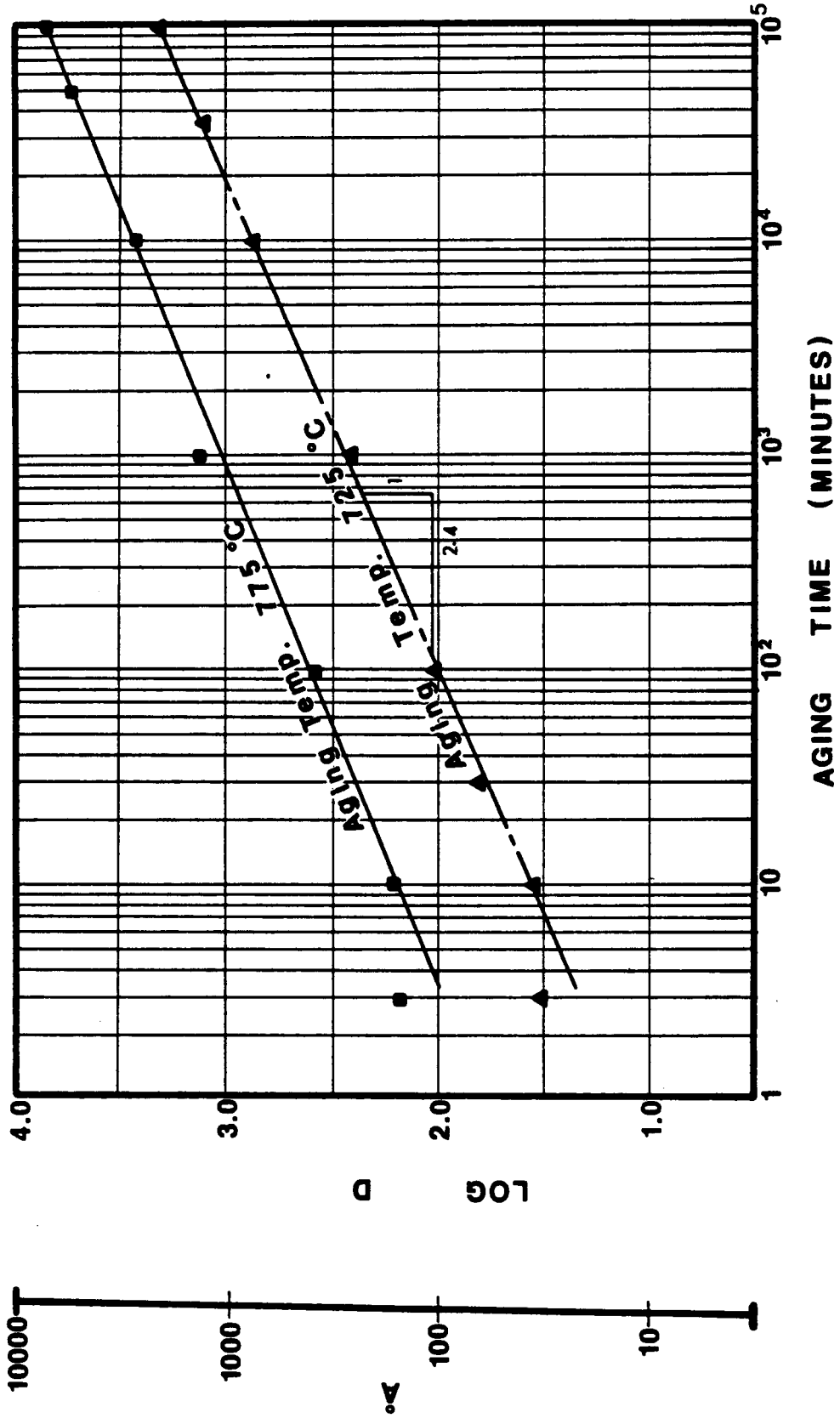


Figure 28. Effect of aging time on the domain size (log-log plot).

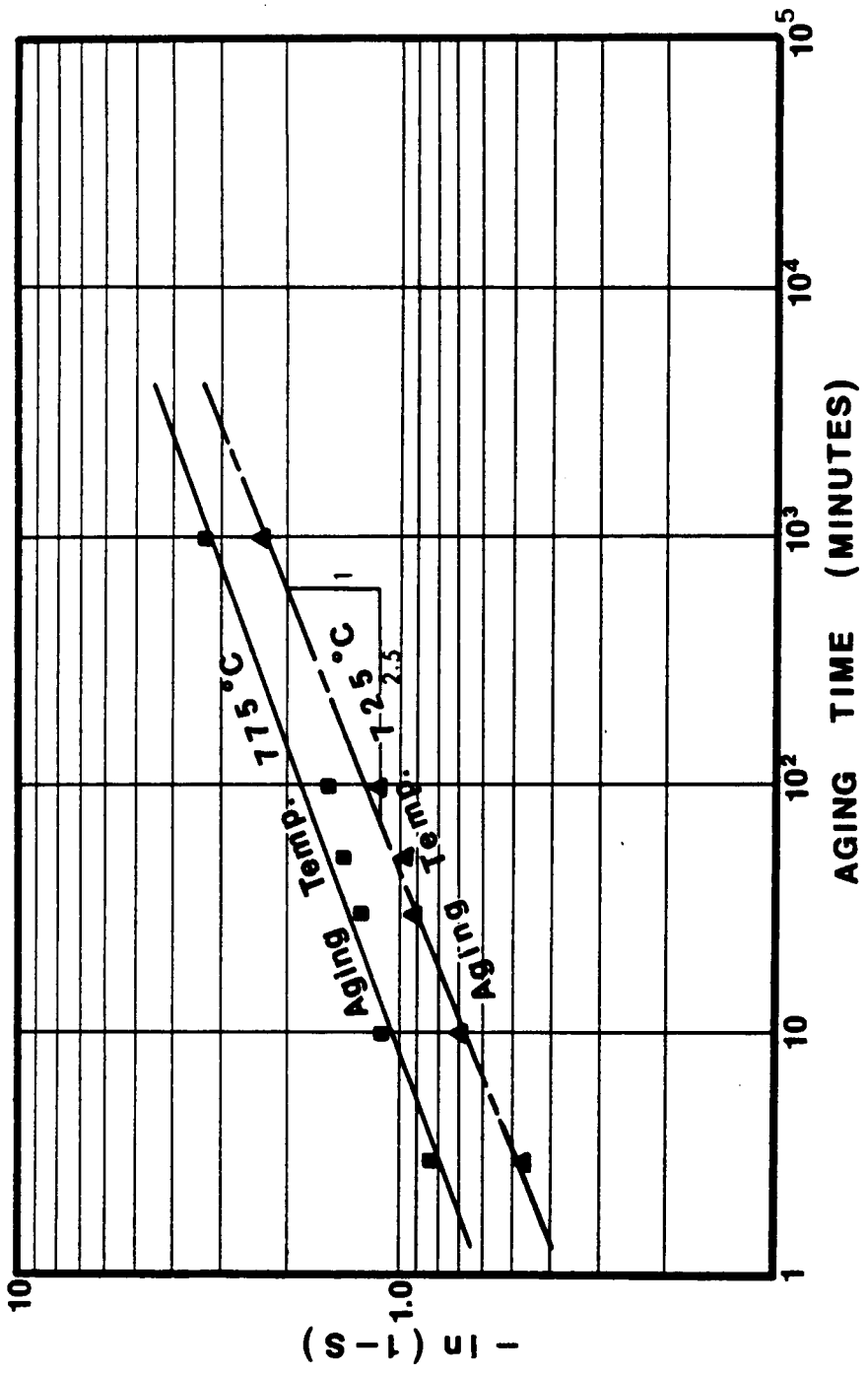


Figure 29. Effect of aging time on the long-range order parameter (log-log plot).

$$K = K_o \cdot \exp(-Q_d/RT)$$

where Q_d is the domain growth activation energy which can be calculated from the two sets of data obtained at 725 °C and 775 °C; the average Q_d value around 725-775 °C is calculated as 127 Kcal/mole (5.31×10^5 joules/mole).

The LRO parameter follows the

$$\ln(1-S) = -G \cdot \exp(-Q/RT) \cdot t$$

rule, where n=3.3. The average value of the ordering activation energy (Q) around 725-775°C is calculated as 19.4 Kcal/mole (8.12×10^5 joules/mole).

Now the question arises as to what degree the domain size and the LRO parameter are controlling the strength. The yield strength and hardness decrease continuously after attaining maximum values. One reason may be that for longer aging the larger domain size results in a decrease in the amount of anti-phase boundaries, so domain hardening decreases. Another reason may be that the higher LRO parameter lowers the stacking fault energy. Although this would allow dislocations to glide easier, cross slip would be more difficult. Hence the dislocation will tend to pile up on the high angle grain boundaries. This would develop a high stress concentration locally, and lead to crack initiation and low yield strengths.

Replotting the data differently gives insight into the contribution to strengthening from the domain size and the degree of LRO. In Figure 30 is plotted the yield strength versus the LRO parameter, using data for both aging temperatures. By most of the data points are the domain sizes. Note that as the LRO parameter increases the strength passes through a maximum, and that along this curve the domain size is continously increasing. The maximum strength corresponds to a value of S of around 0.7. Figure 31 shows a similar plot for the hardness, and the result is similar to that for the yield strength (Figure 30). The maximum hardness corresponds to a value of S of about 0.95. Also shown in Figure 32 is the elongation versus the degree of order.

If the yield strength values for both aging temperatures are plotted versus the domain size, a common curve cannot be used to describe the relationship, but as shown in Figure 33, a separate curve is required for each temperature. Hence, the yield strength is more dependent on the LRO parameter than the domain size, especially when the domain size becomes large enough.

In the early stages of aging, the strength and hardness increase. At this stage, the domain size is small, but increasing, and the degree of order is small, but increasing. In the early stage of aging it is difficult to separate the contribution to the strength

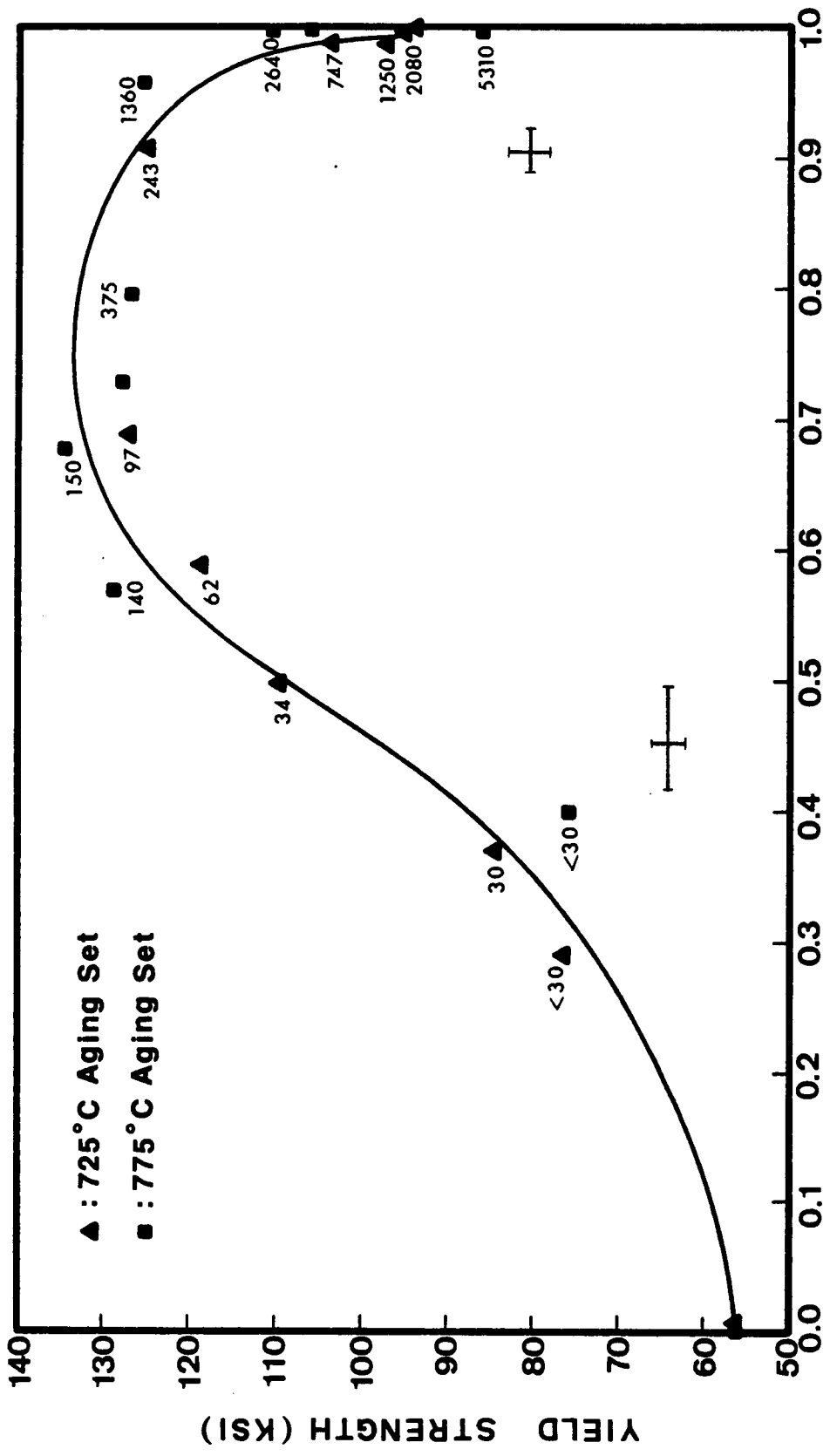


Figure 30. The relationship between yield strength and long-range order parameter. (The domain size is listed by the data points and the bars give the estimated error in the measurements.)

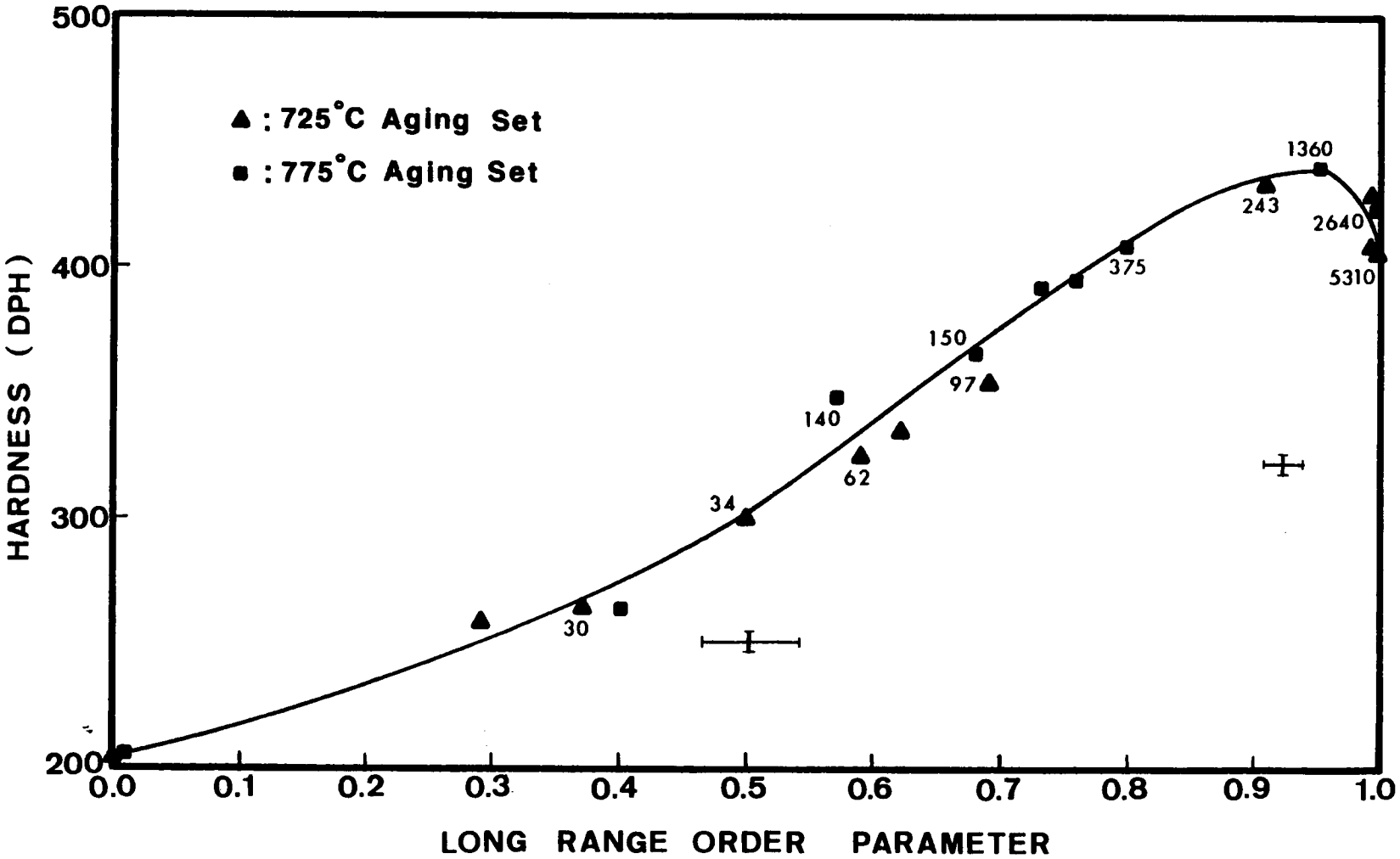


Figure 31. The relationship between hardness and long-range order parameter. (The domain size is listed by the data points and the bars give the estimated error in the measurements.)

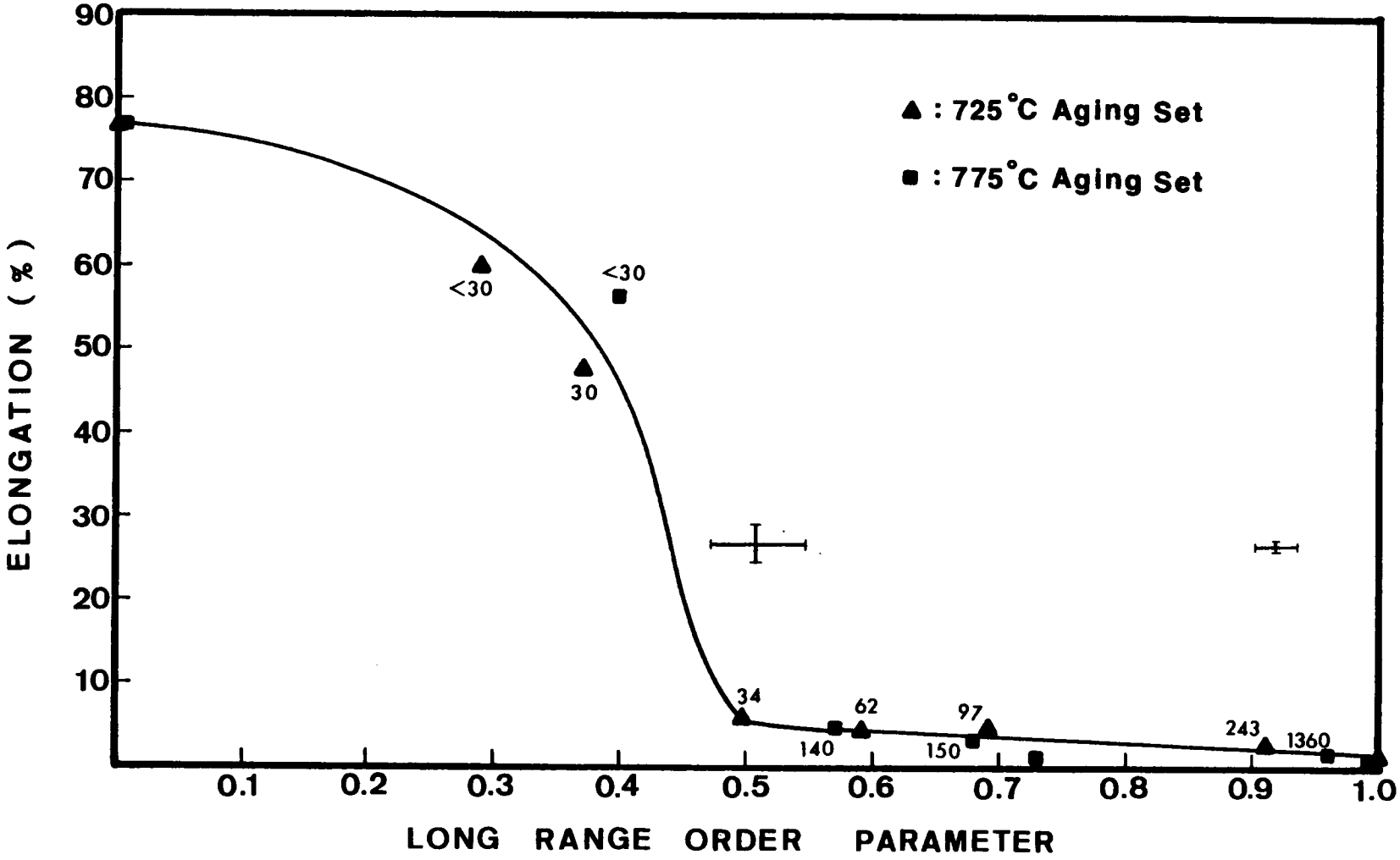


Figure 32. The relationship between the elongation and the long-range order parameter. (The domain size is listed by the data points and the bars give the estimated error in the measurements.)

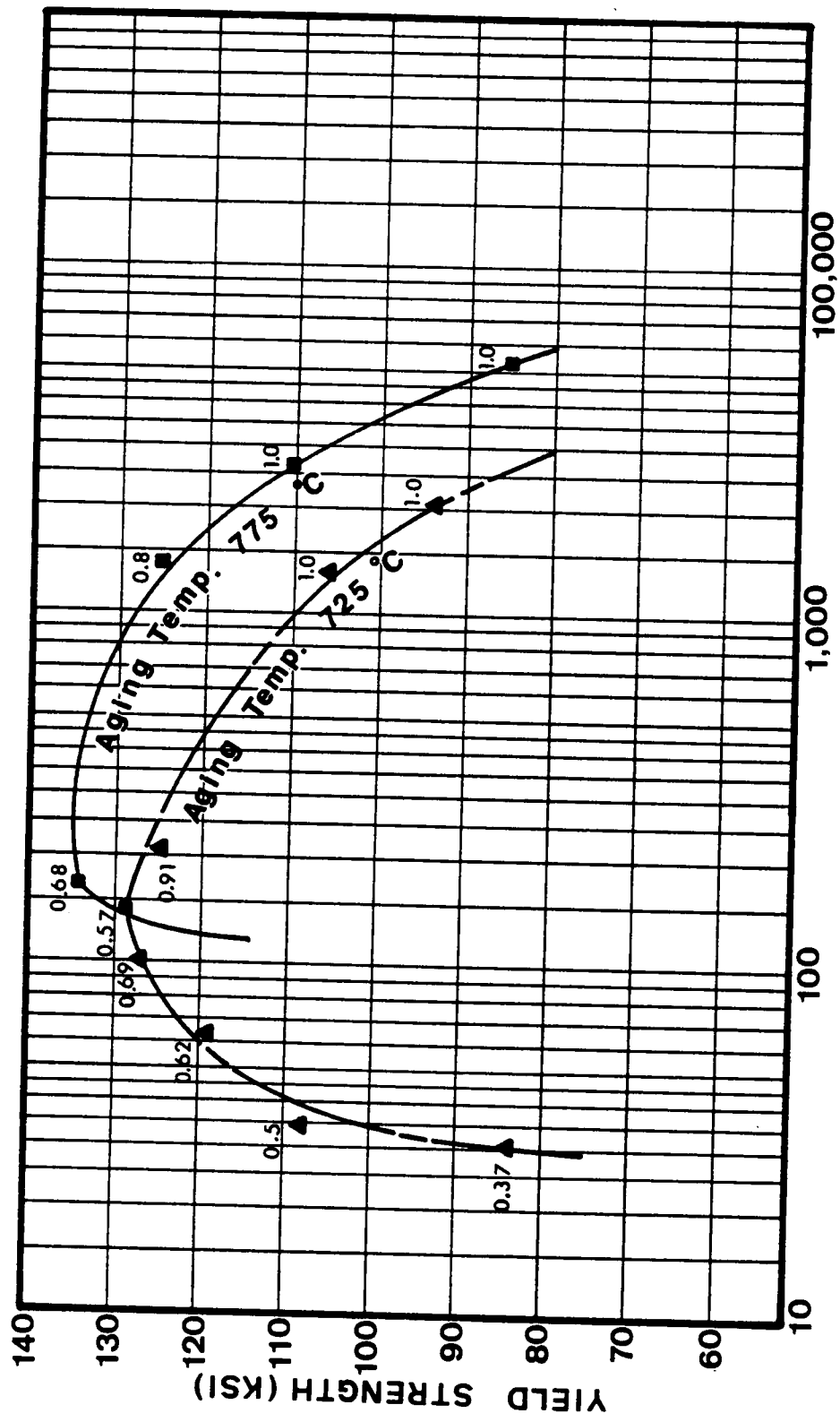


Figure 33. Yield strength as a function of domain size. (Number by data points are long-range order parameter S values.)

from these two factors. The decrease in strength after the domain size becomes about 300 Å can be attributed to an increase in LRO from about 0.75 to unity.

4.1.3 Part 2: Quenching temperature effect.

The relationship between LRO parameter and quenching temperature is shown in Table 6 and Figure 34, and the relationship between the mechanical properties and quenching temperatures is shown in Table 7 and Figure 35.

It is seen in Figure 35 that the yield strength, elongation and hardness are all strongly dependent upon the quenching temperature. Above the critical temperature (868 °C), the structure is SRO, and this structure is retained upon quenching, as reflected in S=0. The mechanical properties are essentially independent of the quenching temperature over the range used (up to 1000 °C).

Below about 800 °C, the LRO parameter is about 0.9 or above. Also, the mechanical properties are almost constant. As the quenching temperature approaches the critical temperature, the LRO parameter decreases rapidly, approaching zero. However, the mechanical properties don't show a significant decrease until about 850 °C. Above this temperature, the hardness and yield strength decrease drastically, and the elongation increases. Before reaching 868 °C, these values attain the constant values retained for quenching temperature above 868 °C.

Table 6. The effect of quenching temperature on the LRO parameter S

Sample Number	Holding Temp. (°C)	Holding Time (min.)	E_{110}	E_{420}	$\frac{E_{110}}{E_{420}}$	S
II-1	750	120	1010	6664	0.152	0.90
II-2	780	120	633	4051	0.146	0.92
II-3	810	120	1719	11376	0.151	0.90
II-4	834	60	315	3055	0.103	0.75
II-5	845	60	355	4071	0.087	0.69
II-6	855	60	351	7549	0.046	0.50
II-7	862	60	55	3349	0.016	0.30
II-8	865	60	21	3375	0.0062	0.20
II-9	870	60	0	4163	0	0
II-10	880	60	0	4552	0	0

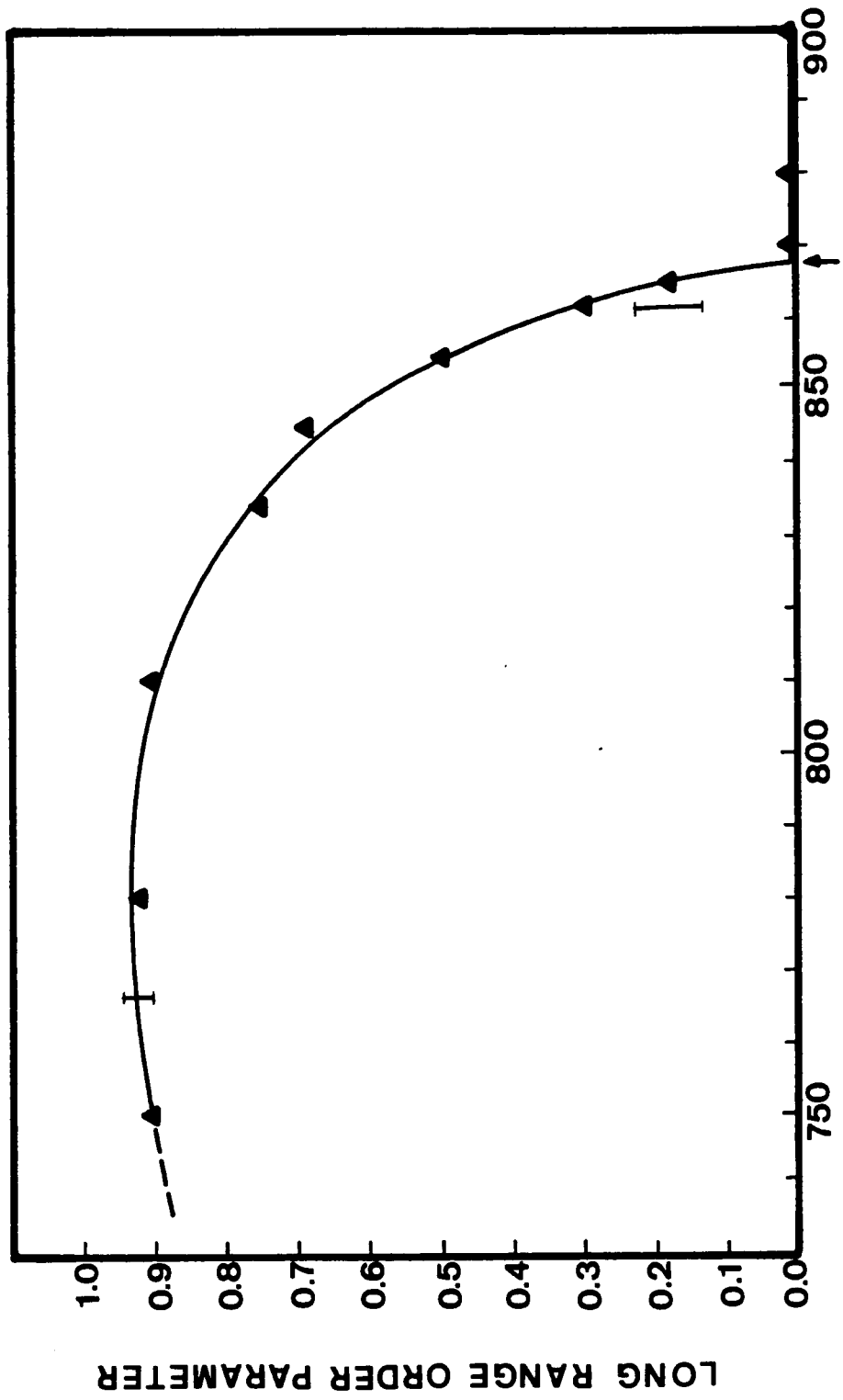


Figure 34. The relationship between the long-range order parameter and the quenching temperature. (The bars give the estimated error in the measurement.)

Table 7. The effect of quenching temperature on the mechanical properties as measured at 25 °C

Sample Number	Holding Temp. (°C)	Holding Time (min.)	Hardness (DPH)	Y. S. (Ksi)	T. S. (Ksi)	Elongation
II-1	750	120	383	---	---	*
II-2	780	120	390	99.2	106.0	1.2%
II-3	810	120	388	---	---	*
II-4	834	60	390	---	---	*
II-5	845	60	391	101.0	107.0	1.4%
II-6	855	60	327	83.8	109.5	4.4%
II-7	862	60	218	55.4	122.5	80%
II-8	865	60	202	55.2	125.8	74%
II-9	870	60	205	56.3	128.9	74%
II-10	880	60	198	56.9	129.0	78%
II-11	900	30	197	56.1	128.8	75%
II-12	950	30	201	55.23	128.7	77%
II-13	1000	30	202	55.9	129.3	81%
II-14	1100	30	200	56.6	128.8	78%

*: Cracked after heat treatments.

Heat Treatment Procedure: Step 1, Solution Heat Treatment: 1100 °C, 30 min. then water quenched. Step 2, Held at different temperatures, for 30 min. to 120 min., then water quenched (using vertical furnace and using He as protection gas).

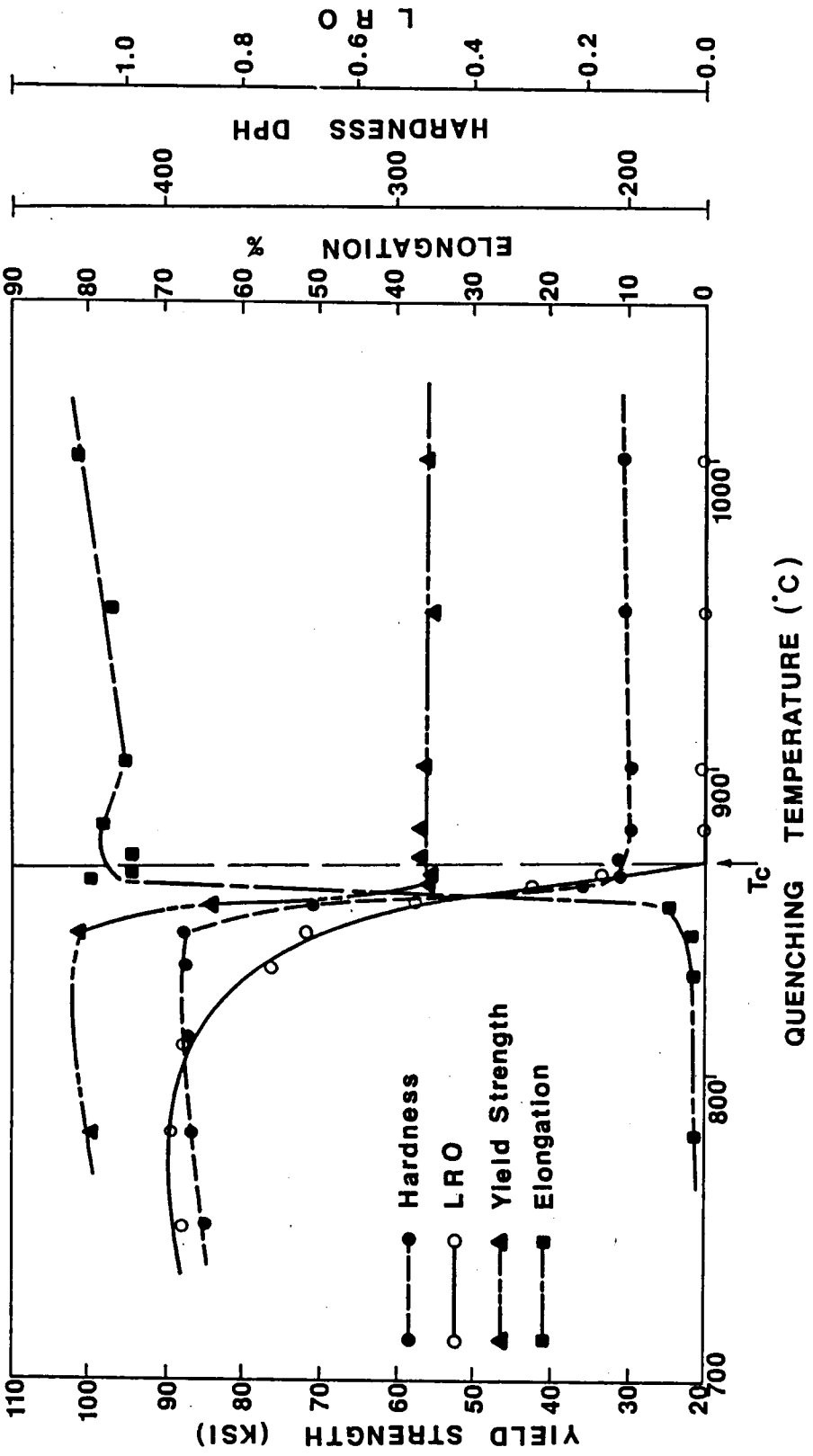


Figure 35. The relationship among the mechanical properties long-range order parameter and quenching temperature.

This reflects the strong influence of the degree of order on the mechanical properties. For Ni_4Mo to have relatively high strength and hardness, the degree of order must be about 0.7 or higher.

4.1.4 Part 3: High temperature softening resistance.

In order to examine the effect of temperature on the tensile mechanical properties of Ni_4Mo, it was necessary to develop a prior structure that would not change significantly during testing. Thus, tensile samples were aged at 725°C for 1,000 minutes, which gave a domain size of 240 Å and a LRO parameter of 0.9. The previous studies indicate that the domain size would change negligibly during the tensile testing. However, above 800 °C, the LRO parameter approaches the equilibrium value before the tensile test begins. For testing, the samples were heated from 25°C to the test temperature in about 5 minutes, held 10 minutes to get a stable thermal condition, then tensile tested. The strain rate was about 0.2/min, so that the testing time was from 1 to 5 minutes.

The results are shown in Table 8 and Figure 36. As the test temperature increases, the yield strength decreases slightly, becomes constant from about 400 to 800 °C, then decreases drastically as the temperature approaches the highest test temperature, 1000°C. The elongation is quite low until the temperature reaches the

Table 8. The elevated temperature mechanical properties of Ni_4Mo for small domain size condition

Sample Number	Test Temp.(°C)	Y. S. (Ksi)	T. S. (Ksi)	Elonga-tion
III-1	25	125.3	150.3	2.44%
III-2	25	124.9	129.2	*
III-3	300	110.0	112.0	0.4%
III-4	400	102.9	105.8	3.0%
III-5	500	101.0	104.7	2.08%
III-6	600	100.1	104.4	0.98%
III-7	700	103.5	109.1	1.52%
III-8	750	101.2	107.7	1.44%
III-9	800	100.3	113.0	1.94%
III-10	820	90.0	98.1	1.4%
III-11	830	81.5	100.3	1.8%
III-12	850	74.4	88.9	*
III-13	900	46.7	51.9	6.6%
III-14	1000	28.2	28.6	37%

*: Broken at pin hole during tensile testing.

Heat treatment procedure: Step 1, Solution heat treated at 1000°C, 30 min., then water quenched. Step 2, Aged at 725°C for 1000 min. then water quenched (domain size about 240 Å).

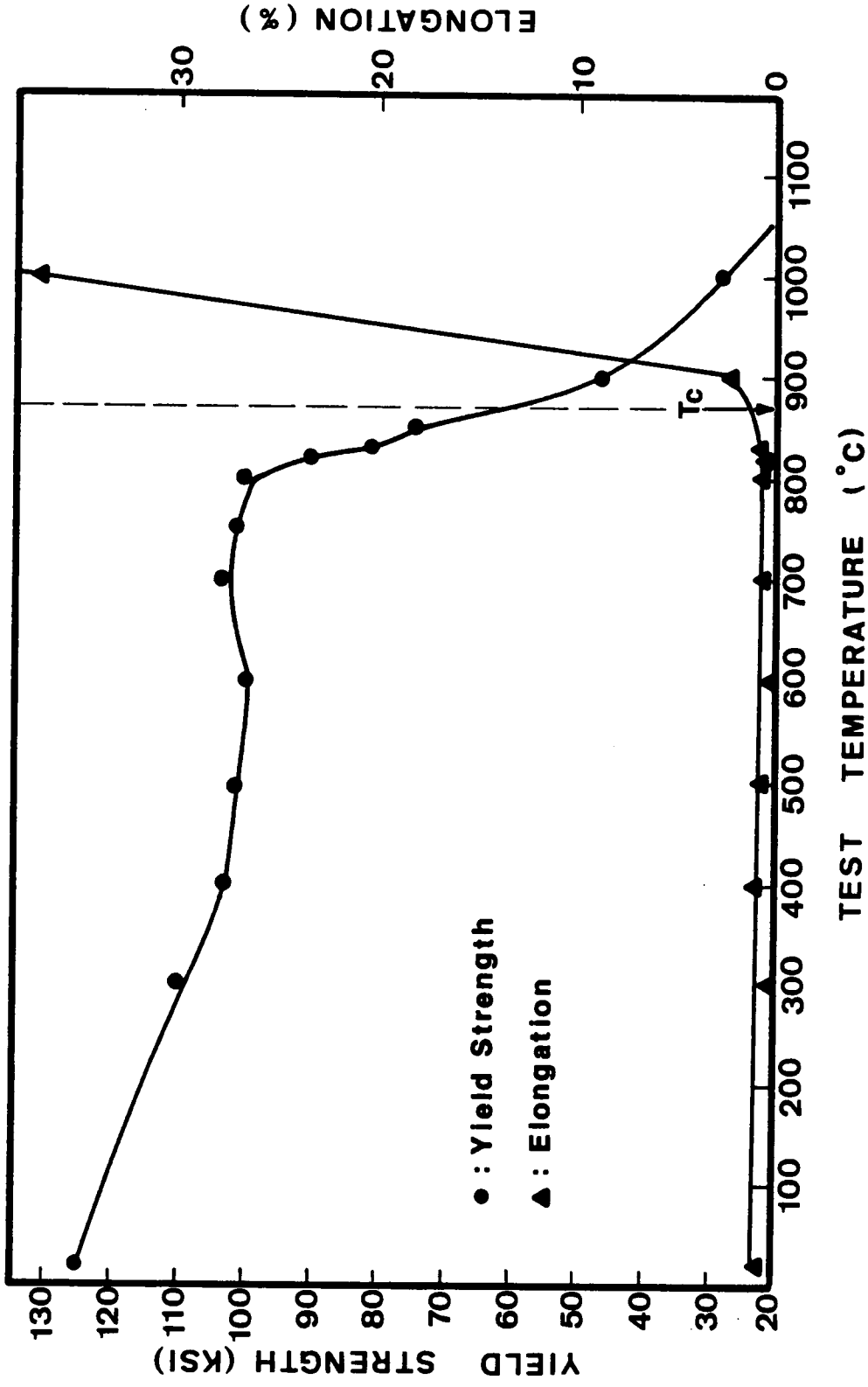


Figure 36. The effect of test temperature on the yield strength and elongation. (The prior treatment consisted of aging at 725°C for 1000 minutes.)

critical temperature. Note that the strength decreases significanty from 800 °C to the critical temperature, consistent with the effect of a reduction in the LRO parameter expected in this range. Also note that the strength continues to decrease above 868 °C, in the range where the structure is SRO α; this decrease is probably caused by increase in α grain size.

The Ni_4Mo alloy shows excellent resistance to short-time, high-temperature softening. In Figure 37 the data for Ni_4Mo are compared to the strength for four other alloys. The intermetallic compound Ni_3Al has sufficient high-temperature strength to make it a serious candidate for applications in this temperature range. The Waspalloy alloy is a currently used high-temperature superalloy, and it is seen that Ni_4Mo has a strength quite comparable to this alloy over the entire temperature range.

In order to examine the effects of domain size and LRO parameter on the high temperature mechanical properties, samples were aged for 14,400 minutes at 850 °C. This gave a domain size of 30,000 Å (3 μm). The value of S was not determined. The samples were sealed in silica tubes and were cooled from 850 °C by breaking the silica tubes in water. The cooling rate is unknown and may not have been sufficiently rapid to retain the value of S at 850 °C. This structure had a yield strength at 25 °C of 92,000 psi, compared to a value of 125,000 for a domain

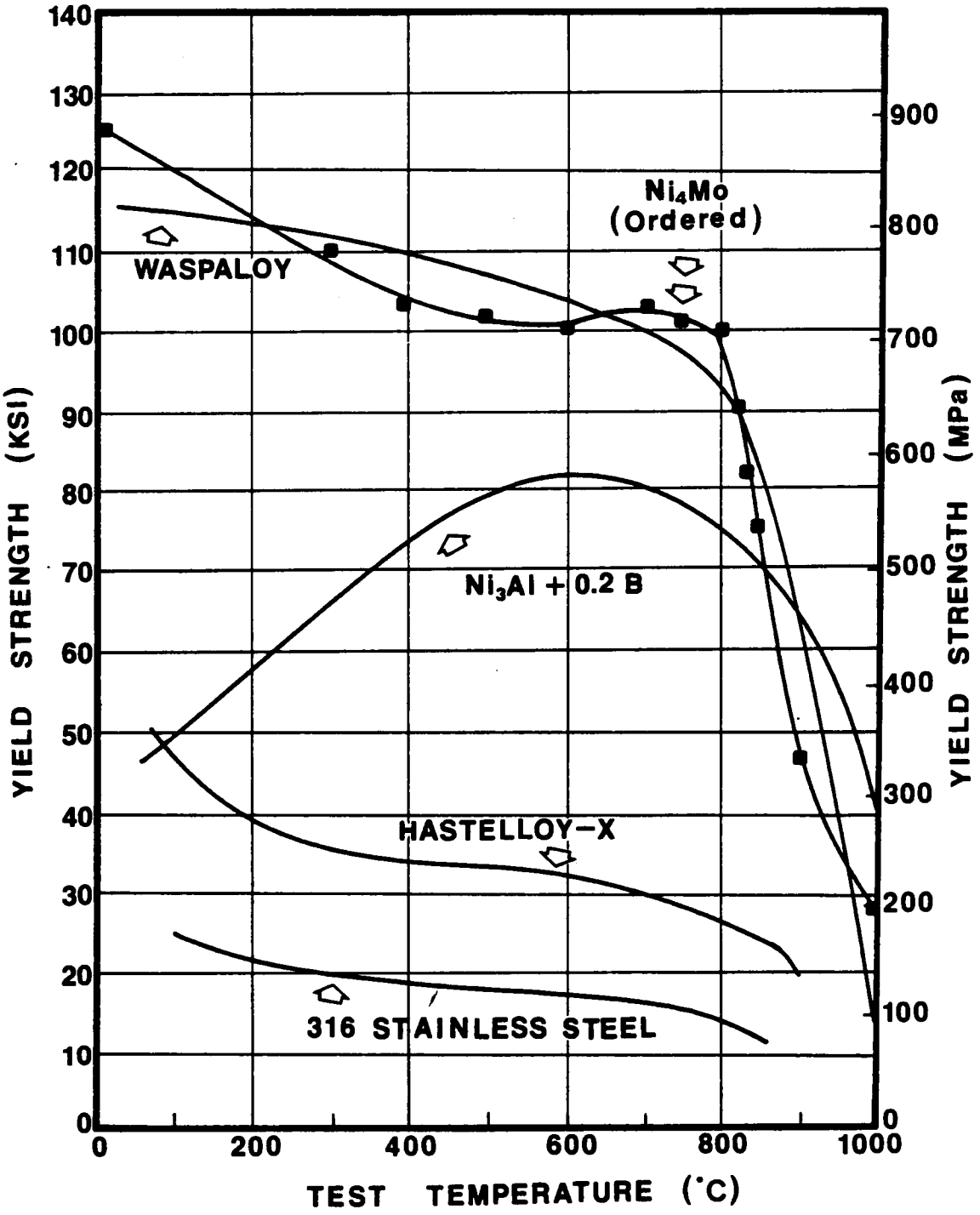


Figure 37. Yield strength as a function of test temperature for the ordered Ni_4Mo alloy, the commercial alloys, 316 stainless steel, Hastelloy-X, Waspaloy and the intermetallic compound alloy Ni_3Al.

size of 240 Å and a LRO parameter of 0.9 (Figure 36).

The results are shown in Table 9 and Figure 38. The yield strength decreases slowly with temperature up to the highest test temperature, 1000 °C. The elongation is very low (1 % or less) up to the critical temperature, then increases greatly above it. These results are similar to those shown in Figure 36 for the structure containing a finer domain size (240 Å).

The elongation obtained upon testing samples quenched from 1000 °C is about 80% (Figure 35), whereas the elongation obtained upon testing at 1000 °C is 30% (Figures 36 and 38). This indicates a basic difference in the deformation mechanism, and this point will be examined further in the section in which the fractography of these samples is presented.

4.1.5 Part 4: LRO effect.

To examine the effect of the degree of LRO on the mechanical properties, samples were prepared with an identical, large domain size but different values of S. The tensile samples were first aged at 850 °C for 14,000 minutes to give a domain size of approximately 35,000 Å. These samples were heated to various temperatures for 60 minutes, then quenched directly into water to retain the LRO structure. The results are tabulated in Tables 10 and 11, and plotted in Figure 39.

Table 9. The elevated temperature mechanical properties of Ni_4Mo for large domain size condition

Sample Number	Test Temp.(°C)	Y. S. (Ksi)	T. S. (Ksi)	Elongation
IV-1	25	91.4	91.4	Nil
IV-2	600	76.0	80.9	Nil
IV-3	750	70.6	74.3	Nil
IV-4	800	68.5	70.2	Nil
IV-5	850	64.0	68.6	*
IV-6	900	52.9	54.0	Nil
IV-7	1000	23.6	25.2	26.1%

*: Broken at pin hole.

Heat treatment procedure: Step 1, Solution heat treated at 1000°C for 30 min., then water quenched. Step 2, Aged at 850°C for 14400 min. (10 days) to get large domain size (about 3 μm), then water quenched.

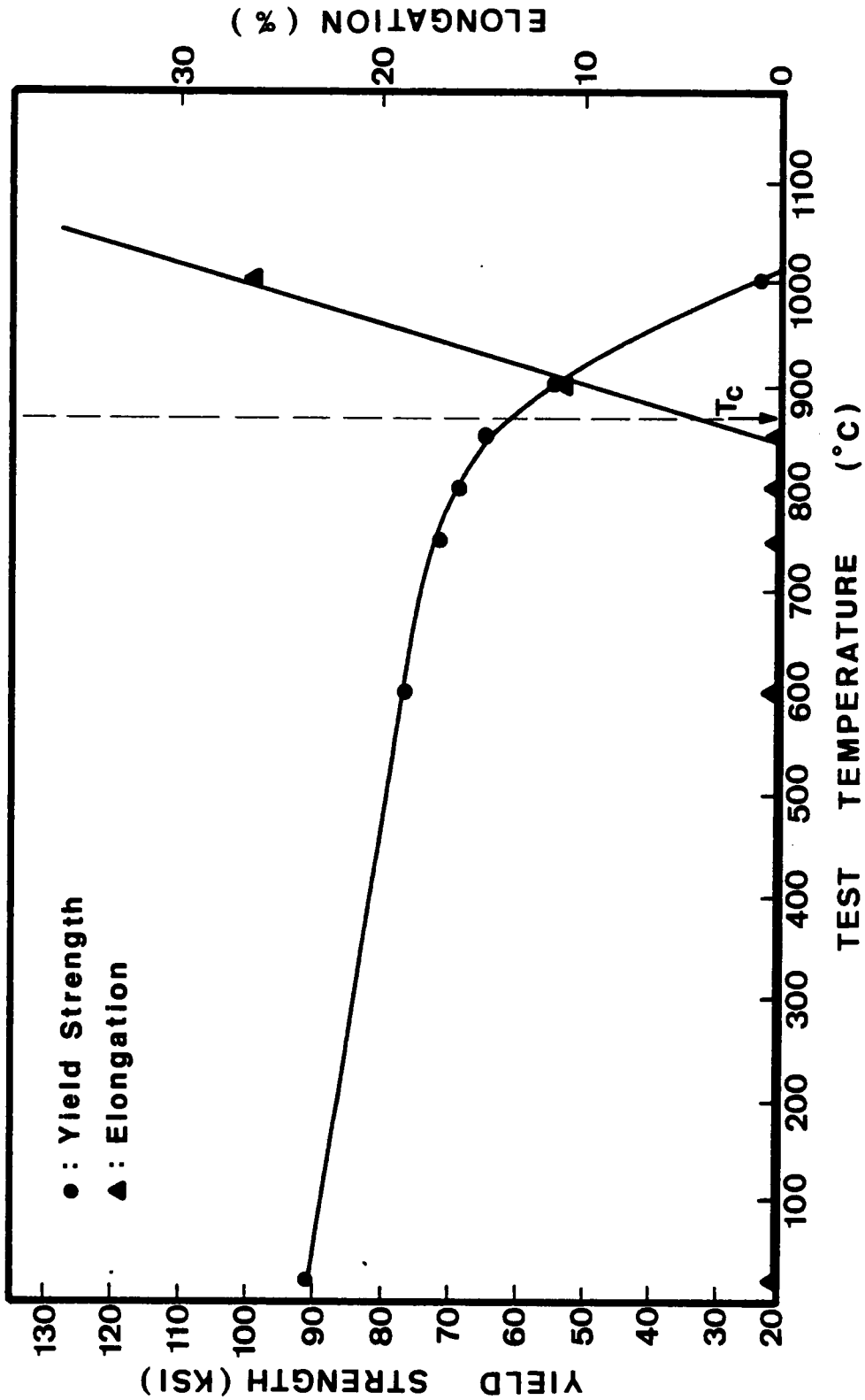


Figure 38. The effect of test temperature on the yield strength and elongation. (The prior treatment consisted of aging at 850 ℃ for 14000 minutes.)

Table 10. The room temperature mechanical properties of Ni_4Mo for different LRO parameter values

Sample Number	Quench Temp. (°C)	Holding Time (min.)	Hardness (DPH)	Y. S. (Ksi)	T. S. (Ksi)	Elongation
V-1	850	60	356	104	116	1.24%
V-2	850	60	356	97.5	109	*
V-3	845	60	368	92.2	93.5	0.3%
V-4	835	60	371	81.0	81.0	0.5%
V-5	800	60	369	86.3	86.3	0.24%
V-6	800	1440	363	84.3	84.3	0.28%
V-7	780	1440	381	74.5	74.5	*
V-8	750	1440	355	70.7	70.7	0.22%

*: Broken at pin hole.

Heat Treatment Procedure: Step 1, Solution Heat Treatment: 1000°C, 30 min. then water quenched. Step 2, Aged at 850°C for 14,400 min. (10 days) to get large domain size (about 3 μm). Step 3, Shifted to vertical furnace held at different temperatures for 60 or 1440 min., then water quenched.

Table 11. The effect of quenching temperature on the LRO parameter for large domain size condition

Sample Number	Holding Temp. (°C)	Holding Time (min.)	E_{110}	E_{420}	$\frac{E_{110}}{E_{420}}$	S
V-1	850	60	279	3720	0.075	0.64
V-2	850	60	285	4199	0.068	0.61
V-3	845	60	389	4399	0.089	0.69
V-4	835	60	376	3024	0.124	0.82
V-5	800	60	421	3175	0.133	0.85
V-6	800	1440	385	2411	0.160	0.93
V-7	780	120	422	2779	0.152	0.90
V-8	750	1440	515	3028	0.170	0.96

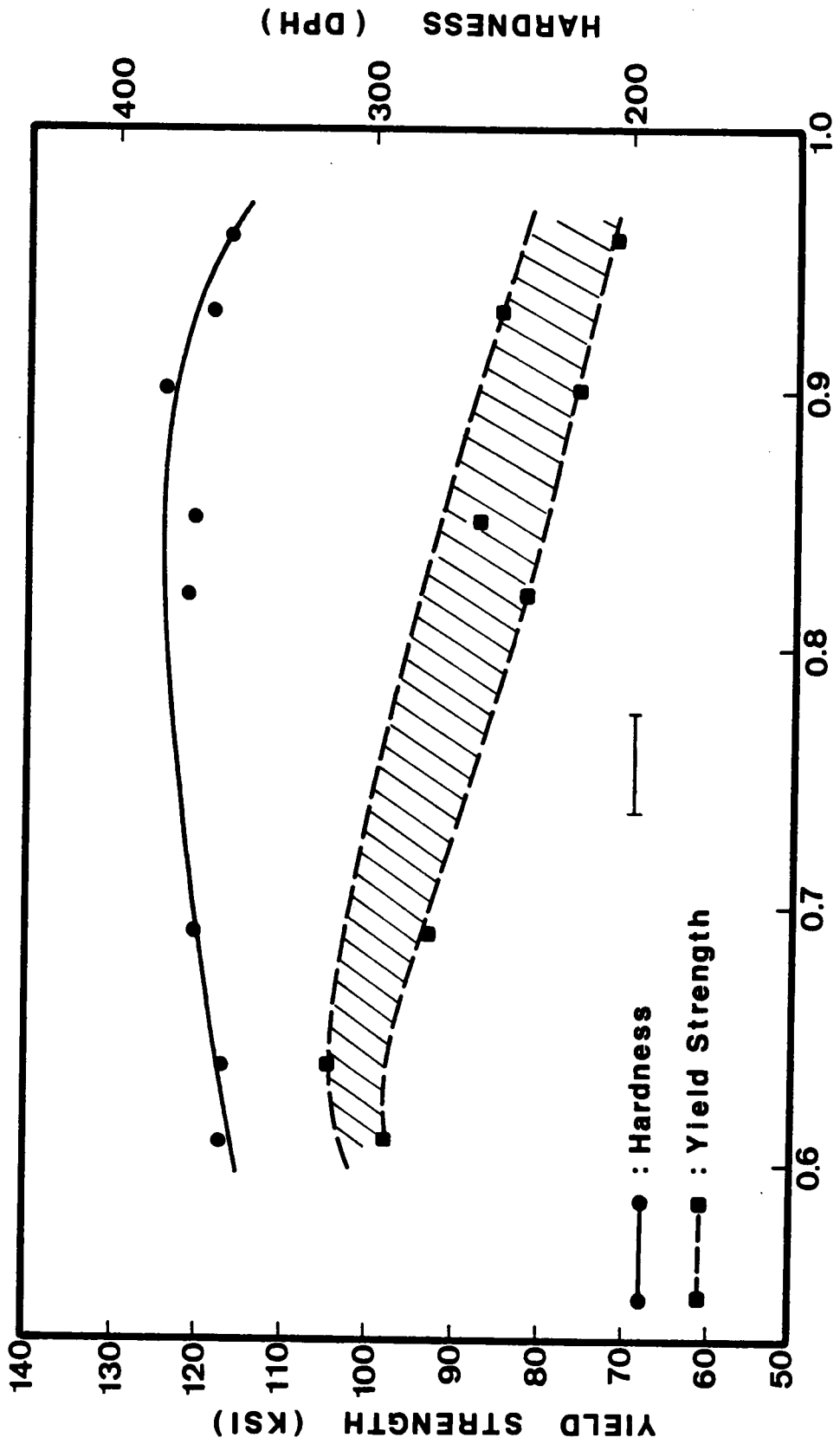


Figure 39. The relationship between the yield strength and hardness and the long-range order parameter, compared under the same large domain size.(domain size = 3.5 μm and the bar give the estimated error in the measurements.)

The degree of order has little effect on the hardness, but it is seen that the greater S, the lower the yield strength.

4.1.6 Part 5: Grain size effect.

It would perhaps be expected that the yield strength of the ordered alloy would not be affected by the size of the former α grains, but only by the structure inside these grains. To establish the influence of the prior α grain size, tensile samples were solution heated at different temperatures (from 950 to 1200°C) for different times (from 30 minutes to 2 hours), then quenched. These tensile samples then were all aged at 725°C for 100 minutes, giving a structure with a domain size of about 100 Å and a LRO parameter of 0.7.

The effect of the prior α grain size on the yield strength is shown in Figure 40; the data are tabulated in Table 12 and 13. The effect of the grain size is quite prominent.

As shown in Figure 41, these data do not follow the Hall-Petch relation

$$\sigma_y = \sigma_o + K \cdot \bar{d}^{-1/2}$$

However, if the data are plotted versus $\bar{d}^{0.75}$, a straight line is clearly followed (Figure 42). A similar relationship has been found by Shulson (88) for Ni_3Al.

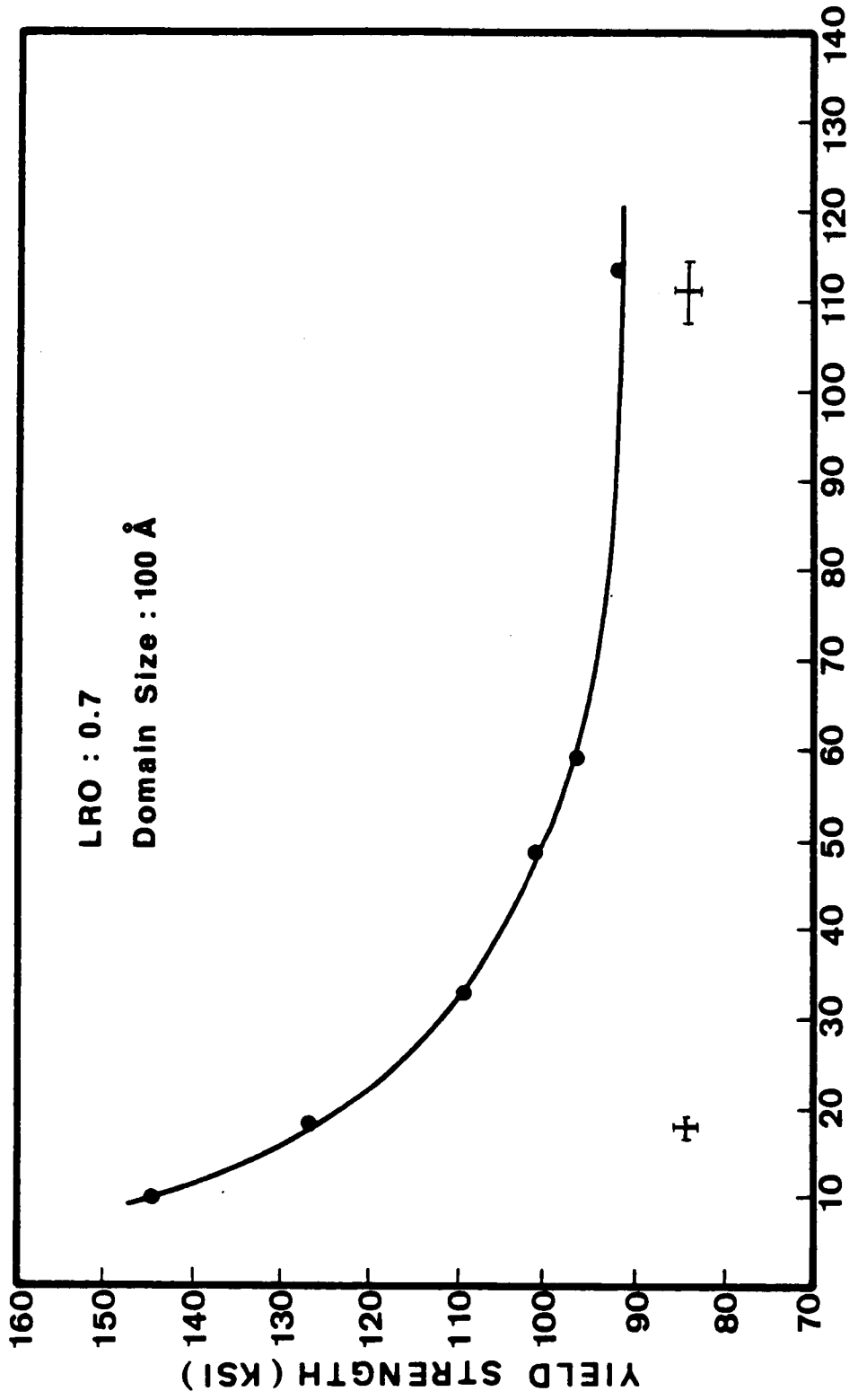


Figure 40. The effect of prior α grain size on the yield strength of ordered Ni_4Mo alloy (Yield strength vs. grain side d). (The bars give the estimated error in the measurement.)

Table 12. The effect of annealing temperature and time on the α grain size (The measurement (of the grain size was by quantitative metallography.)

Sample Number	Annealing Temp. (°C)	Annealing Time (min.)	Average Grain Size (μm)	ASTM No.
VI-1	950	30	12.0	9.4
VI-2	1000	30	18.1	8.2
VI-3	1100	30	33.1	6.5
VI-4	1100	120	48.6	5.4
VI-5	1200	120	59.2	4.8
VI-6	1200	1440	113	2.9

Table 13. The effect of prior α grain size on the mechanical properties measured at 25 °C (Grain size values are given in Table 12.)

Sample Number	Annealing Temp. (°C)	Annealing Time(min)	Y. S. (Ksi)	T. S. (Ksi)	Elongation
VI-1	950	30	144.2	156.1	2.6%
VI-2	1000	30	126.5	146.4	4.4%
VI-3	1100	30	109.0	112.0	0.7%
VI-4	1100	120	100.83	102.5	0.2%
VI-5	1200	1203	95.83	95.8	0.5%
VI-6	1200	1440	92.0	92.0	0.1%

Heat Treatment Procedure: Step 1, Annealing at separate temperatures (950 °C, 1000 °C, 1100 °C, and 1200 °C) for 30, 120, or 1440 min. to get different grain size, then water quenched. Step 2, Aged at 725 °C for 100 min., then water quenched to get same LRO parameter (0.7) and same domain size (100 Å).

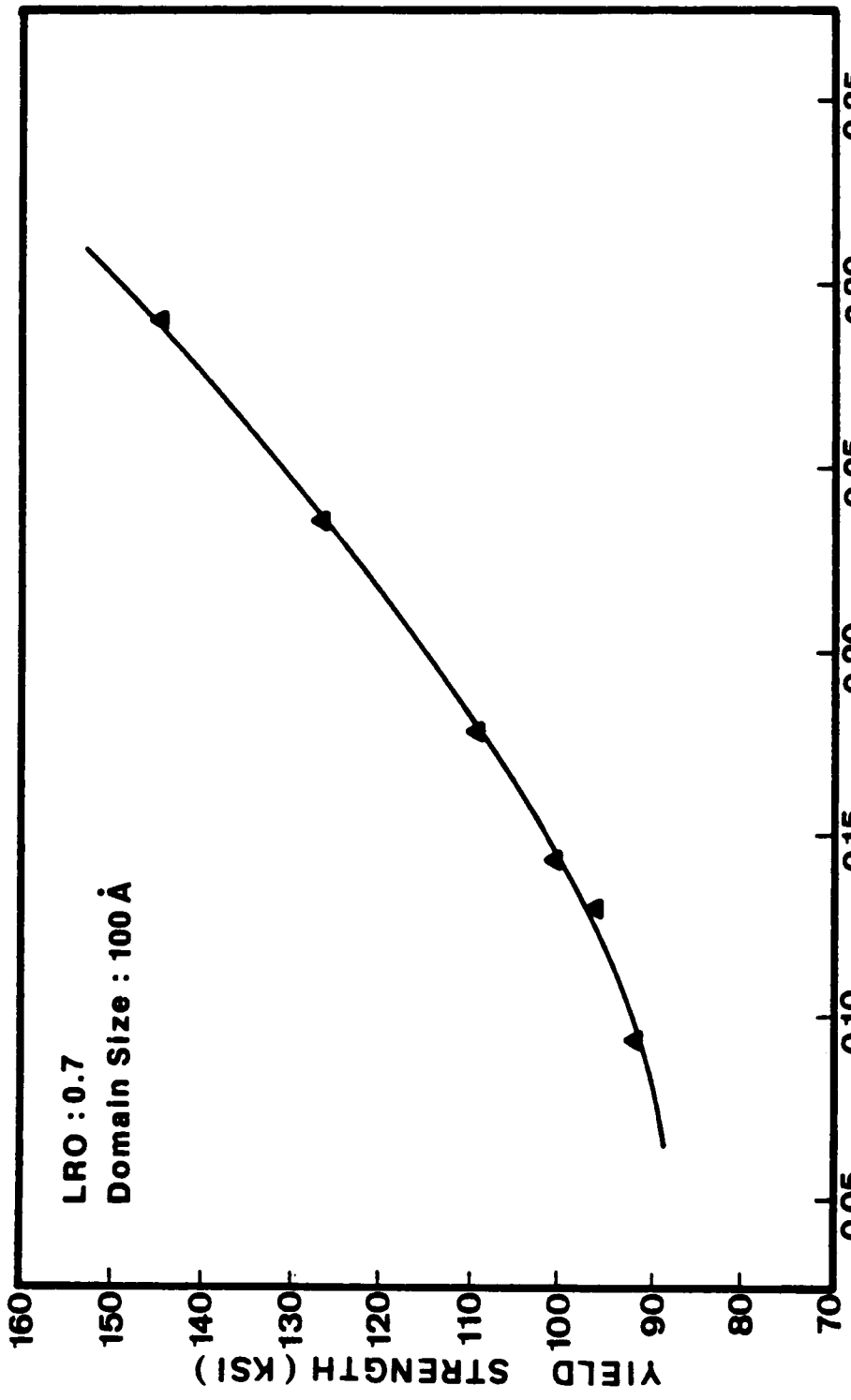


Figure 41. The effect of prior α grain size on the yield strength of ordered Ni_4Mo alloy (Yield strength vs. grain size $d^{-1/2}$).

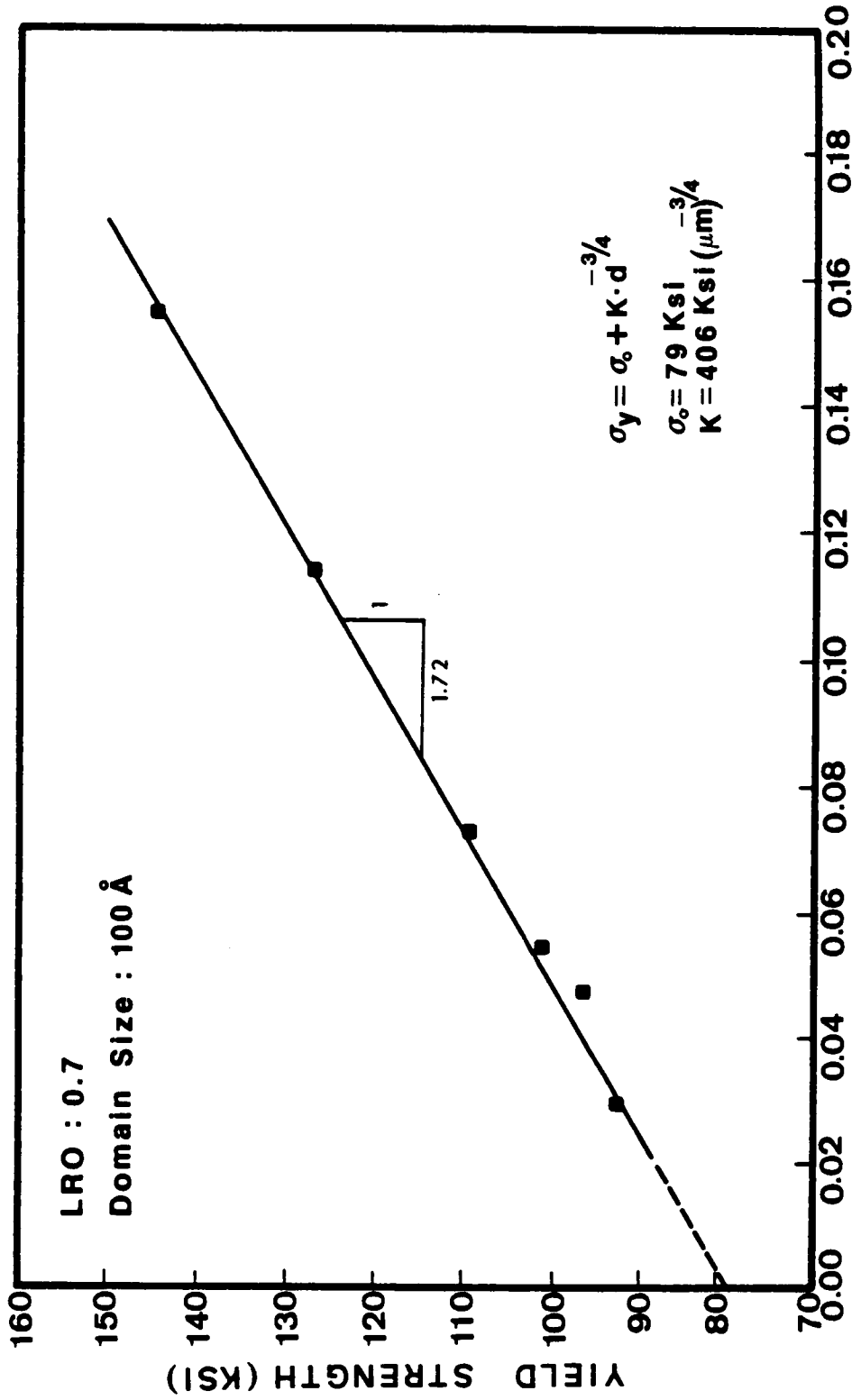


Figure 42. The effect of prior α grain size on the yield strength of ordered Ni_4Mo alloy (Yield strength vs. grain size $d^{-3/4}$)

From these results, it is clear that the high angle boundaries (formerly the α boundaries) play an important role in dislocation motion. It was found that the ductility increased with decreasing grain size (Table 13). Thus, these boundaries play a role in fracture.

4.1.7 Closure.

For the results described in Part 1 through 5 above, some conclusions are reached which are summarized here.

(1). The strength and hardness of ordered Ni_4Mo are more dependent on the degree of LRO than on the domain size.

(2). The highest yield strength occurs for a LRO parameter of about 0.7.

(3). The domain size growth follows the rate equation $D^n - D_o^n = K \cdot t \cdot \exp(-Q_d/RT)$, where n=2.4 (D in Å). The activation energy $Q_d = 5.31 \times 10^5$ J/mole (127,000 cal/mole) and $K = 7.78 \times 10^{28}$/sec.

(4). The LRO parameter S increases according to the relation in $\ln(1-S) = -G \cdot (\exp(-Q/RT)) \cdot t^{n-2/2}$, where n=3.3; $Q = 8.12 \times 10^5$ J/mole (19,400 cal/mole) and $G = 1.80 \times 10^{31}/\text{sec}^{0.394}$

(5). The yield strength depends upon the prior grain size, following the relation $\sigma_y = 79{,}000 + 406{,}000 \cdot \bar{d}^{0.75}$ (stress in psi, d in μm).

(6). The grain boundary interfaces play a very important role in the deformation mechanism and fracture mechanism in ordered Ni_4Mo.

(7). The ordered Ni_4Mo alloy has a high potential to be used as a high temperature structural material, up to about 800 °C.

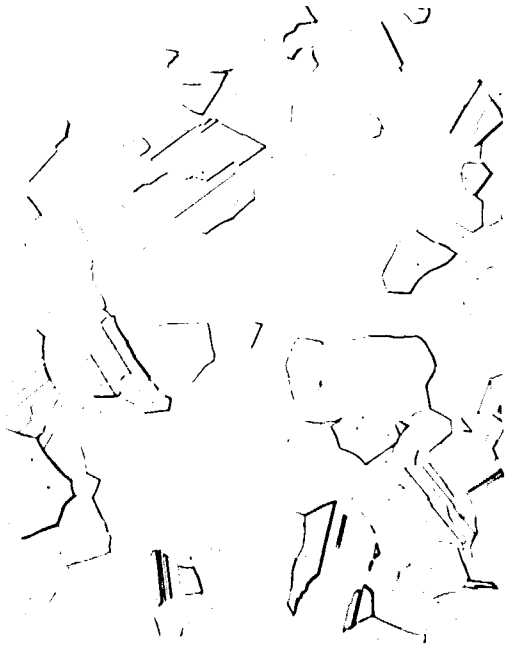
4.2 Microstructural Observations

4.2.1 Microstructure changes with aging time.

In the previous Sections, the changes in mechanical properties of Ni_4Mo with aging time have been described. In this and the following Sections, the microstructures are described and correlated to the mechanical behavior.

The characteristics of the microstructure of the solution treated alloy are exemplified by Figure 43a. The grains are uniform and equi-axed. A very small fraction of inclusions is present, which do not change with aging nor enter into the microstructural changes.

Microstructural changes upon aging at 725°C are illustrated in Figure 43b-43j. Two etchants were used, but the best results were normally obtained with a solution of one part of CrO_3 solution-five part HCl. However, for the short aging time of 10 minutes, this etchant did not reveal any structural change,whereas an etchant of one part HCl-one part H_2O_2-one part CH_3OH did. The latter etch attacked the former α grain boundaries,



(a) Solution heat treatment (1000°C , 30 minutes W. Q.) Inclusions in the equiaxial α matrix. 340X



(b) After aging 725°C, 10 minutes No. 2 Etchant. 220X



(c) After aging 725°C, 1000 minutes. Recrystallization along primary α grain boundaries. 220X

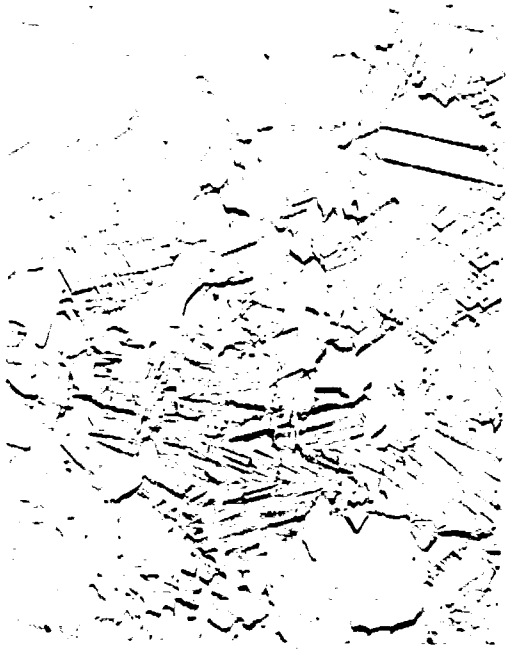


(d) After aging 725°C, 1000 min.. Grain boundary migration. 550X

Figure 43. The change of optical microstructure with aging time at 725°C.



(e) After aging 725 °C, 10,000 min. Recrystallization region grown larger. 220X



(f) After aging 725 °C, 10,000 min. Striations appear. 550X

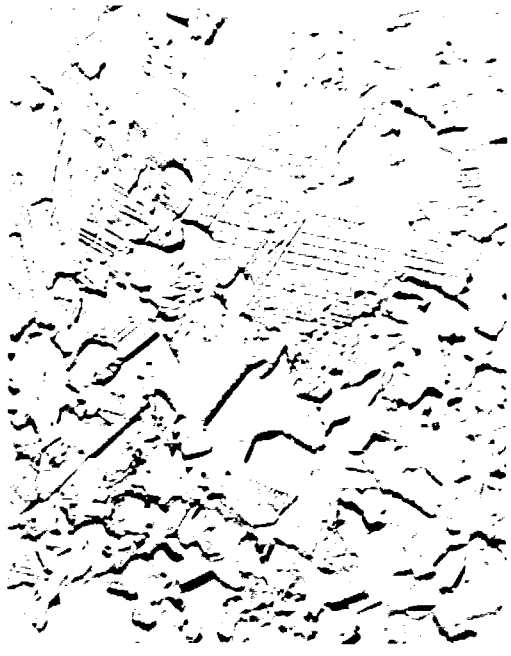


(g) After aging 725 °C, 10,000 min. Microhardness indentations shown. 500X



(h) After aging 725 °C, 50,000 min. Recrystallization region grown larger than (e). 220X

Figure 43 (Continued)



(i) After aging 725°C, 50,000 min. Higher magnification of (h). 550X



(j) After aging 725°C, 100,000 min. Recrystallization region grow larger than (h). 200X

Figure 43. (Continued)

outlining the grains clearly (Figure 43b). This is reflecting the presence of an unresolved, grain boundary, reaction product, which could only be resolved by TEM (described later).

Aging for 1000 minutes produced a clear grain boundary reaction product (Figure 43c). At higher magnification (Figure 43d) it is seen that the former grain boundaries have migrated, moving in both directions from the initial grain boundary locations. This migration increases with aging time, and results in the formation of patchy regions with wavy outlines. Between 1000 and 10,000 minutes, striations appear within the grains. Their appearance is well known and their origin has been discussed (51).

Microhardness measurements reveal differences in the hardness of the newly formed, coarser domain structure and the finer domain structure from which these are forming. This is shown in Figure 43g. In the starting, fine structure, the average hardness was 441±10 DPH, whereas in the recrystallized regions it was 407±10 DPH.

The grain boundary reaction appears to have completely consumed the matrix after aging for 100,000 minutes (Figure 43j). Note that the new grain size is about that of the original α (Figure 43a).

Aging at 775°C produces microstructures similar to those at 725°C. A grain boundary reaction begins (Figure 44b) at about 1000 minutes, but is not complete after 100,000 minutes (Figure 44e). The domains grow somewhat more rapidly at 775 than at 725°C.

To produce large domains, alloys were aged for 10 days at 850°C. Figure 45 shows typical microstructures. The domains are now sufficiently large that they are resolved, being about 3 μm.

The aged samples were observed using a scanning electron microscope in order to better reveal the grain boundary reaction product. No clear boundary migration is seen for short aging times (Figure 46a-b), although the mechanical properties are changing (see Figures 24 and 25).

Figures 46c and 46d show the structure after the reaction has produced a patchy appearance. The structure shows clear striations in nearly all grains. The relation of these grains to the original α boundaries is not particularly evident. However, Figure 46d does show a location where the former α boundary migration can be seen, as shown in the accompanying sketch. Note that the recrystallized region has developed etching striations.



(a) After aging 775 °C, 30 min. No evident microstructural change. 220X



(b) After aging 775 °C, 1000 min. Recrystallization along former grain boundaries. 220X

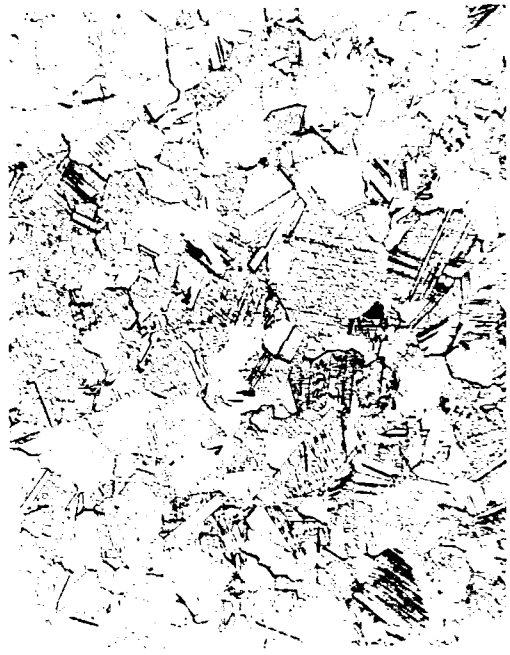


(c) After aging 775 °C, 10,000 min. Recrystallization continuing. 220X



(d) After aging 775 °C, 50,000 min. Recrystallization continuing. 220X

Figure 44. The change of optical microstructure with aging time at 775 °C.



(e) After aging 775 ℃, 100,000 min. Recrystallization region grown larger. 220X



(f) Higher magnification of (e). Showing that the domain size has grown to be resolvable. 500X

Figure 44. (Continued)

(a)

After aging 850 °C,
10 days.
Large recrystallization region and large domain size.

220X



(b)

Higher magnification of (a).
Domain size is about 3 μm.

550X

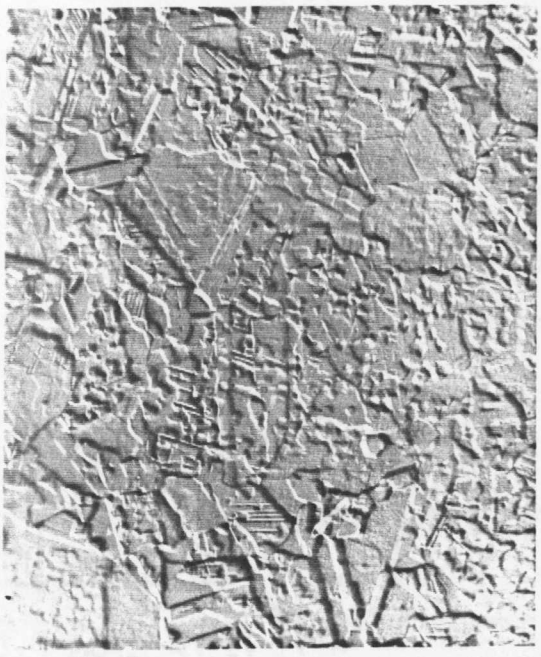


Figure 45. The optical microstructure after aging 10 days at 850 °C.

(a)

After aging 725 ℃, 1 minute.
The structure is the same as the solution heat treated condition.

1000X



(b)

After aging 725 ℃, 10 minutes.
Grain boundary morphology changed.
Using No. 2 Ethant.

1000X

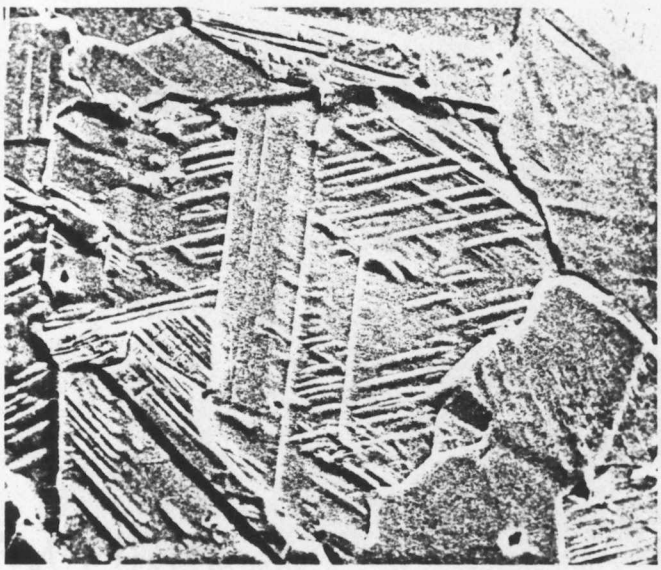


Figure 46. The change of microstructure with aging time at 725 ℃ as observed in the SEM.

(c)

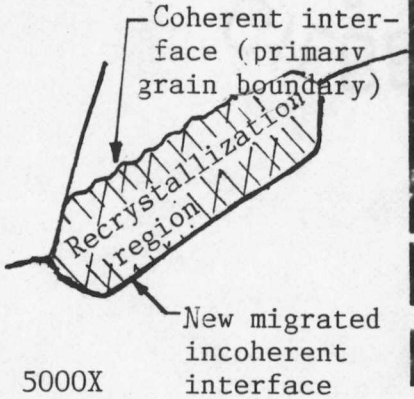
After aging 725°C, 10,000 minutes. Patchy regions with wavy outlines.

1000X



(d)

Same condition as (c) but higher magnification.



5000X

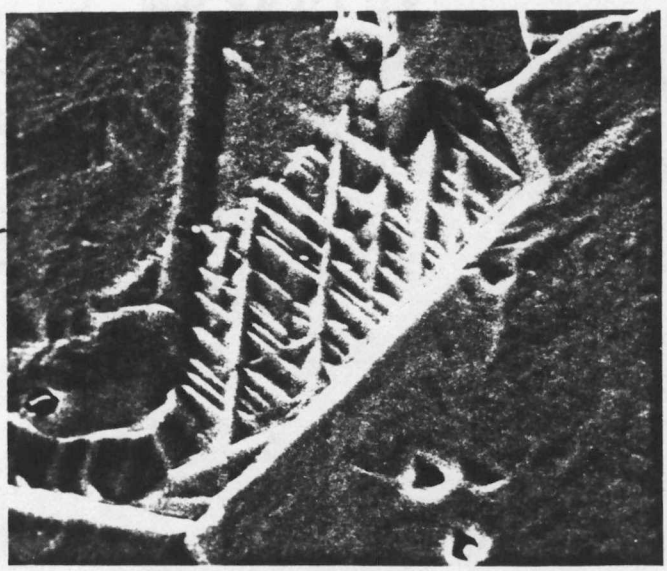


Figure 46. (Continued)

(e)

After aging 725°C, 50,000 minutes. Finer striation structure.

1000X

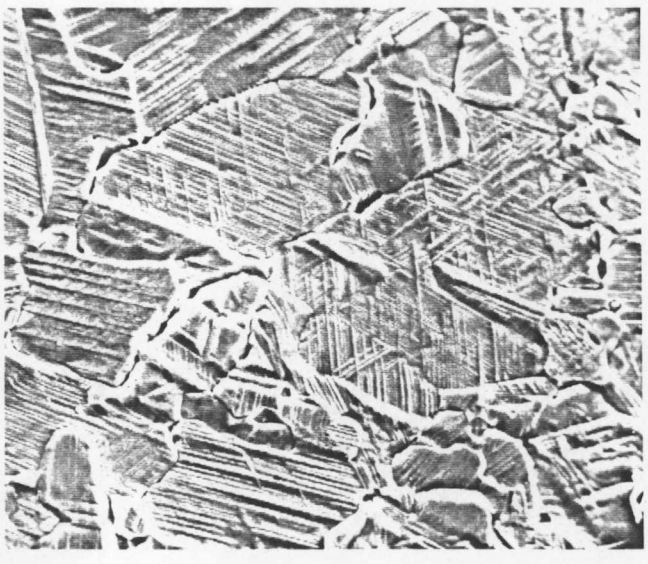


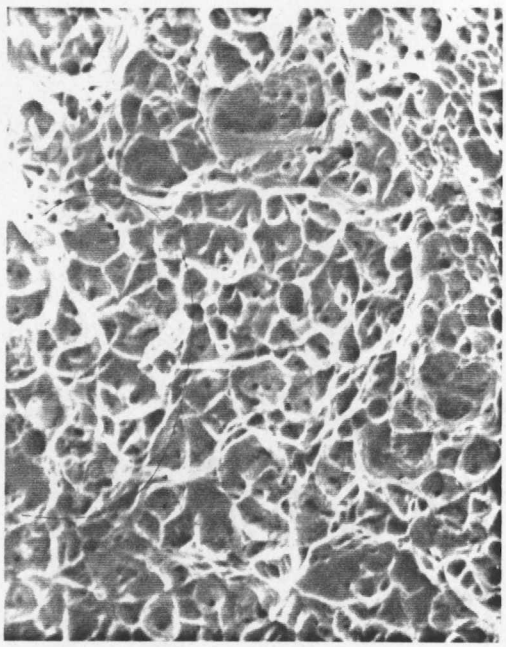
Figure 46. (Continued)

4.2.2 Fracture morphology of ordered Ni_4Mo tensile tested at 25°C.

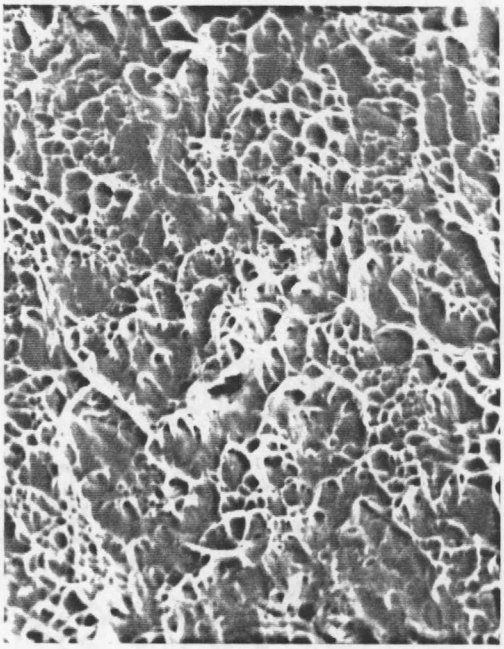
The morphology of the fracture surface of tensile samples of the ordered Ni_4Mo when tested at 25°C depends upon the structure, and hence the aging time. In the as-quenched condition, where the structure is SRO α, the material is quite ductile, and the fracture mechanism is by void coalesence, as illustrated by the fractograph in Figure 47a. Aging at 725°C for one minute produces a slight decrease in ductility (Figure 24) , but the fracture mechanism is still void coalesence (Figure 47b).

However, aging for 3 minutes produces a marked change in the fracture surface topology, as shown in Figure 47c. Some intergranular separation along the location of the former α grain boundaries occurs; the ductility has now decreased to about 50 % (Figure 24). Aging for 10 minutes reduces the ductility to less than 10 % (Figure 24), and the fracture surface is essentially completely intergranular (Figure 47d), with the fracture faces appearing quite smooth. However, at high magnification (Figure 47e) slip traces can be seen on the faces.

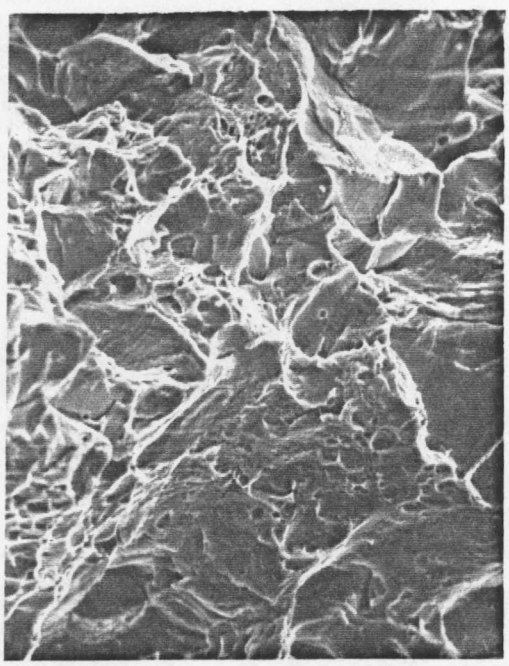
Aging for 100 minutes at 725°C produces the beginning of the grain boundary recrystallization structure, and this coincides with a change in the fracture morphology (Figure 47f). The surface topology becomes somewhat finer and less intergranular appearing, but void coalesence is



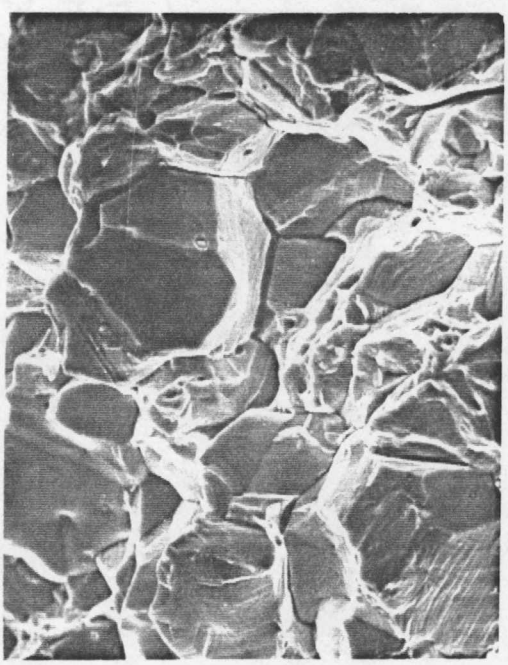
(a) Solution heat treatment (1000 ℃, 30 minutes W. Q.)
1000X



(b) 725 ℃ aged 1 minute.
1000X

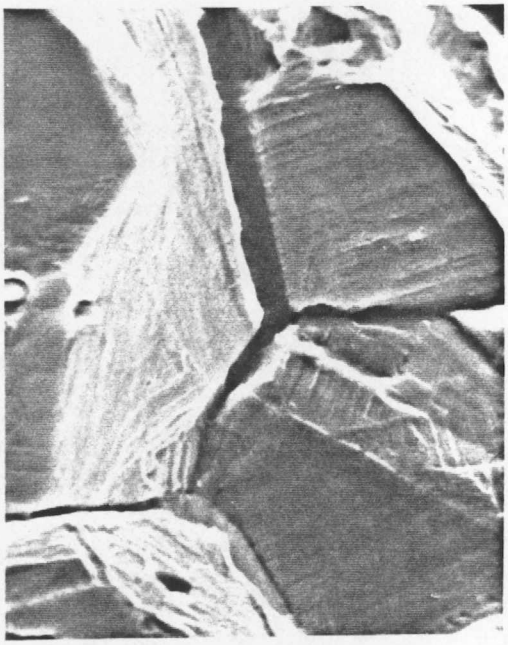


(c) 725 ℃ aged 3 minutes.
1000X



(d) 725 ℃ aged 10 minutes.
1000X

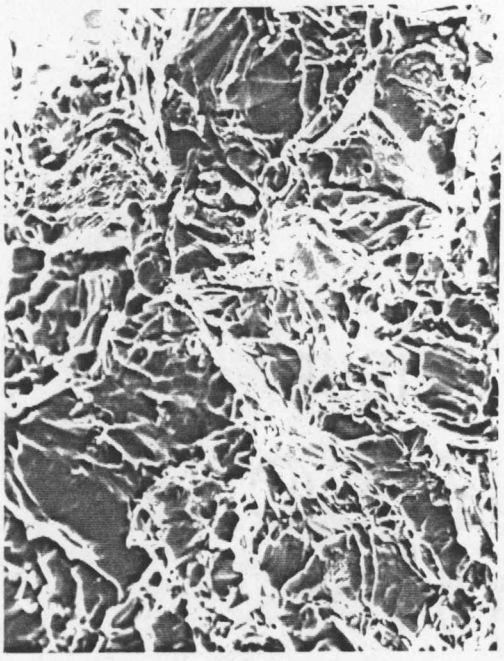
Figure 47. Fractography of tensile samples tested at 25 ℃.



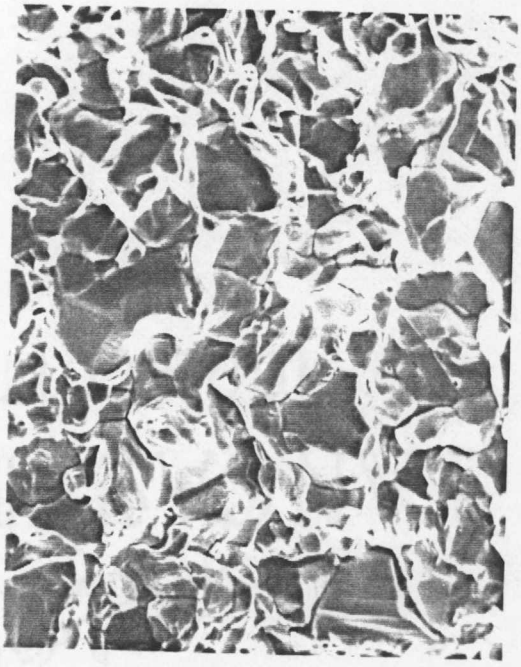
(e) 725 ℃ aged 10 minutes. 5000X



(f) 725°C aged 100 minutes. 5000X

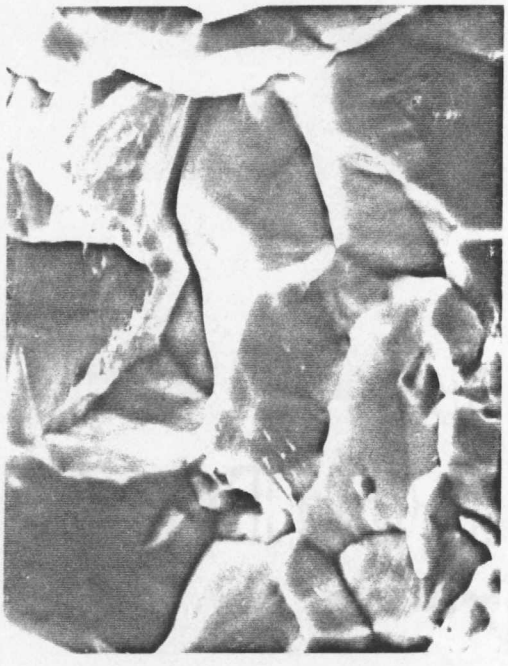


(g) 725℃ aged 1000 minutes. 900X

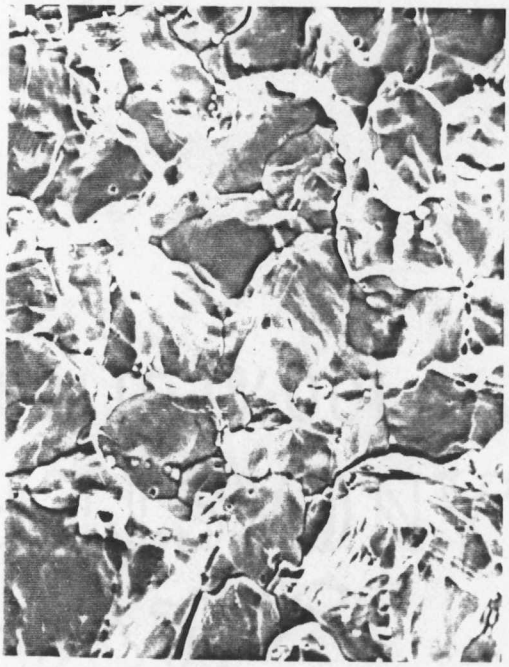


(h) 725℃ aged 36,000 minutes. 1000X

Figure 47 (Continued)



(i) 725°C aged 36,000 minutes. 5000X



(j) 850°C aged 10 days. 1000X

Figure 47. (Continued)

absent. Aging for 1000 minutes shows a similar structure (Figure 47g), although there is some evidence of void coalesence; however, in this condition, the alloy is still quite brittle. Aging for 36,000 minutes produces a domain size about 1250 A. The fracture surface (Figure 47h and 47i) shows completely intergranular fracture.

The formation of relatively large domains (e.g., 3 μm) causes the fracture surface to be intergranular but the surfaces are not flat, but wavy (Figure 47j).

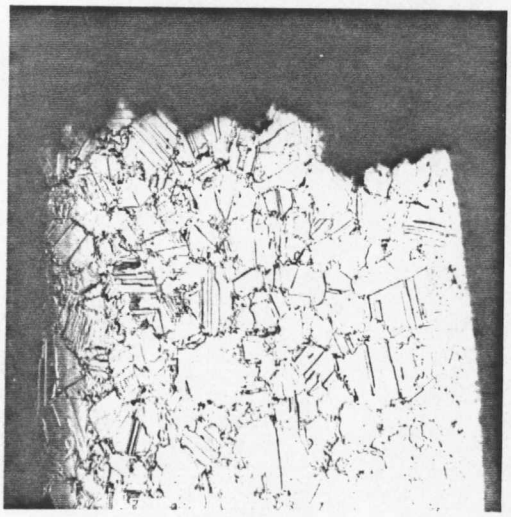
For relatively short aging times (less than 1000 minutes), the fracture is clearly along the former α, high angle boundaries. When the aging time allows development of the grain boundary, recrystallized structure, fracture still occurs along the high angle boundaries, but they now have migrated slightly from their original locations. Figure 47g shows the fracture morphology typically associated with this structure. Figure 48 shows a cross-sectional view through the fracture surface, confirming the fracture surface morphology. Note that near the gage length, grain boundary separation has occurred in many locations.

Figure 49 shows a cross-sectional view for the alloy aged for much longer times, which allowed the grain boundary, recrystallization structure to predominate in the microstructure. Fracture has continued to occur along the migrated, high-angle boundaries. Also, near the

(a)

Intergranular fracture and voids along recrystallization region under broken surface.

150X



(b)

Higher magnification.

300X

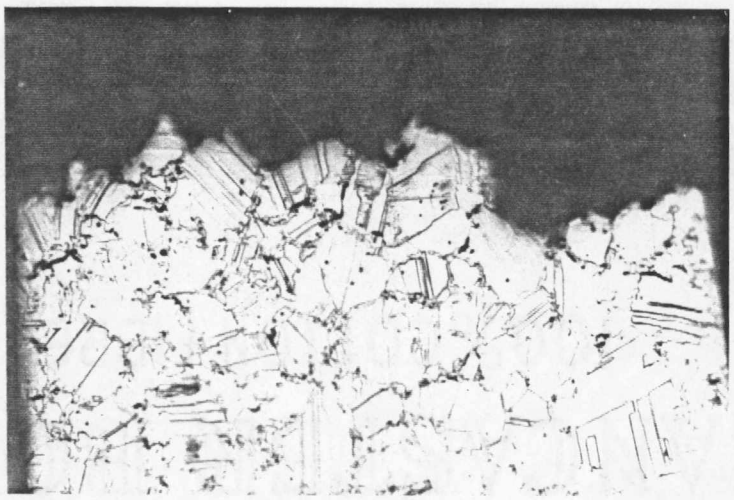
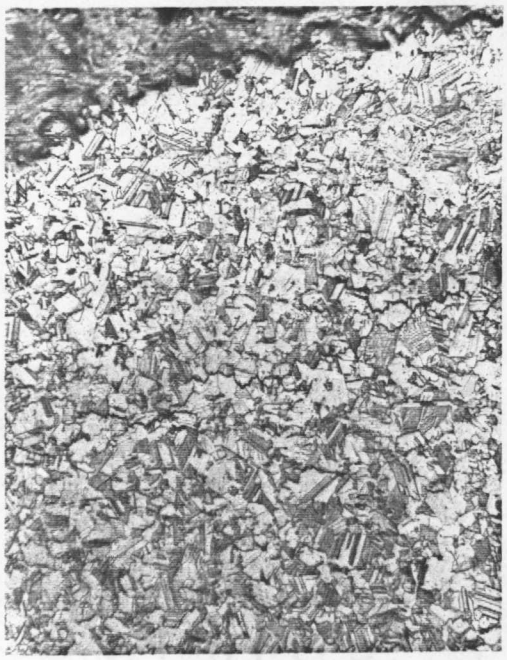


Figure 48. Cross-section through fracture surface of tensile sample aged 1000 minutes at 725 °C.

(a)
Note crack under the broken surface.

125X



(b)
Higher magnification.

250X



Figure 49. Cross-section through fracture surface of tensile sample aged 14,000 minutes at 775 °C.

fracture surface there are regions in which the grain boundaries have separated. Since fracture is occurring along these migrated boundaries, the clearly intergranular fracture topology characteristic of shorter aging times (i.e., compare the fractograph in Figure 47d to that in Figure 47g) is less apparent, because the intergranular fracture path is now through a finer structure.

When the domain structure is fine, and no grain boundary recrystallization structure has yet formed, the ordered alloy is brittle and fracture occurs along the high angle boundaries (the former α boundaries). The structure coarsens by the migration of these high angle boundaries, leaving behind a coarser domain structure. At this stage, and even later when these boundaries have progressed considerably into the center of the former grains, the alloy is still brittle, and fracture now ocurs along these migrated, and still high-angle, boundaries. Thus it is emphasized that the fracture sites in the microstructure, and hence the fracture surface topology, are controlled by the location of the high-angle β boundaries, and not by the domain structure. This indicates that the embrittlement leading to fracture along the former α boundaries for small domain size is not related to some type of intrinsic embrittlement associated with the locations of these boundaries, but instead is

associated with an intrinsic low strength of these high angle β boundaries.

4.2.3 Fracture morphology of Ni_4Mo tensile tested at elevated temperatures.

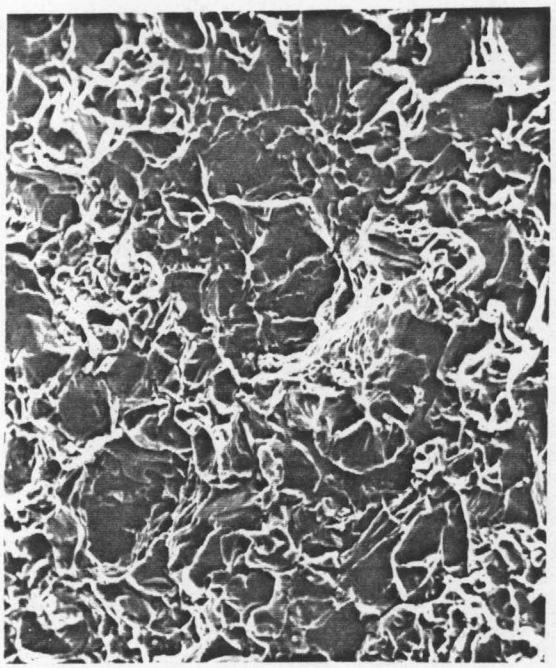
The topology of the fracture surface of the tensile samples which were tested at elevated temperatures showed some fundamental differences from those tested at 25°C. Here the samples which were aged prior to testing at 725°C for 1000 minutes are considered. Upon testing at 700°C or below, the fracture surface (Figure 50a) is similar to that for the sample tested at 25°C (Figure 47g). For testing above 700°C, but below the critical temperature of 868°C, the fracture surfaces had the general appearance of being intergranular, but the apparently intergranular surfaces were not smooth, but rough (Figure 50b). This probably reflects a fundamental change in the fracture mechanism, probably involving diffusional processes.

Samples which were tested above the critical temperature of 868°C showed considerable ductility (Figure 36). As described in the previous section, samples quenched from the α region and tensile tested at 25°C fractured by void coalesence, giving a dimpled fracture surface topology (Figure 47a). However, samples tensile tested at temperatures in the α region had a different morphology, as shown in Figure 51a-b. Note that the fracture surface is rough, but not transgranular, and

(a)

725 °C aged 1000 minutes.
Tested at 700 °C.

1000X



(b)

725 °C aged 1000 minutes.
Tested at 800 °C.

1000X

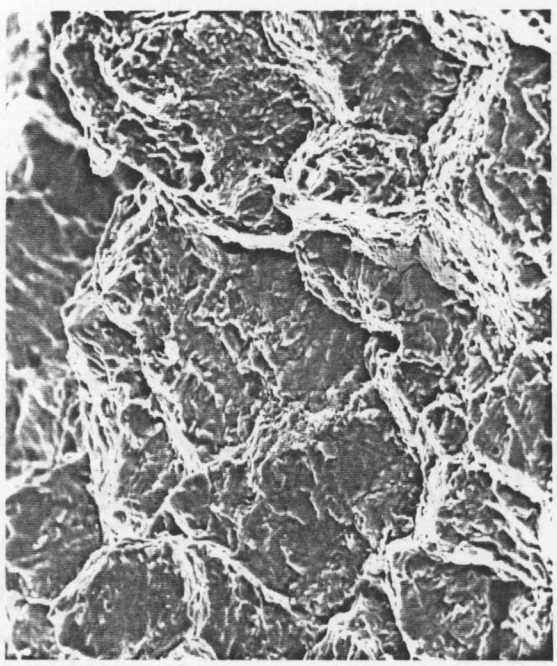
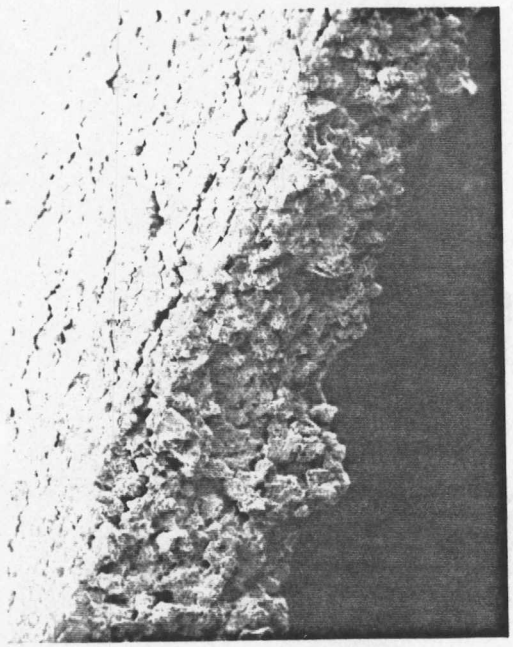
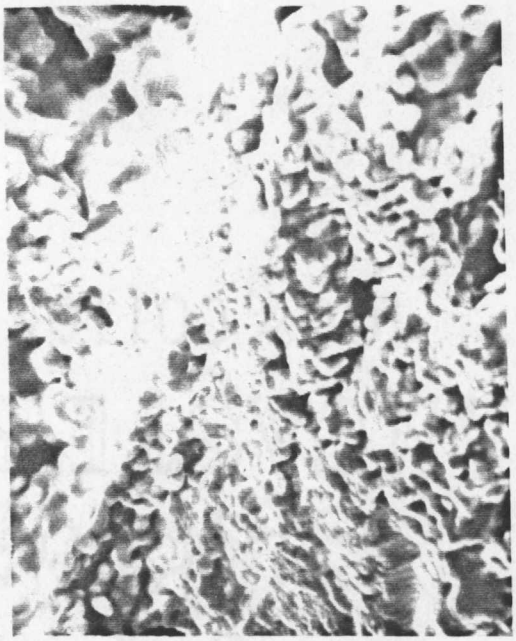


Figure 50. Fractography of tensile samples tested at elevated temperature.



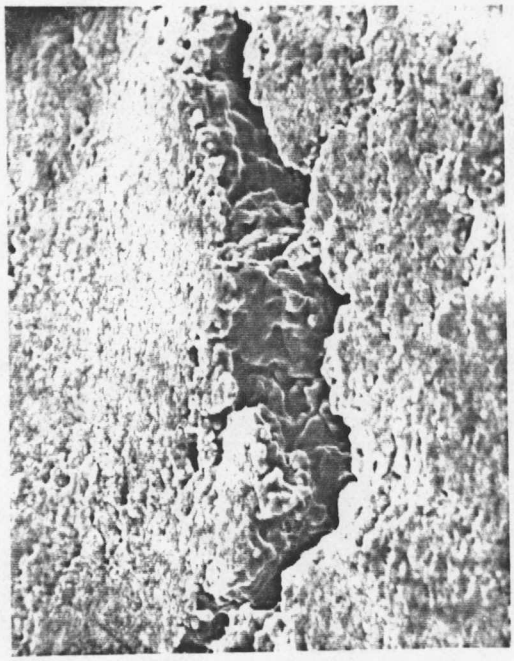
(a) Broken surface. 50X



(b) Broken surface at higher magnification. 1000X



(c) Gage surface. 200X



(d) Nodules at grain boundaries. 1000X

Figure 51. Fractography of tensile samples tested at 1000 °C.

neither is it clearly dimpled. Also numerous separations have formed along the gage length (see Figure 51c-d and Figure 52a-b). Examination of the fracture surface and the surface of these cracks shows a nodule-like structure. This fracture surface topology reflects the creep-type fracture associated with testing at sufficiently elevated temperatures.

4.3 Transmission Electron Microscopy

4.3.1 Superlattice diffraction pattern of Ni_4Mo.

In order to analyze the dislocation and domain structure of the Ni Mo alloys, a Kikuchi map was determined. Since the structure can be based on the face-centered cubic lattice, the pattern is that of an fcc crystal, such as shown in Figure 53a.

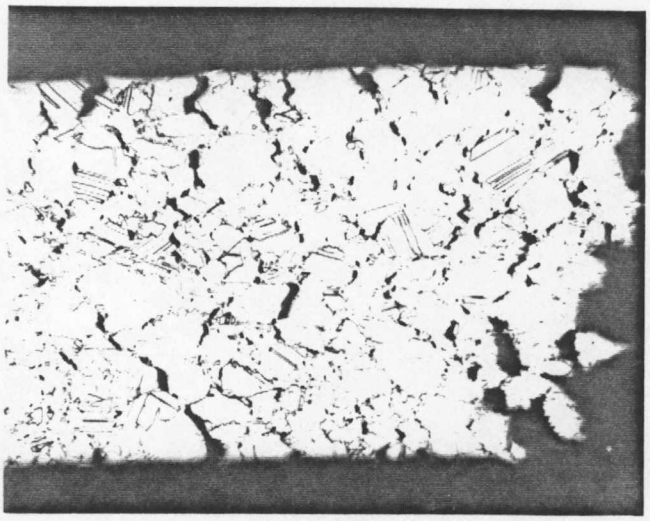
In the as-quenched condition, in which the structure is short-range ordered, fcc structure, the electron diffraction pattern contains diffuse spots from the SRO structure along with the fundamental spots. These diffuse, SRO spots can be sharpened by a relatively low temperature, short time heat treatment. A SRO diffraction pattern is shown in Figure 53b for a [001] axis.

The presence of superlattice spots in the diffraction pattern depends upon the zone axis and the type of domains enclosed in the selected area diffraction aperture. Examples of different patterns are shown in Figures 53c-g.

(a)

Intergranular micro-cracks formed at grain boundaries.

100X



(b)

High density of discontinuous microcracks or voids along grain boundaries.
This area was 6 mm from the fracture surface.

200X

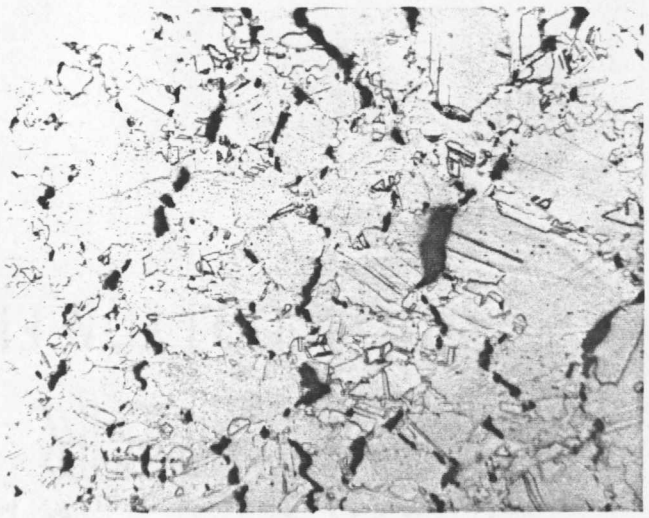
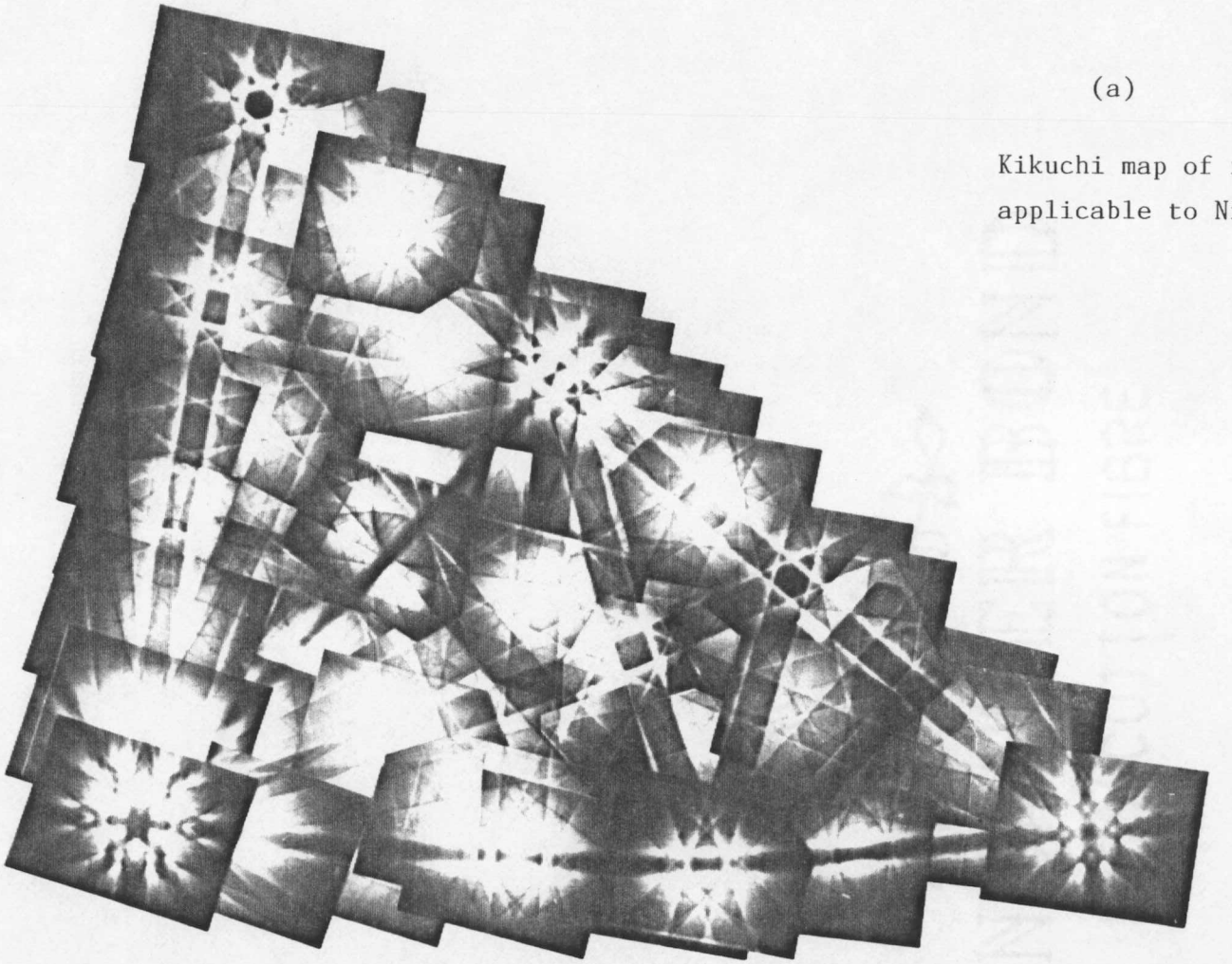


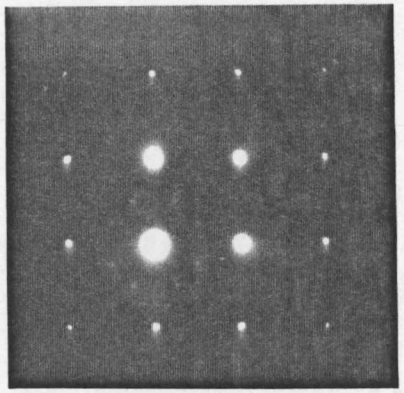
Figure 52. Cross-section through fracture surface of tensile sample tested at 1000 °C.



(a)

Kikuchi map of f.c.c.
applicable to Ni_4Mo

Figure 53. The Kikuchi map and the diffraction pattern of Ni_4Mo.

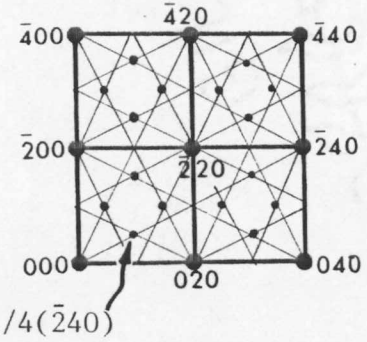


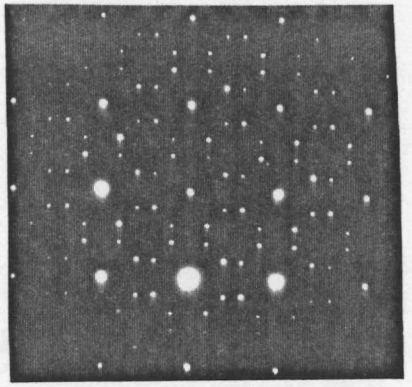
(b)

[001] pole

SRO

(725°C aged 1 min.)



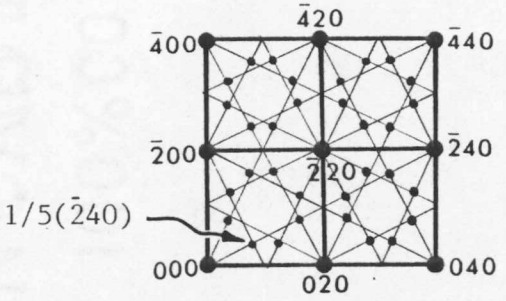


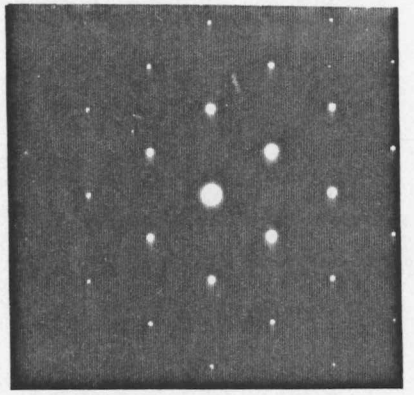
(c)

[001] pole

Two varients LRO

(725°C aged 1000 min.)

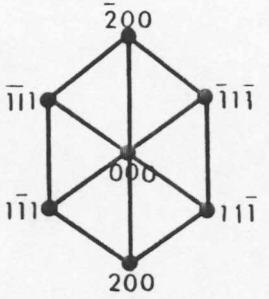




(d)

[011] pole

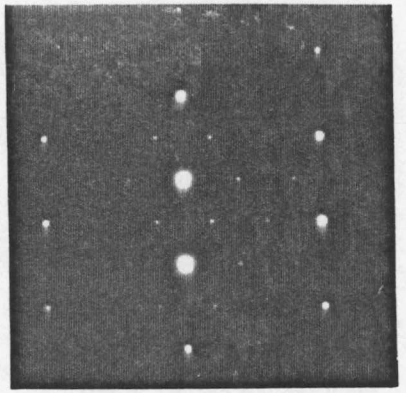
No superlattice spots
can be seen
(725°C aged 1000 min.)



● Fundamental spots

• Superlattice spots

Figure 53. (Continued)

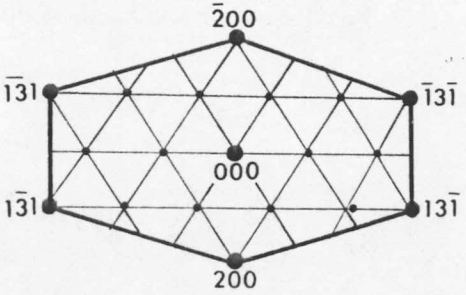


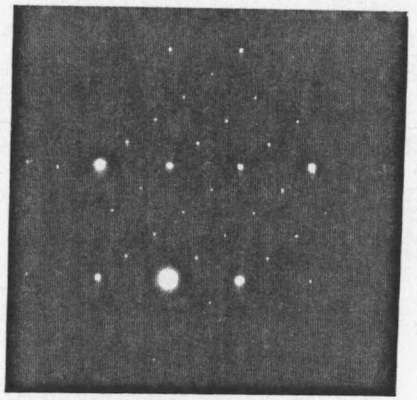
(e)

[013] pole

Two varients LRO

(725 ℃ aged 1000 min.)



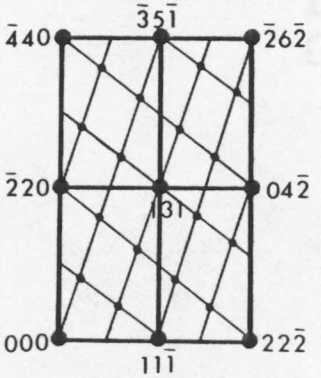


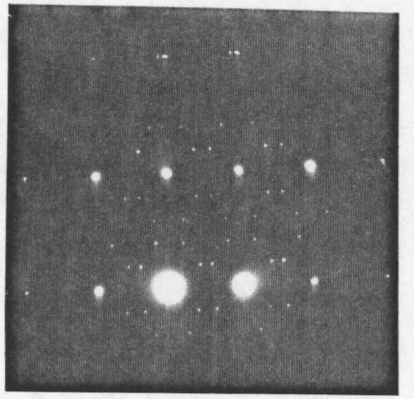
(f)

[112] pole

One varients LRO

(725°C aged 1000 min.)





(g)

[112] pole

Two varients LRO

(725°C aged 1000 min.)

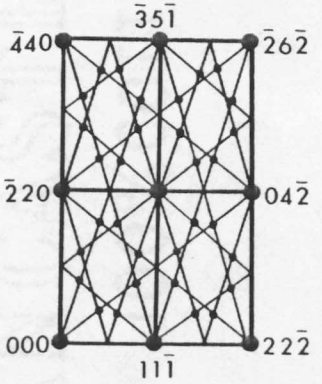


Figure 53. (Continued)

In Figure 53f only one variant is present, whereas in Figure 53g, two are present.

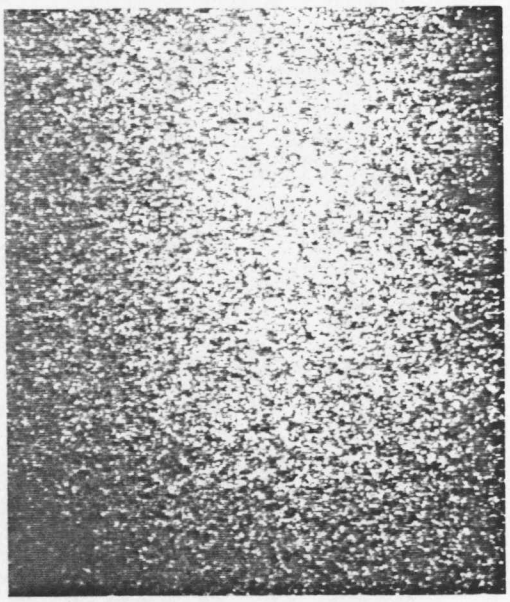
4.3.2 Domain structure and domain size measurement.

The domain structure can be observed easily in transmission electron microscopy (TEM), especially using a dark field image from a superlattice spot. This was the method employed to obtain the domain size values reported previously (see Table 4). Examples of dark field imaging of the domains are shown in Figure 54, which shows the domain coarsening with aging time.

4.3.3 Grain boundary recrystallization.

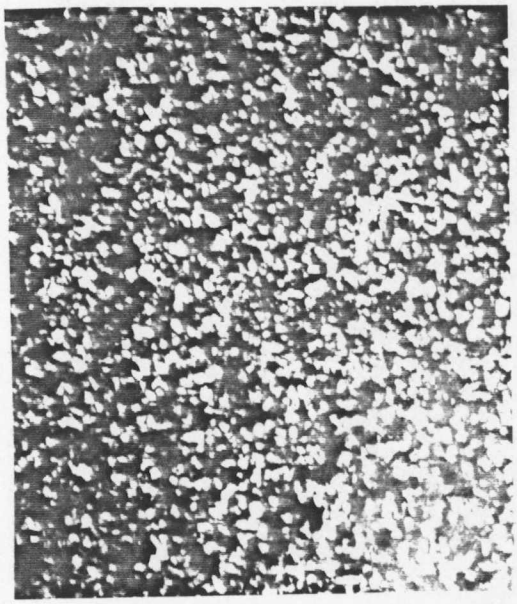
In Sections 4.2.1, optical and scanning electron micrographs were presented which showed that for short aging times a grain boundary reaction (along the former high-angle, α boundaries) occurred. This structure developed after the grains had already ordered to a fine domain size. It appeared to be a "recrystallization" reaction associated with the migration of the high angle boundaries. In this Section are presented transmission microstructures of this grain boundary reaction product.

The microstructures in Figure 55 typify those observed. It is clear that the former α boundary is migrating, leaving behind a coarser domain structure. The migrating interface contains numerous dislocations, and stacking faults are found in the recrystallized domains.



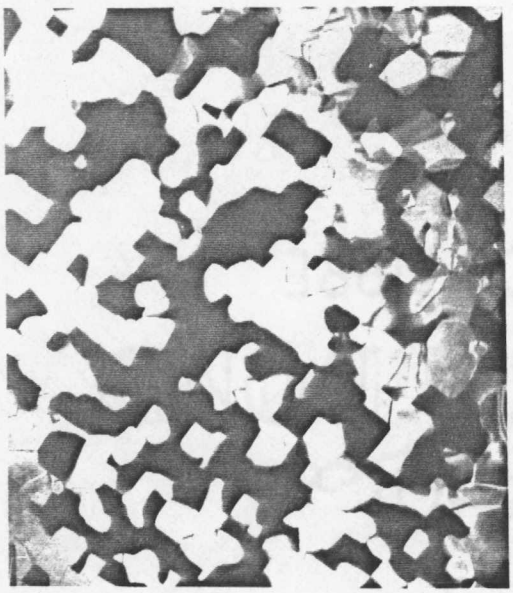
(a) 725°C aged 3 minutes.
D = 30 A

66KX



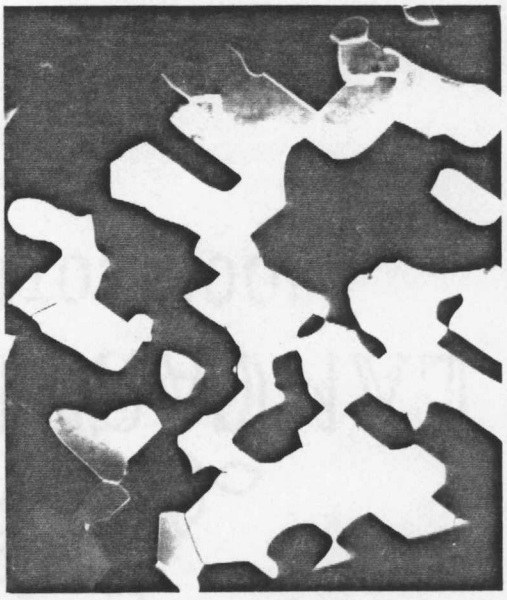
(b) 775°C aged 10 minutes.
D = 170 A

66KX



(c) 725°C aged 10,000 minutes.
D = 700 A

50KX



(d) 775°C aged 100,000 minutes.
D = 7000 A

16KX

Figure 54. Dark field TEM micrographs showing the effect of aging temperature and time on the domain size.

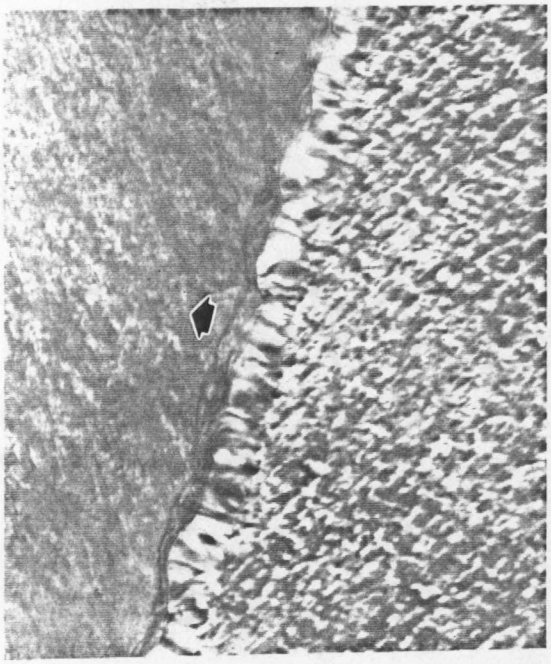
(a)

725 ℃ aged 30 minutes.

Thin recrystallization layer, 1000 Å.
Dislocations along the incoherent side of grain boundary.

Arrow presents the growth direction.

66K X



(b)

725 ℃ aged 100 minutes.

Recrystallization layer 7000 Å thick.
Stacking faults found in recrystallization region.
Domain size is bigger in the recrystallization region.

20K X

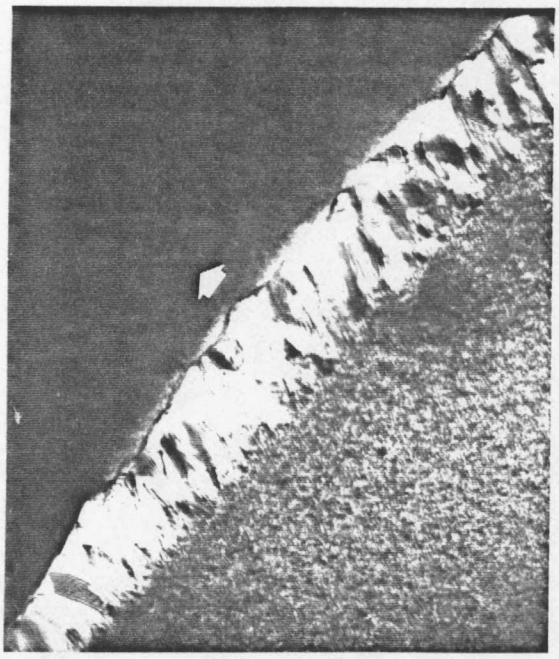


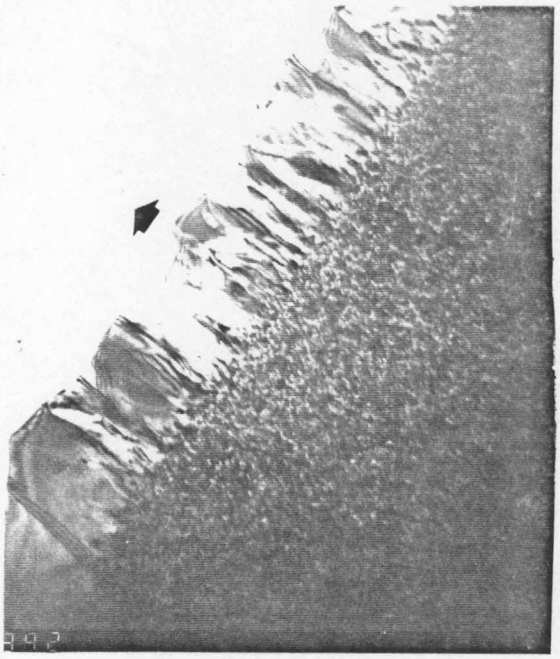
Figure 55. TEM micrographs showing the grain boundary coarsening by "recrystallization".

(c)

725 ℃ aged 100 minutes.

The new migrated grain boundary is irrequalar.

26K X



(d)

725 ℃ aged 100 minutes.

Three recrystallization regions growing in different direction.

10K X

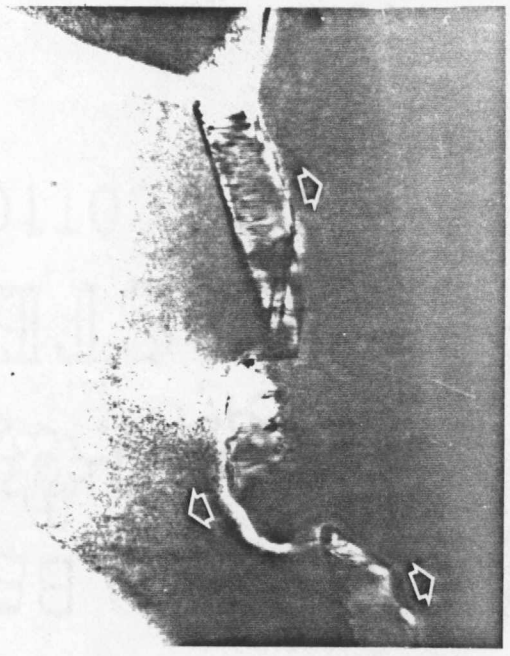


Figure 55. (Continued)

Along a grain boundary, different regions can be migrating simultaneously in opposite directions, as shown in Figure 55d.

Selected area electron diffraction was utilized to show that the coarse domain structure is coherent with the grain into which the recrystallized structure is not growing. Thus, the migrating boundary is the original high angle, incoherent boundary.

4.3.4 General deformation structure in SRO condition.

To examine the dislocation structure of the short-range ordered α, the structure of the gage length of a tensile sample was examined. The sample had been aged for one minute at 725 °C. The ductility was about 60%.

The dislocation structure is illustrated in Figure 56. There is a high density of planar type dislocations, but no stacking fault fringes are observed. Dislocations are piled up at the grain boundaries, but it appears also that they are emitted from these boundaries.

Hirth (89) has described mechanisms of interest here. One is that when the dislocations pile-up at the boundary, they produce a stress concentration because of plastic incompatability across the boundary. Futher slip can be initiated if the leading dislocation is forced through the boundary into the next grain. This entails supplying the energy of the grain boundary step (or of jogs in the

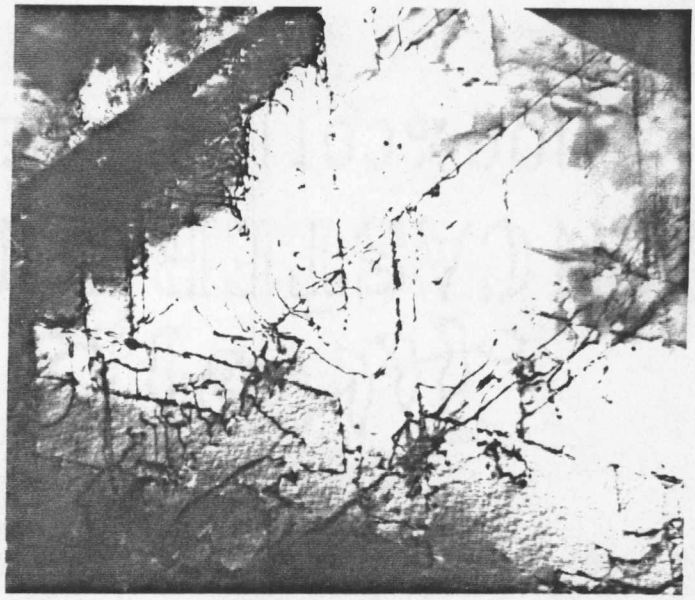
(a)

725°C aged 1 minute.

Tensile tested at 25°C.

Plannar type dislocations.

33K X



(b)

A triple point grain boundary junction.

26K X

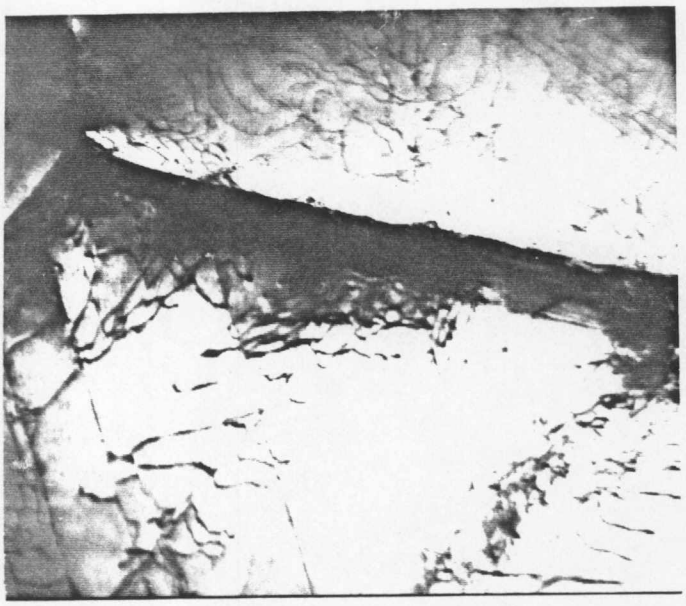


Figure 56. Deformation structure in the short aging time condition (725°C aged 1 minute).

(c)

Dislocations piled up on the grain boundary and reacting with grain boundary dislocations.

50K X



(d)

Some dislocations emitted from grain boundary into neighboring grain.

66K X

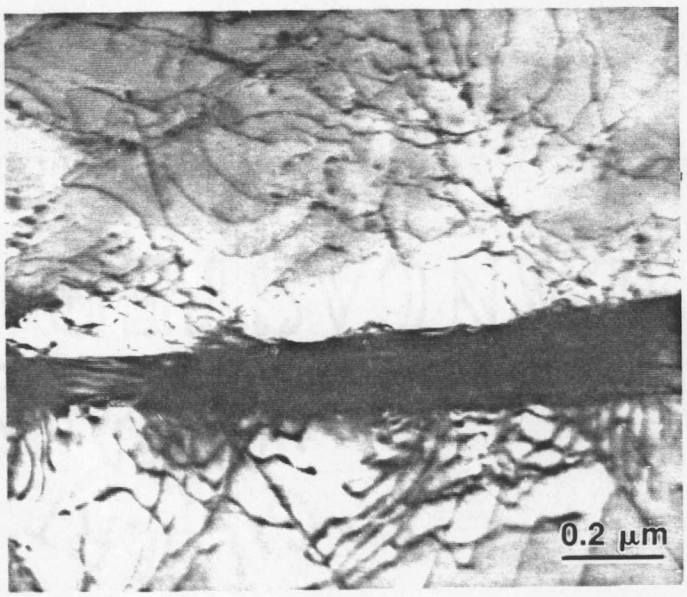


Figure 56. (Continued)

boundary dislocations) and of the residual dislocation left in the boundary if the Burgers vectors are not colinear in the two grains.

A second mechanism entails forcing a boundary dislocation to act as a glide source under the stress concentration caused by the dislocation pile-up. Another mechanism is that the stress concentration can activate a Frank-Read source near the boundary in the grain in which slip has not yet occurred.

4.3.5 Deformation structure in high LRO condition.

The dislocation structure from the gage section of tensile samples which had been heat treated to give a large LRO parameter (e.g.,S=0.9) is illustrated by Figure 57. The dislocations are restricted to bands. In Figure 57a, the dislocations have easily propagated across the twin interfaces. However, the dislocations cannot easily propagate across the high angle boundaries (Figure 57b-d).

Every plastic deformation band contains numerous stacking faults with widely separated partial dislocations. These dislocations pile up at the grain boundary, and have difficulty in propagating into the next grain and in moving along the boundary. This plastic incompatability leads to a large stress concentration. It appears that after ordering, the stacking fault energy

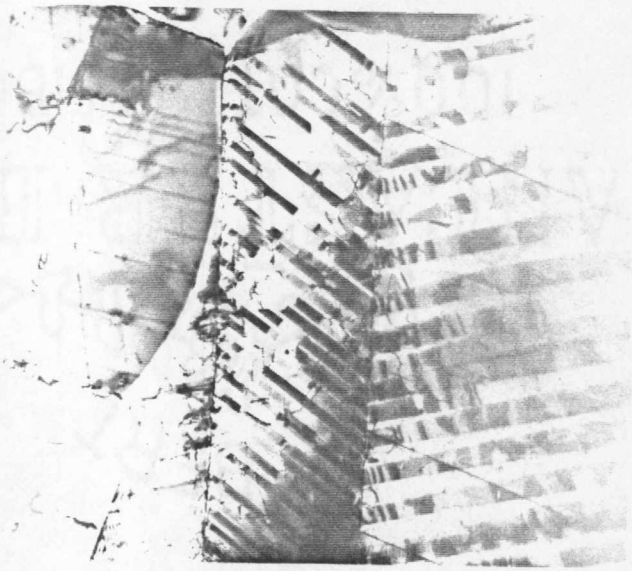
(a)

725 ℃ aged 1000 minutes.

Tensile tested at 25 ℃.

Some sets of plastic deformation bands existing inside the grains and conecting each other on the annealing twin boundaries.

6.6K X



(b)

A triple point grain boundary junction.

10K X

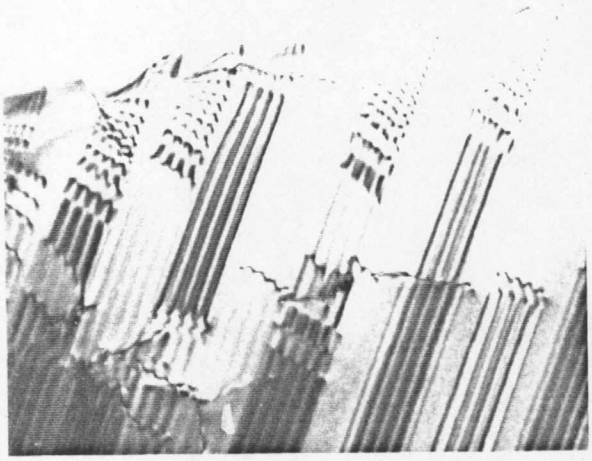


Figure 57. Deformation structurein the high LRO (S=0.9)conditionunder tensile stress.

(c)

Dislocations, gliding along plastic deformation bands to the grain boundary, are stopped and can not cross over or move inside the grain boundary.
Stacking fault fringe image is clear.

66K X



(d)

Two sets of plastic deformation bands meet on the grain boundary, dislocations are piled up.

33K X

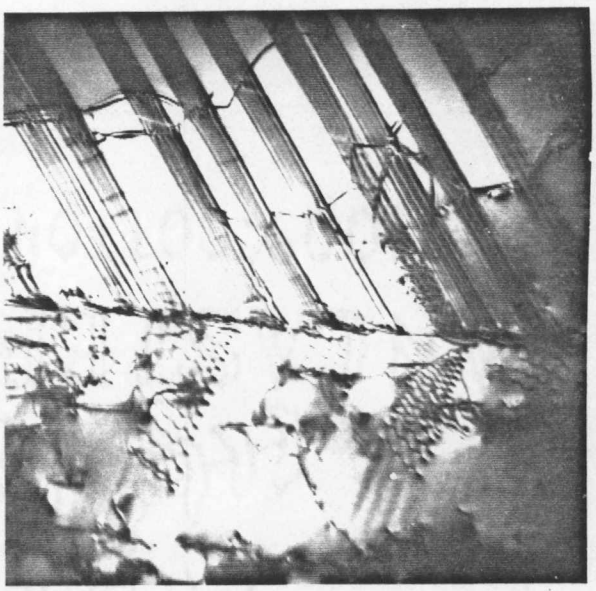


Figure 57. (Continued)

becomes very low, as stacking faults were not observed in the SRO condition.

In compression, the ordered Ni_4Mo alloy can be deformed more than in tension prior to fracture. Thus, samples which had been heat treated to form the desired degree of LRO were rolled up to 10 % prior to thinning.

The dislocation structure is illustrated in Figures 58 and 59. With 3 % deformation (Figure 58), the dislocation structure is similar to that from the tensile samples. But when 8 % deformation was used, many twins were present in addition to the bands. This is shown in Figure 59. In Figure 59c and 59d are shown dark field micrographs using the twin spots for imaging. The bright field view of this region is shown in Figure 59b. Trace analysis established that the habit plane of these twins is $\{111\}$.

4.3.6 Trace analysis of plastic deformation bands.

In order to determine the slip plane of the bands induced by deformation, a region of a TEM sample prepared from the tensile sample which had been tested at 850 °C was chosen which showed four sets of bands. These are shown in Figure 60. The stereographic analysis is shown in Figure 60c. The bands lie on the four $\{111\}$ planes.

(a)

850°C aged 10 days then 725°C aged 1400 minutes and rolled 3%.

Some sets of plastic deformation bands existing inside the grain and connecting each other on the grain boundaries.

5K X



(b)

At higher magnification, stacking faults fringe and partial dislocations image can be seen on the plastic deformation bands.

10K X



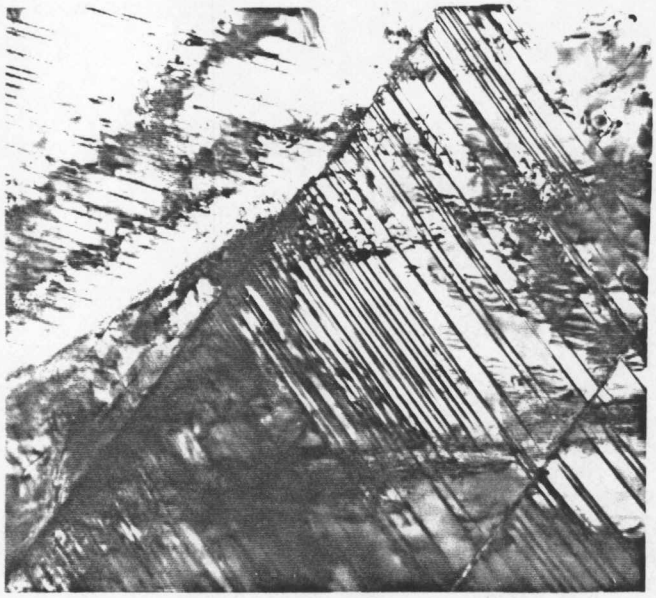
Figure 58. Deformation structure (rolled 3%) in the high LRO (S=0.9) condition.

(a)

725 ℃ aged 10,000 min.
+ rolled down 8%.

High density of twins.

33K X



(b)

Two directional twins
intersect each other.

10K X

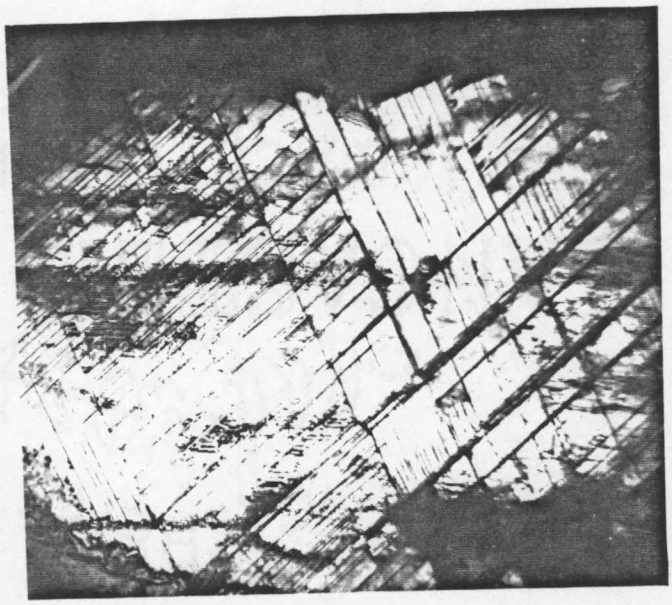
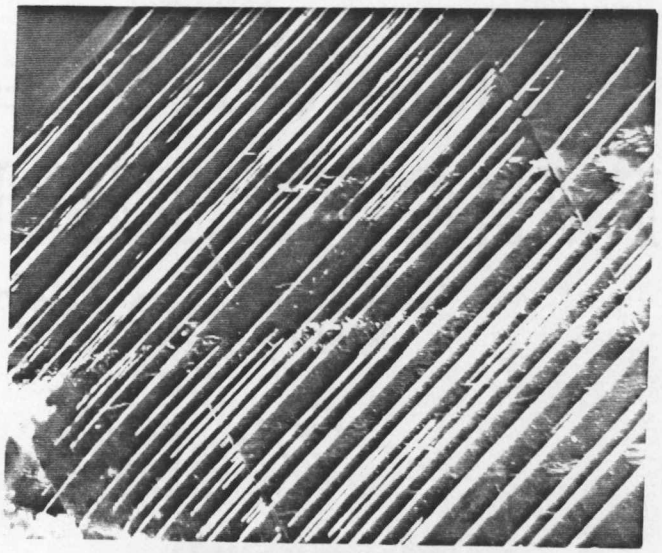


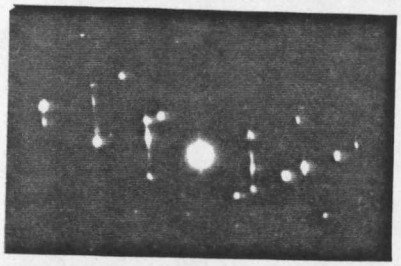
Figure 59. Deformation structure(rolled 8%) in the high LRO (S=0.9) condition.

(c)

CDF of (b)
Using one of twin spots
to see one set of twins.

20K X





(d)

CDF of (b)
Using another twin spot,
to see another set of twins.

20K X

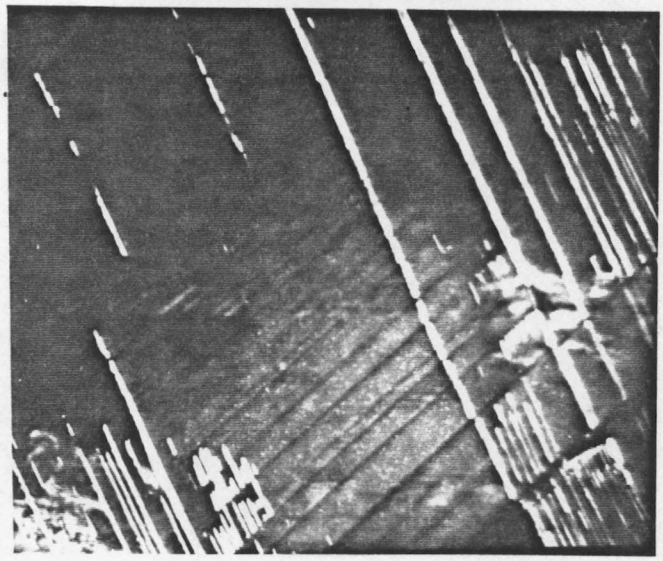


Figure 59. (Continued)

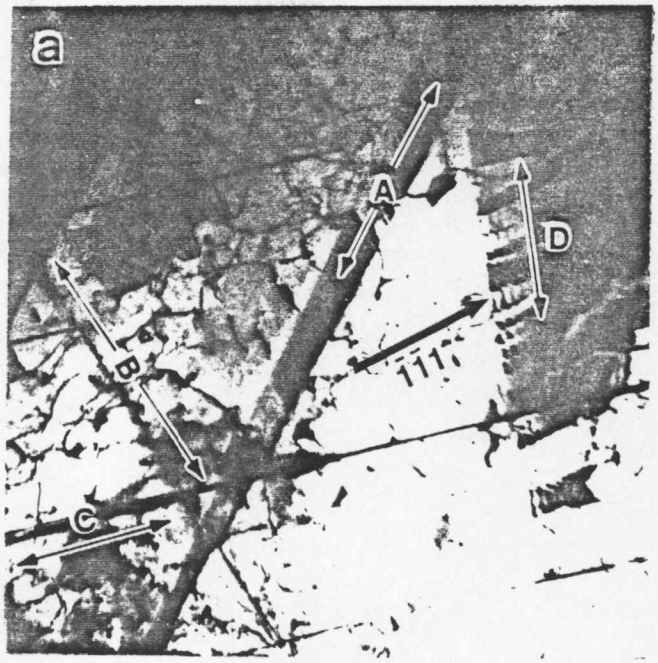
(a)

725 °C aged 1000 min.
tensile tested at 800 °C.

B=[011]

g=[$\bar{1}\bar{1}1$]

10K X



(b)

B=[112]

g=[$2\bar{2}0$]

10K X

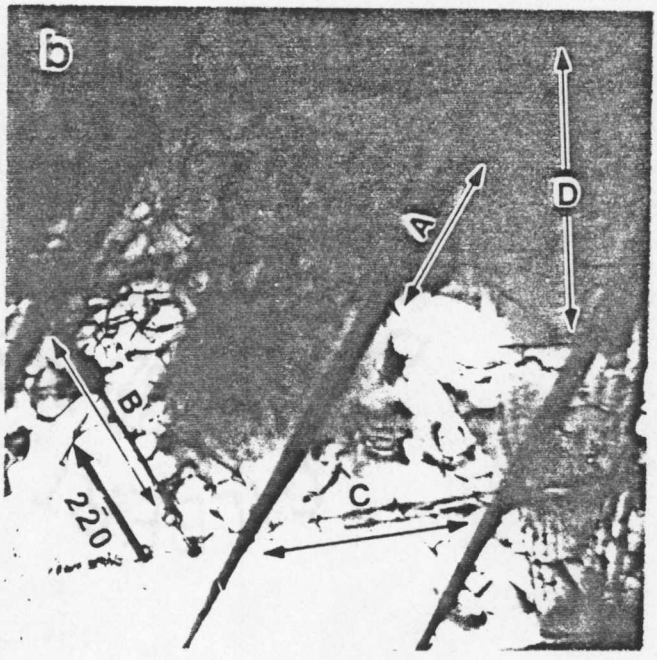
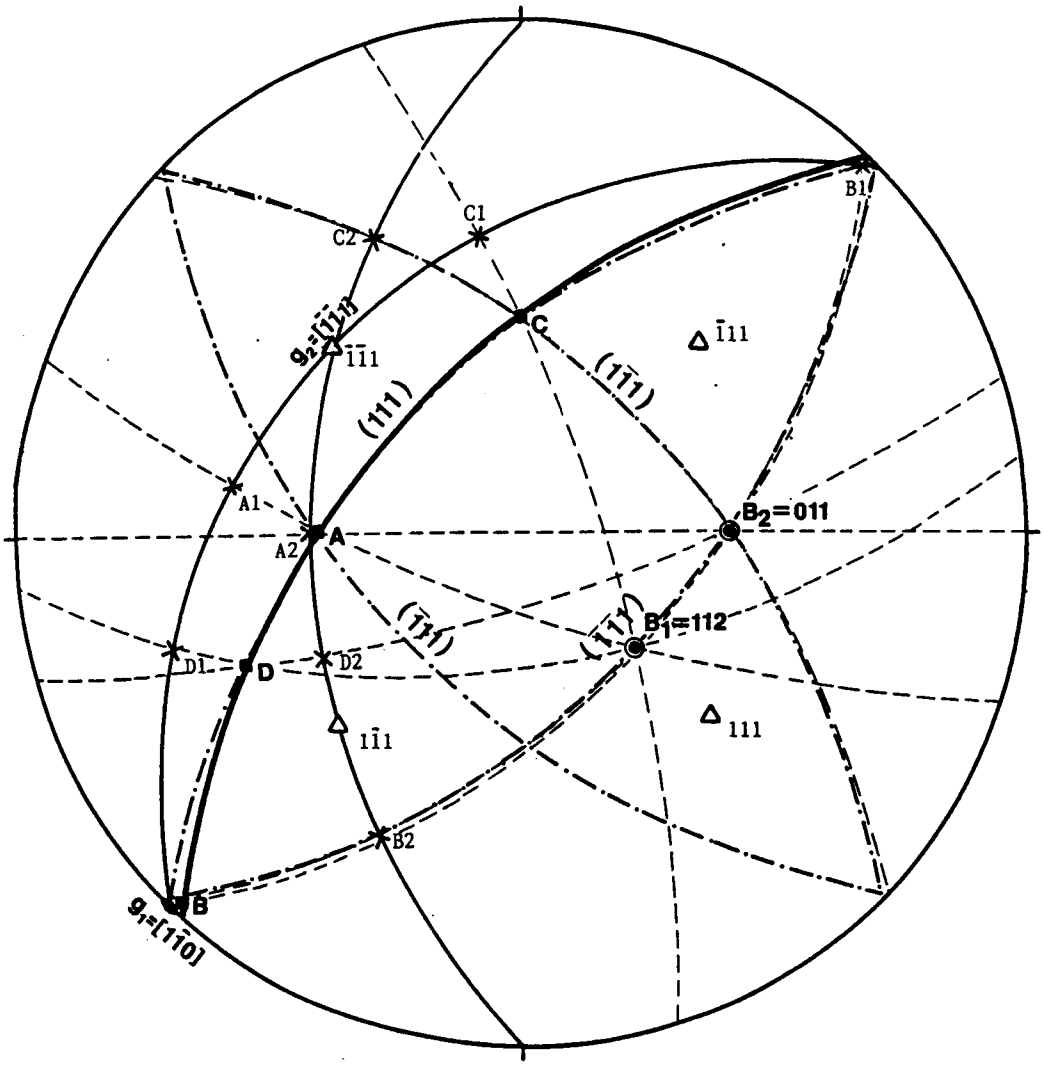


Figure 60. Trace analysis of the plastic deformation bands.



(c) Trace analysis

A ⟶ $(\bar{1}11)$ B ⟶ $(\bar{1}\bar{1}1)$

C ⟶ $(1\bar{1}1)$ D ⟶ (111)

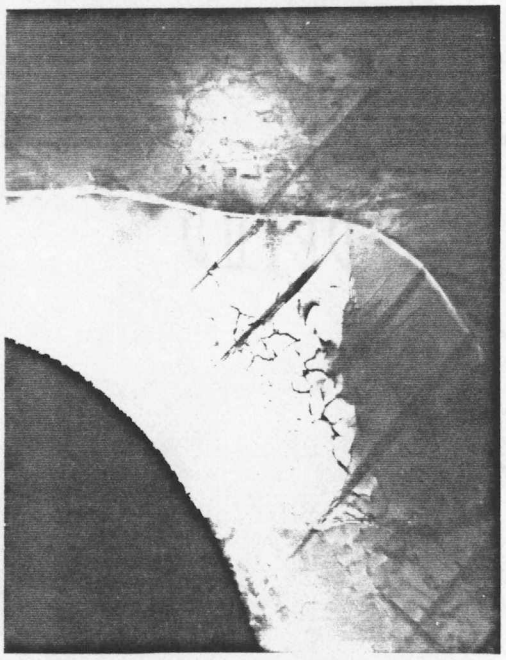
Figure 60. (Continued)

4.3.7 Burgers vector analysis of matrix dislocations.

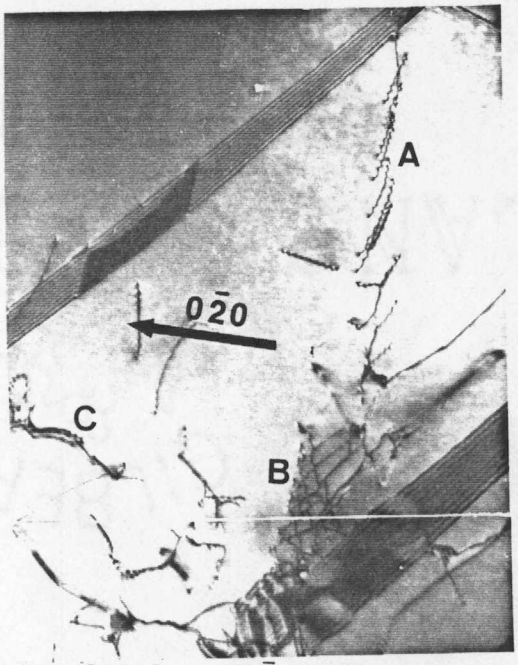
There are two general types of dislocations in the deformed ordered alloy. One type is associated with the bands, and the other dislocations are referred to here as matrix dislocations. In this Section is described the analysis performed to determine the Burgers vector of the latter type.

The sample analyzed has been aged at 850°C for 10 days to obtain a large domain size (3 μm), then aged 1440 minutes at 725°C to induce a high degree of order (S>0.9). The sample was not cold worked, but there were many dislocations. Although these may have been induced by sample preparation and handeling, the extensive number of samples examined in this research indicates that they are intrinsic to the sample, and are probably generated by thermal stresses or transformation stresses.

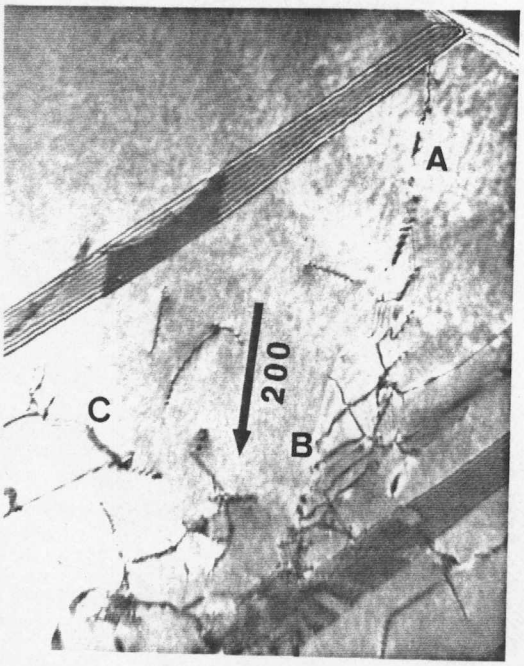
The Burgers vector analysis was conducted on the four sets of dislocations marked A, B, C and D in Figure 61, using the invisibility rule. A series of two-beam conditions were used in order to get different g values. The results are shown in Table 14. The results showed that the matrix dislocations are 1/2<110> type unit dislocations.



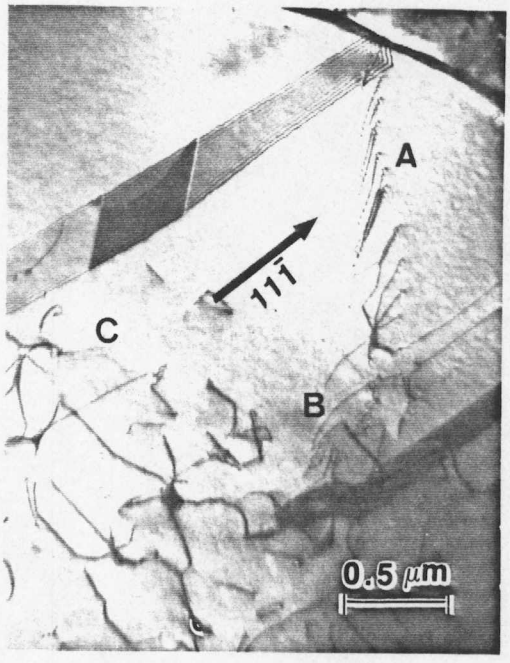
(a) Show analysis area
Dark field image
5K X



(b) B=[001]; g=[0$\bar{2}$0]
A,B,C all visible 26K X

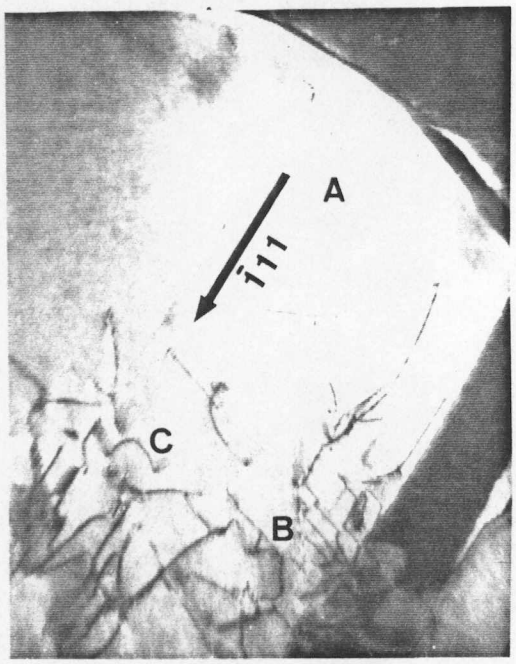


(c) B=[001]; g=[200]
B become invisible. 26K X



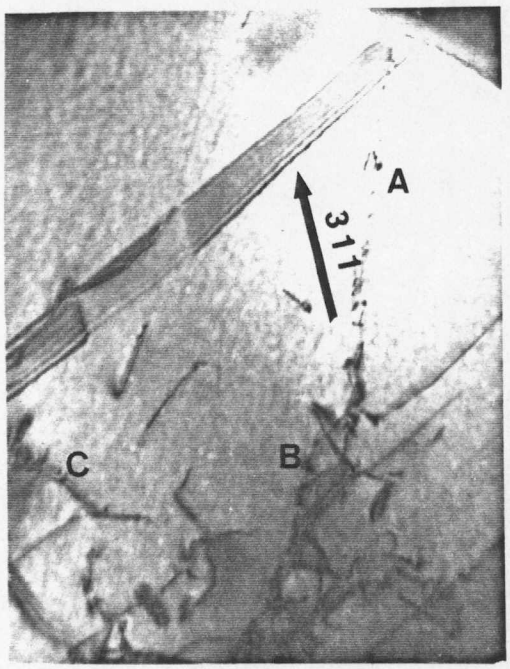
(d) B=[112]; g=[11$\bar{1}$]
C become invisible. 26K X

Figure 61. Burgers vectoranalysis of the matrix dislocations.



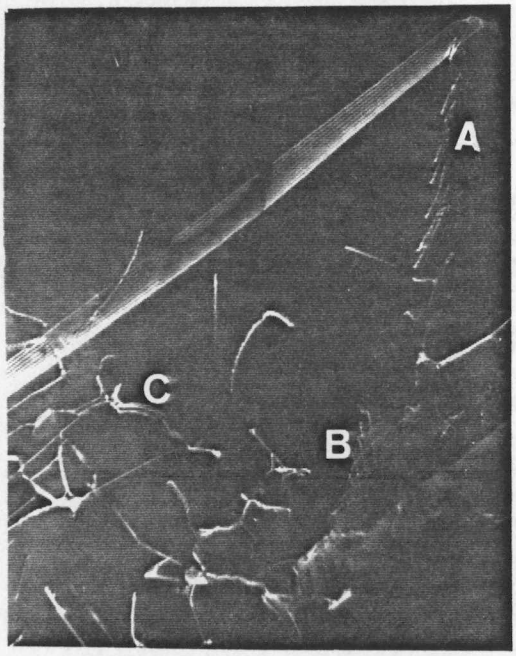
(e) B=[101]; g=[$\tilde{1}11$]

A and C become invisible. 26KX



(f) B=[$\bar{1}03$]; g=[311]

A become invisible. 26K X



(g) B=[001]; g=[$0\bar{2}0$]

CDF of (b) 26K X

Figure 61. (Continued)

Table 14. Burgers vector analysis of matrix dislocation (see Figure 61)

Beam Direction B	Two Beam Condition g	Analysis Area		
		A	B	C
001	$0\bar{2}0$	V	V	V
001	020	V	V	V
001	200	W	I	W
001	$\bar{2}20$	V	V	V
112	$11\bar{1}$	V	I	I
112	$13\bar{1}$	V	W	I
101	020	V	V	V
101	$\bar{1}11$	I	V	I
103	$\bar{3}\bar{1}\bar{1}$	I	W	V
001	$\bar{2}\bar{2}0$	V	V	W
Bugers Vector $\vec{b}$		$\pm 1/2[01\bar{1}]$	$\pm 1/2[011]$	$\pm 1/2[101]$

V=Visible; W=Weak; I=Invisible.

Check Burgerss vector by invisible rule:

A: $[\bar{1}11]*[311]=\pm 1/x[01\bar{1}]$

B: $[200]*[11\bar{1}]=\pm 1/x[011]$

C: $[11\bar{1}]*[13\bar{1}]=\pm 1/x[101]$

4.3.8 Burgers vector analysis of glide dislocations.

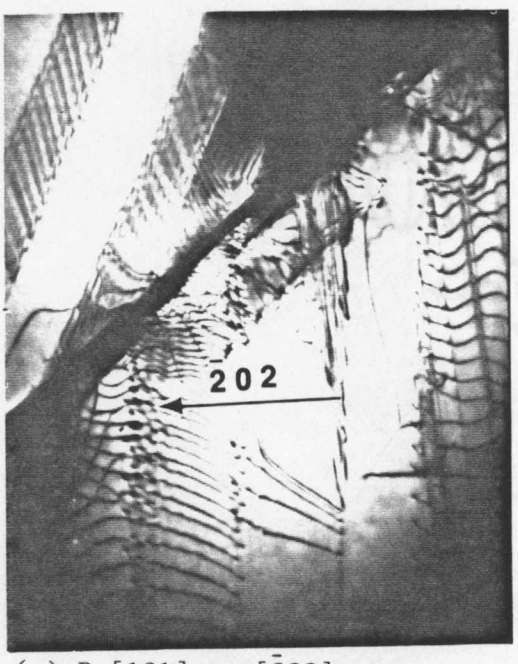
In this Section is described the analysis which determined the Burgers vector of the dislocations in the bands which showed internal band contrast. The sample used had been aged for 10,000 minutes at 725°C, giving a domain size of 770 Å and a LRO parameter of 0.99 and then rolled 6%.

The region analyzed is shown in Figure 62. Again, the invisibility criteria was used to determine the Burgers vector, and the results are tabulated in Table 15. The dislocations are all of the single $1/6[11\bar{2}]$ type partial dislocations. A check on the fringe configuration of the contrast inside the bands also confirms that these are stacking faults.

4.3.9 Evidence of 5 unit superdislocations.

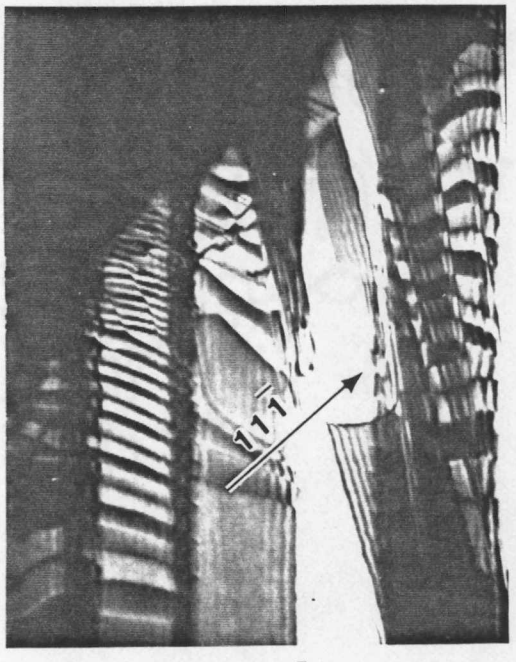
The movement of five dislocations on the same slip plane and in the <110> direction will bring the lattice of the ordered Ni_4Mo structure back into coincidence, and thus their presence is expected. However, they have only have been reported in Ni-rich, off-stoichiometric alloys and in Ni_4Mo with very fine domains.

To examine this perplexing problem, samples of Ni_4Mo were heat treated to develop a large domain size (3 μm) and a high LRO parameter (S>0.6). Such samples were tensile tested at 25°C and at elevated temperatures. The



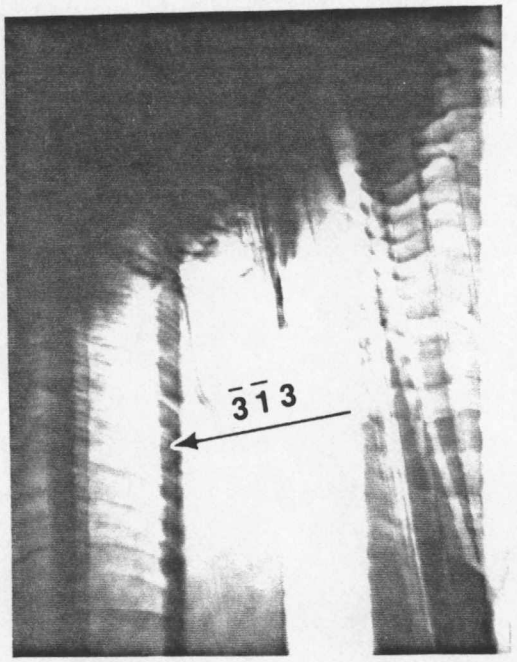
(a) B=[101]; g=[$\bar{2}02$]

33K X



(b) B=[101]; g=[$11\bar{1}$]

33K X



(c) B=[101]; g=[$\bar{3}\bar{1}3$]

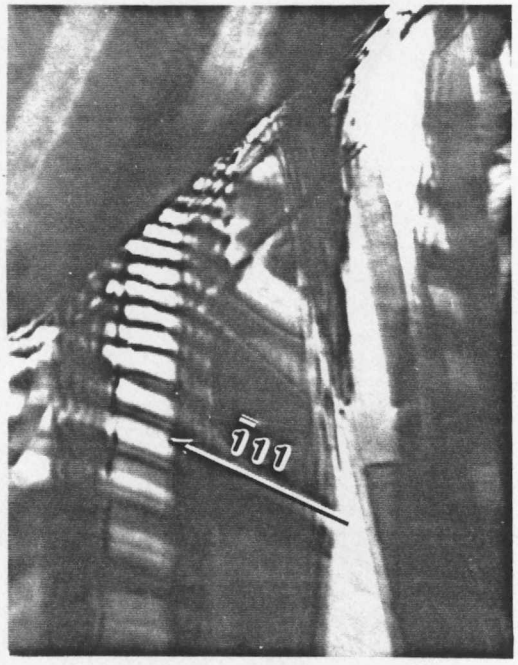
33K X



(d) B=[101]; g=[$0\bar{2}0$]

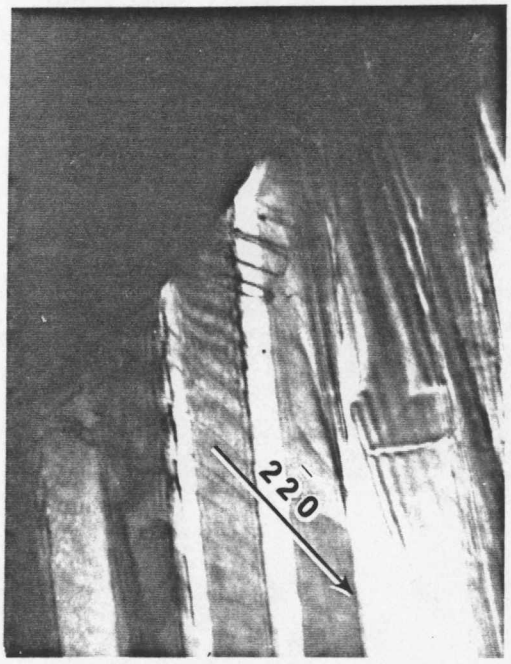
33K X

Figure 62. Burgers vector analysis of the partial dislocations in the plastic deformation bands.



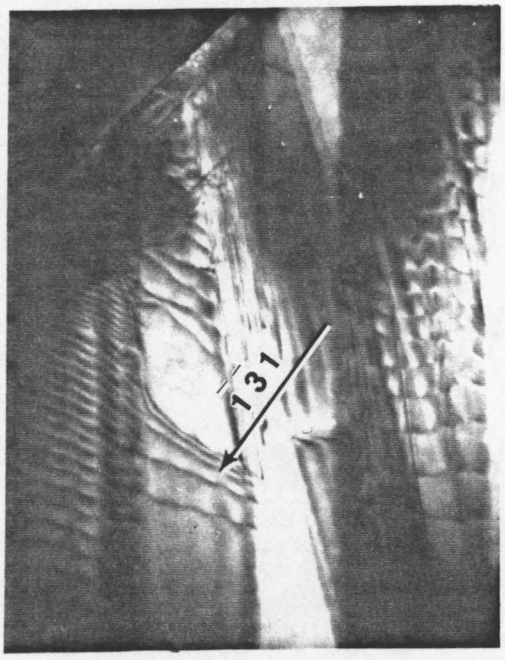
(e) B=[101]; g=[$\bar{1}11$]

33K X



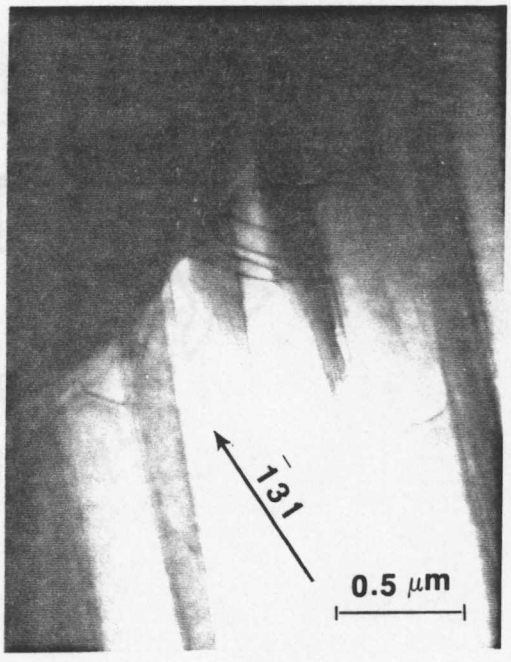
(f) B=[111]; g=[$2\bar{2}0$]

33K X



(g) B=[101]; g=[$\bar{1}\bar{3}1$]

33K X



(h) B=[101]; g=[$\bar{1}31$]

33K X

Figure 62. (Continued)

Table 15. Burgers vector analysis of partial dislocations in the bands (see Figure 61)

Beam Direction B	Two Beam Condition g	Dislocations		Stacking Faults	
		$g\cdot\vec{b}$ ($b=1/6[11\bar{2}]$)	Observed	$\alpha=2\pi g\cdot R$ ($R=1/3[111]$)	Observed
101	$\bar{2}02$	-1	S	0	I
101	$11\bar{1}$	2/3	S	$2\pi/3$	V
101	$\bar{3}\bar{1}3$	-1/3	W	$2\pi/3$	V
101	$\bar{1}\bar{3}1$	-1	S	-2π	I
101	$0\bar{2}0$	-1/3	M	$-2\pi/3$	V
101	$\bar{1}31$	0	I	2π	I
101	$\bar{1}11$	-1/3	W	$2\pi/3$	V
111	$2\bar{2}0$	0	I	0	I
Results:	1. Dislocations' Burgerss vector $\vec{b}$ is $1/6[11\bar{2}]$. 2. Stacking faults habit plane is (111).				

V=Visible; I=Invisible; S=Strong; M=Medium; W=Weak.

Check Burgerss vector by invisible rule:
$[\bar{1}31]*[2\bar{2}0]=\pm 1/x[11\bar{2}]$.

Criterion of dislocations image contrast:
$|g\cdot\vec{b}|>1$ image is strong
$|g\cdot\vec{b}|=2/3$ image is medium
$|g\cdot\vec{b}|=1/3$ image is weak
$|g\cdot\vec{b}|=0$ image is invisible.

Criterion of stacking faults image contrast:
$\alpha=+2\pi/3$ S. F. is visible
$\alpha=n\pi$ S. F. is invisible.

five unit superdislocations were only rarely seen, and an example is shown in Figure 63. This region was analyzed (Table 16) using the invisibility rule to establish the Burgers vector. It was found to be $1/2\langle\bar{1}10\rangle$ or in the tetragonal notation $1/5\langle\bar{2}10\rangle$.

The average separation distance between each unit dislocation in Figure 63 is about 280 Å. This is close to the caculated value obtained from the relation (88)

$$\gamma = \frac{G\,b^2}{2\pi E_{III} S^2}\left[\frac{\mathrm{Cos}(\theta+\pi/3)\mathrm{Cos}\,\theta}{1-\nu} + \mathrm{Sin}(\theta+\pi/3)\mathrm{Sin}\,\theta\right]$$

where θ: The angle between the Burgers vector and the dislocation line

S: LRO parameter

E_{III} : Anti-phase boundary energy

G: Shear modulus

b: Burgers vector

The values used are

θ: 90° (from trace analysis)

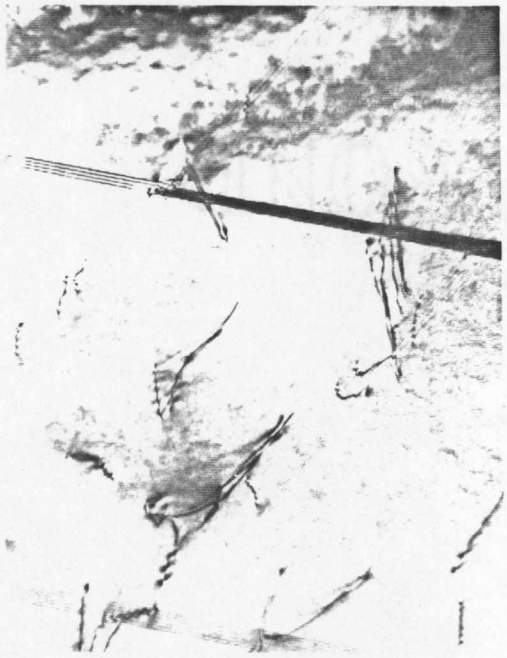
S: 0.65

E_{III}: 40 erg/cm (12)

G : 70000 Kg/mm

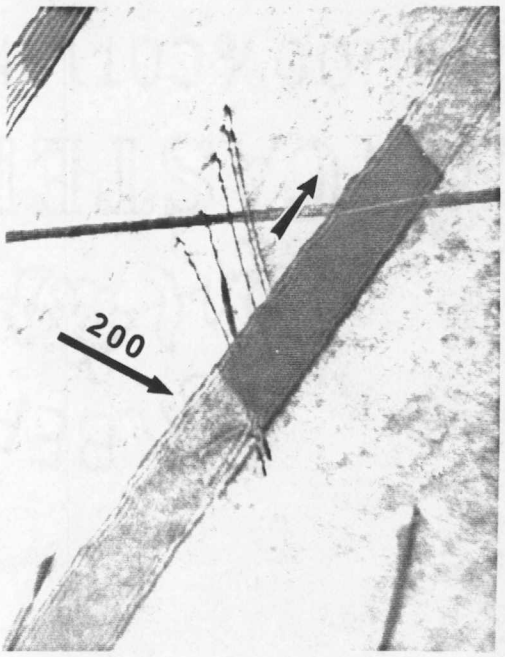
b: 2.56 Å

This gives a separation of 317 Å, in good agreement with the observed value.



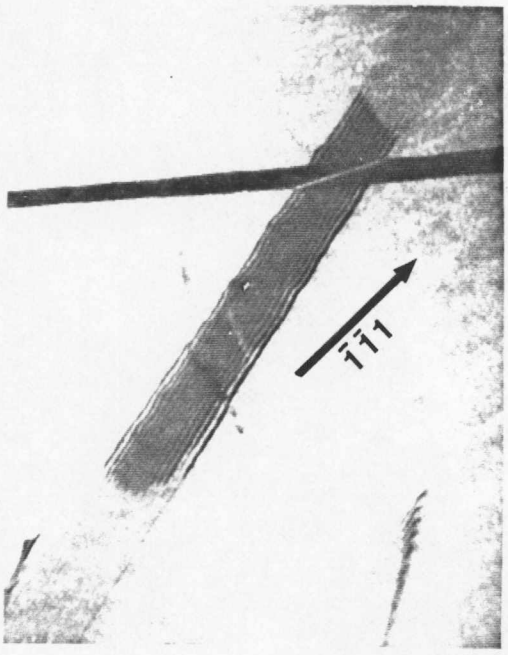
(a) Showing analysis area.

26K X



(b) B=[011]; g=[200]

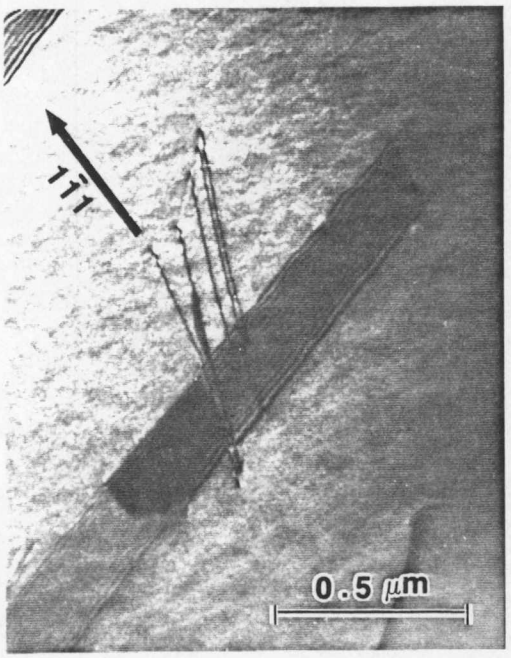
50K X



(c) B=[011]; g=[$\bar{1}\bar{1}1$]

Invisible

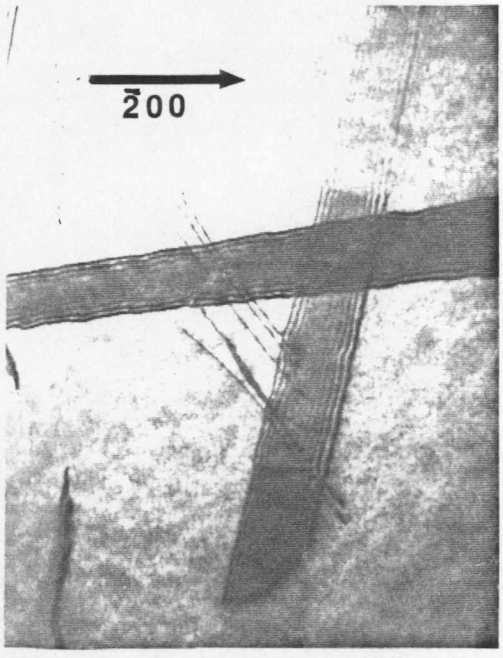
50K X



(d) B=[011]; g=[$1\bar{1}1$]

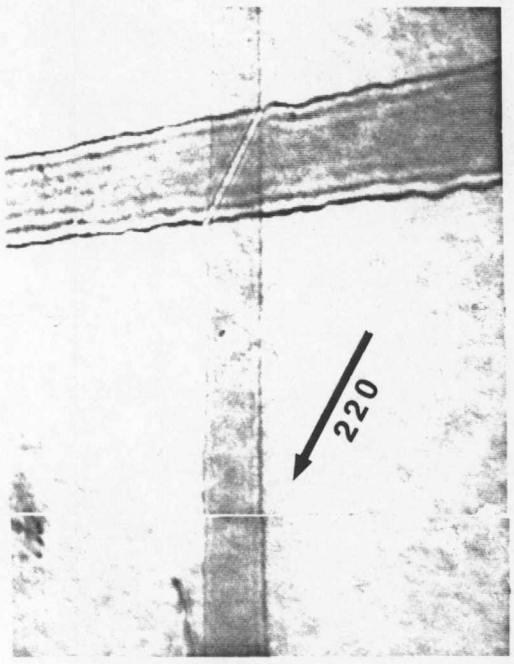
50K X

Figure 63. 5 unit superdislocation.



(e) B=[001]; g=[$\bar{2}$00]

50K X



(f) B=[001]; g=[220]

Invisible

50K X

Figure 63. (Continued)

Table 16. Burgers vector analysis of the superdislocation (see Figure 63)

Beam Direction B	Two Beam Condition g	Observed	Beam Direction B	Two Beam Condition g	Observed
111	$0\bar{2}2$	V	001	$\bar{2}00$	V
111	$\bar{2}20$	V	001	220	I
111	$\bar{2}02$	V	001	020	V
011	200	V	112	$1\bar{3}1$	V
011	$\bar{1}\bar{1}1$	I	112	$3\bar{1}\bar{1}$	V
011	$1\bar{1}1$	V			
Result:	Bugers vector $\vec{b}$ is $\pm 1/2[\bar{1}10]$ (f.c.c. coordination) or $\pm 1/5[\bar{2}10]$ (b.c.t. coordination).				

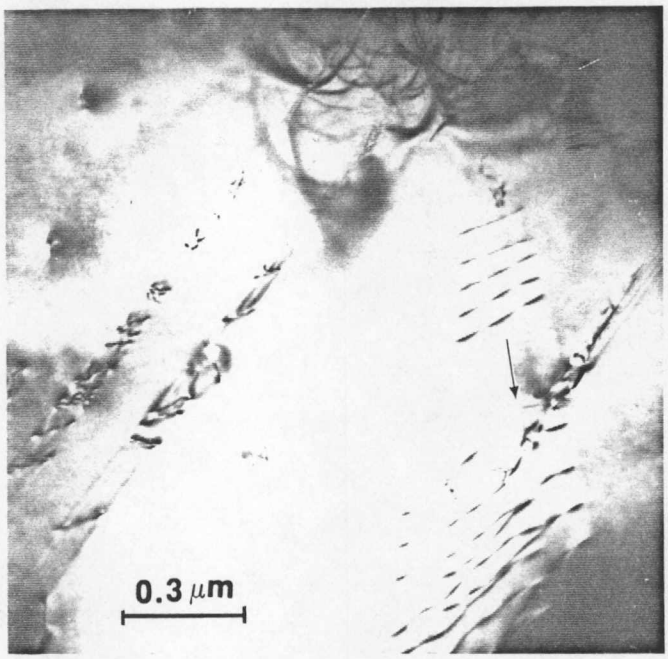
V=Visible; I=Invisible.

Check Burgerss vector by invisible rule:
$[\bar{1}\bar{1}1]*[220]=\pm 1/x[\bar{1}10]$.

The line direction of the superdislocation was determined by trace analysis as <112>. Because the angle between the dislocation line direction ξ and the Burgers vector ($b=1/2\langle\bar{1}10\rangle$) is 90°, this set of superdislocatioons is of the edge type. The slip traces in Figure 63 were found to be on the {111} planes. Thus this set of 5 unit dislocations is arranged parallel to trace B, so they are on the $(1\bar{1}1)$ plane. Consideration of the bonding across the slip plane (anti-phase boundary energy) shows that when five such dislocations move along a slip plane, the separation should be least between the leading edge, and greatest between the final two dislocations. Thus, the direction of movement of the superdislocation in Figure 63b is shown by the arrow.

Another example showing superdislocations is shown in Figure 64. Here the domain size is 3 μm. It is important to note that in this example extensive tilting did not develop any stacking fault contrast.

It is emphasized that five unit superdislocations, such as shown in Figure 63 and 64, were very rarely seen. They just do not commonly exist. The five unit superdislocation will be about 1500 Å wide, and for domain structure finer than this, it would not be expected to see them. However, these superdislocations are also rare in the samples with a domain size of 30,000 Å. It is observed, as discussed in previous Sections, that the



850°C aged 10 days, then cold workeded.

The moving direction of 5 unit superdislocations is shown by the arrow.

50K X

Figure 64. Another example of 5 unit superdislocation.

dislocation structure of deformed Ni_4Mo, even of large domain material, consists of bands containing partial dislocations. This means that in the ordered alloy the stacking fault energy is quite low. Thus, these partial dislocations cannot easily recombine to form the superdislocation configuration.

4.3.10 Stacking fault analysis.

In Figure 62a,f,g, and h, the stacking faults are out of contrast, and for these cases g=$\bar{2}02$, $2\bar{2}0$, $\bar{1}\bar{3}1$ and $02\bar{2}$, respectively. Use of the invisibility criterion for stacking faults, $\alpha = 2\pi \cdot g$ $R = n2\pi$ (90) reveals that the stacking fault vector, R, is $\pm 1/3[111]$. The sign of a fault can be determined from an inspection of the edge fringes in the bright field image; both edge fringes are dark for $\alpha = -2\pi/3$ (91). For the stacking faults in Figure 62, both edge fringes are dark for g=020 (Figure 62d). Hence, $R = 1/3[\bar{1}\bar{1}\bar{1}]$, which corresponds to the removal of a plane of atoms and is the description of an intrinsic stacking fault on (111) planes.

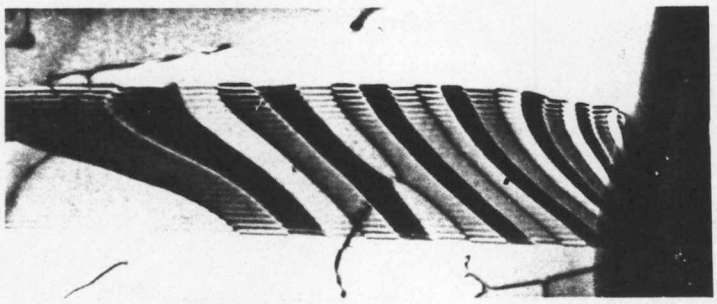
The contrast change in the faults in Figure 62d shows a repeating sequence with every third fault nearly invisible. That is, the contrast change of the typical one is G-D-W-G-D-W-G-D-W-W-D-G-W-D-G-W-D-G Where G=gray, W=white and D=dark. This appearance can be explained by

overlapping intrinsic stacking faults as shown in Figure 65.

Figure 66 shows additional evidence of overlapping stacking faults. In this special tilt angle, the overlapping faults can be observed directly as they appear in the same band, but on parallel slip planes.

4.3.11 Interaction of gliding dislocations with grain boundaries.

The dislocations which are gliding on the plastic deformation bands (consisting of overlapping intrinsic stacking fault planes) are stopped upon encountering the high angle grain boundaries. An example is shown in Figure 67a, where the dislocations are stopped upon reaching both sides of the grain. In Figure 67b, two different sets of plastic deformation bands meet at a common same grain boundary. At a special tilt (Figure 67c), the intrinsic dislocation structure of these grain boundaries can be seen. Because the gliding lattice dislocations do not match the intrinsic grain boundary dislocations, the gliding dislocations cannot pass through the grain boundary interface. Thus, upon continued plastic deformation, these dislocations pile-up, developing a localized stress concentration. The stress eventually attains a magnitude sufficient to cause



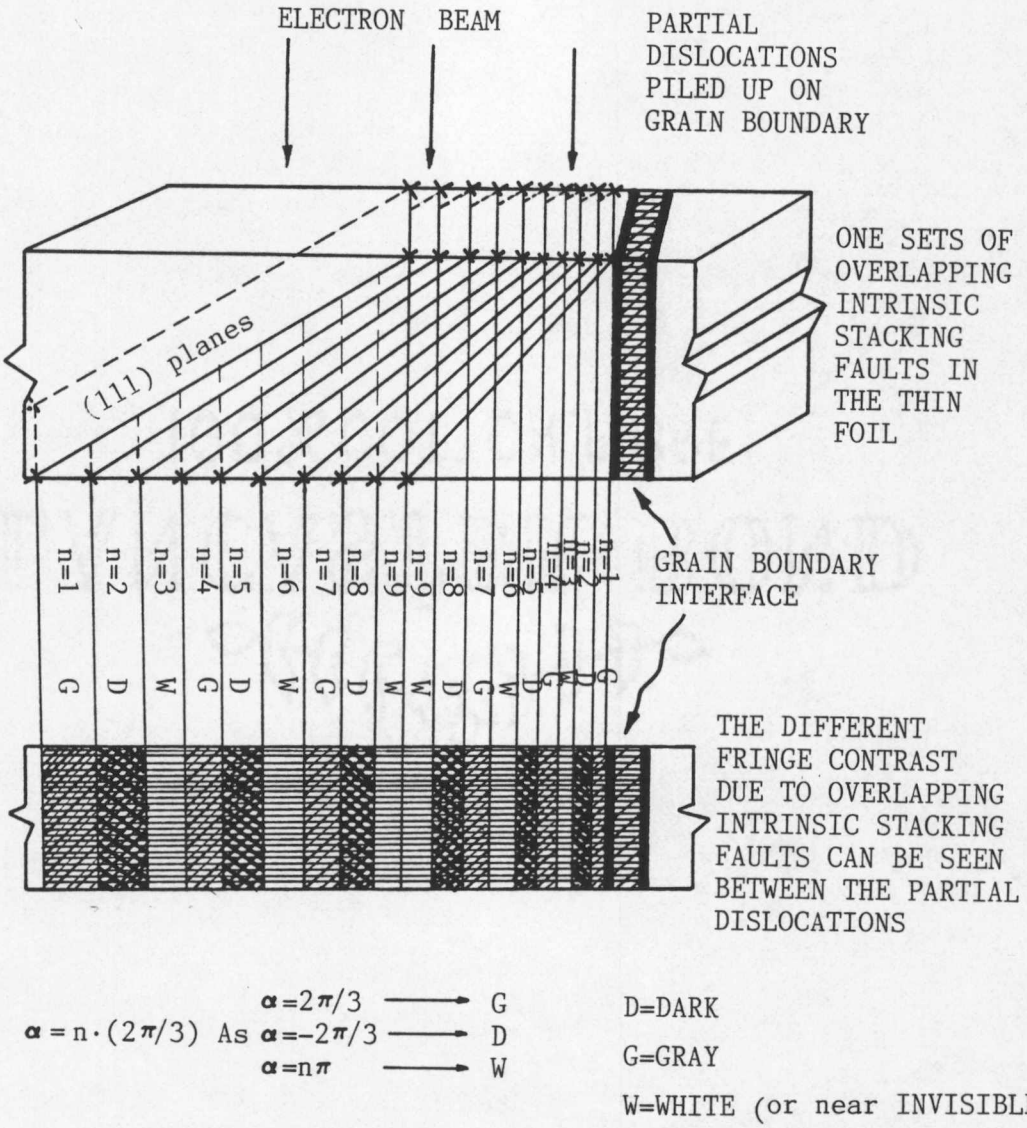


Figure 65. schematic illustration of stacking fault contrast from overlapping intrinsic stacking faults.

(a)

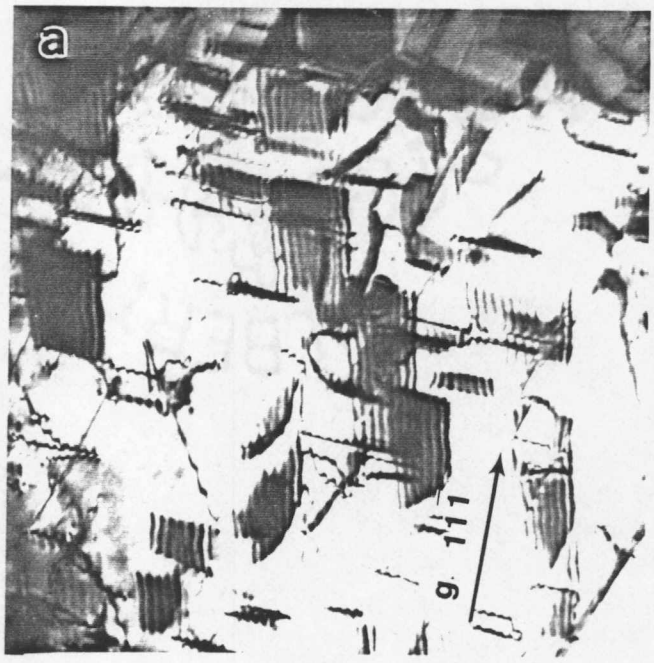
850°C aged 10days, then rolled 7.6%.

B=[134]

g=[111]

Bright field of overlapping stacking faults.

50K X



(b)

Central dark field of above.

50K X

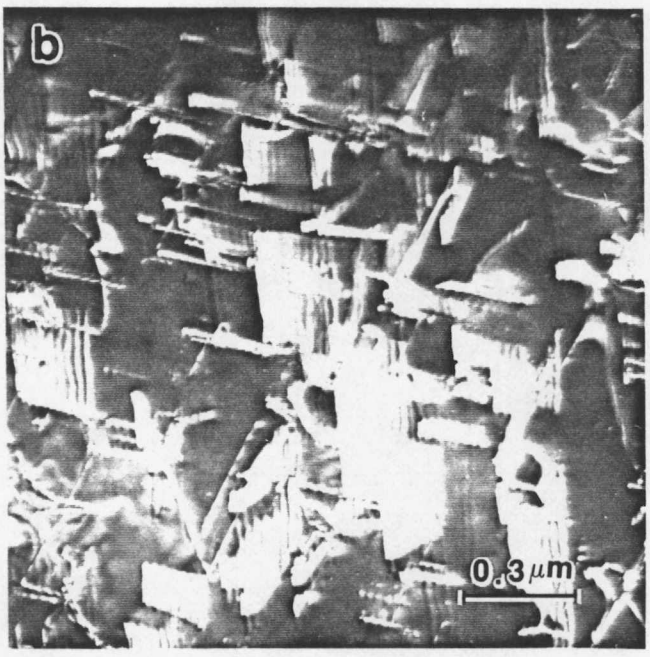


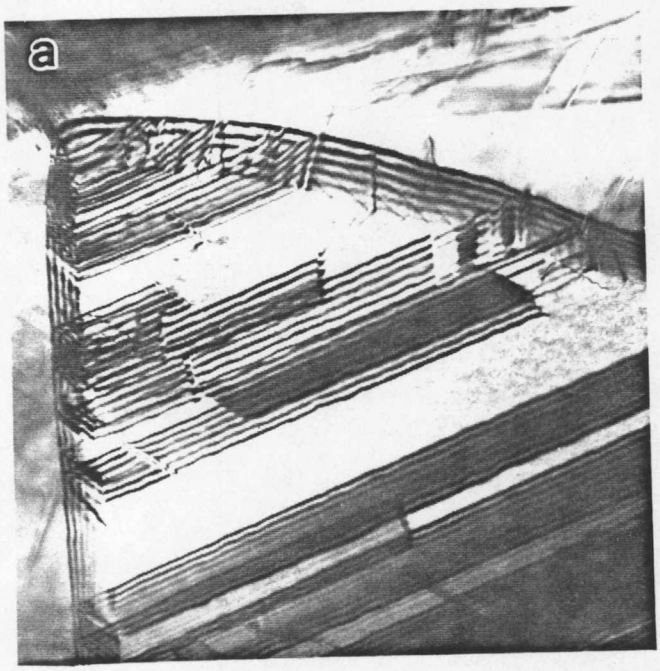
Figure 66. Overlapping stacking faults.

(a)

725°C aged 100,000 min. and rolled 6%.

showing plastic deformation bands which connect with each side of grain boundary.

50K X



(b)

Showing two directions of plastic deformation bands meeting at same gram boundary.

50K X

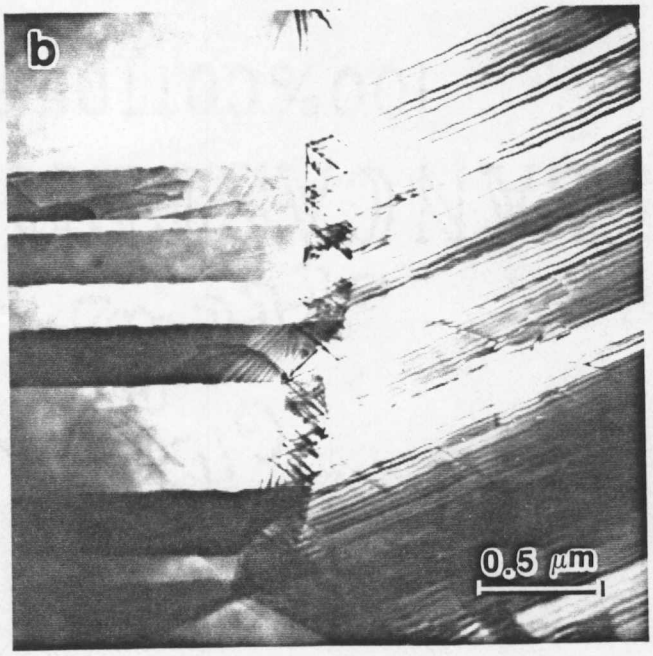
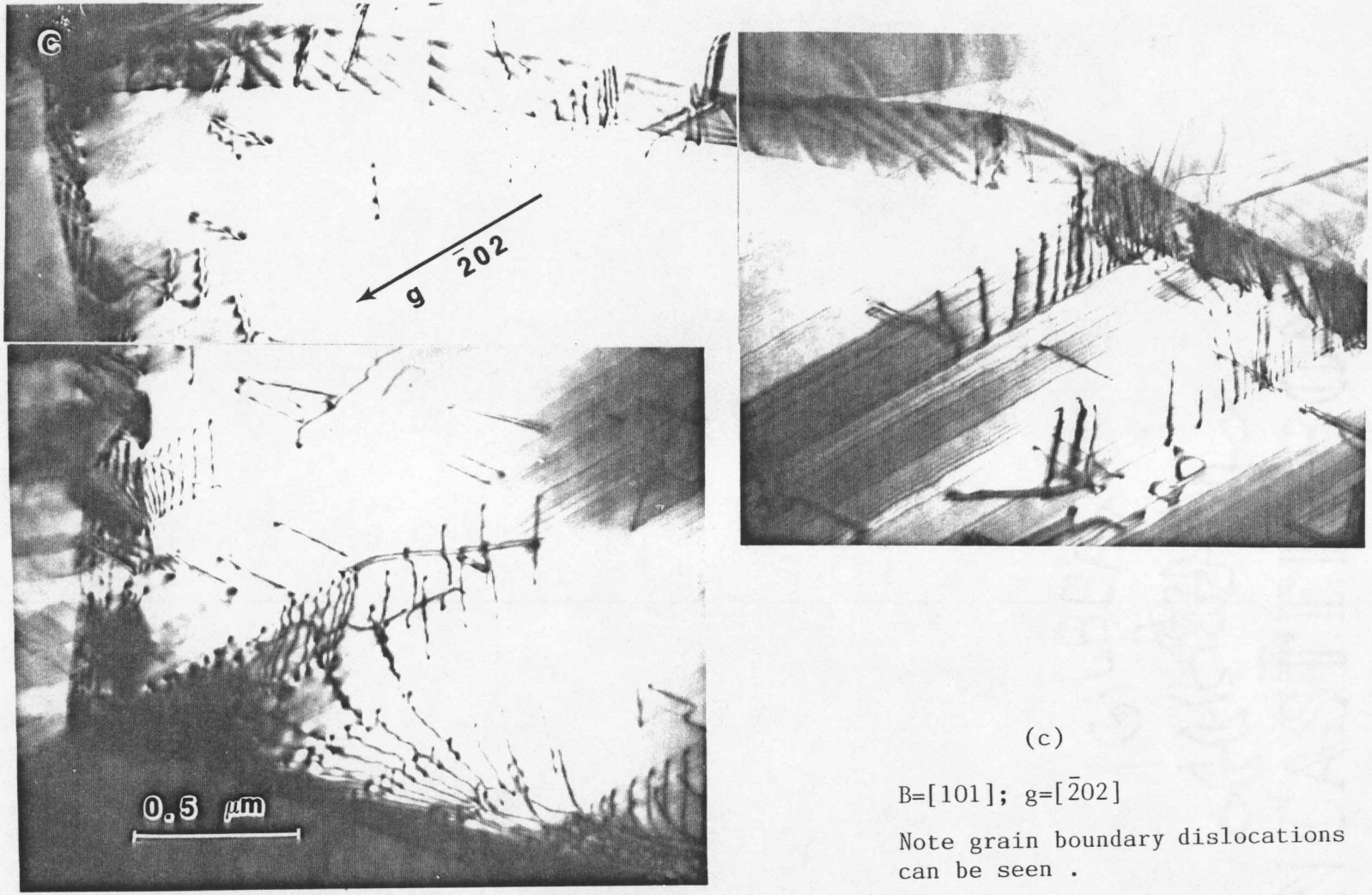


Figure 67. Gliding lattice dislocations reacting with high angle grain boundary.



(c)

B=[101]; g=[$\bar{2}02$]

Note grain boundary dislocations can be seen .

Figure 67. (Continued)

separation of the boundaries, causing intergranular separation with little ductility.

The boundaries referred to in the previous paragraph were high angle boundaries, as established by electron diffraction patterns of neighboring grains. Similarily, low angle boundaries were identified, such as shown in Figure 68. Note that here most of the gliding dislocations are also stopped and are piled up, although some are able to propagate across the boundary. Figure 69 shows an example of dislocation interaction with a twist boundary. The gliding dislocations in plastic deformation bands marked II are able to propagate through this boundary, whereas those of the plastic deformation bands marked I could not.

When the gliding dislocations encounter a twin boundary, the crystallographic compability allows propagation of the dislocations across the twin boundary. This is illustrated by the examples in Figure 70.

It is clear from these observations that the structure of the boundary encountered by gliding dislocations plays a very important role in impeding dislocation motion, and hence in strengthening and in intergranular fracture.

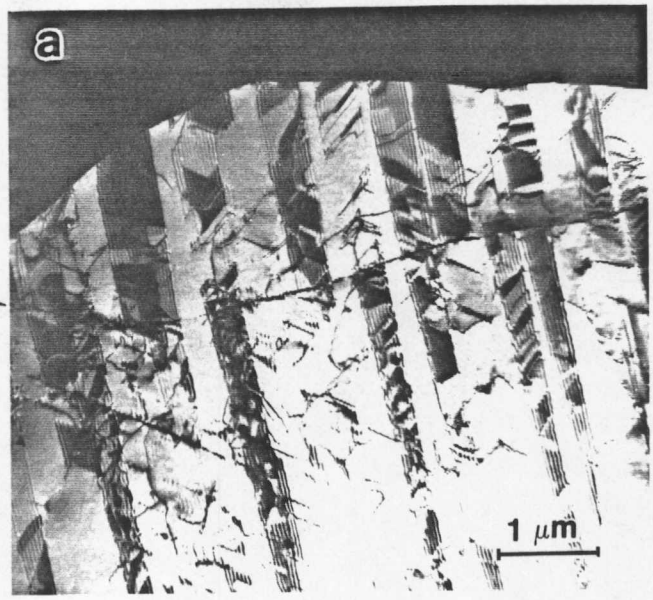
(a)

850°C aged 10 days and rolled 3%.

B=[101]; g=[$\bar{1}\bar{1}1$]

LOW ANGLE GRAIN Boundaries

13K X



(b)

Higher magnification

Some of gliding lattice dislocations can go through low angle grain boundary.

B=[101]; g=[13$\bar{1}$]

33K X

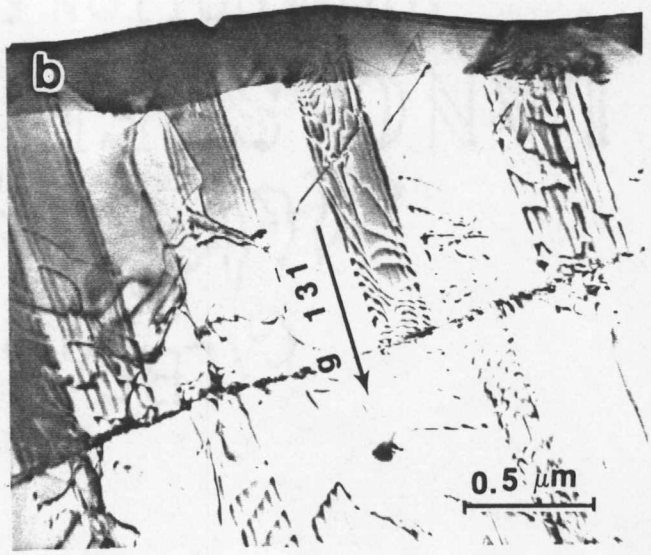


Figure 68. Gliding lattice dislocations reacting with low angle grain boundary.

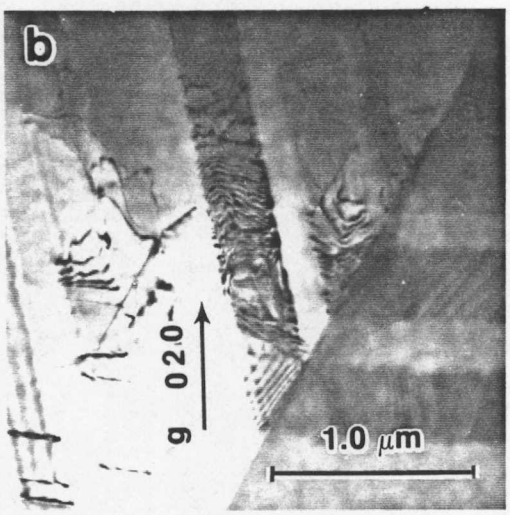
(a)

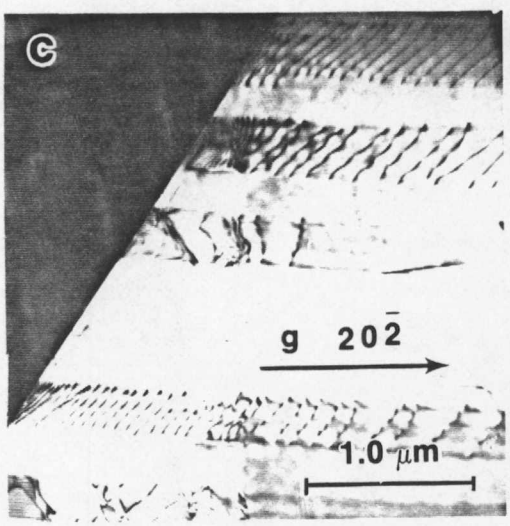
725°C aged 100,000 min. and rolled 6%.

Typical twin boundary.

20K X







(b) Left of (a)
B=[101]; g=[020]
33K X

(c) Right of (a)
B=[101]; g=[20$\bar{2}$]
33K X

Figure 69. Gliding lattice dislocation reacting with twin boundary.

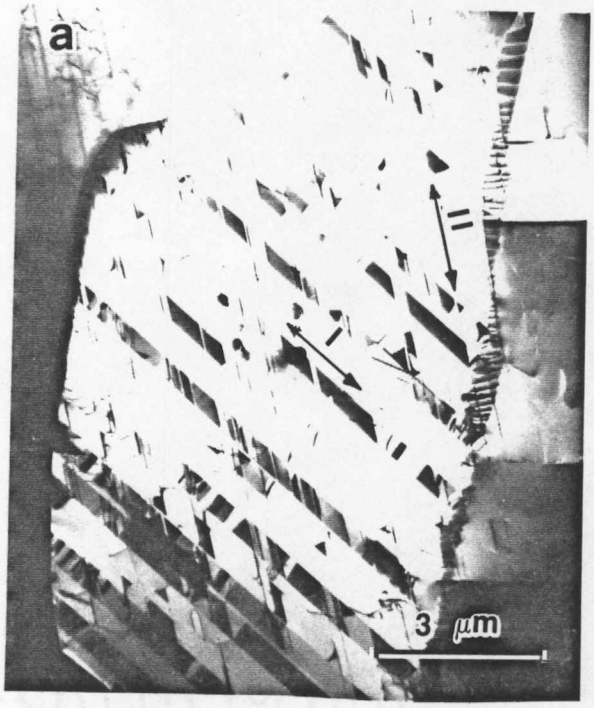
(a)

725°C aged 1000 min.

Taken from 800°C tensile tested specimen, very close to the broken surface.

Showing twisted grain boundary.

6.6K X



(b)

Higher magnification of (a).

Gliding lattice dislocations in the plastic deformation II can go through the grain boundary.

B=[101]; g=[020]

26K X

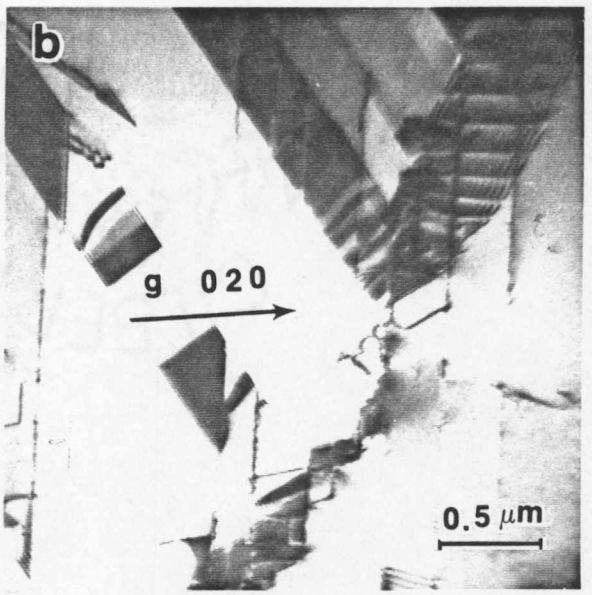


Figure 70. Twisted grain boundary.

4.3.12 Glide system analysis.

From the analysis in Section 4.4.8, it was determined that the Burgers vector of the glide dislocations belongs to a single 1/6[112] type partial dislocation. From the stacking fault contrast analysis in 4.4.10, it was determined that the deformation bands consist of overlapping intrinsic stacking faults and that all the partial dislocations do not lie on a single stacking fault plane, but on parallel planes.

Venable (92) has demonstrated that a twinned crystal may be built up by a series of intrinsic stacking faults on successive close-packed planes in a face-centered cubic lattice. This particular model inherently requires that these stacking faults be produced by partial dislocations of the same Burgers vector on each close-packed plane. Thompson and Gleiter (93,94) have indicated that once a twin is formed, the twin lamellae can grow more easily because of reduction of the stacking fault energy in the vicinity of the twin boundary.

It is concluded that the overlapping stacking faults represent twin lamellae which can grow easily (see Section 4.3.5). Hence, the deformation mechanism in the ordered Ni_4Mo alloy can be thought of as predominately due to dislocations forming twins instead of slip.

In order to establish an integrated glide model of ordered Ni_4Mo, a detailed analysis of a glide system in an individual grain which consists on only one domain was carried out. The procedure is described in the following steps.

Step 1. Determining the index of the deformation band by trace analysis.

In Figure 71a, there are two sets of deformation bands, denoted by A and B. By trace analysis, it was established that trace A corresponds to the (111) plane, and B to the $(\bar{1}11)$ plane.

Step 2. Determination of Burgers vector for all partial dislocations in the A (111) deformation bands.

Because the fault lies on the (111) plane, the possible Burgers vectors for the partial dislocations are $\pm a/3[111]$, $\pm a/6[11\bar{2}]$, $\pm a/6[\bar{2}11]$ or $\pm a/6[1\bar{2}1]$. The results of this analysis (Figure 71b-i and Table 17) show that only $1/6[11\bar{2}]$ in the series can agree with the invisibility rule. The magnitude of the Burgers vector is also confirmed to be 1/6 since no double image appears in the s=0 condition. (If it is 1/3,

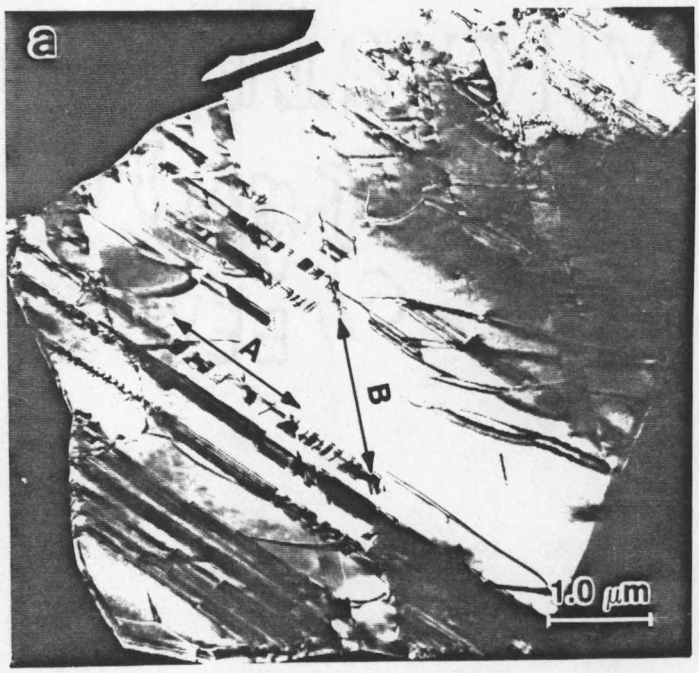
(a)

850°C aged 10 days then 725°C aged 1400 min. and rolled 3%.

CDF of fundamental spot of (112) pole.

Two sets of deformation bands (A & B) and APDBs can be seen.

13K X



(b)

B=[112]

g=[11$\bar{1}$]

20K X

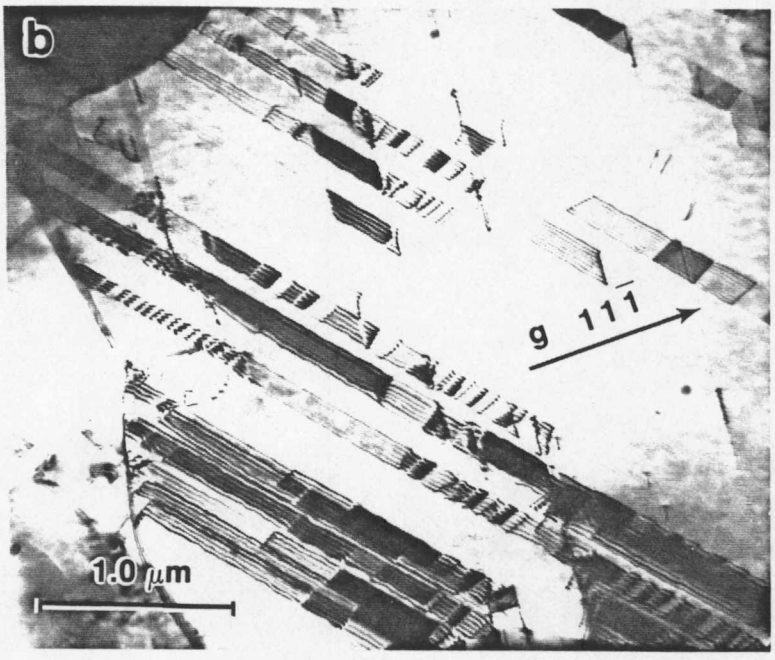


Figure 71. Burgers vector analysis of gliding partial dislocation in (111) plastic deformation bands.

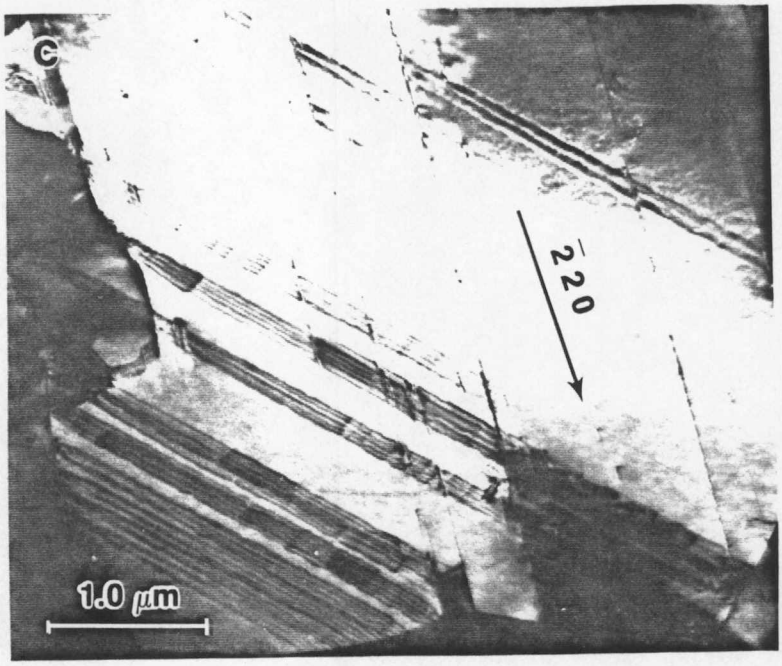
(c)

B. F.

B=[112]

g=[$\bar{2}$20]

20K X



(d)

CDF (S=0)

B=[112]

g=[$\bar{3}$11]

20K X

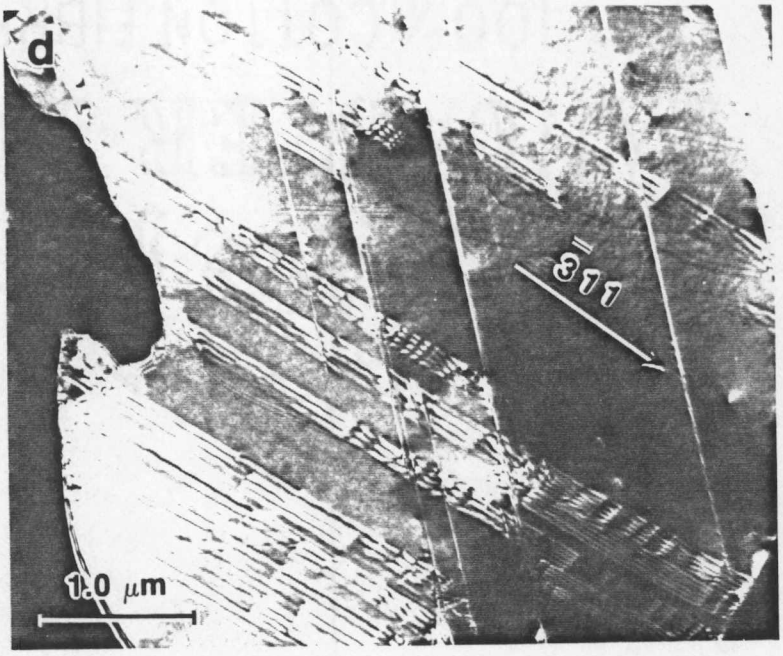


Figure 71. (Continued)

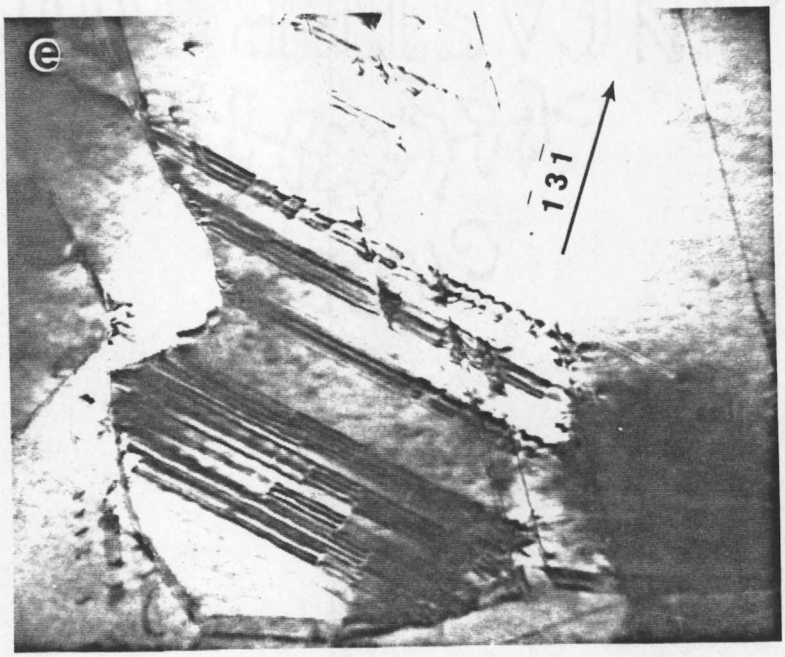
(e)

B. F.

B=[112]

g=[$\bar{1}3\bar{1}$]

20K X



(f)

B. F.

B=[111]

g=[$\bar{2}20$]

20K X

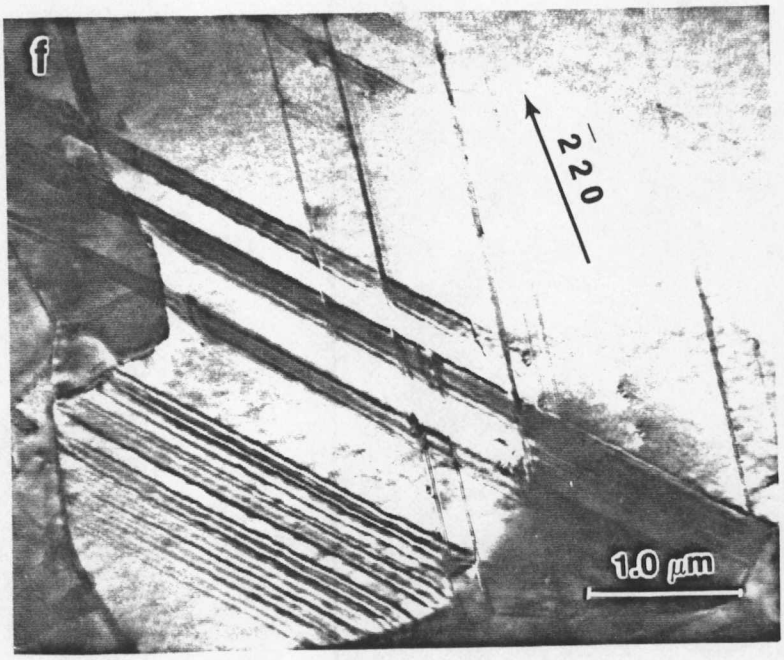


Figure 71. (Continued)

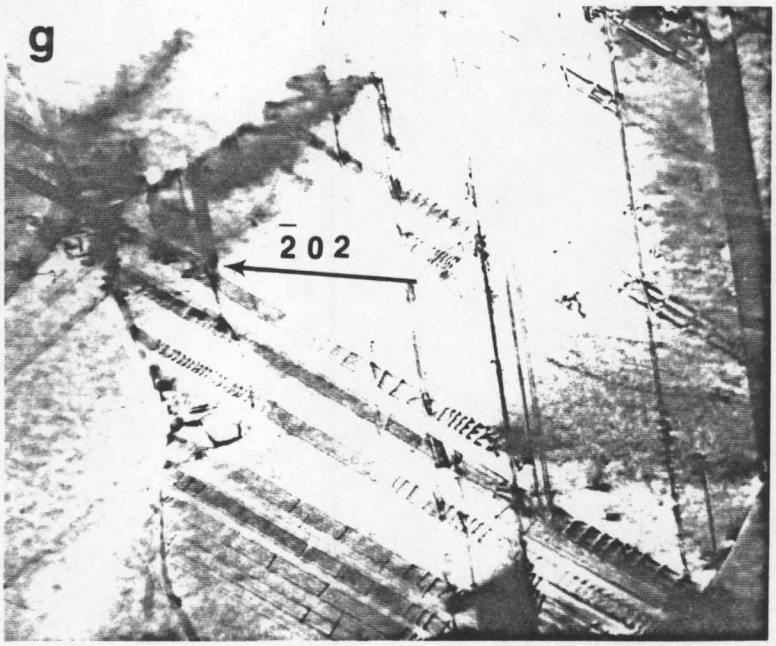
(g)

B. F.

B=[111]

g=[202]

20K X



(h)

B. F.

B=[111]

g=[022]

20K X

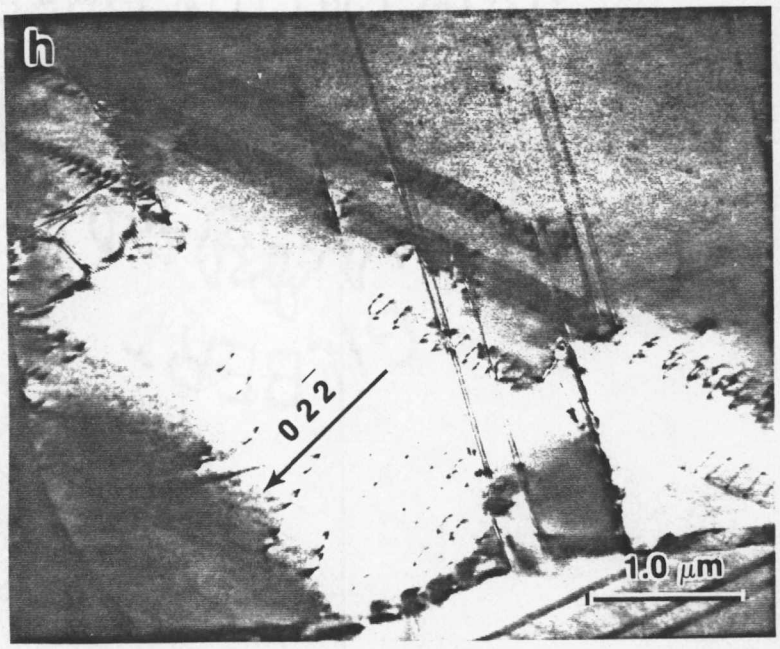


Figure 71. (Continued)

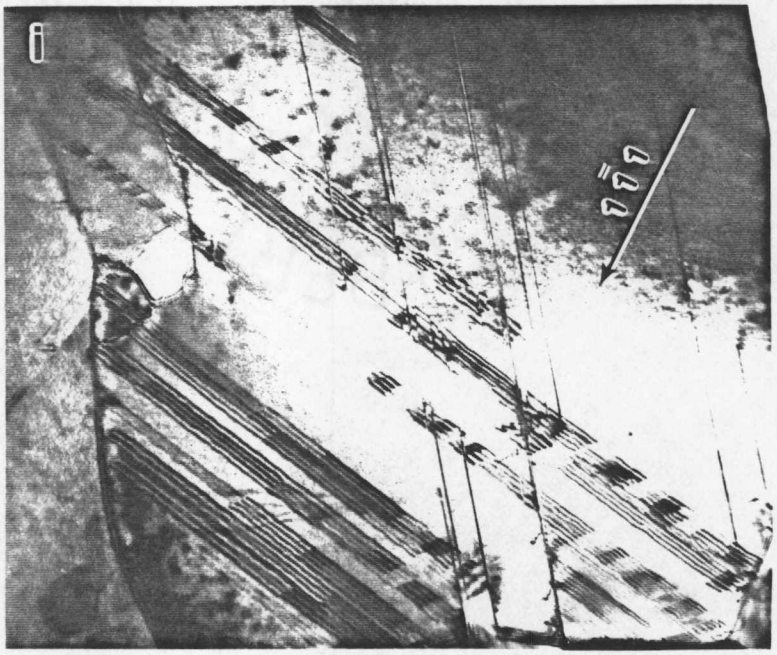
(i)

B. F.

B=[011]

g=[1$\bar{1}$1]

20K X



(j)

B. F.

B=[011]

g=[$\bar{1}\bar{1}$1]

20K X

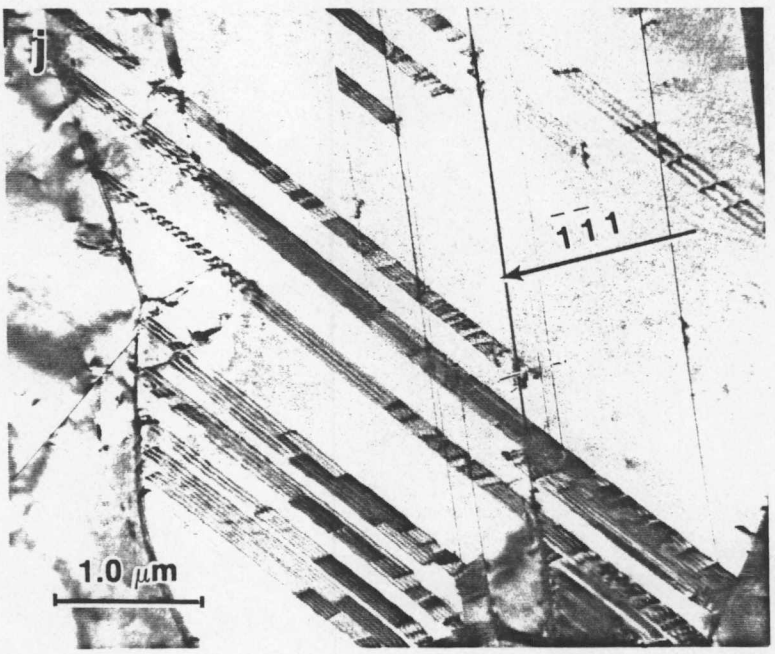


Figure 71. (Continued)

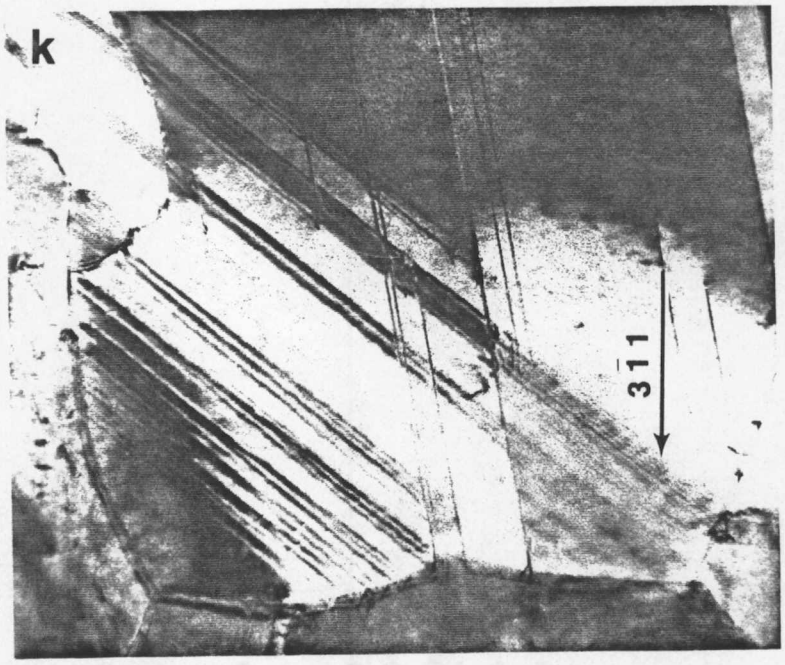
(k)

B. F.

B=[011]

g=[3$\bar{1}$1]

20K X



(l)

B. F.

B=[011]

g=[200]

20K X

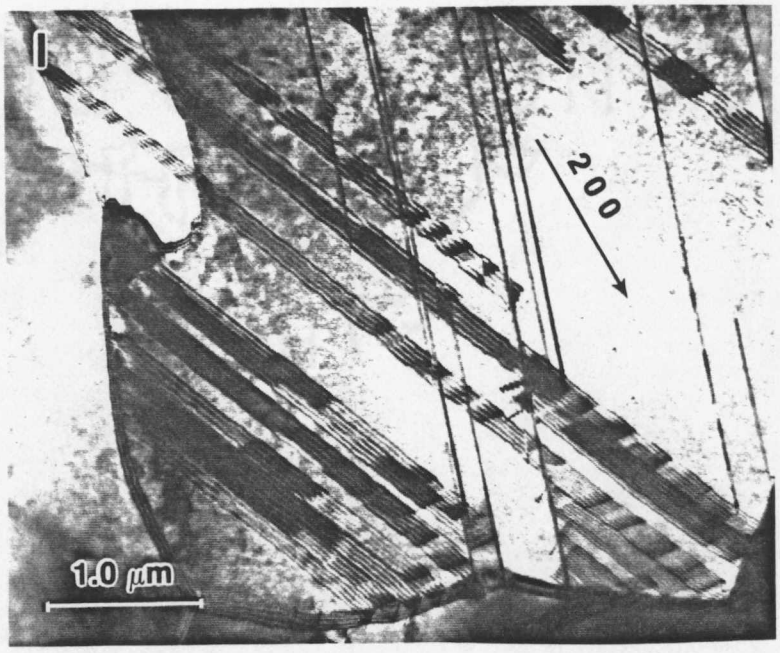


Figure 71. (Continued)

Table 17. Burgers vector analysis of gliding partial dislocations on the (111) plastic deformation plane (see Figure 71)

Beam Direction B	Two Beam Condition g	$g\cdot\vec{b}$				Observed
		$\vec{b}=1/6[11\bar{2}]$	$\vec{b}=1/6[\bar{2}11]$	$\vec{b}=1/6[1\bar{2}1]$	$\vec{b}=1/6[111]$	
112	$11\bar{1}$	2/3	-1/3	-1/3	1/3	S
112	$2\bar{2}0$	0	-1	1	0	I
112	$\bar{3}11$	-2/3	-2/3	-2/3	-1/3	M
112	$\bar{1}3\bar{1}$	2/3	2/3	-2/3	1/3	M
111	$\bar{2}20$	0	1	-1	0	I
111	$\bar{2}02$	-1	1	0	0	S
111	$0\bar{2}2$	-1	0	1	0	S
011	$1\bar{1}1$	-1/3	-1/3	2/3	1/3	W
011	$\bar{1}\bar{1}1$	-2/3	1/3	1/3	-1/3	M
011	$3\bar{1}1$	0	-1	1	2/3	I
011	200	1/3	-2/3	1/3	2/3	W
Result:	Only $1/6[11\bar{2}]$ series can match all the conditions.					

V=Visible; I=Invisible; S=Strong; M=Medium; W=Weak.

Check Burgerss vector by invisible rule:
$[2\bar{2}0]*[3\bar{1}1]=\pm 1/x[112]$.

Criterion of dislocations image contrast:
$|g\cdot\vec{b}|>1$ image is strong
$|g\cdot\vec{b}|=2/3$ image is medium
$|g\cdot\vec{b}|=1/3$ image is weak
$|g\cdot\vec{b}|=0$ image is invisible.

a double image will appear when $g=\bar{2}02$ since $g*\vec{b}=2.$)

It is also seen in Figure 71a that some partial dislocations were impeded by anti-phase boundaries and interaction with other bands. However, the predominate feature is partial dislocations piled-up at high angle grain boundaries.

Step 3. Determination of the domain type.

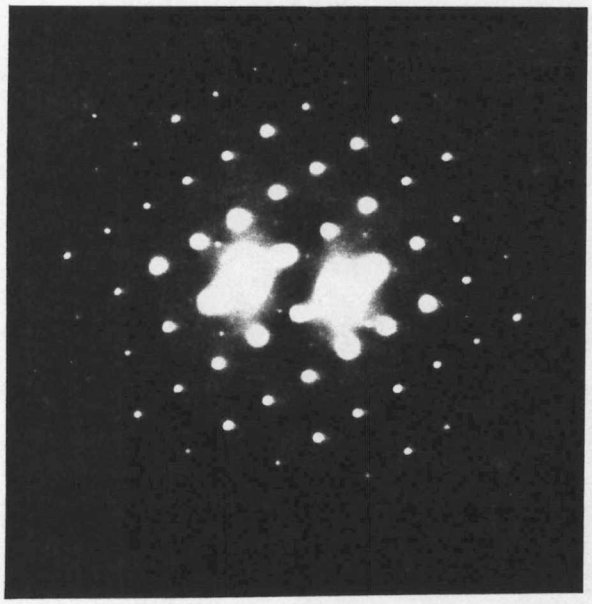
The selected area diffraction pattern of this grain when oriented for a 112 pole is shown in Figure 72a. Only one variant of superlattice spots is observed, which means that the a axis of the β phase is parallel to the 112 beam direction, and only one type of domain exists in this grain. We know that the {550} plane of the superlattice coincide with the {420} plane of the face-centered cubic fundamental lattice. After indexing the selected area diffraction pattern (see Figure 72b), the value $a_1=0$, $a_2=4$, $a_3=\bar{2}$ are substituted into the formula previously shown in Table 18. The domains in this area are found to be of type D (see Figure 72a and Table 18).

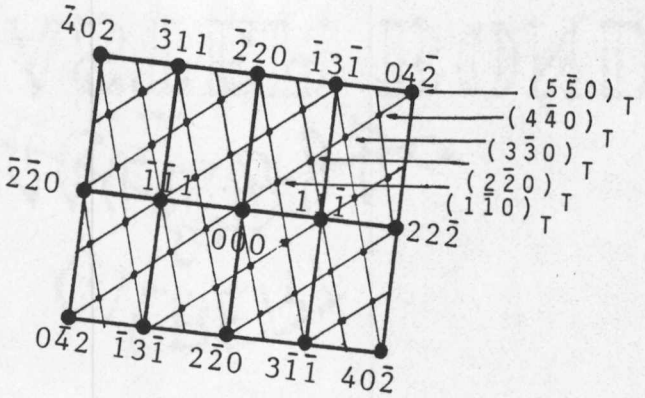
Step 4. Determination of the primitive unit meshes

(a)

Showing the 112 SADP of grain analyzed.

Only one variant of superlattice appears.





(b) Index above SADP.

Figure 72. Selected area diffraction pattern of grain analyzed in Figure 71.

Table 18. Domain type determination (see Figure 72)

Domain Type	Formula to Calculate a_1', a_2', a_3'			Calculated Results		
	a_1'	a_2'	a_3'	a_1'	a_2'	a_3'
A	$1/2(3a_1-a_2)$	$1/2(a_1+3a_2)$	a_3	-2	6	-2
B	$1/2(3a_1+a_2)$	$1/2(-a_1+3a_2)$	a_3	2	6	-2
C	$1/2(3a_2-a_3)$	$1/2(a_2+3a_3)$	a_1	7	-1	0
D	$1/2(3a_2+a_3)$	$1/2(-a_2+3a_3)$	a_1	5	-5	0
E	$1/2(3a_3-a_1)$	$1/2(a_3+3a_1)$	a_2	-3	-1	4
F	$1/2(3a_3+a_1)$	$1/2(-a_3+3a_1)$	a_2	-3	1	4
Result:		Only domain D is resonable.				

Where; $a_1=0$; $a_2=4$; $a_3=-2$.

and the stacking sequences on the (111) plane.

Once the domain type was determined, the primitive unit cell meshes and the stacking sequence on the (111) planes was determined, as shown in Figure 73.

Step 5. Gliding simulations on the D1a atomic model, to check the change in the first nearest neighbor atomic bonding and to determine if APB, SISF or SESF are created.

In this exercise, the plane above the one shown in Figure 73 was moved along various slip vectors and the change in the type of nearest neighbor bonds determined. 1/2<110> type glide always changes the number of bonds, so it is not considered to be a preferred type. Instead, 1/6<112> type is preferred. There is no net change in bonding for $1/6[11\bar{2}]$ or $1/6[1\bar{2}1]$, but there is a change for $1/6[\bar{2}11]$ (see Table 19), and this latter type was not observed in the examination made in this study. However, the $1/6[1\bar{2}1]$ also was never observed, and its absence cannot be explained by consideration of nearest neighbor bonding. A possible explanation is that in the regions examined

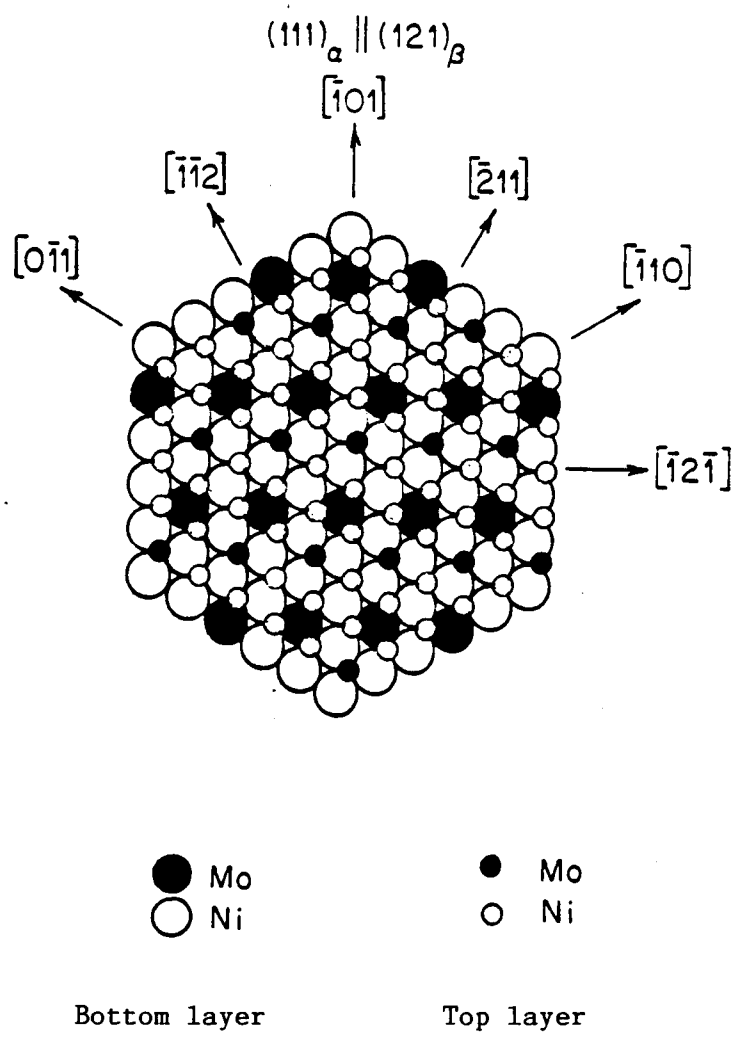


Figure 73. Primitive unit "meshs" and the stacking of type D domain of Ni_4Mo viewed on (111) plane.

Table 19. Gliding simulation and check of the nearest neighbor (N.N.) bonding change

Condition	Central Atom	1st N.N. Bonding		Remarks
		Ni	Mo	
Before Gliding	Mo Ni	12 9	0 3	---
Gliding Along 1/6[11$\bar{2}$]	Mo 1/3 Ni 1/3 Ni 1/3 Ni	12 8 10 9	0 4 2 3	The average 1st N.N. bonding is not changed, but SISF created.
Gliding Along 1/6[$\bar{2}$11]	Mo 1/2 Ni 1/2 Ni	11 10 9	1 2 3	The 1st N.N. bonding changed and SISF created.
Gliding Along 1/6[1$\bar{2}$1]	Mo Ni	12 9	0 3	The 1st N.N. bonding is not change but SISF created.

SISF=Superlattice Intrinsic Stacking Fault.

the orientation of the crystal was such that the resolved shear stress for $1/2[1\bar{2}1]$ slip was never attained.

In any case, the glide model based on the mechanism of twin formation by dislocations is consistent with the results of the nearest neighbor bonding considerations.

4.3.13 Observations of dislocations generated in situ using a TEM deformation stage.

In previous Sections, many observations about the structure of dislocations of Ni_4Mo (for various heat treatments), generated by both tensile loading and by rolling, have been reported. The Burgers vector of the dislocations has been determined, and compared to that predicted from gliding simulation. The evidence points towards a deformation mechanism involving the formation of twins.

However, the mechanism of the formation of the dislocations and of their movement, and of fracture, had to be inferred from the observation of dislocations already present upon observation. To help confirm the conclusions drawn from these observations, dislocations were generated by use of a deformation stage in the transmission electron microscope, and hence were observed in situ.

In Figure 74 is shown a sequence in which fracture has occurred by intergranular separation along the former, α, high angle grain boundaries. Although extensive bend contours are formed, it was seen that bands form in the grains (although not necessarily in contrast in all grains in Figure 74). It is not clear exactly where the crack initiated, but it clearly is being extended along the boundaries as additional straining occurs.

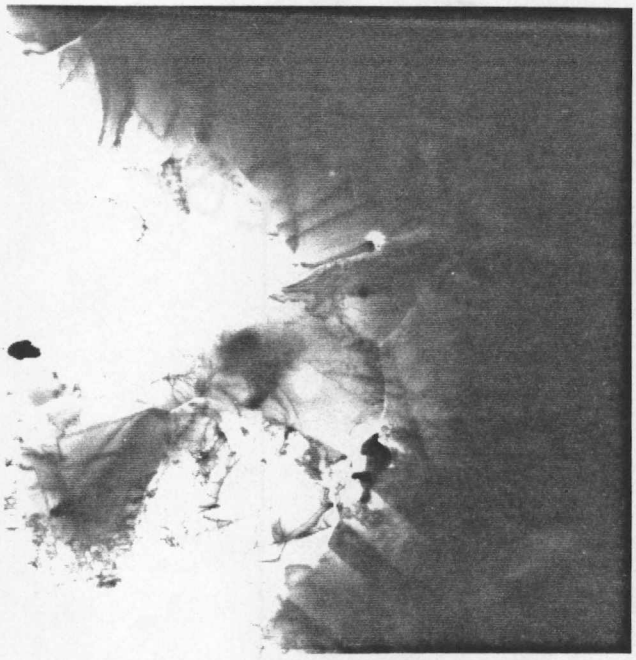
Another example is shown in Figure 75. In Figure 75a, the structure before straining contains only isolated dislocations. Straining generated bands in the grains, several of which are in contrast in Figure 75b; further straining continued to increase the density of these bands. Note in Figure 75c that a crack has formed along a section of a grain boundary.

In Figure 76a is shown a grain in which several bands are present, and some overlapping stacking faults are observed. In this region, the dislocation movement in the bands is beginning to form twins. In Figure 76b, at higher magnification, is seen several dislocation bands which terminate at a domain boundary, only faintly in contrast here. It was observed that upon straining these bands suddenly appeared, moving from one side or the other of the domain boundary. (In Figure 76b, they have moved up or down.) Thus, upon sufficient straining, the dislocations already in the domain boundary moved along a

(a)

Before in situ tension

1600 X



(b)

After straining

1600 X



Figure 74. A sequence of change of plastic deformation structure.

(c)

Strained more

1600X

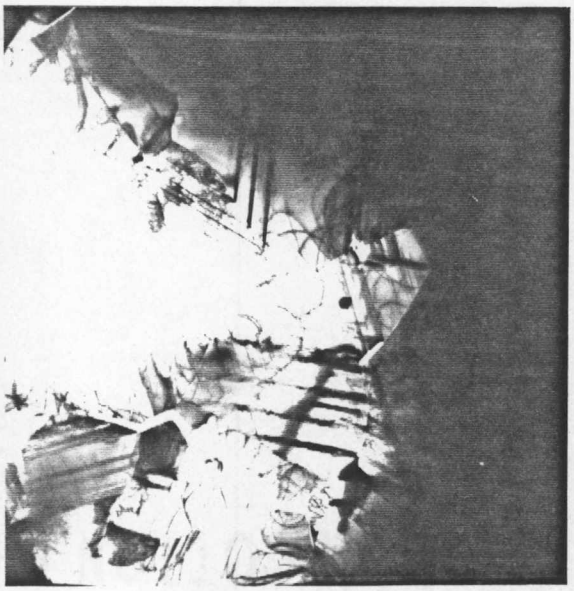


Figure 74. (Continued)

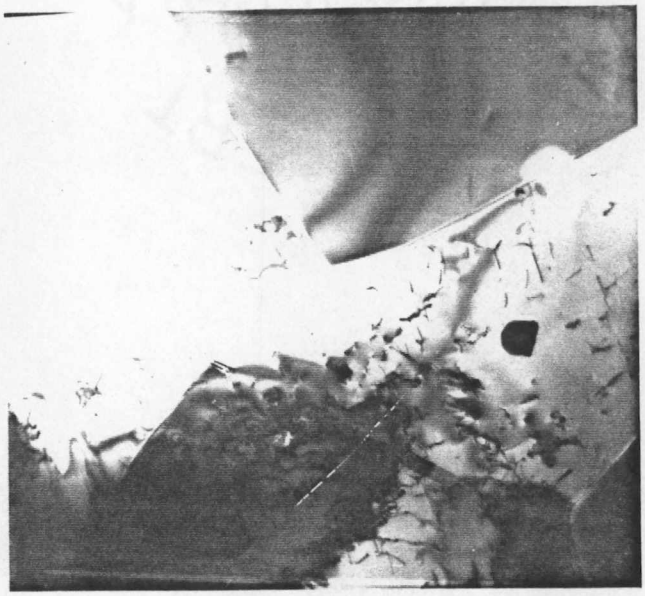
(a)

Before

in situ

tension

6100 X



(b)

After

straining

6100 X

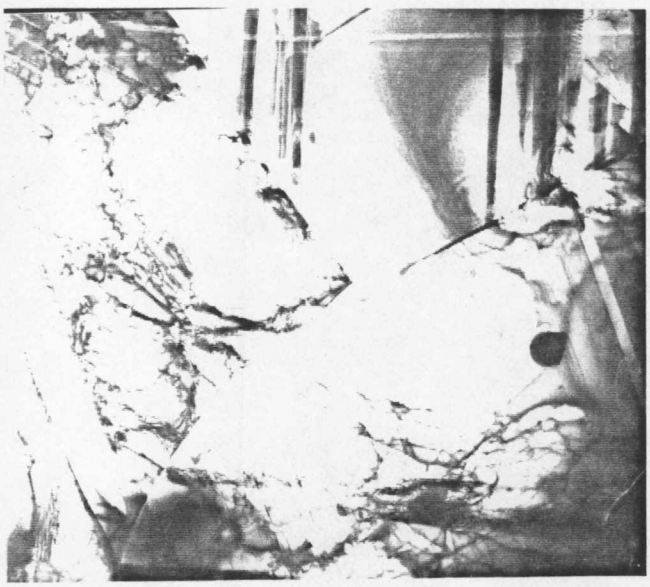


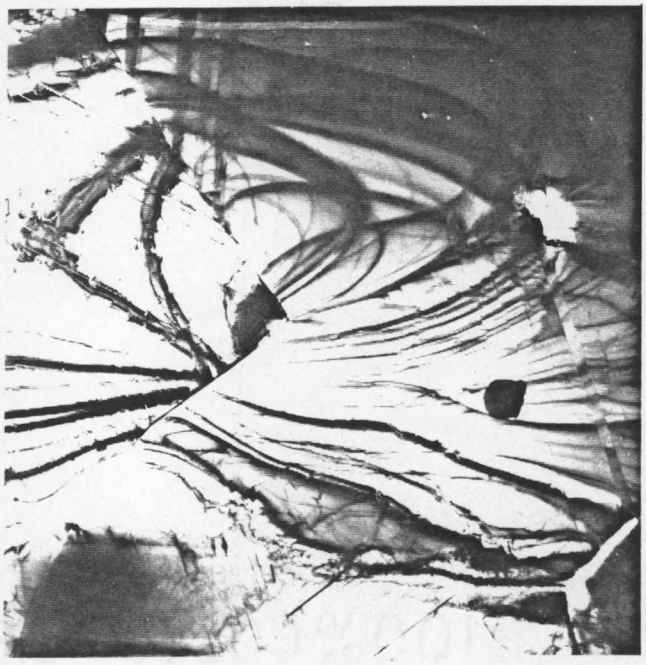
Figure 75. Another sequence of change of plastic deformation structure.

(c)

Strained

more

6100 X



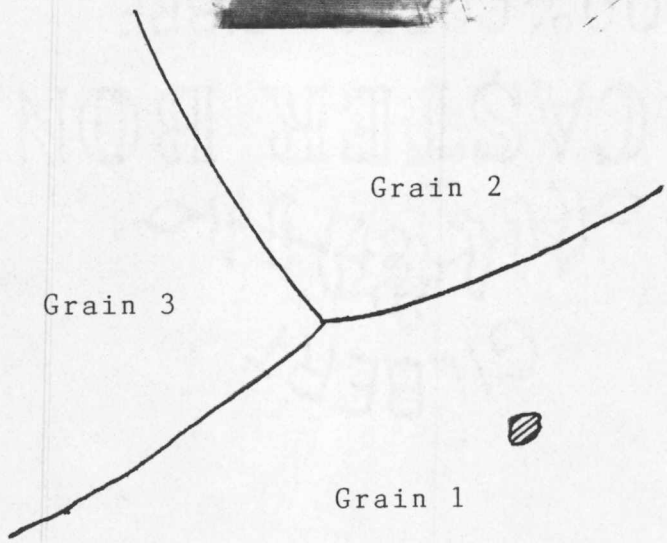
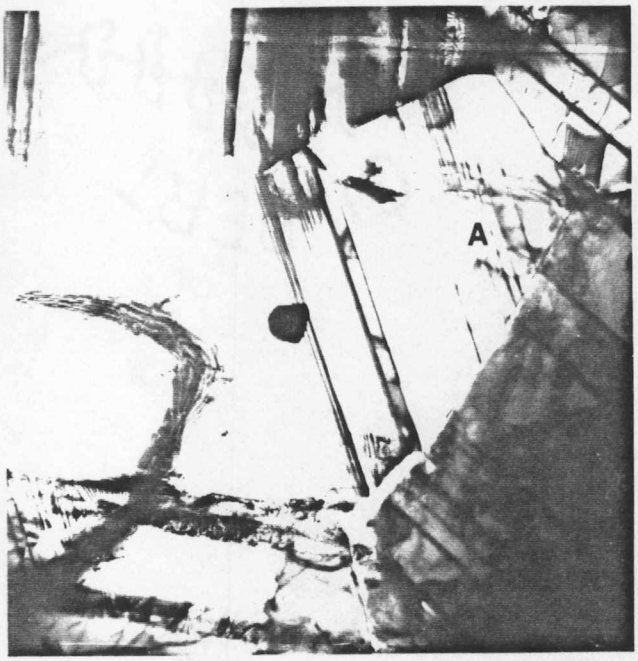


Figure 75. (Continued)

(a)

Whole grain 1

6100X



(b)

Higher magnification of above A.

Note domain boundary.

50,000 X

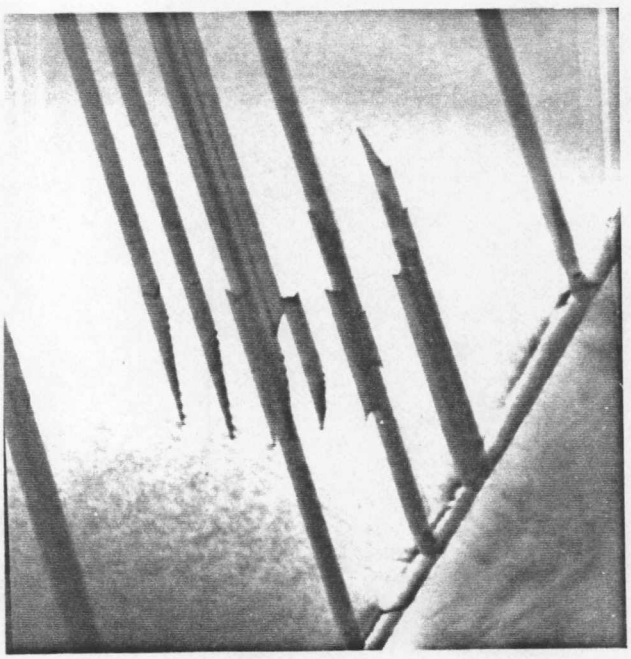


Figure 76. The deformation structure inside G 1.

slip plane, creating a stacking fault.

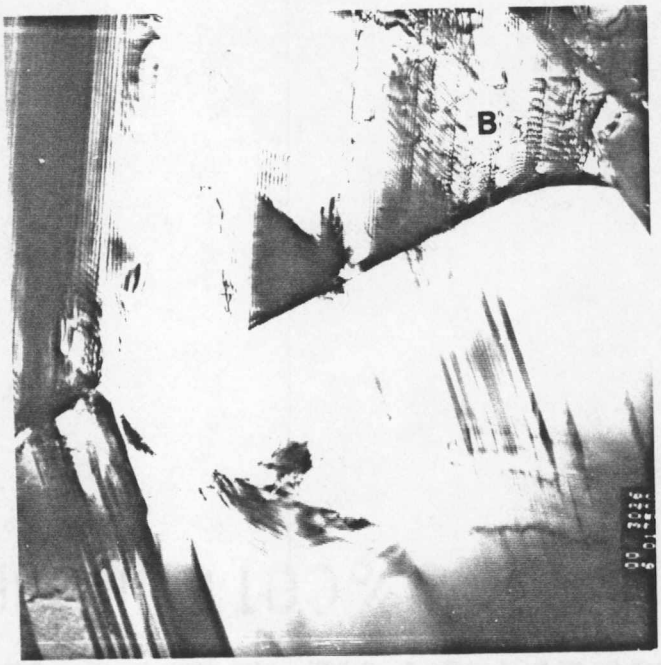
Note in Figure 76b that the dislocations have piled-up at a high angle grain boundary. A pile-up along the boundary between grain G1 and G2 is shown in more detail in Figure 77 and similarily the structure along the boundary between grain G2 and G3 is shown in Figure 78.

All of the dislocation structures observed by these in situ experiments were identical to those observed (and described in the previous Sections) in specimens deformed by tension or by rolling prior to sample preparation. The glide dislocations had Burgers vectors of the 1/6<112> partial dislocation type.

Other examples of the dislocations observed during in situ straining are shown in the following figures. Figure 79 shows a region displaying extensive bands with stacking fault contrast. In Figure 80 is shown the beginning of the formation of stacking faults from sessile matrix dislocations. Figure 81 shows dislocations piled-up along a high angle grain boundary. Figure 82 shows the reaction of piled-up dislocations with an incoherent twin boundary. And Figure 83 shows an example of a band consisting of overlapping stacking faults which have piled-up at a grain boundary. The analysis of the contrast in such a case was analyzed in Section 4.3.10.

(a)
Grain
boundary
between
G 1 & G 2

17500 X



(b)
Higher
magnification
of area B
above.
Piled up
dislocations.

51000 X

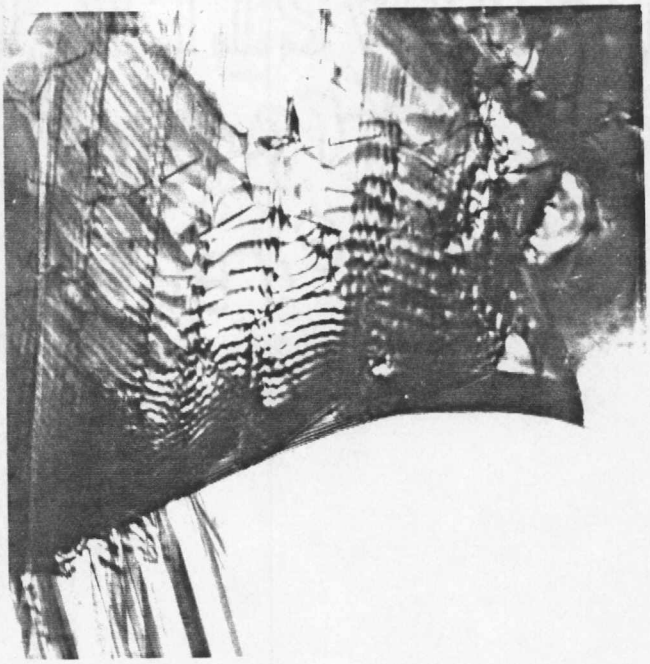
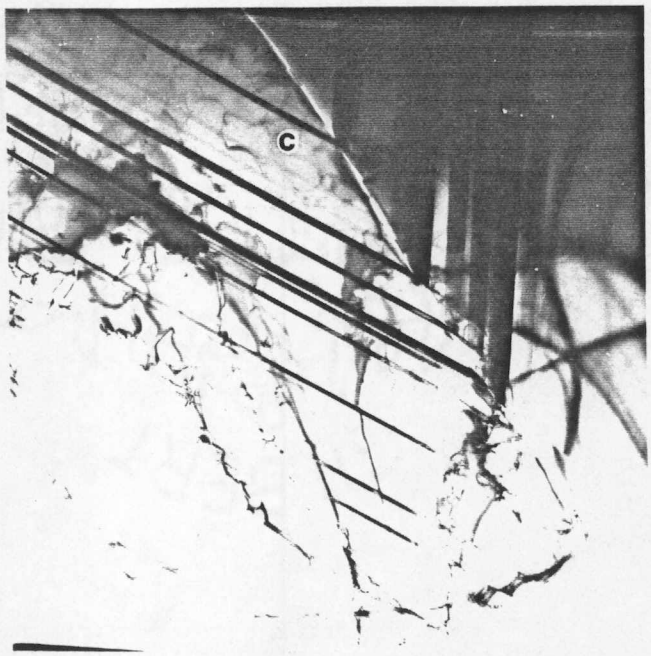


Figure 77. The deformation structure between G1 and G2.

(a)
Grain
boundary
between
G2 & G3.

9700 X

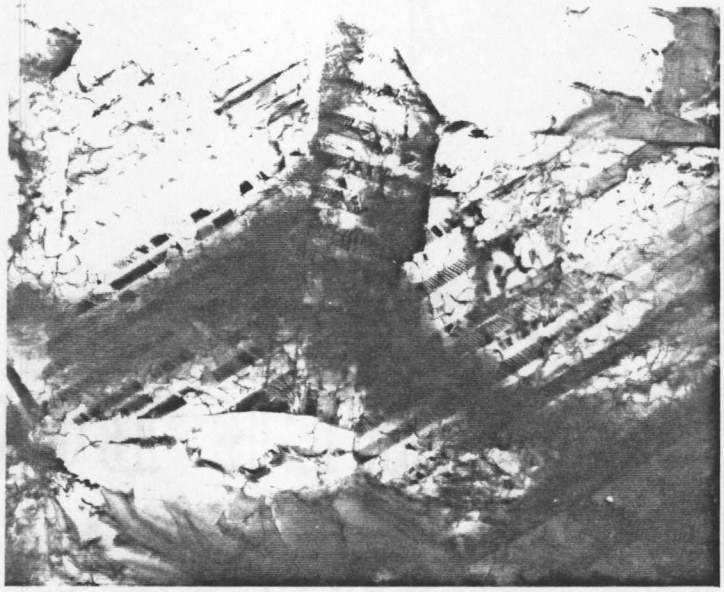


(b)
Higher
magnifica-
tion of
above C
area.

40,000 X

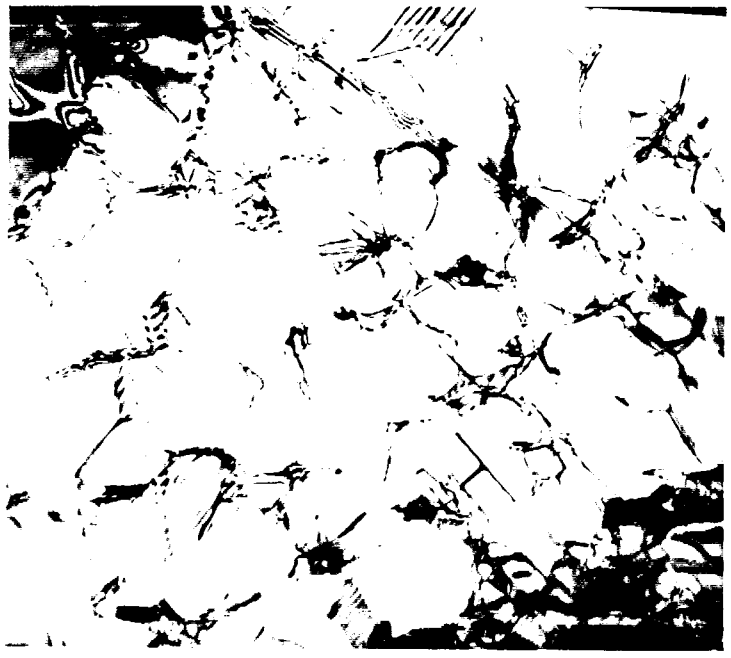


Figure 78. The deformation structure between G2 and G3.



6100 X

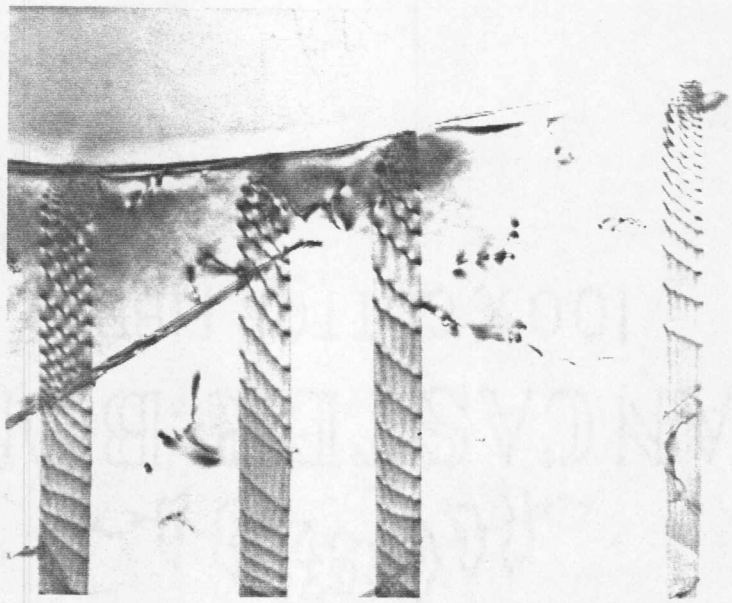
Figure 79. A typical deformation structure formed by in situ straining.



40K X

Stacking faults created from sessile matrix dislocations.

Figure 80. Another typical deformation structure formed by in situ straining.

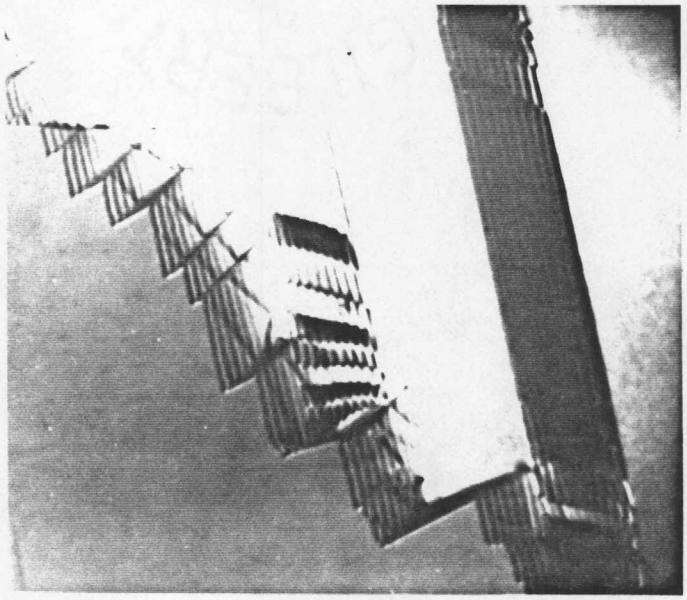


40,000 X

Figure 81. An example of pilled-up dislocations and their reaction with a high angle grain boundary.

(a)

40,000 X



(b)

After a special tilt grain boundary dislocation structure can be observed.

40,000 X

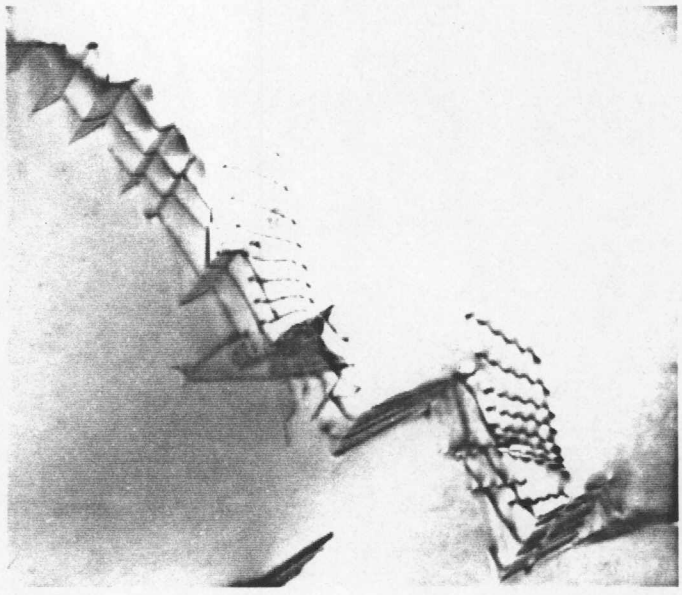


Figure 82. Piled-up dislocations reacting with an incoherent twin boundary.

40,000 X

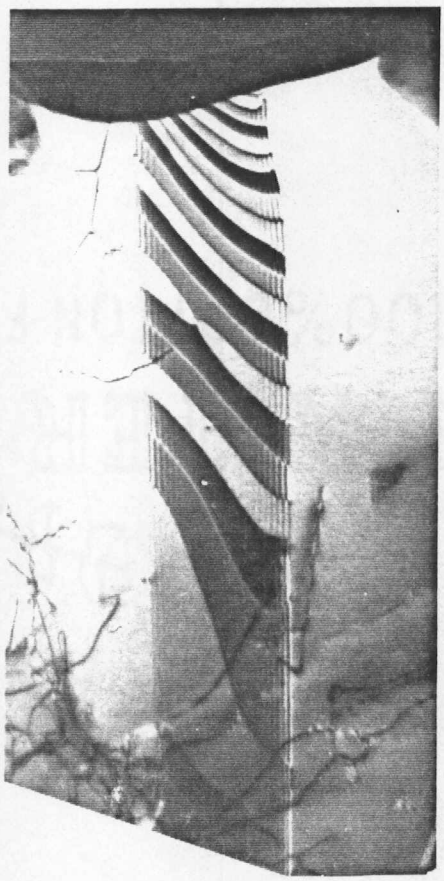


Figure 83. A typical stacking fault contrast exhibiting a periodic sequence.

4.4 Auger Electron Analysis of Fracture Surface

It was desired to examine the high angle, former α grain boundaries along which fracture occurred in many of the embrittled aged alloys in order to determine if element segregation to these boundaries was related to the embrittlement. However, a sample was analyzed in which the grain boundaries recrystallization had occurred, and in this case fracture was along the migrated, high angle boundaries. Thus, it is these boundaries which were analyzed, and the results are reported here. A sample with the proper heat treatment will be analyzed soon.

The sample was prepared as a tensile sample, as shown in Figure 23, and had been solution heat treated then aged for 1000 minutes at 725 °C.

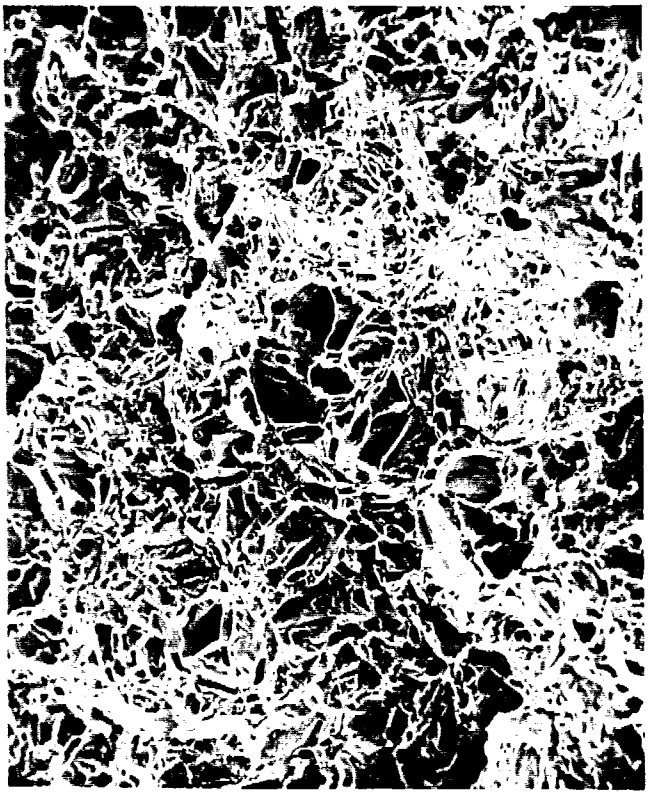
The sample was fractured inside an ultra-high vacuum attachment to an Auger microscope. The straining rate was about 0.2/minute, similar to that used in the tensile tests. After fracture, the sample was transferred under this high vacuum to the Auger analysis chamber. Auger spectra were obtained for several regions, especially those which appeared to be flat. However, the resolution of the electron image was poor, and the regions tested were examined later in a scanning electron microscope in order to obtain clear pictures of the regions of the fracture surface which were analyzed. In the description to follow, only a few of the many analysis are presented;

they are typical of all of those obtained.

Figure 84 shows a region from which an analysis was obtained, and the spectrum is shown in Figure 85a. This region was then sputtered with argon for 2 minutes, in order to remove layers of atoms parallel to the surface, and the freshly exposed surface analyzed; the spectrum is shown in Figure 85b. This procedure was then repeated for an additional 8 minutes, and the spectrum in Figure 85c was obtained.

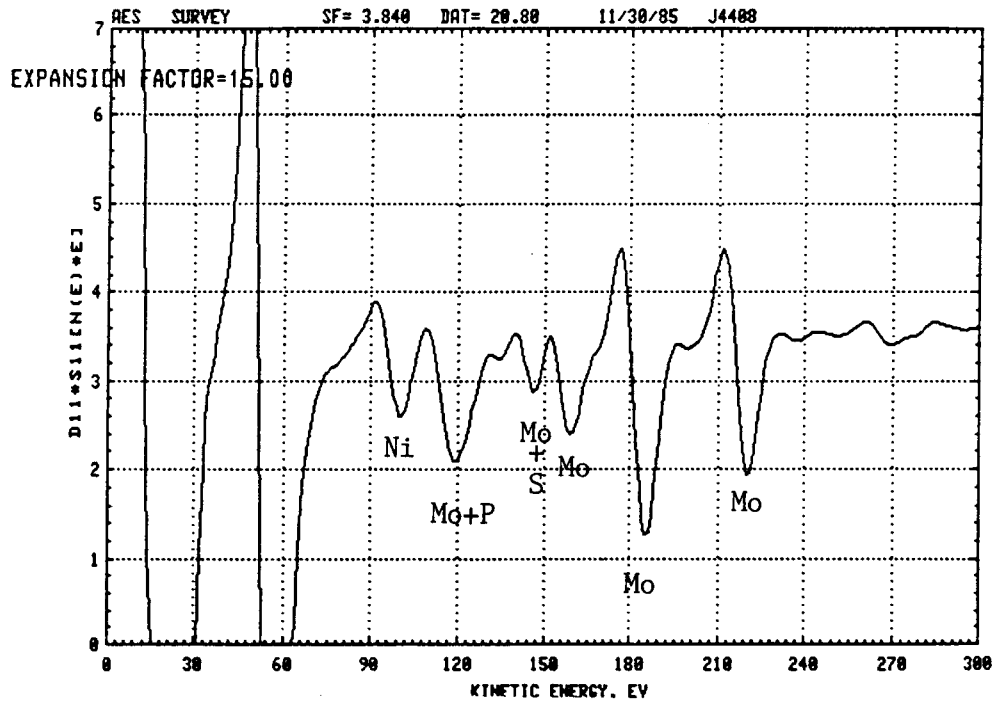
Figures 86 and 88 show two regions at high magnification from which spot Auger analysis were obtained. The Auger analysis of the fracture surface, and of the same regions after sputtering 2 and 10 minutes, are shown in Figures 87 and 89.

All of the analysis show only Ni and Mo. Elements such as carbon and oxygen were not detected. However, the elements S (at 152 eV) and P (at 120 eV) are masked by Mo. Some indication of the presence of these two elements can be obtained by comparing the peak height of a Mo peak with that of a Mo peak which masks these elements. Thus, in Table 20 are listed calculated values of the ratio of the assumed superposed peaks Mo+S (at 148 eV) and Mo+P (at 120 eV) to that of Mo (at 185 eV). Also tabulated is the ratio of Ni (at 102 eV) to Mo (at 185 eV).

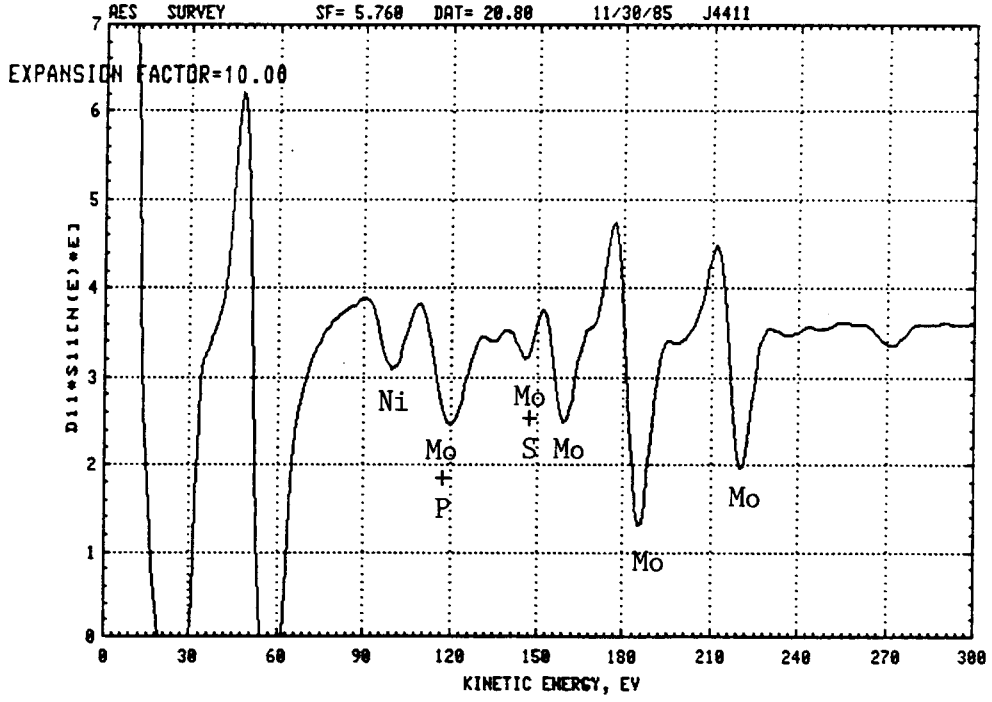


450 X

Figure 84. SEM micrograph showing area analyzed in the Auger microscope.

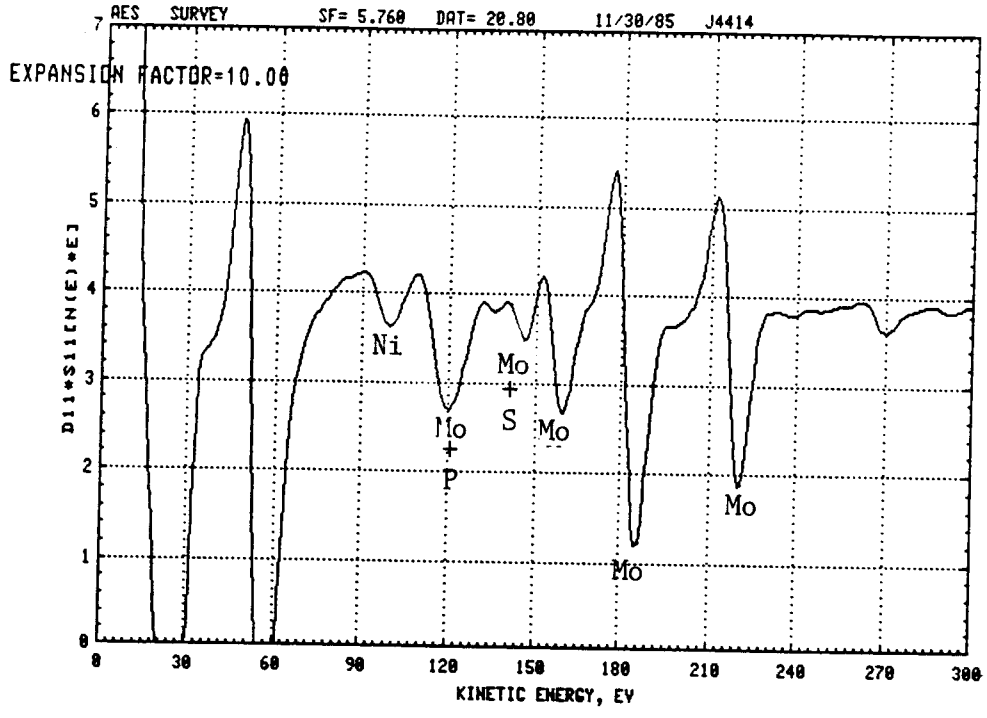


(a) The fresh fracture surface



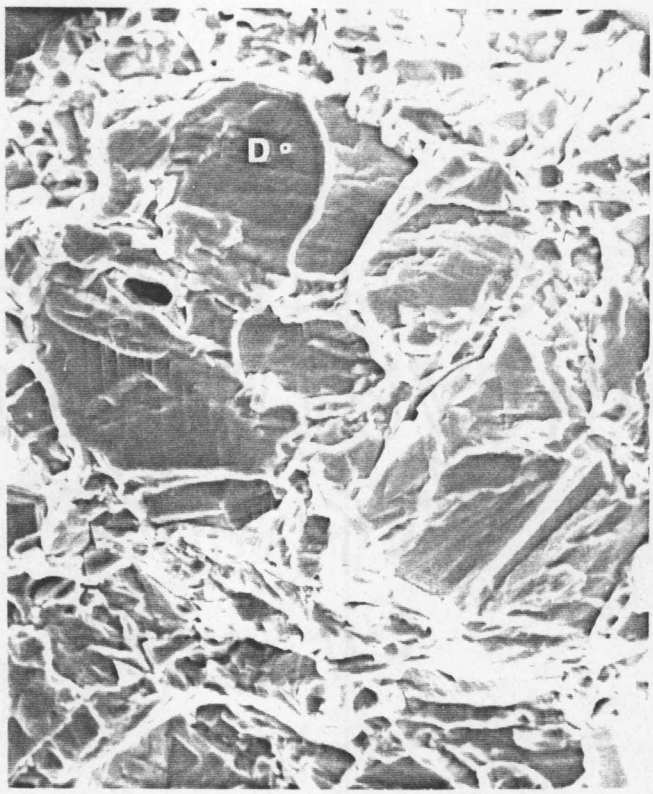
(b) After 2 minutes sputtering

Figure 85. Auger electron spectrum of the area shown in Figure 84.



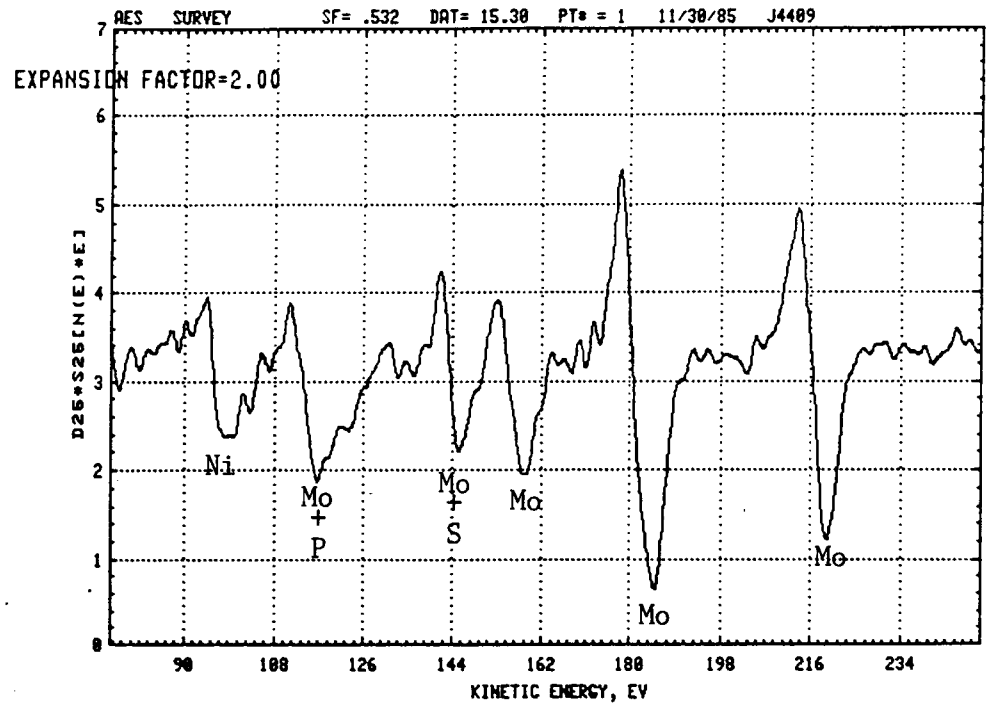
(c) After 10 minutes sputtering

Figure 85. (Continued)

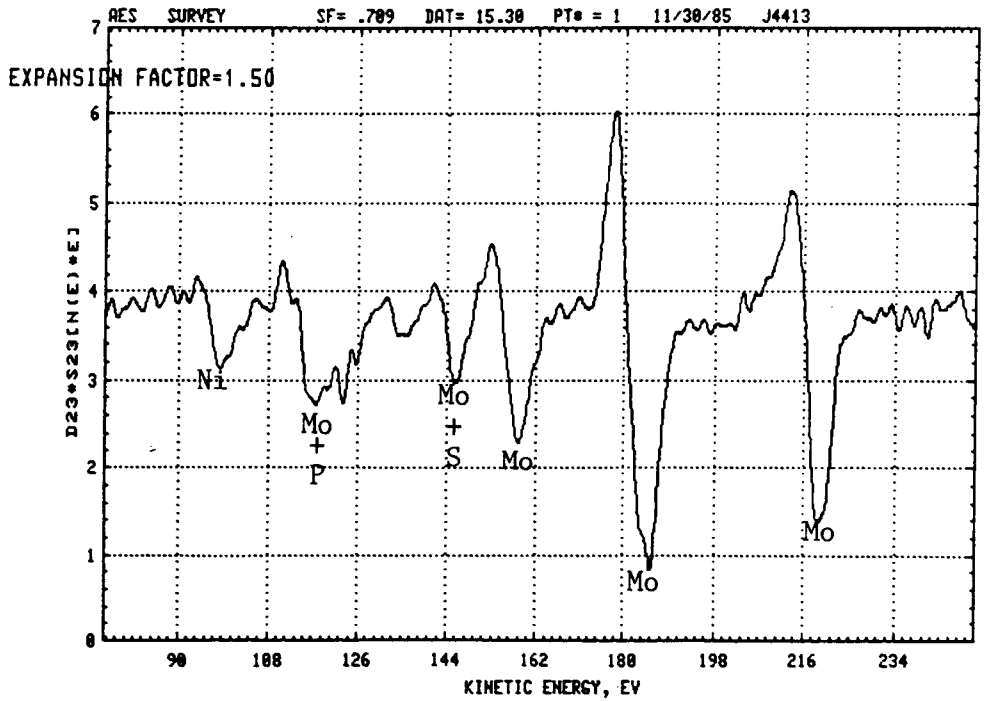


1800 X

Figure 86. SEM micrograph showing location of spot analysis D.

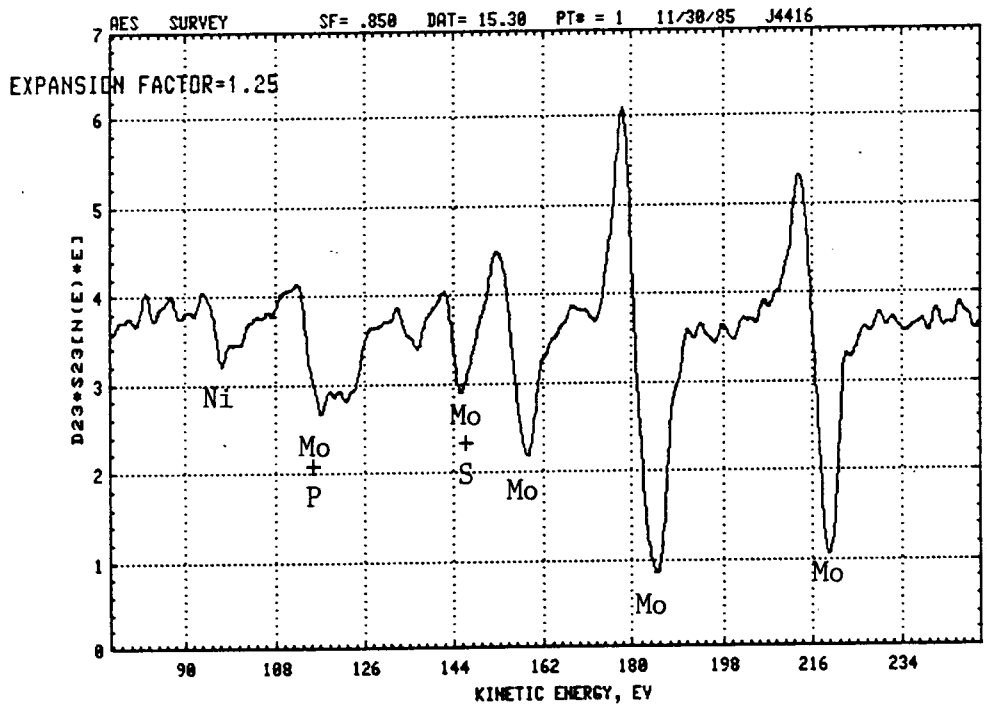


(a) The fresh fracture surface.



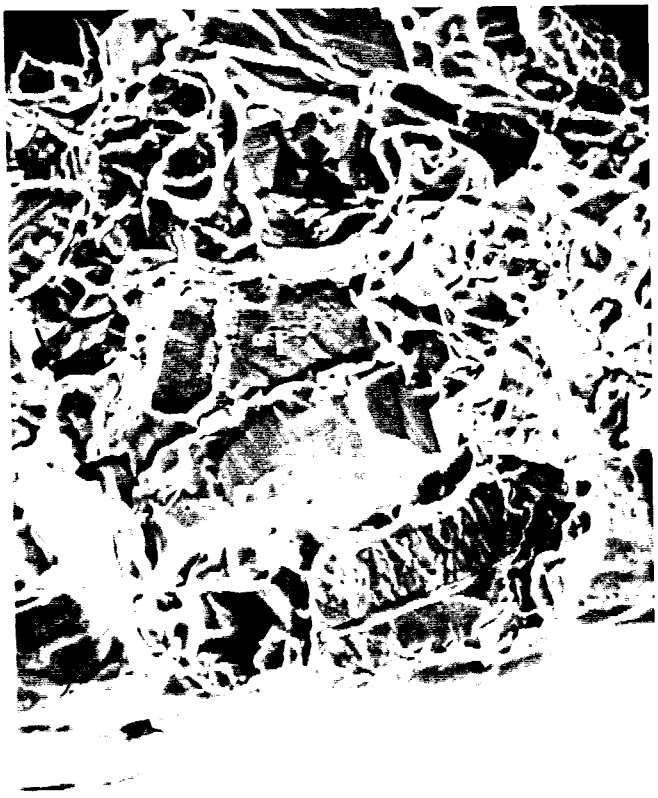
(b) After 2 minutes sputtering.

Figure 87. Auger electron spectrum of the selected spot D (Figure 86).



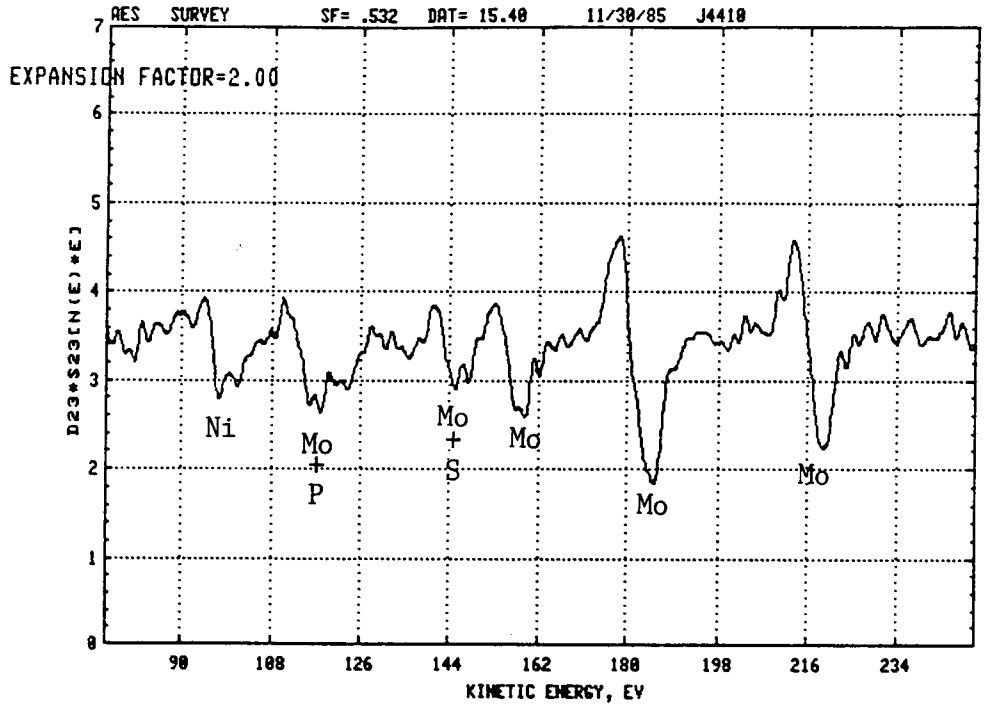
(c) After 10 minutes sputtering.

Figure 87. (Continued)

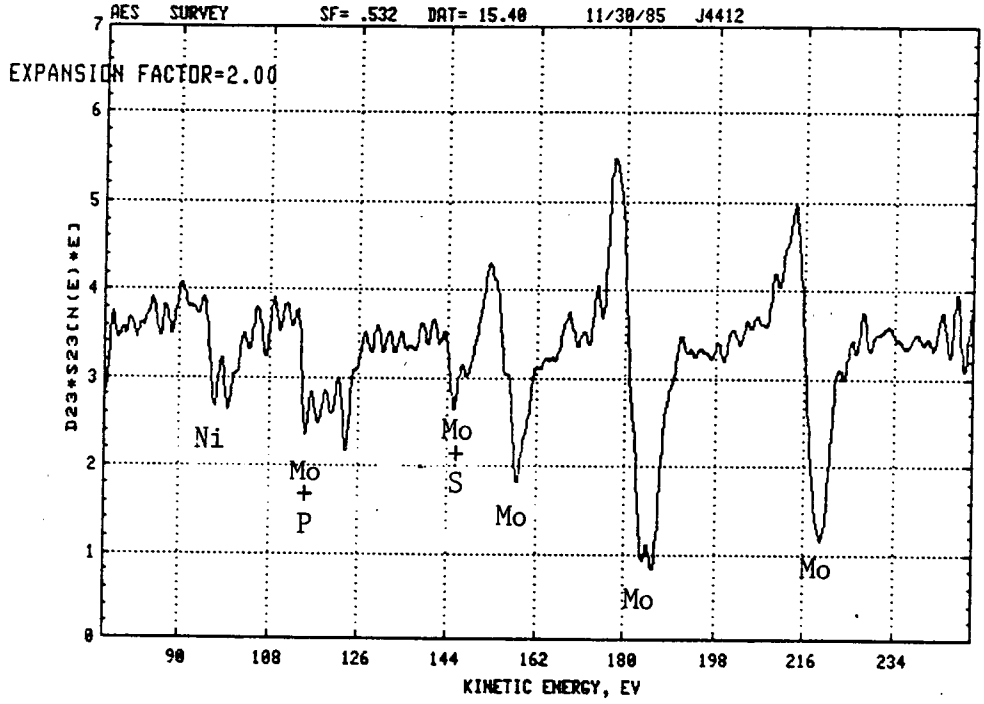


1800 X

Figure 88. SEM micrograph showing location of spot analysis I.

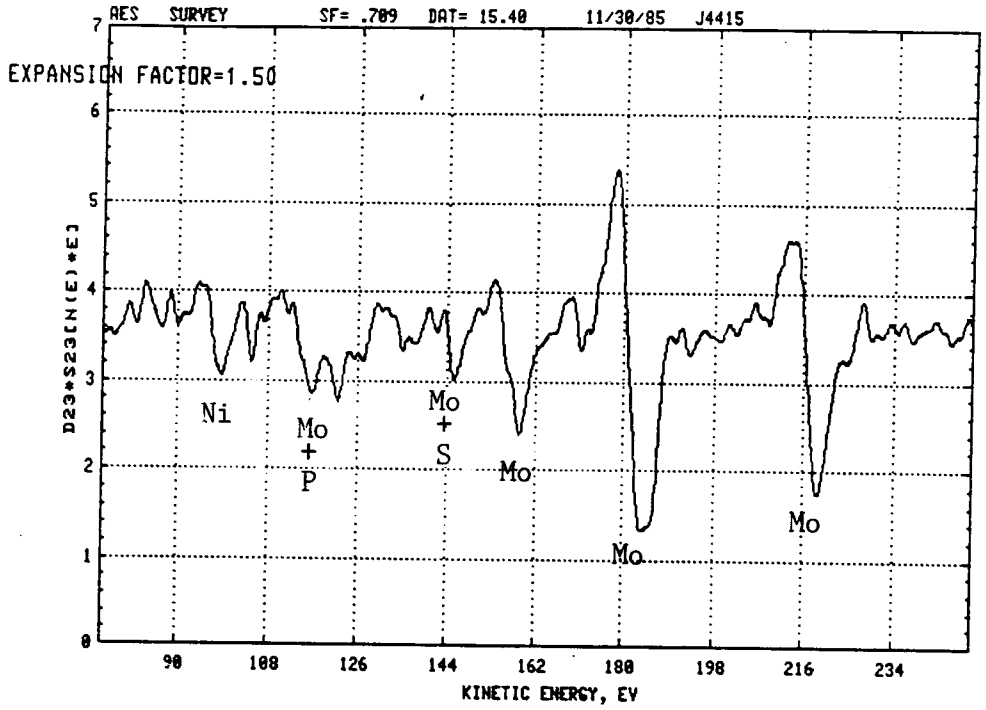


(a) The fresh fracture surface.



(b) After 2 minutes sputtering.

Figure 89. Auger electron spectrum of the selected spot I (Figure 88).



(c) After 10 minutes sputtering.

Figure 89. (Continued)

Table 20. The Auger electron microanalysis of ordered Ni_4Mo alloy

Analysis Area	Analysis Condition	Peak Height (mm)				Each P.H./P.H. of Mo(185)			Fracto-graph	Spectro-scopy
		Ni (102)	Mo+S (148)	Mo+P (120)	Mo (185)	Ni(102)/Mo(185)	Mo+S(148)/Mo(185)	Mo+P(120)/Mo(185)		
Whole Area	Fracture Surface	32.3 23.0	17.0 11.8	40.2 26.7	96.2 57.7	0.336 0.399	0.177 0.205	0.418 0.463	Fig.84	Fig.85a
	2 Minutes Sputtering	14.2	5.8	24.0	61.6	0.231	0.094	0.390	---	Fig.85b
	10 Minutes Sputtering	11.0	7.5	27.5	75.5	0.146	0.100	0.364	---	Fig.85c
Spot D	Fracture Surface	28.2 31.0	36.3 40.5	31.0 32.3	84.8 87.3	0.333 0.355	0.428 0.460	0.366 0.370	Fig.86	Fig.87a
	2 Minutes Sputtering	18.2	20.1	28.3	92.8	0.196	0.217	0.305	---	Fig.87b
	10 Minutes Sputtering	15.4	20.8	26.2	93.9	0.164	0.222	0.279	---	Fig.87c
Spot I	Fracture Surface	20.3	16.9	24.6	50.0	0.406	0.338	0.492	Fig.88	Fig.89a
	2 Minutes Sputtering	22.5	18.0	25.5	82.0	0.274	0.220	0.307	---	Fig.89b
	10 Minutes Sputtering	18.3	14.0	20.4	72.5	0.252	0.193	0.281	---	Fig.89c

The differences in the values of the ratios for Mo+S and of Mo+P peaks are considered negligible, within the expected scatter for such an analysis (95). Thus, there is no conclusive evidence of either P or S on the fracture surfaces.

A similar result was obtained by Ogura et al. (96) for Ni_3Al. Using Auger analysis, they did not find any impurities segregation on the grain boundaries in Ni_3Al.

It is to be noted that there is a change in the Ni (at 102 eV) to Mo (at 185 eV) ratio as a function of sputtering time. This could be due to two causes.

(a) A real composition change as a function of depth from the fracture surface.

(b) An artifact of the sputtering process caused by "preferential sputtering" of Ni compared to that of Mo, since for argon sputtering, the yield of Ni is about 2 to 3 times of Mo (for pure Ni and Mo under 5 keV sputtering conditions) (95).

There are no compelling reasons to expect such excessive segregation of Mo at these migrated grain boundaries on which fracture occurred. Thus, it is concluded that the effect is an artifact as described in (b).

4.5 Strengthening Mechanism During Aging

In this section, an examination is made of the data obtained during aging in order to establish the factors that control the strength of ordered Ni_4Mo.

During aging, three structural changes occur which can affect the strength: ordered domains form and grow in size; the degree of order increases; and the elastic strain increases. In this study, the former two were measured for aging at 725 and 775°C. The lattice strain has been measured for aging at 700°C by Ling and Starke (14), and their results will be used to compare to the data at 725°C.

Data of both hardness and yield strength are available for analysis. It was pointed out in the description of the tensile testing that the load-strain curves were used to obtain the 0.2% yield strength. For all the load-strain curves for the ordered alloys (even for rather short aging times), the 0.2% yield strength was very close to the stress at which the sress-strain curve deviated from linearity. Thus, the measured yield strength is a good measure of yielding, and significant strain hardening did not begin until the strain was beyond 0.2%. An important disadvantage of using yield strength as a measure of strength in these alloys is their brittleness; the measured values may be quite sensitive to microcracking, although the reproducibility of the yield

strength values was quite good. The point is that the better measure of strengthening is hardness.

At 725 °C, the hardness begins to measurably increase at about 3 minutes, and attains a maximum at about 1,000 minutes (Figure 24). The domain size begins to increase between 100 and 1,000 minutes, and is continuing to increase at 100,000 minutes (Figure 26). As discussed in Section 3.4, the long-range order parameter S must reach a value of about 0.3 for the value to be considered reliable. Upon aging at 725°C, S attains this value in about 3 minutes; reaches a value of about 0.7 after 150 minutes, and a value of unity in about 10,000 minutes. (Figure 27). The data of Ling and Starke (14) show that at 700 °C, the elastic strain reaches a measurable value between 10 and 100 minutes, and reaches an approximate constant value at about 1,000 minutes.

Ling and Starke (14) conclude that the lattice strains that they measured were almost entirely due to dislocations present which were created by domain mismatch strains. From the present work it is also felt that the lattice strain is due to dislocations from this type of origin. However, for the following reasons, it is not felt that these lattice strains, via the dislocations present, make a significant contribution to the strength of the ordered alloy. First, as mentioned above, the measured 0.2% yield strength is very close to the

deviation of the load-strain curves from the linear elastic line. This deviation is a better measure of the yield stress than the 0.2% yield strength, but the closeness of the two indicates that the stress to begin to move the dislocations is about the same as that to continue to move dislocations created by 0.2% plastic strain. Second, the data of Ling and Stark show that the strain is continuing, although at a decrease rate, in the time range where the hardness is about contant, or slightly decreasing (Figure 24).

It is be expected that the domain size would have a prominent effect of the strength, as dislocations cutting domains would develop energetically unfavorably domain boundaries. However, the following reasons are put forward as evidence that this contribution is not important. First, for long aging times the parameter S is greater than 0.9 and the domain size is increasing with increasing time, but the hardness is approximately constant, or only decreases slightly (Figure 24). Also, attempts to correlate the hardness (and the yield strength) with the domain size, via a plot of these properties versus domain size to various exponents (such as 1/2) did not give a plot with any kind of trend. In addition, as will be discussed in the next section, TEM observations show that dislocations moved usually through the lattice without any indication of retardation from the

domain boundaries. This was especially true when the domain size was small. This is the most direct observation that the domain size is not significantly affecting the strength of the ordered alloy.

Now the effect of the degree of long-range order on the strength is examined. Note in Figure 35 that there is a direct relationship between the long range order parameter S and the yield strength. The data in Figure 34 show that the long-range order parameter S is approximately constant up to about 800 ℃, and decreases drastically to zero as the critical temperature of 868 ℃ is approached. The data in Figure 35 show that when S decreases below about 0.7 the hardness (and strength) decrease drastically. It is also important to note that these data were obtained with a constant domain size. This is seen more prominently from the data in Figure 39. These data are for a large domain size (3.5 μm), and it is seen that the hardness is approximately constant for S values from 0.6 to 1.0 (Note that the yield strength decreases only about 20%).

Another indication that the degree of long-range order is the main factor in strength, and not the domain size, is shown by the data in Figure 30 and 32. Here the yield strength and hardness are plotted versus the long-range order parameter S, and values corresponding to treatments at both aging temperatures can be represented

by a common curve, and irrespective of the domain size.

The above analysis shows that the most important factor controlling the strength of the ordered Ni_4Mo is the degree of long-range order. When the ordering reaction starts, very small domains nucleate in the disordered α, or are already present and the cause of the short-range order. Whatever the structure of quenched α, upon aging at 725°C and 775°C, a fine domain structure soon appears (e.g., within 3 minutes), with no α remaining. With continued aging, these domains grow and coarsen. Inside these domains, the structure becomes incresingly long-range ordered, approaching an equilibrium value of about 0.7 at the time at which the hardness maximizes. The hardness remains approximately constant for values of S above 0.7.

One reason that the degree of long-range order is the controlling factor in the strengthening is that the crystal structure formed has less slip systems than the face-centered cubic structure from which it is formed. Also important is that the long-range ordered structure has a considerably lower stacking fault energy than the face-centered cubic α, and hence dislocations decompose into widely separated partials, making cross slip very difficult. (These aspects of the dislocation structure are covered in the next section.) It is also felt that this factor is what allows the strength to remain high

with temperature (Figure 36). Only when a temperature of about 800 °C is reached does the strength begin to decrease; this temperature corresponds to the range where the long-range order parameter begins to decrease below unity.

4.6 Disocation Structure and Strengthening.

From the TEM analysis of the dislocation structure a clearer picture of the role of the dislocations in strengthening in Ni_4Mo is revealed.

Examination of undeformed samples for various heat treatments showed many disocations present. Only 1/2<110> type dislocations were found, and many of these dislocations were in the domain boundaries interfaces. The in situ deformations experiments showed that the dislocations not in the domain boundaries remain sessile during straining. Nearest-neighbor bonding considerations show that these 1/2<110> dislocations should not glide easily because anti-phase boundaries would be created.

It is the dislocations in the domain boundaries that move, forming a band with stacking fault contrast. The formation of these partial dislocations, and their movement, is very erratic and sudden. As deformation proceeds, more partial dislocations appear. They are not effectively retarded by domain boundaries, but they do pile up at the high angle, former α grain boundaries,

giving rise to the dependence of the strength on the former α grain size (Figure 40). It is not clear whether these dislocations are partial dislocations which are in the domain boundaries, or whether they are some type of single dislocation which can separate into partials. The in situ observations did indicate that these dislocations move only in one direction. That is, one of which moved in one direction and the other in the other direction.

With continued straining, more dislocations form on adjacent {111} planes in the bands, revealed by overlapping stacking fault contrast, and eventualy thin twins develop from these bands. This is referred to as a twin mechanism, but it is not the same as the conventional macroscopic twinning. Although the formation of such twins has been observed before (89) and discussed, the mechanism of their formation is not clear. Models put forward to explain their formation are complex (89).

There are two features which account for the strength of ordered Ni_4Mo. One is the change in crystal structure. The prediction of the observed 1/6<112> single Burgers vector partial dislocation, and the absence of the other types, based on determination of the change in the type and number of nearest-neighbor bonds, clearly shows that the reduction in the number of slip systems is a factor in strengthening. However, probably the most important factor is that upon deformation of the ordered alloy, the

glissile dislocation structure consists of widely separated partial dislocation. For the alloy in the disordered conditions, any separation into partials is slight (e.g.,<50Å). But upon deforming the ordered alloy, the domain boundary dislocations form widely separated partials, which essentialy make cross slip impossible before grain boundary fracture occurs (see next section).

The reason that the partial dislocations are much more widely separated in the ordered structure than the disordered structure is not clear. The separation is very great, being perhaps several microns for the ordered alloy (but only about 50 Å in the disordered alloy). The separation distance betwen partial dislocations is proportional to the product of the square of the Burgers vector and the elastic shear modulus, and inversely proportional to the stacking fault energy. The difference in the Burgers vector and the shear elastic modulus between the disordered and the ordered structre cannot account for the large difference in partial dislocation separation. Thus, the wide separation in the ordered alloy must be caused by a greatly lowered stacking fault energy.

4.7 The Cause of Embrittlement in Ordered Ni_4Mo

The observations made in this research lead to the conclusion that the brittleness of the ordered Ni_4Mo alloy is due to lack of slip and intrinsic weakness of the high angle boundaries. Basically, upon deformation, the widely separated partial dislocations, which are incompatable with the lattice across such a boundary and which also cannot easily cross slip, pile up at the high angle boundaries. Continued deformation builds the local stress at these boundaries to a level that the intrinsic boundary separation strength is exceeded.

That the intrinsic strength of the high angle boundary is the limiting factor here is revealed by two observations. For short aging times, for which the grain boundary recrystallization structure has yet to begin to form, but for which the alloy is brittle, fracture occurs along the high-angle, former α boundaries. For longer aging times, these grain boundary regions are covered by the recrystallization product consisting of a coarser domain structure. However, this product forms by the migration of the high angle boundaries. With this microstructure, the alloy is still quite brittle, but now fracture occurs by separation along the migrated boundaries, and not at the original location of the boundaries. Note that these migrated boundaries are still the high angle boundaries. Thus, the fracture along the

high angle boundaries, for aging times prior to the appearance of the recrystallization structure, cannot be due to an intrinsic weakness due to impurity segregation at the original location of the high angle boundaries. Also, the Auger analysis, even though it was of the fracture surfaces of the samples which had the grain boundary recrystallization structure, showed no evidence of impurity segregation.

Thus, all of the information points towards the weakest location in the structure being the high angle boundaries. Takasugi and Izumi (97) examined the fracture surfaces of the ordered compound Ni_3Al, which fractures brittlely along the high angle boundaries. They found no impurity segregation, and concluded that fracture occurred because the intrinsic grain boundary strength was exceeded. They discuss the reasons for this weakness in terms of the distribution of electron charge along the grain boundary. The issue of grain boundary embrittlement is very complex and not well understood.

It is clear that for commercial development of ordered Ni_4Mo the grain boundary embrittlement must be prevented. One avenue of study is to examine the effect of boron additions, a method which has been succesful in preventing such embritlement in Ni_3Al (27).

CHAPTER 5

CONCLUSIONS AND RECOMMENDATIONS

Conclusions

(1) Upon aging at 725 and 775°C, the ordering reaction proceeds by the formation of a fine domain size within minutes, followed by a continued coarsening. Also, a "recrystallization" reaction began at the high, prior α grain boundaries by the migration of the boundaries, leaving behind a coarser domain structure.

(2) During aging, the degree of long-range order increases, and follows the relationship $\ln(1-S)=G\cdot\exp(-Q/RT)\cdot t^{n-2/2}$. where n=3.3; $G=1.80X10^{31}/sec^{0.39}$ and $Q=8.12X10^{5}$ J/mole (19,400 cal/mole).

(3) The domain size follows the relationship $D^{n}-D_{o}^{n}=K\cdot t\cdot\exp(-Q_{d}/RT)$. where n=2.4; $K=7.78X10^{28}/sec$ and $Q_{d}=5.31X10^{5}$ J/mole (127,000 cal/mole).

(4) During aging, the strength and hardness approximately double, and the alloy becomes very brittle, fracturing along the former α grain boundaries. This embrittlement persists up to the maximum aging time (100,000 minutes).

(5) The degree of long-range order is much more important in strengthening than is the domain size.

(6) For the same domain size and degree of long-range order, the yield strength was dependent on the prior α grain size, given by $\sigma_y = \sigma_o + K \cdot d^{-3/4}$. where σ_o=79,000 psi and K=406,000 psi $(\mu m)^{3/4}$.

(7) The ordered Ni_4Mo shows good resistance to softening at high temperatures. The yield strength is approximately constant up to 800°C (although the alloy remains brittle), and the strength is comparable to the superalloy Waspaloy. Thus, the ordered Ni_4Mo has good potential to be used as a high temperature structural material.

(8) The aged, undeformed material contained 1/2<110> dislocations in the matrix and in the domain boundaries. The matrix dislocations were sessile, but the domain dislocations were glissle (see below).

(9) The deformation structure of Ni_4Mo consisted mainly of overlapping {111}, intrinsic type, stacking faults on a distinct slip trace. These faults were bounded by widely separated partial dislocations. Upon sufficient deformation, some of these bands had thickened into twins. The dislocations piled up at the high angle, former α boundaries, but moved freely across the domain boundaries.

(10) The gliding dislocations in the plastic deformation bands (whether initiated by tension, rolling or in situ deformation) always belonged to 1/6<112> type, sigle Burgers vector, partial dislocations.

(11) In situ deformation experiments showed that the dislocations in the domain boundaries separated into partial dislocations. Additional dislocations on adjacent slip planes formed into bands of overlapping stacking faults.

(12) Five unit superdislocations were only very rarely observed.

(13) Considerations of the nearest neighbor bonding predicted the 1/6<112> type dislocation.

(14) The two factors which cause the strengthening upon ordering are the reduction in the number of slip systems and the widely separated partial dislocations, which make cross slip impossible. This latter factor is believed to be caused by the very low stacking fault energy of the ordered structure.

(15) The brittleness of the ordered alloy is caused by the pile up of dislocations at the high angle, prior α grain boundaries (across which they cannot propogate), which causes a high localized stress and grain boundary separation.

(16) The Auger analysis indicated that the high angle boundaries in the ordered structure are intrinsically weak, and not weak because of impurity segregation.

Recommendations

(1) It is recommended that a more detailed study be made of the dislocation development using the in situ straining stage of the TEM. The samples used in this study should be examined in more detail, and also samples for short aging times, where the domain size is small but for which grain boundary fracture occurs, should be examined.

(2) An Auger analysis should be made of a sample for short aging time for which fracture is intergranular, along the prior α boundaries, and of a sample for very long aging times, for which similar fracture occurs.

(3) The dislocation structure of the samples tested at high temperatures should be examined in more detail, in order to more clearly establish the types of dislocations present.

(4) The effect of boron additions on the embrittlement should be examined, as this may alleviate this problem.

(5) An examination of possible alloying additions to Ni_4Mo to further increase the strength, and especially the high temperature strength, should be carried out.

REFERENCES

REFERENCES

1. Hastelloy-Developmental alloy B-2, Stellite Division, Cobot Corp, Kokomo, Indiana (1974).

2. W. Z. Friend, Corrosion of Nickel and Nickel-base Alloys, New York: Wiley (1980).

3. H. M. Tawancy,"Ordering Behavior and Corrosion Properties of Ni-Mo and Ni-Mo-Cr Alloys"; in High-Temperature Ordered Intermetallic Alloys, (Edited by C. C. Koch, C. T. Liu, and N. S. Stoloff), MRS, 39, 485 (1985).

4. J. H. Westbrook (ed.), Mechanical Properties of Intermetallic Compounds, New York: Wiley (1967).

5. N. S. Stoloff and R. G. Davies, Prog. Mater. Sci., 13, 1 (1966).

6. B. H. Kear, C. T. Sims, N. S. Stoloff and J. H. Westbrook (eds), Ordered Alloys, Baton Ronge: La. Claitor's Publishing Division (1970).

7. N. S. Stoloff,"Intermetallic Compounds and Ordered Phases"; in Strengthening Methods In Crystals, (Edited by A. Kelly and R. B. Nicholson), ASM, 193-257 (1971).

8. N. S. Stoloff, Int. Met. Rev., 123, 29(3) (1984).

9. H. Warlimont (ed.), Order-Disorder Transformation in Alloys, New York: Springer-Verlag (1974).

10. R. E. Clausing, P. Patriarca, and W. D. Manly, Trans. ASM, 51, 123 (1959).

11. C. R. Brooks and J. E. Spruiell, and C. K. H. DuBose, Mater. Res. Bull., 3, 381 (1968).

12. B. Chakaravarti, E. A. Starke and B. G. Lefevre, J. Mater. Sci., 5, 394 (1970).

13. W. B. Snyder and C. R. Brooks, in Ordered Alloys, (Edited by B. H. Kear, C. T. Sims, N. S. Stoloff, and J. H. Westbrook), Baton Ronge: La. Claitor's Publishing Division, 275 (1970).

14. Fu-Wen Ling and E. A. Starke, Acta Met., 19, 759 (1971).

15. T. Saburi, H. Fuji and S. Nenno, J. Phys. Soc., Japan, 35, 1386 (1973).

16. R. S. Irani, Fu-Wen Ling and R. W. Cahn, Metallography, 6, 141 (1973).

17. K. C. Chen, Fu-Wen Ling and E. A. Starke, Mater. Sci. Eng., 13, 255 (1974).

18. G. I. Nosova and N. A. Polyakova, Phy. Met. Metallogr., 39(4), 140 (1975).

19. D. Y. Roan and C. R. Brooks, Met. Trans., 6A, 1829 (1975).

20. J. E. Spruiell, L. M. Ruch and C. R. Brooks, Met. Trans., 6A, 1301 (1975).

21. G. I. Nosova and N. A. Polyakova, Phy. Met. Metallogr., 42(5), 98 (1976).

22. J. W. Goodrum and B. T. Lefevre, Met. Trans., 8A, 939 (1977).

23. G. I. Nosova and N. A. Polyakova, Phy. Met. Metallogr., 46(3), 178 (1978).

24. L. A. Nesbit and D. E. Laughlin, Acta Met., 28, 989 (1980).

25. G. I. Nosova and N. A. Polyakova, Phy. Met. Metallogr., 47(5), 139 (1980).

26. C. R. Brooks, J. E. Spruiell and E. E. Stansbury, Int. Met. Rev., 29(3), 210 (1984).

27. C. T. Liu, C. L. White and J. A. Horton, Acta Met., 33, 213 (1985).

28. K. Aoki and O. Izumi, J. Jpn. Inst. Met., 43, 1190 (1979).

29. E. Schulson and D. R. Barker, Scripta Met., 17, 519, (1983).

30. C. C. Koch, J. A. Horton, C. T. Liu, O. B. Cavin and J. O. Scarborough, Proc. 3rd Int. conf. on Rapid Solidification Processing, (Edited by R. Mehrabian), pp. 264-9, NBS, Gaithersburg, Md, Dec. (1982).

31. C. C. Koch,"A Review of Rapid Solidification Studies of Intermetallic Compounds", in High-Temperature Ordered Intermetallic Alloys, (Edited by C. C. Koch, C. T. Liu and N. S. Stoloff), MRS, 39, 397, (1985).

32. C. T. Liu, Int. Met. Rev., 29(3), 168 (1984).

33. S. K. Das, L. A. Davis, J. R. Y. Wang and D. Kapoor., in Third conference on RSP, Gaithersbug Md., 559, Dec. (1982).

34. K. Sumino, Sci. Rept. Res. Inst. Tohuku Univ., A10, 283 (1958).

35. J. S. Koehler and F. Seitz, J. App. Mech., 14, 217 (1947).

36. N. S. Stoloff and R. G. Davis, Acta Met., 12, 473 (1964).

37. G. W. Ardley, Acta Met., 3, 525 (1955).

38. A. H. Cottrel, in Relation of Properties to Microstructure, ASM, 151 (1953).

39. J. C. Fisher, Phys. Rev., 91, 232 (1953).

40. R. W. Guard and J. H. Westbrook, Trans. AIME, 215, 805 (1959).

41. V. Gerold and H. Haberkorn, Phys. Status Solidi, 16, 675 (1966).

42. A. U. Seybolt and J. H. Westbrook, Acta Met., 12, 449 (1964).

43. R. P. Elliott, Constitution of Binary Alloys, First Suppl., New York: McGraw-Hill (1965).

44. M. Hansen and K. Anderko, Constitution of Binary Alloy, New York: McGraw-Hill (1958).

45. F. A. Shunk, Constitution of Binary Alloys, Second Suppl., New York, McGraw-Hill (1969).

46. R. E. W. Casselton and W. Hume-Rothery, J. of the Less Common Metals, 7, 212 (1964).

47. P. V. Guthrie and E. E. Stansbury, X-ray and Metallographic Study of the Nickel-Molybdenum System II, Report ORNL 3078, Oak Ridge National Laboratory, Tenn. (1961).

48. C. P. Heijwegen and G. D. Rieck, Z. Metalallkd., 64, 450 (1973).

49. E. V. Kozlov and V. M. Kushnayenko, Phys. Met. Metallogr., 46, 75 (1978).

50. W. Gest, T. Nguyen-Tat and B. Predel, Z. Metallkd., 70, 241 (1979).

51. T. S. Lei, Ph.D. Dissertation, University of Tennessee (1979).

52. G. Grube and H. Schlect, Z. Electrochem., 44, 413 (1938).

53. D. Harker, J. Chem. Phys., 12, 315 (1944).

54. P. R. Okamoto and G. Thomas, Acta Met., 19, 825 (1971).

55. E. Ruedl, P. Delavignette and S. Amelinckx, Phys. Status Solidi, 28, 305 (1968).

56. J. E. Spruiell and E. E. Stansbury, J. Phys. Chem. Solids, 26, 811 (1965).

57. J. E. Spruiell, PhD Dissertation, University of Tennessee (1963).

58. T. Saburi, E. Kanai and S. Nenno, J. Less-Common Met., 37, 59 (1974).

59. H. M. Tawancy, Scripta Met., 18, 343 (1984).

60. H. Thomas, Z. Phys., 129, 219 (1951).

61. P. C. Clapp and S. C. Moss, Phy. Rev. 171, 764 (1966).

62. Chakravarti, E. A. Starke, Jr. C. I. Sparks and R. O. Williams, J. Phys. Chem. Solids, 35, 1317 (1974).

63. G. Van Tendeloo, Mater. Sci. Eng., 26, 209 (1976).

64. T. Saburi, K. Komatsu, M. Yamamoto, S. Nenno and Y. Mizutani, Trans. AIME, 245, 2348 (1969).

65. S. K. Das and G. Thomas, in Order-Disorder Transformations in Alloys, (Edited by H. Warlimont), New York: Springer-Verlag, 332 (1974).

66. W. M. Stobbs and J. P. Chevalier, Acta Met., 26, 233 (1978).

67. J. P. Chevalier and W. M. Stobbs, Acta Met., 27, 1197 (1979).

68. M. Yamamoto, S. Nenno, T. Saburi and Y. Mizutani, Trans. Jpn. Inst. Met., 11, 120 (1979).

69. J. P. Chevalier and W. M. Stobbs, Acta Met., 24, 535 (1976).

70. G. Thomas and R. Sinclair, Acta Met., 25, 231 (1977).

71. S. K. Das, P. R. Okamoto, P. M. Fisher and G. Thomas, Acta Met., 21, 913 (1973).

72. B. G. Lefevere and R. W. Newman, in ApplicatIon of Field Ion Microscopy in Physical Metallurgy and Corrosion, (Edited by R. F. Hochman et al.), Georgia Institute of Technology, 243 (1969).

73. L. E. Tanner and H. J. Leamy, in Order-Disorder Transformation in Alloys, (Edited by H. Warlimont), New York: Springer-Verlag, 180 (1974).

74. T. Saburi, K. Komatsu and S. Nenno, Phil. Mag., 20, 1091 (1969).

75. H. E. Cook, Mater. Sci. Eng., 25, 127 (1976).

76. Y. N. Vlasova, Phys. Met. Metallogr., 23, 113 (1967).

77. G. I. Nosova and N. A. Polyakava, Phys. Met. Metallogr., 47, 139 (1980).

78. L. A. Nesbit and D. E. Laughlin, Acta Met., 26, 815 (1978).

79. S. J. Block, MS thesis, University of Tennessee (1961).

80. F. W. Ling and E. A. Starke, in Advances in X-ray Analysis, Vol. 15 (ed. K. F. J. Heinrich et al.), New York: Plenum, 319 (1974).

81. F. W. Ling and E. A. Starke, Scripta Met., 5, 741 (1971).

82. K. Vasudevan, MS Thesis, University of Tennessee (1982).

83. R. J. Arsenault and J. H. Frye, Acta Met., 12, 1303 (1964).

84. T. C. Tiearney and N. J. Grant, Met. Trans., 13A, 1827 (1982).

85. Y. Nakada and T. C. Tisone, in Second International Conference on the Strength of Metals and Alloys, Vol. I. 288, Metals Park, Ohio, American Society for Metals (1970).

86. P. A. Flinn, Trans. AIME, 218, 415 (1960).

87. E. M. Schulson,"The Effects of Grain Size on the Flow and Fracture of Long-range Ordered Alloys", in High-Temperature Ordered Intermetallic Alloys, (Edited by C. C. Koch, C. T. Liu and N. S. Stoloff), MRS, 39, 193 (1985).

88. J. Friedel, Dislocations, Addison-Wesley Publishing Co. Readind Mass. (1964).

89. J. P. Hirth and J. Lothe, Theory of Dislocations, New York: Mcgraw-Hill (1968).

90. P. B. Hirsch, A. Howie, R. B. Nicholson, D. W. Pashley and M. J. Whelan, Electron Microscopy of Thin Crystals, Krieger, New York (1977).

91. H. Hashimoto, A. Howie, and M. J. Whelan, Phil. Mag. 5, 967 (1962).

92. J. A. Venables, in Deformation Twinning, (Edited by R. E. Reed-Hill, J. P. Hirth, and H. C. Rogers), Gordon and Breach, New York (1964).

93. N. Thompson, in Fracture, (Edited by B. L. Averbach, D. K. Felbeck, G. T. Hahn and D. A. Thomas), Wiley, New York, 369 (1959).

94. H. Gleiter and H. P. Klein, Phil. Mag., 27, 1009 (1973).

95. C. L. White, Oak Ridge National Laboratory, Private Discussion, Jan. (1986).

96. T. Ogura, S. Handa, T. Masumoto and O. Izumi, Met. Trans., 16A, 441 (1985).

97. T. Takasugi and O. Izumi, Acta Met., 33, 1247 (1985).

VITA

The author was born in the Taiwan Province of Republic of China on Aug. 13, 1950. He earned his Bachelor degree in the Material Science Department at the Chung-Chen Institute of Technology in 1972. After two years army service, he entered the Mechanical Engineering Department of Chung-Chen Institute of Technology in the Fall of 1974, and received a M.S. degree in Mechanical Engineering in the Summer of 1976. He got a job as an assistant researcher in Chung-Shan Institute of Science and Technology (CSIST) in Taiwan. After five and half years service, he was sent to America to continue his Ph.D. research program sponsored by CSIST. He entered the Chemical, Metallurgical and Polymer Engineering Department (now Material Science and Engineering Department) of The University of Tennessee, Knoxville, in the Spring of 1982. He is a member of the American Society for Metals, the Materials Research Society and Chinese Engineering Society.